Characterisation of Mechanically Alloyed Feedstock for Laser-Powder Bed Fusion: Titanium Silicon Carbide Metal Matrix Composite

IAIN LYALL

A thesis submitted in partial fulfilment of the requirements of the University of Wolverhampton for the award of Doctor of Philosophy

March 2020

Declaration:

This work or any part thereof has not previously been presented in any form to the University or to any other body whether for assessment, publication or for any other purpose (unless otherwise indicated). Save for any express acknowledgements, references and/or bibliographies cited in the work, I confirm that the intellectual content of the work is the result of my own efforts and of no other person.

Signature.....

Date.....

Acknowledgements

The author would like to express gratitude to my supervisors Professor Mark Stanford, Professor Kevin Kibble, Dr Arun Arjunan and Professor Nduka Nnamdi Ekere for their patience and guidance throughout this period of study. My sincere thanks to the staff within the Faculty of Science and Engineering at the University of Wolverhampton and specifically to those within the School of Engineering who have advised and guided me.

The author would also like to thank the industrial manufacturers of the equipment used during this research. Many items were new not only to me but also the manufacturers and I appreciate their patience while we found innovative solutions to challenging questions. I look forward to continuing this relationship in expanding the limits of the technology.

The author would also like to thank the technical staff within the Faculty of Science and Engineering and specifically to those within the School of Engineering who have advised guided and supported me.

Abstract

The research presented investigates the characterisation of new materials for the additive manufacturing (AM) industry. Herein, a metal matrix composite (MMC) with a titanium ($Ti6Al_4V$) matrix reinforced with silicon carbide (SiC) is characterised. The research investigated an innovative and novel feedstock production process involving elements of mechanical alloying, tailored to the requirements of the layer based additive manufacturing (ALM) process. Systematic evaluation and subsequent characterisation of process parameters including laser power, scan speed and hatch spacing are presented.

A new and novel experimental route is discussed. Detailed findings are presented with a robust methodology for producing elemental feedstock in small batch sizes, and process parameter characterisation for in-situ alloying for laser bed fusion.

Evidence showed that acceptable parameters could be found for mechanical alloying with a rotational speed of 500 rev/min and an alloying time of twenty-four minutes that showed minimal and acceptable changes in size and morphology, therefore enabling the feedstock to be used within the Laser-Powder Bed Fusion (L-PBF) process also referred to as Powder Bed Fusion (PBF).

New knowledge is presented in the form of experimental methodologies, namely single bead evaluation in relation to energy density, the evaluation and comparison of single beads, the use of mini-chambers to experiment with reduced levels of feedstock, the two-rail system to accurately deliver powder for single layer experimentation and equations developed to calculate energy density for single beads and the maximum volume of reinforcement material achievable from particle size data.

MMC material was successfully synthesised due to the use of the methodologies described, with silicon carbide (SiC), silicon oxide (SiO_2) and titanium silicide (Ti_5Si_4) detected as chemical compositions within the sample.

Table of contents

List of Figures

List of Tables

Nomenclature

1-Q3 (b/l = 0.850) ..... Inverse Volume fraction of round particles

α ..... Alpha, used to describe a metallic phase

α1 ..... First contact angle

α2 ..... Second contact angle

β ..... Beta, used to describe a metallic phase

b/l ..... Aspect ration

b/l3 ..... Mean aspect ration

c ..... Specific heat capacity (j/kg ^{o}C)

cos *θ* ..... cosine of the contact angle (Deg)

D10 ..... 10 Percentile

D50 ..... 50 Percentile

D90 ..... 90 Percentile

D_m ..... Average particle size ($X_{c\ min}$) of the matrix material (μm)

D_r ..... Average particle size ($X_{c\ min}$) of the reinforcement material (μm)

Ed ..... Energy density

f ..... Volume fraction

f_W ..... Weight fraction of reinforcement material

g ..... Grams

h ..... Hatch spacing

h1 ..... Bead height

h2 ..... Substrate penetration

l ..... Spot size

m ..... Mass (kg)

min ..... Minutes

MVR ..... Maximum Volume of Reinforcement

Mv3($\bar{x}$) ..... Mean sample size

p ..... Density

P ..... Laser power

P_f ..... Density of the reinforcement material (g/cm^3)

P_m ..... Density of the matrix material (g/cm^3)

P ..... Laser power

Q3 ..... Volume based distribution

S ..... Spreading coefficient

s ..... Spot size

sec ..... Seconds

t ..... Layer thickness

v ..... Scan speed

Vol.% ..... Percentage by volume

W ..... Watts

Wt.% ..... Percentage by weight

w1 ..... Width of bead

w2 ..... Width of dilution area

$\bar{x}$ ..... Mean

X_{area} ..... Width of circumferential particle boundary

xc_{min} ..... Shortest particle length

X_{Fe} Max ..... Longest particle length

γ_{sl} ..... solid–liquid interfacial tension (N/m)

γ_{sv} ..... Solid– vapour interfacial tension (N/m)

γ_{lv} ..... Liquid–vapour interfacial tension (N/m)

γ_s^d γ_s^d ..... Dispersion forces (Substrate)

γ_s^p γ_s^p ..... Polar forces (Substrate)

γ_s ..... Surface free energy (mJ/m^2)

ΔEt ..... Change in thermal energy (J)

$\Delta Ø$ ..... Temperature Change (^{o}C)

Glossary of Acronyms.

3D..... Three-Dimensional

Al.....Aluminium

AM ..... Additive Manufacturing

ASTM.....American society for testing and materials

Ar .....Argon

$\mathcal{AR}$.....Aspect Ratio

BCC..... Body Centred Cubic

BPR ..... Ball to Powder Ratio

BS..... British standards

CAD .....Computer Aided Design

C.....Carbon

Co..... Cobalt

DED .....Direct Energy Deposition

DMLS..... Direct Metal Laser Sintering

EDS ..... Energy dispersive X-Ray Spectroscopy

EIGA ..... Electrode Induction melting Gas Atomisation

Fe ..... Iron

FCC .....Face Centred Cubic

GA.....Gas Atomisation

HCP .....Hexagonal Close Packed

H ..... Hydrogen

ISO.....International standards organisation

LM.....Laser Melting

L-PBF.....Laser-Powder Bed Fusion

MA ..... Mechanical Alloying

Mg..... Magnesium

MMC.....Metal Matrix Composite

Mo..... Molybdenum

N_2 ..... Nitrogen

Nd: YAG ..... Neodymium-doped Yttrium Aluminium Garnet (Nd: $Y_3Al_5O_{12}$)

Ni .....Nickel

O_2..... Oxygen

PA ..... Plasma Atomisation

PBF..... Powder Bed Fusion

PM .....Powder Metallurgy

PREP ..... Plasma Rotating Electrode Process

Pt.....Platinum

SC.....Stir Casting

Si .....Silicon

SiC..... Silicon Carbide

SiO_2.....Silicon Oxide

SEM ..... Scanning Electron Microscopy

SPHT ..... Sphericity

STL.....Standard Triangulation Language or Standard Tessellation Language

Ti.....Titanium

TiB_2 ..... Titanium Diboride

TiC ..... Titanium Carbide

Ti_5Si_4 ..... Titanium Silicide

V.....Vanadium

VIM GA ..... Vacuum Induction Melting Gas Atomisation

W ..... Tungsten

Wc.....Tungsten Carbide

XRD ..... X-Ray Diffraction

Papers and Conferences

Robinson, J. Arjunan, A. Stanford, M. Lyall, I and Williams, C (2021) Effect of silver addition in copper-silver alloys fabricated by laser powder bed fusion in situ alloying. *Journal of alloys and compounds*, **857**. 157561.

Lyall, I. Stanford, M. Kibble, K. and Lister, P A. (2015) Reliable manufacture of Additive Layer Manufacturing feedstock for the Selective Laser Melting process via Mechanical Alloying. *FAIM, Flexible Automation and Intelligent Manufacturing*, Wolverhampton, UK, 23rd – 26th June 2015.

Olowofela O. H. Lyall, I. Stanford, M. Zhang, L. Oduoza, C. (2013) Mechanical Alloying (MA) of composite materials for the laser melting (LM) process. *World journal of engineering.*

Chapter One

1.0 Introduction

The adoption of Laser-Powder Bed Fusion (L-PBF) for metal parts is becoming more prevalent. Whilst this is a small proportion of the global three-dimensional (3D) printing industry, it stands at the pinnacle of the 3D industry due to the technological level, engineering expertise and infrastructure required (Algardh, et al., 2017). Technological advances over the last ten years have seen the technology transformed from prototype / rapid visualisation to one of fabricating fully functional parts with additional functionality, unachievable through other processing routs (Gupta 2017, Negi 2013). Current users of the technology have reached a position of confidence with the process, confident that parts manufactured through this manufacturing route will offer, functionality, accuracy, reliability and will be fit for purpose. As the industry expands with new companies joining each year bringing fresh ideas and innovation, the industry has recognised that moving forward there are three key areas of development namely:

- Process,
- Applications,
- Materials (Chalabyan, 2017; Sculpteo, 2017).

1.1 Process

The process of L-PBF is part of the engineering field of AM. Unlike traditional subtractive engineering processes such as machining that begins with a billet of material or casting with the aim of remove material to achieve the components net shape, AM fabricates components through the addition of material to realise the net shape based on a 3D computer model. Within the metal AM industry there are a total of eighteen technologies currently available from one hundred and forty suppliers (AM-power 2020), of these there are three key technological areas currently within the metal AM industry:

- Wire,
- Powder and
- Other AM technologies.

Within wire AM there are four key technologies making up approximately twenty three percent of the AM industry, these are: wire ark, Wire feed, resistance welding and liquid metal printing (AM-power 2020) with twenty-three suppliers.

Other AM technologies represent approximately twenty seven percent of the industry and include: pellet, filament, dispersion rod and sheet technologies (AM-power 2020) and nineteen suppliers.

Powder is the most widespread of these, representing fifty percent of the industry with nine discreet technologies and over one hundred suppliers. The key technologies being blown powder or Direct Energy Deposition (DED), electron beam powder bed fusion and laser beam powder bed fusion. Of these L-PBF represents the majority of the market with approximately sixty suppliers.

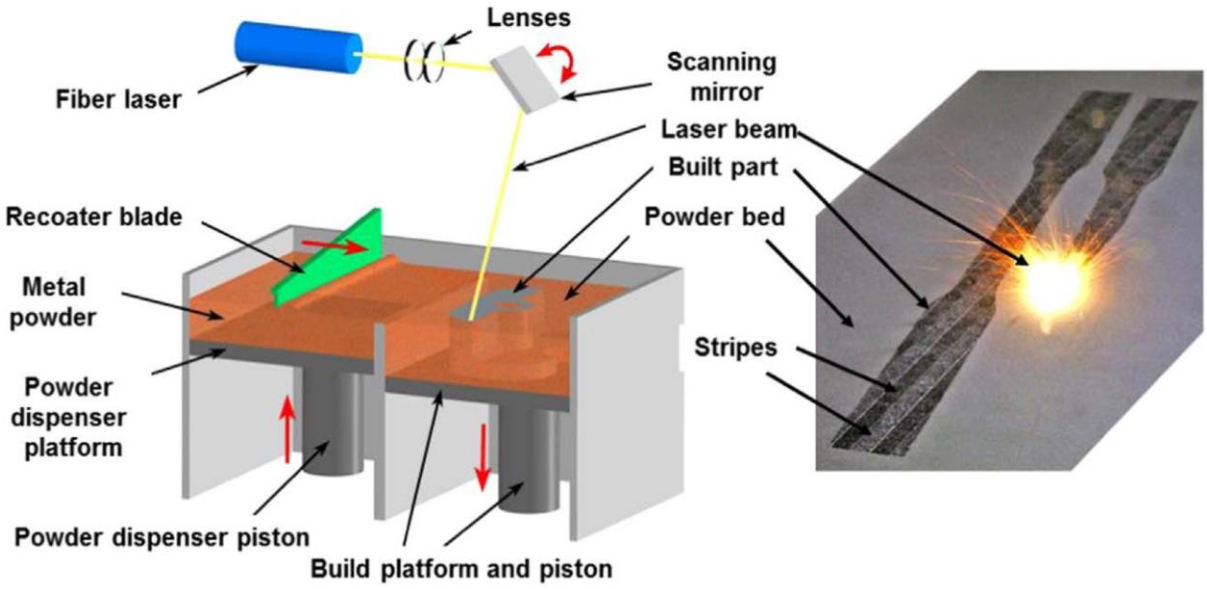

Figure 1 - The laser powder bed fusion system (Criales et al., 2017)

The L-PBF process consists of a flat powder bed typically 250 mm square directly beneath a laser beam to form the build area (Figure 1). Thin layers of powder are accurately spread across this area and predetermined slices of a computer model are exposed by the laser, fusing the powder to the previous layer (substrate). Subsequent layers are exposed with new layers of metal powder until a finished component is constructed. This process is conducted within an inert atmosphere, typically Argon or nitrogen (Criales et al., 2017).

The L-PBF process is advancing with new machines being developed by multiple manufacturers including EOS GmbH, Renishaw Plc, Concept Laser GmbH, Trumpf and SLM Solutions GmbH. Quality, accuracy, and repeatability are key areas of concern for the customer (Sculpteo, 2017) and manufacturers have developed better in-process monitoring and feedback systems that assist in accurately setting the build process and

monitoring it to produce parts with fewer defects and in process build failures. Areas of process development include the development of laser technology, larger build volumes, layer thicknesses, and improved scanning strategies (Sevcik, 2017).

1.2 Applications

Applications are being presented by a range of industrial sectors such as aerospace, space, medical, jewellery, automotive, toolmaking and electronics (Algardh, et al., 2017). However, many sectors wrongly believe that materials used in their industry will translate across to the L-PBF process. As more research is undertaken into how materials behave during L-PBF processing, it is becoming evident that simply converting metals to powders and building with them does not work (Cordova, et al., 2019). Materials when processed as powders exhibit qualities unlike their wrought or cast counterparts (Kusuma, 2014). Post-processing has also demonstrated that established regimes for wrought and cast materials do not translate directly, hence new regimes are needed to be developed (Renishaw PLC. 2016).

1.3 Materials

Materials that are suitable for the PBF process have traditionally been slow to be introduced to the marketplace due to the extensive and time-consuming development process required for characterisation. Current materials such as titanium alloys (Ti6Al4), aluminium alloys (Al), maraging steel, cobalt chrome steel, Inconel 718 and stainless steel have been available for some time now (Eos GmbH, 2018). Research into new materials such as gold, silver (Cooksongold 2016, Robinson, et al., 2020), copper (Citim-am 2016), Waspaloy and zirconia (Mumtaz, and Hopkinson, 2007) exemplifies that the industry requires complex materials for specific applications and therefore by association a robust method of characterising materials adequately for further “end user optimisation” is needed (Locker, 2018).

1.4 Research Justification

This research investigates the characterisation of titanium (Ti) based Metal Matrix Composites (MMCs) with silicon carbide (SiC) reinforcement, employing Laser-Powder Bed Fusion (L-PBF) techniques and the theoretical feasibility of processing such materials. MMCs are difficult to process using conventional material-removal techniques; material-removal is normally kept to a minimum while processing, as this requires specialised tooling or grinding processes to achieve satisfactory components (Kainer, 2006). This can be cost prohibitive and time-consuming (3T RPD, 2018). Through the additive route, however, the manufacture of components is achieved by the fabrication of near net shape parts in individual layers requiring minimal finishing to

only the critical surfaces, an allowance of around 0.2 mm to 0.4 mm is added to the CAD model at the design stage (Vrancken, et al., 2014).

Currently, the additive manufacturing (AM) industry is experiencing high confidence in manufacturers and their equipment. Sales of equipment have been steadily increasing year on year (Figure 2).

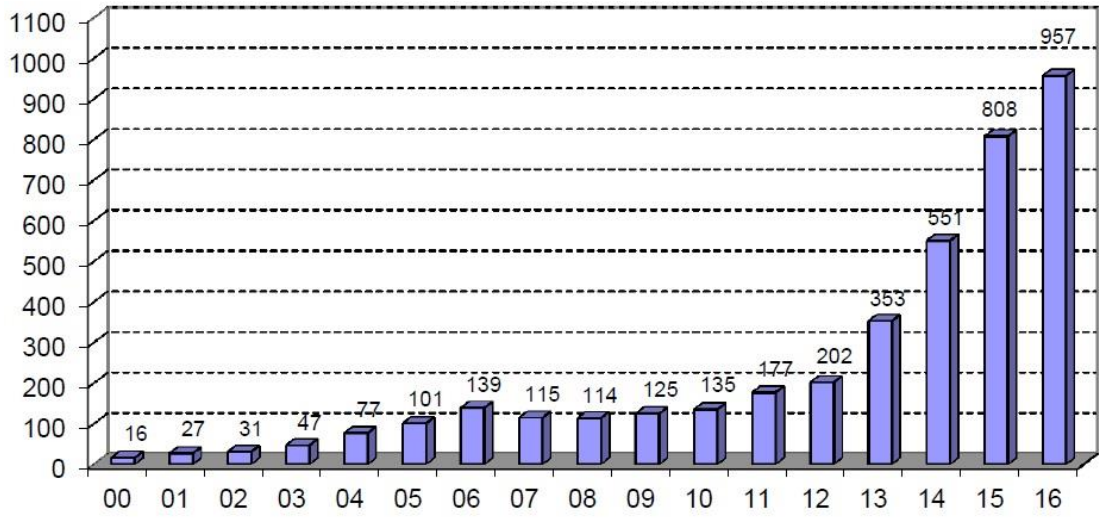

Figure 2 - Number of AM systems for metal parts sold, according to Wohler's report 2017 (Algardh, et al., 2017)

However, the development of materials (Feedstock) for the process has been slow in comparison.

Algardh (2017) wrote about the number of alloys available, voicing concerns over, what he called "a tedious and expensive process with trial and error" the overriding conclusion from his work was that if PBF is more widely adopted, a larger number of materials and materials suppliers were required.

Table 1 shows current powders available to the PBF process (Algardh, et al., 2017).

Table 1 - Powders available for PBF manufacturing (Algardh, et al., 2017)

Stainless	Fe-based tool and steel	Titanium	Aluminium	Hard Metals	Nickel based	Cobalt based	Precious
304L S30403 1.4307	H13 T20813 1.2344	Pure Titanium	AlSi12		625 No06625 2.4856	CoCr F75 R31537	Gold
304L S30403 1.4307	X40Cr14 1.2083	Ti6Al4V	AlSi25		718		Silver
420 S42000 1.4034	4140 G41400 1.27225	Ti5Al2.5Sn	AlMg3		738		99.9% Cu
J94224 1.4848	M300 (K93120) 1.2709	Ti6Al2.5Sn	AlSi10Mg		939		CuSn
15-5PH S15500 1.4545	INVAR 36 K93601 1.3912	Ti5Al5Mo5V3Cr	AlSi7Mg		230 No06230 2.4733		
17-4Ph S17400 1.4542		Ti6Al7Nb	AlSi9Cu3		Waspaloy No7001 2.4654		
347 S34700 1.4550			AlMg4.5M No.4		HX No6002 2.4665		
Duplex 2205 S32205 1.4462					C-276 (N10276) (Ni 6276)		
2507 S32750 1.4410					(C-1023)		

Looking at the state of the industry in the UK, Dickens and Minshall (2015) commented on what they considered were the fundamental barriers to the adoption of PBF, namely:

- materials,
- design, skills, and education,
- costs and investment,
- standards and regulations,
- measurement and testing, and
- IP and protection.

Regarding materials, they considered that a better understanding of materials properties was required going forward, but also how the PBF machines affect the material characteristics within the process (Dickens and Minshall 2015).

Powder manufacturers have offered enhancements to existing materials, optimised for the additive process such as "Ancor TiTM" by Hoeganaes Corporation and Micro-Melt® powders by Carpenter Powder Products (US), but only a small percentage offer new material. This is due to several factors including development cost, equipment, reliability, insurance, and industry confidence in the technology. Mostly it is due to no one having clearly defined a material characterisation methodology that works for all materials. Developers are realising that simply taking an existing material, making powder and fabricating parts is naive and simplistic. A more mature manufacturing approach is needed where AM engineers will be able to:

- Design the process as they would design parts.
- Exploit sophisticated process monitoring and controls.
- Vary microstructure and properties within parts.
- Choose from a wide variety of powders (Beuth, 2017)

Historically, composite materials have offered engineers advanced material solutions for thousands of years, combining compatible materials such as metals, alloys, polymer blends and so on. Combining materials from dissimilar groups presents additional challenges in the form of chemical compatibility in bonding, but at the same time offers benefits that utilise the best properties from the material types employed. MMC components exhibit improved properties such as wear resistance chemical and corrosion resistance, improved fatigue life, compressive strength, and could maintain their mechanical properties at elevated temperatures whilst resisting heat damage (Beuth, 2017). However, due to the complex process for MMC production it can be challenging to achieve characteristics within the component and care must be taken to ensure that the reinforcement is homogeneously distributed throughout the part, often achieved through constant stirring of the molten material, referred to as Stir Casting (SC) (Miracle, 2005). This is also a concern in the additive process, as consecutive layers must achieve identical properties to the previously manufactured layers. The challenge here is to deliver the reinforcement evenly throughout the build and use the build process parameters to optimise the materials unique characteristics.

The benefits of making Ti based MMC over standard monolithic Ti alloys has been extensively explored. Authors such as Singerman and Jackson (1996) considered the many applications for the aerospace industry and the practicalities of production against prohibitively high production costs. They said that aerospace engineers were constantly seeking lighter weight, higher strength materials to improve performance, claiming that

Ti MMC had offered the promise of significant weight saving since the 1960's but the high cost of production and poor quality had prevented their introduction into mainstream production (Singerman and Jackson, 1996). This highlights the requirement for high-quality cost-effective production of components for this material. Alman, and Hawk, (1999) further expand on the need for reducing the cost of MMCs. They advocated the use of particulates rather than fibres, pointing out that for many years Ti alloys and composites were only considered aerospace materials and that they were now being considered for non-aerospace applications including automotive and consumer products. They attributed this to the material's superior properties related to:

- Strength/density,
- Stiffness/density, and modulus/density,
- Creep and corrosion resistance

They proposed that these properties could be augmented by composite strengthening. However, pointing out that continuous filament reinforced titanium-matrix composites were expensive, limited by formability and highly anisotropic. They advocated the use of particulates or discontinuous reinforcement due to low cost and near isotropic properties (Alman, and Hawk, 1999). Gu et al., (2008) whilst considering Cu particulate reinforced MMCs also highlighted the benefits of particulate reinforced MMCs but stressed the unique contribution of Direct Metal Laser Sintering (DMLS), stating that the process exhibited great potential for net-shape fabrication of complex shaped particulate reinforced Cu matrix composites.

Ti has been used predominately within the additive industry for its light weight and strength. Ti is nonmagnetic, corrosion resistant and relatively inert, which makes it a good choice for medical applications (Le Razer and Kilburn, 2009).

Key disadvantages such as poor wear resistance and being difficult to shape and machine conventionally means that there is considerable scope within PBF to improve its properties by using it as a matrix in an MMC condition (Liu, 2015).

The addition of SiC to the Ti matrix is somewhat ambitious as there are other materials such as titanium diboride (TiB_2) or titanium carbide (TiC) with proven results (Gu, et al., 2009 and Liang, et al., 2009), however, little research has been conducted around the use of SiC for the reinforcement of Ti or the use of PBF as a processing method.

In addition, there are some unique research opportunities related to MMCs, specifically in the areas of:

- Small volume feedstock production,
- In-situ MMC fabrication through L-PBF,

- Reliable, homogeneous in-process reinforcement delivery method,
- Innovative process parameter development for new materials.

1.5 Aim and Objectives

To fully realise the manufacture of Ti reinforced SiC MMC material by PBF, the underlying metallurgy and manufacturing characteristics must be understood, therefore the following aim and objectives have been set for the research.

1.5.1 Aim

The aim of this research is to characterise MMC feedstock production through a mechanical alloying (MA) route and evaluate the materials characteristics with regard to its use within the PBF process.

1.5.2 Objectives

Objective one, MMC feedstock production and characterisation

The processing of suitable feedstock is essential to ensure in-process reliability and stability, (Wegner and Witt, 2012). Inconsistencies in the feedstock such as particle size shape and other rheological characteristics will lead to an unsuccessful build or part failure, (Sustarsic *et al.*, 2005). Hence, objective one, is to devise a suitable MA processing regime and characterise MMC feedstock in accordance with the requirements of the PBF process.

Objective two, PBF process parameter characterisation for processing MMC.

It has been established, (Kruth, 2007), that the behaviour of materials within the PBF process is markedly different from other manufacturing methods such as casting or material removal. Materials processed by PBF must first possess an ability to change state from solid (feedstock), to liquid (melt pool) and solidify back to a solid (part) in a controllable, predictable, and repeatable manner. Unlike traditional manufacturing methods where few parameters are required to process parts, the PBF process can be influenced by many complex parameters that affect the above stages and process conditions, (Kurzynowski, et al., 2012), many of which are still not fully understood for the currently available materials. Objective two is to characterise the PBF process parameters. Whilst it is accepted that there are many process parameters and apparatus that cannot be modified, the objective is to process the material by modifying a key range of parameters and benchmark against the characteristics of commercially available Ti6Al4V.

Chapter two

2.0 Literature Review

2.1 Scope of the literature review

This review focusses on the literature within the following areas:

- The PBF process. Chapter 2.2
- Materials - Titanium alloy and Silicon carbide. Chapter 2.3 to 2.4
- Metal matrix composites. Chapter 2.5
- Conventional Feedstock production for PBF. Chapter 2.6
- Mechanical alloying. Chapter 2.7

Ti is a highly valued material for the PBF process. It is reliably processed with consistent results, having a relatively wide processing window, it can be used for the manufacture of finely detailed structures (Arjunan, et al., 2020) and can be post processed through heat treatment and post machining (Negi et al., 2013). Processing with Ti powder, however, has its challenges. Ti6Al4V is chemically reactive with oxygen (O_2) and nitrogen (N_2), producing highly flammable and in some cases explosive, fine particulates whilst being processed. This material is commonly referred to as a condensate and is liberated during the PBF process. Ti also suffers from the effects of internal stresses developed during processing. Research to date has informed and allowed mitigation against these challenges and over recent years the process has become safer and easier to manage (Van Zyl, et al., 2016).

SiC has been selected as the reinforcement material. SiC has been used to improve strength and wear characteristics of Ti MMCs with success (Nelson et al., 2017 and Lu et al., 2006) however, it is unknown how such materials react when processed by PBF. SiC is a relatively common ceramic material, commercially produced from C and Si. It's uses are varied, from abrasives to jewellery. Industrial applications find SiC used in automotive and aerospace applications due to its high wear resistance and endurance to temperatures above 1800^{o} C (Yamada and Mohri. 1991).

MMCs are far from a recent engineering development; their use has been widespread for many years, offering an opportunity to experience the properties of combined materials unachievable by a single material alone. Combining properties such as wear resistance with ductility or strength while offering weight reduction and temperature resistance has made them desirable. MMCs comprise a matrix material and a reinforcement

element. MMCs promise potential within engineering but can also pose significant challenges to manufacture namely regards the homogeneity of reinforcement throughout the part, cost, batch-size, and post processability (Anish et al., 2012). MMCs are most commonly used within high strength and / or high temperature applications where the stability of the product can be more reliable over conventionally manufactured components (Singerman, and Jackson, 1996).

The PBF process has in recent years established a reputation within the advanced manufacturing sector as a reliable and repeatable process to produce complex and intricate parts that cannot be produced using traditional manufacturing routes. Complex freeform structures both internally and externally can be fabricated from a modest range of alloys from materials such as Al, steel and Ti (Le Razer and Kilburn, 2009).

Despite this, the raw material for the PBF process, that of metal powder feedstock, is a significant controlling element. Successful downstream processing is reliant on reliable feedstock that is consistent and predictable. To this end several powder characteristics have been established as being essential to ensure process success; these are reported as chemical composition, rheology, particle size, size distribution, particle shape and layer packing density amongst others (Berretta et al., 2013). The PBF process interaction with feedstock has been shown to have a direct influence on the produced materials mechanical properties. The processing window varies from material to material but must be understood in order to select optimal process parameters for serial part production (Berretta et al., 2013).

2.2 The Powder Bed Fusion Processes

2.2.1 Melt pool formation and Dynamics

The formation of the melt pool is a key element of the powder bed fusion process and fundamental to understanding the mechanics of the process. Research conducted in this area (Khairallah, et al., 2016) has shed light on the complex interaction between laser, powder and substate. The formation of beads, being a complex balance of temperature, force, pressure, and time. LPBF is a heat driven state change process that on a single bead level, sees powder feedstock transformed through a sequence of stages, shown in Figure 3.

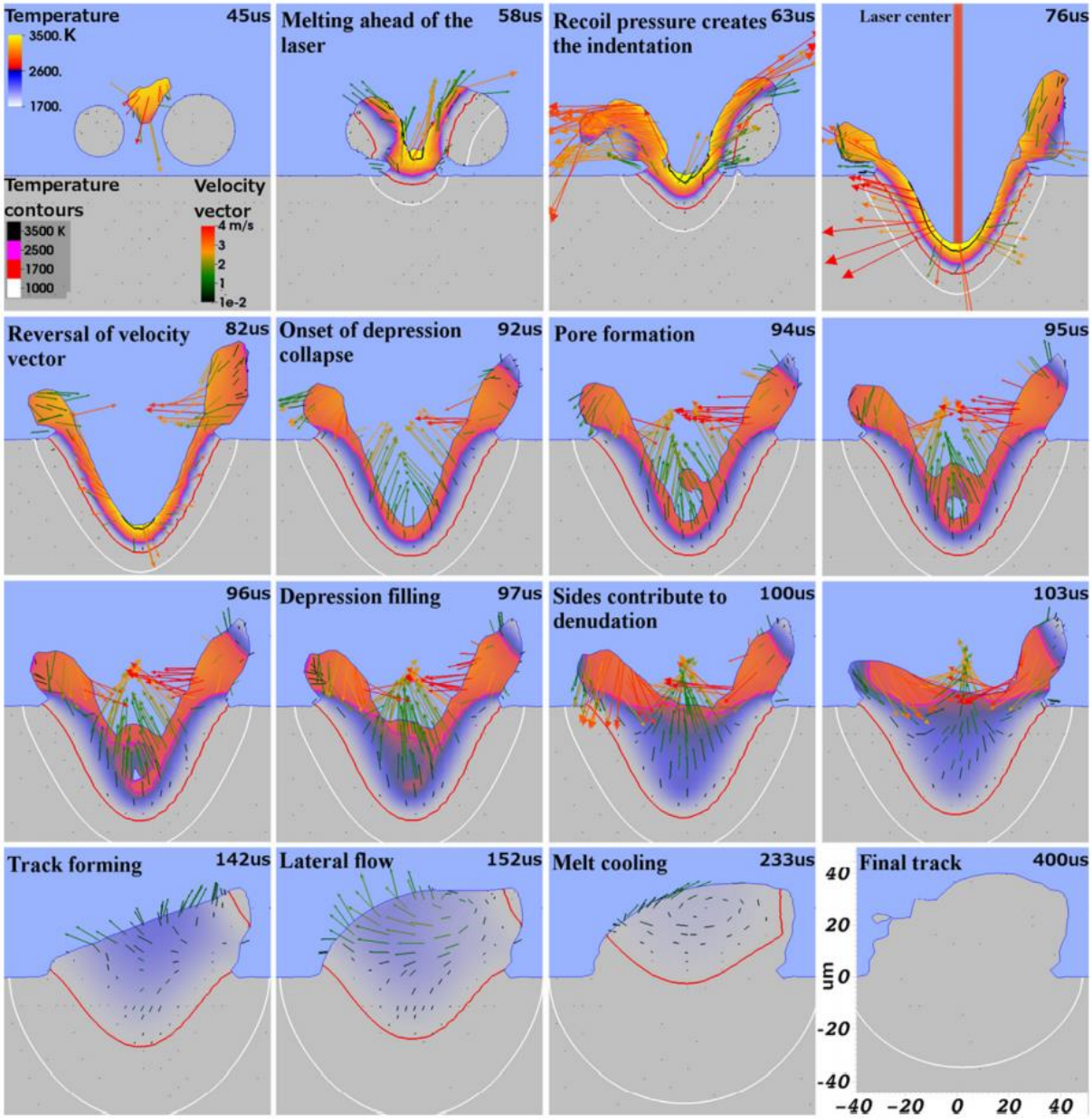

Figure 3 - Lateral 2D slices of bead formation and solidification, (Khairallah, et al., 2016)

It can be seen that initial interaction by the laser beam is with the feedstock at 45 – 76 µs. as the feedstock is heated, the transfer of heat is preferentially through the connectivity or point contact of individual particle. Packing density is shown to play a key role in the transfer of heat through the feedstock (Korner, 2011). This interaction up to 76 µs, is with the periphery of the laser beam, the centre of which appears at 76 µs where interaction with the substate occurs forming a depression, strong forces with an outward vector, melt the substrate unhindered by feedstock or a cooling effect to form a depression. As the laser travels on, solidification begins as the surrounding area begins to reduce the temperature of the depression (82 – 94 µs), it is here that velocity vectors are reversed leading to additional material being added to the melt from surrounding feedstock forming the denuded zone either side of the newly formed bead. The formation of a pore can be seen from 94 µs as strong forces formed by surface tension force material from the upper part of the depression to link. By 97 µs the depression is predominantly filled however it can be seen that the bead is continuing to be fed with additional material from the denuded zone contributing to the final formation of the bead. From 97 – 400 µs final solidification takes place demonstrating the presence of residual heat for some time after the laser has passed. In terms of simulation, Khairallah and his team have taken the understanding of melt pool mechanics further by including the lasers interactions with the feedstock in exceptional detail. The lateral 2D section of the bead also demonstrates the effect of powder particle size on the formation of the bead due to the inclusion of powder particle data. Previous authors (Schoinochoritis et al. 2014 and King et al. 2015) rely on a number of assumptions such as treating the powder as a homogeneous continuous body with effective thermomechanical properties, or by treating the laser energy as a volumetric delivery of energy (Yuan and Gu 2015), whilst such assumptions yielded useful knowledge regarding the formation of the weld bead, it is becoming more apparent that more complex and holistic modelling is required to fully capture this complexity.

2.2.2 Process Parameters

EOS M270 and M290 metal melting machines were used for the experimentation throughout the work presented. The key process parameters for the PBF process are:

- Layer thickness,
- Laser power,
- Scan speed,
- Hatch distance,
- Scan strategy,
- Environmental conditions (Tucho, et al., 2018).

In combination these process parameters produce what is referred to as volume energy density (Neilson, 1993).

$$Ed = \frac{P}{h * v * t}$$ Equation 1 (Williams, et al., 1996, Savalani, et al., 2011)

Where: ***Ed*** is the Laser Energy Density (J/mm^3)

P is the Laser Power (W)

h is the Hatch Spacing (mm)

v is the Scan Speed (mm/s)

t is the Layer Thickness (mm)

Within a range of correctly optimised energy densities, feedstock is melted in a controlled, accurate and repeatable manor to produce a part of known mechanical properties. The energy densities translate into an operating range for laser power, layer thickness, scan speed and hatch distance. This gives an operating window in which the resulting mechanical properties are stable. There is a processing window for all available materials, within this range of parameters, a part produced at the top of the range, i.e., highest laser scan speed and wider hatch distance are typically faster to manufacture and thus more economical to produce, however they are generally of a lower quality standard, having a higher percentage of porosity and shorter fatigue life. Parts produced at the bottom of the range i.e., slow laser scan speed and closer hatch distance, are typically slower to process thus more expensive but tend to exhibit reduced porosity improved mechanical properties and superior quality but have increased internal stress levels. Most production parts are produced using parameters to the middle of the range to allow for process variations (Prashanth, et al., 2017).

2.2.3 Laser Power

Laser power, (*P*) is the amount of energy available to the process. Referenced as a maximum, most systems currently available will supply up to 400W as with the EOS M290. Older machines are limited to 200W (M270), however, machines are emerging into the market with the capability of power levels up to 1KW. Researchers have used 1.5KW systems in research processing 17-4PH Stainless steel with promising results (Yadroitsev, et al., 2010). and predictable laser power is essential to a stable and reliable process, different types of laser work better with certain materials as do specific wavelengths. The EOS M290 uses a wavelength of 1067nm, giving efficient energy delivery for most materials; however, other manufactures have reported success with alternative laser sources, wavelengths, and beam delivery (pulsed laser, Renishaw).

2.2.4 Layer Thickness

Layer thickness refers to the depth of the individual slice layers being lased. Component CAD is digitally sliced into discreet layers for processing. On process completion, a solid part is produced. Layer thickness is, however, critical to mechanical properties as variations in layer thicknesses during processing will result in stress concentrations within the part and unbalanced microstructures leading to part failure (Dadbakhsh, and Hao, 2014).

Whilst it is possible to produce parts with different layer thicknesses, it is with the understanding that the mechanical properties will be different and parameter sets are modified to compensate for material being lased thus maintaining the energy density. It is generally understood that thinner layer thicknesses give better surface finish but at the sacrifice of cost as thicker layered parts are faster to produce and thus more cost effective. Within commercial machines, layer thickness has traditionally been a fixed parameter, however, more system manufacturers are opening parameter sets to enable users to alter layer thickness. This should only be attempted with an understanding of the processing window. As layer thickness and laser power increase the material produced subsequently, will alter in grain structure and chemical composition (Dadbakhsh and Hao, 2014).

2.2.5 Scan Speed

Scan speed is the speed at which the laser moves across the surface of the powder bed melting the feedstock. It is not essential to have a given scan speed for a given material, the faster the scan speed the quicker the part will build, and this will have a dramatic effect on reducing cost. What is important, however, is the energy being delivered into the feedstock. If this energy is increased by increased laser power, then the scan speed must be balanced with the laser power and volume of material (feedstock) being melted. The speed at which the laser moves across the feedstock does have limits also. Excessive velocity can cause turbulent conditions that disrupt the feedstock, moving it away from the melt pool leading to a starved melt pool resulting in porosity and part failure. It has been observed from work with single tracks (Kusuma, 2014) that as the scan speed increases the beads width, height, and depth of penetration decrease. This analysis is significant as scan speed is a parameter that is open to the operator and can be altered at their discretion.

2.2.6 Hatch Distance

Hatch distance refers to the distance between individual beads of processed feedstock. This distance must be optimised for the material, layer thickness, scan speed and laser power to match the weld bead size produced. Should this distance be too large, there will be an increased risk of porosity in the finished part due to unmelted powder being

left between beads and layers. Similarly, if the hatch distance is too small, the melting process has insufficient feedstock to add to the process and repeatedly melts material previously lased (Yadroitsev and Smurov, 2011). This results in porosity in the finished part leading to inadequate mechanical properties. The hatch distance parameter can also be altered by the operator.

2.2.7 Scan Strategy

Scan strategy refers to the method used to cover the slice area with the laser. The most common strategy consists of stripes scanned as a raster pattern which is rotated by 67 degrees after each layer. The stripe width can be modified by the operator and this will have a direct effect on the energy delivered into the substrate due to the time the laser spends in a vicinity. Raising the temperature of the substrate by reducing the stipe width results in less energy needed to raise the local temperature by the laser, this can result in excessive laser power being delivered and thus higher residual stresses (Kusuma, 2014). Due to the nature of each build being different, with the current level of technology, the substrate temperature is unknown, therefore, the precise level of energy required to achieve optimal melt conditions cannot be determined accurately hence the reliance on remaining within the materials operating window (Hanzel, et al., 2015).

A checkerboard strategy can help to reduce localised heating for materials that suffer detrimentally from thermal shock. By lasing random squares across the layer, the lased section has longer to reduce temperature and residual stresses. This method can also reduce processing time by increasing the scan speed for the inner volumes of the part; this can increase productivity by scanning the core areas of a part with a larger hatch distance and faster laser scan speed, however, this can influence part strength which must be taken into consideration when selecting this strategy. The skin aspect is scanned with standard parameters thus giving predictable mechanical properties in these areas (Dimitrov, 2016).

2.2.8 Environmental Conditions

For a PBF process to operate the melting must be carried out in an inert atmosphere to prevent O_2 contamination. The environmental conditions must be maintained throughout the build process to ensure accuracy and stability of the process. These environmental conditions can influence the melt pool significantly by influencing the crystallographic microstructure of the material in selective areas or producing unmelted areas or voids in the part, (Tucho et al., 2018).

The environmental conditions controlled include the:

- Build platform and substrate temperature,
- Environmental atmosphere (Gas and O_2 content),
- Filtration and condensate removal,
- Gas flow and Recoat Speed.

Changes in the environmental conditions can have a detrimental effect on the process's ability to deliver precise energy levels into the feedstock and substrate. Manufacturers devote large amounts of research time and money looking at the effects of environmental conditions within the process (Zhang, et al., 2013).

2.2.8.1 Build Platform and Substrate Temperature

Build platform and substrate temperatures are key factors when considering the reaction mechanics of the melt pool. It is well established that under specific conditions of laser power, scan speed, layer thickness and hatch distance a suitable energy density (Gu, et al., 2013) can be achieved that will melt a given volume of powder and substrate and produce reliable and predictable mechanical properties expressed by Equation 1 (Witsa, et al., 2016). This energy density sometimes referred to as the Andrew Number, (Williams, *et al.,* 1996, and Savalani, *et al.,* 2011) is dependent on a reliable substrate temperature, when considering the thermal energy change equation (Equation 2) the energy input into the system required to reach a specific temperature is only that required to effect temperature change ($\boldsymbol{\Delta\emptyset}$)

$$\Delta E_t = m * c * \Delta\emptyset \qquad \text{Equation 2} \qquad \text{(Banerjee, 2008)}$$

Where: $\Delta \boldsymbol{E_t}$ is the Change in Thermal Energy (J)

$\boldsymbol{m}$ is the Mass (kg)

$\boldsymbol{c}$ is the Specific Heat Capacity (J/kg ^{o}C)

$\boldsymbol{\Delta\emptyset}$ is the Temperature Change (^{o}C)

Build platform temperature is elevated prior to commencement of the build process in order to aid adhesion between the build platform and the first few layers of the build, this is 35 ^{o}C for Ti6Al4V on the EOS M290 machine. Once the process advances above this point, approximately 0.3 to 0.5 mm, the heat generated within the melt pool given a constant input energy can vary depending on the temperature of the substrate

(Kusuma, 2014). Research with Ti6Al4V has shown that elevating the platform temperature to 100 ^{0}C can have a significant effect on minimising the build-up of residual stress (Agius, et al., 2017) by reducing the thermal gradient.

2.2.8.2 Environmental Atmosphere (Gas)

The environmental atmosphere (Gas) within the build chamber is typically an inert gas supplied to reduce the O_2 levels in the build chamber. For EOS systems, O_2 levels are typically in the range of 0.1 % (1,000 ppm) to begin the process with a range of, 0.0 % to 0.13 % (0 – 1300 ppm) during operation. The M270 and M290 machines use either Ar or N_2 in the build chamber depending on the material being processed (Table 2).

Table 2 - Environmental Atmosphere (Gas) EOS GmbH (2018)

Material	Ref	Gas
Titanium	Ti6V4Al	Ar
Aluminium	AlSi10Mg	Ar
Maraging Steel	MS1	N
Cobalt Chrome	SP2 – MP1	N
Stainless Steel	GP1	N
Nickel Alloy	IN718	Ar

As new materials are developed for the PBF process along with the use of alternative laser sources, it may become necessary to combine material, laser, and gas to produce the most desirable mechanical properties (Linde, Russia 2018). Further development of process atmosphere gasses may be possible but not within this work, at this stage and for this research it is recognised that this environment must be free from O_2.

2.2.8.3 Gas Flow and Recoat Speed

The M270 uses a top-down fill configuration that utilises the inert atmospheric gas to keep the laser window free from contamination by feeding the gas in past the lens, the gas then falls to the build area. This, however, has been proven through research conducted, by EOS, to be detrimental to the build process (Weilhammer, 2011), due to a combination of the chamber geometry and the position of the recoater arm during lasing and the movement of gas within the chamber, multi directional gas flows are generated. This configuration disturbs the feedstock on the powder bed and prevents condensate produced by the process from evacuating the chamber resulting in interference of the passage of the laser beam causing reduced and unpredictable levels of laser energy being delivered to the workpiece (Schniedenharn, et al., 2018).

Developments in gas flow delivery now used in the EOS M280 and M290 machines, deliver the inert gas from a 'gas blade' style inlet at the rear of the build platform, the gas travels across the build platform from the rear to the front and is extracted by a removable suction nozzle (Figure 4).

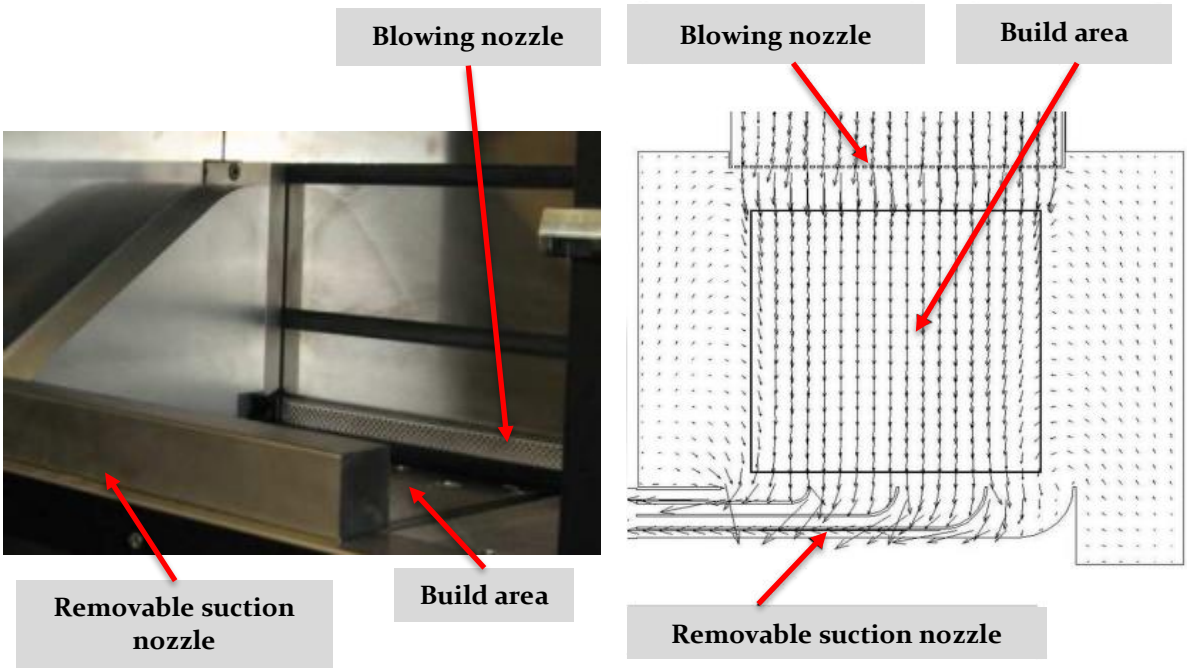

Figure 4 - EOS M280/290 Laminar Inert Gas Flow (Weilhammer, 2011)

The gas flow is designed to be laminar in nature to minimise turbulence and remove condensate producing a clean build area (Shen, et al., 2019). This has been proven to be a major improvement but still requires development work to avoid disruption of the powder bed and interference with the laser beam. Care must also be taken in the placement of parts within the build areas to avoid spatter falling in areas before lasing (Figure 5). Typically, parts are built from the front of the build chamber to the rear; excessive spatter is then removed by the recoater arm on recoat between each successive layer.

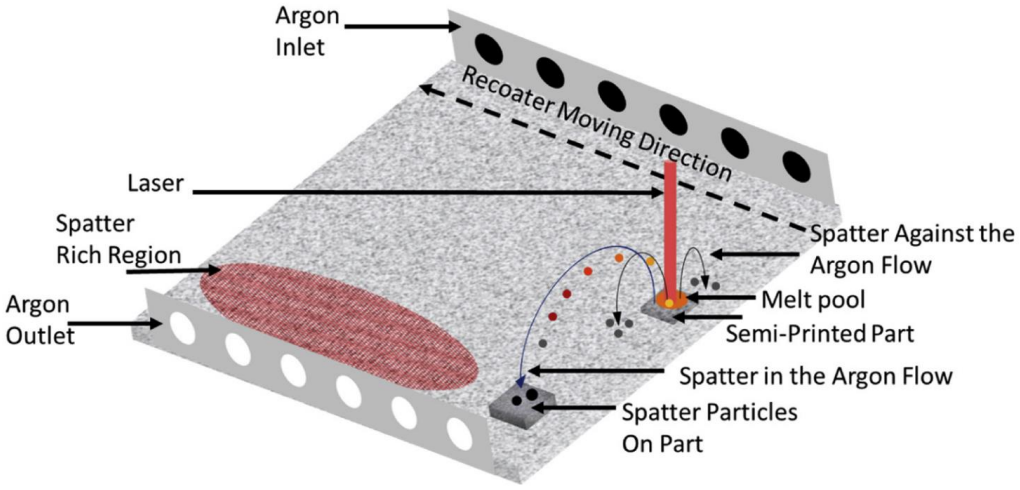

Figure 5 - Schematic representation of spatter formation, types and effect on build plate, powder bed and printed parts (Esmaeilizadeh, 2019)

The recoat speed can also be influential to the build process. By increasing the speed of recoat, build time can be dramatically reduced, however, this increased velocity can cause lighter particles of powder to become airborne impairing the energy levels of the laser by acting as a filter. The reduced volume of powder on the powder bed also effects bead formation by reducing the volume of available feedstock. In this instance, weld beads will be less than optimal leading to porosity in the part. Conversely, by significantly reducing the recoat speed improvements in part density can be achieved however, the build time and production cost will increase (Baitimerov, et al., 2018).

2.2.8.4 Filtration and condensate removal

Within the build area, the environmental gases are continualy monitored for O_2 levels and filtered through a dedicated system in order to remove condensate and contamination generated by the PBF process. Filtration flow rates can be adjusted to optimise environmental conditions providing a clear passage for the laser beam. However, care must be taken to ensure that the flow rate is not too high as particles with lower mass can travel into the filtration system. Filter clogging is monitored by the control system. Users are prompted to replace filters after 200 hours of production and filters are automatically self-cleaned (EOS GmbH 2019).

2.2.9 Wettability

Wettability is one of the most important factors affecting the PBF process. The process requires care in developing parameters that will produce optimal bead geometry, this geometry can also be a good indicator of the process behaviour within the weld pool. The liquid–solid wetting characteristics are crucial for a successful PBF process.

The wetting of a solid by a liquid is related to the surface or boundary energy between the solid–liquid γ_{sl}, solid–vapour γ_{sv} and liquid–vapour γ_{lv} interfaces, as shown in Figure 6.

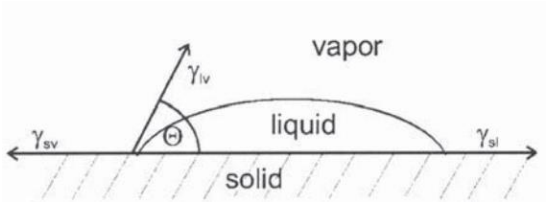

Figure 6 - Vapor Liquid Solid Interface (Hede, 2006)

Wettability can be defined by the cosine of the contact angle θ (Figure 7), and as shown by Kruth, et al., 2007 in Equation 3, as cos θ increases, wettability also increases resulting in the spreading of the liquid material across the solid substrate. As the angle between liquid–vapour γ_{lv} and solid–liquid γ_{sl} interfaces increase towards 90°and the value for cos θ decreases, the likelihood of poor adhesion becomes higher. Beyond this point there is a higher probability of balling, lack of bead continuity and lack of wettability.

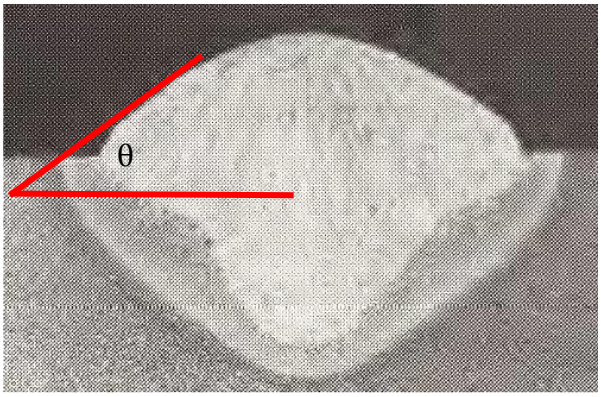

Figure 7 - Wettability Contact Angle θ (Banerjee, 2008)

$$\cos\theta = \frac{\gamma_{sv} - \gamma_{sl}}{\gamma_{lv}} \qquad \text{Equation 3} \qquad \text{(Kruth, et al., 2007)}$$

Where: cos θ is the cosine of the contact angle (Deg)

γ_{sl} is the solid–liquid interfacial tension (N/m)

γ_{sv} is the solid– vapour interfacial tension (N/m)

γ_{lv} is the liquid–vapour interfacial tension (N/m)

The liquid wets the solid as $\cos\theta \rightarrow 1$. When analysing transverse sections of single beads this value provides an indication of the process behaviour as energy density increases.

As continuity between interfacial tensions become more incompatible, the surface tension of the liquid phase is such that it becomes self-sustaining forming a ball that travels away from the reaction zone, this is referred to as "balling" (Tolochko, 2004 and Li, 2011). Incompatibilities between the liquid and solid elements can be caused by:

A. Temperature difference between the molten feedstock, and the substrate,
B. Gas evacuation from feedstock and or weld pool,
C. Contamination in the form of oxides,
D. Substrate surface roughness.

Temperature difference between the molten feedstock, and the substrate

Upon lasing, the energy from the laser penetrates through the powder bed into the substrate to produce a melt pool. This melt pool is sustained through the progression of the laser as it scans across the substrate (Ansari, et al., 2019). If excessive layer thickness or a difference between the substrate temperature and the bead is experienced balling can occur due to insufficient energy in the substrate (Tolochko, 2004).

Gas evacuation from feedstock and or weld pool

Gasses such as O_2 and N_2 can be entrapped within the feedstock (Figure 8) and can be released during the welding process causing a disruption. Similarly, at elevated laser powers typically above 1KW plasmerisation can occur, (Yadroitsev, et al., 2013) disrupting the surface tension by producing a layer of insulation between the molten powder and the substrate known as the Lidonfrost effect, leading to the balling effect.

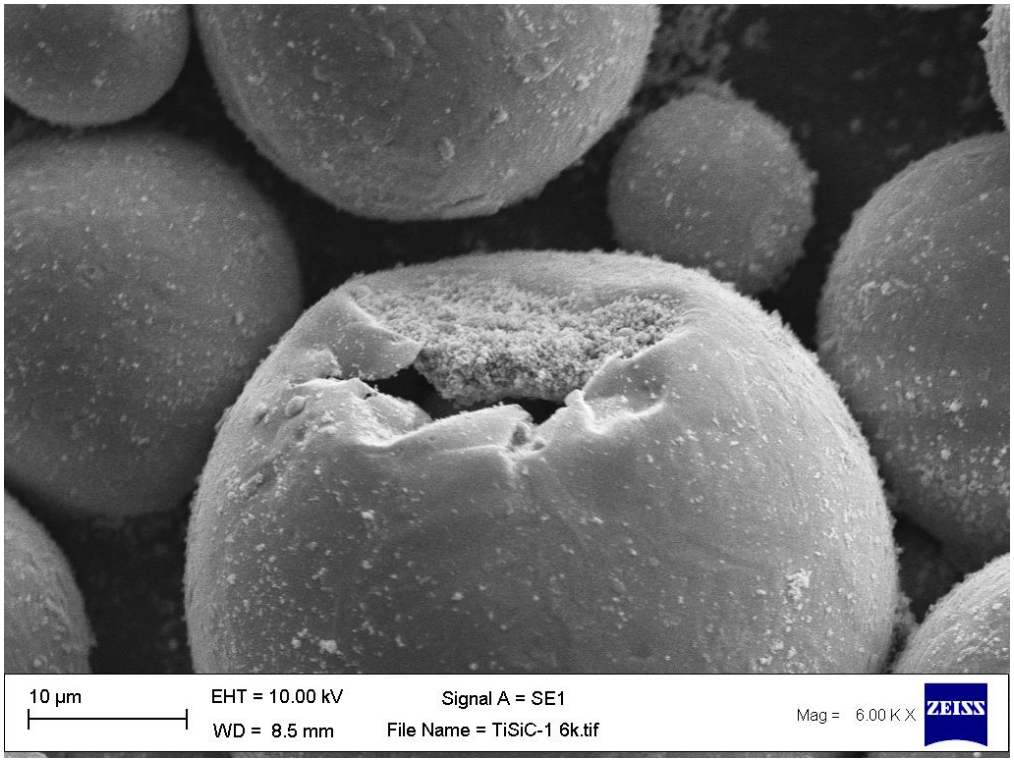

Figure 8 - Evidence of Gas Entrapment in Feedstock (Lyall, 2017).

Contamination in the form of oxides

Contamination in the feedstock can be either through gas entrapment within the feedstock (Figure 8) or O_2 pickup caused by frequent use and handling in an O_2 rich atmosphere between processing (LPW 2018). Fluxing agents or in situ deoxidisers can be used to reduce the effect of oxides within the process. Additives in small quantities can either be mixed or pre-alloyed with the feedstock to aid the wetting activity and flowability. In Kruth's (2007) work, phosphides were added in the form of Fe_3P, SCuP and Cu_3P to Fe based and Cu based powder systems. This was effective in enhancing the wetting behaviour and the reduction of porosity of the material produced.

Substrate surface roughness

Wettability is also a function of surface roughness, the flatter a surface, the easier a liquid can wet that surface (Banerjee, 2008). Within the PBF process the roughness of the substrate is dependent on the surface finish of the previously lased layer, As the substrate becomes rougher the possibility of balling increases leading to increased roughness, porosity, and part failure.

In combination with other measurements such as bead continuity, cracking and coloration, bead height ($h1$), substrate penetration denoted by the depth of the dilution area ($h2$), width of the bead ($w1$), and width of dilution area ($w2$) (Figure 9) the optimal

process parameters that promote compatibility of surface tensions and promote wettability can be determined.

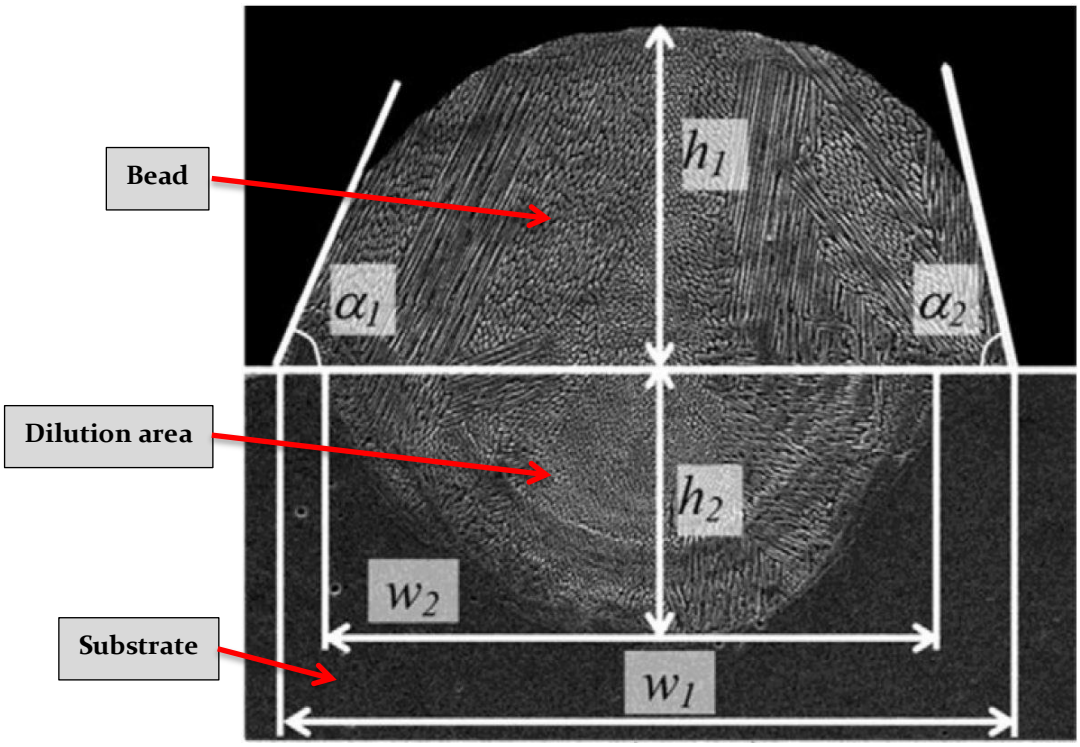

Figure 9 - Dimensioned transverse sectioned 316L stainless steel single beads (Yadroitsev, et al., 2012)

2.3 Materials

2.3.1 Titanium Alloy (Ti6Al4V)

Ti6Al4V has become a common and highly valued material used in PBF, despite it being a costly material to produce (Condliffe, 2015). Two grades of titanium are commonly used: Ti6Al4V ELI (extra low inter-stitials) (grade 23) and Ti6Al4V (grade 5), grade 23 is comparable to grade 5 except that it has reduced levels of O_2, N_2, C and Fe providing increased ductility and fracture toughness (www.Arcam.com 2018). Figure 10 compares Ti6Al4V ELI with other available alloys for the PBF process, tensile strength over Vickers hardness.

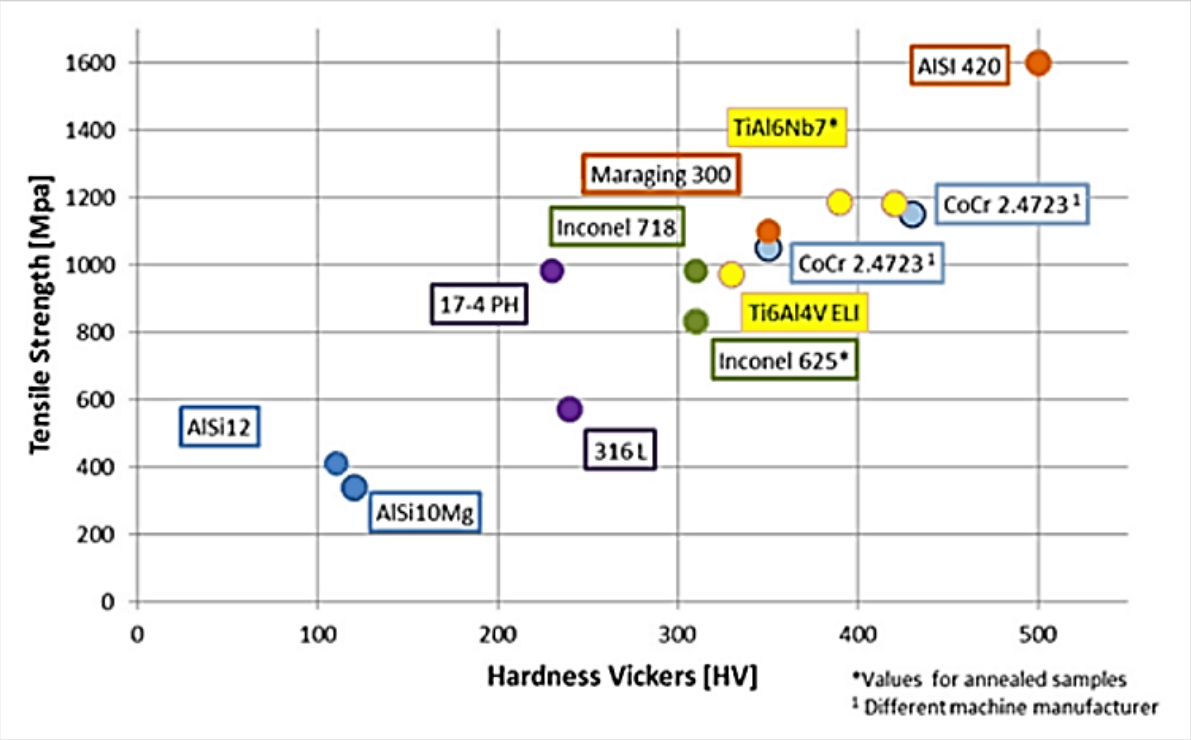

Figure 10 - Available alloys for the PBF process (EPMA European Powder Metallurgy Association 2018)

Within this research Ti6Al4V (grade 5) has been used as this is readily available and its build characteristics are well understood, providing the research with a reliable base line from which to work (Bourell, 2017). From the early days of AM, Ti6Al4V has been a stock material for all feedstock suppliers and is a mainstay for machine manufacturers and users. Whilst Ti6Al4V presents some challenges for machining, having a machinability rating of 54 % compared to B-1112 Steel (100 %) (American Iron and Steel Industry, AISI 2019) it has leant itself well to the additive industry having a reliably wide processing window, thus reducing the risk of build failure.

In Table 3, the typical chemical composition of grade 5 Ti6Al4V (EOS GmbH 2018) is presented.

Table 3 - Ti6Al4V Material Composition (EOS GmbH 2018)

Technical Data

Powder properties

Material composition [wt.%]	Element	Min	Max
	Al	5.50	6.50
	V	3.50	4.50
	O	-	0.150
	N	-	0.040
	C	-	0.080
	H	-	0.012
	Fe	-	0.250
	Y	-	0.005
	Other elemets, each	-	0.10
	Other elemets, total	-	0.40
	Ti		bal.

Table 4 shows a comprehensive list of physical properties for Ti6Al4V giving maximum and minimum values.

Table 4 - Typical Physical Properties of Ti6Al4V (AZo metals 2019)

Property	Minimum Value (S.I.)	Maximum Value (S.I.)	Units (S.I.)
Atomic Volume (average)	0.01	0.011	m^3/kmol
Density	4.429	4.512	g/cm^3
Energy Content	750	1250	MJ/kg
Bulk Modulus	96.8	153	GPa
Compressive Strength	848	1080	MPa
Ductility	0.05	0.18	
Elastic Limit	786	910	MPa
Endurance Limit	529	566	MPa
Fracture Toughness	84	107	MPa.$m^{1/2}$
Elongation at break	14	14	%
Hardness (Vickers)	349	349	
Modulus of Rupture	786	1080	MPa
Poisson's Ratio	0.31	0.37	
Shear Modulus	40	45	GPa
Tensile Strength	862	1200	MPa
Young's Modulus	110	119	GPa
Latent Heat of Fusion	360	370	kJ/kg
Maximum Service Temperature	346	417	°C
Melting Point	1604	1660	°C
Specific Heat	526	526	J/kg- °C
Thermal Conductivity	6.7	6.7	W/m. K
Coefficient of Thermal Expansion	8.9	8.9	10^{-6}/ °C
Volume Resistivity	168x10^{-8}	170x10^{-8}	ohm.m

Whilst these physical properties are important, many are of low significance.

2.3.2 Mechanical Properties for Ti6Al4V Key to This Research

Within this research, the mechanical properties of most significance for Ti6Al4V are:

- Hardness, (Vickers) 349
- Density 4.47 g/cm^3
- Tensile strength 1031 MPa
- Melting point 1604 – 1660 °C
- Expansion coefficient 8.9 x 10^{-6}/ °C (Hidnert, 1943)

These characteristics make Ti6Al4V an ideal choice for lightweight structures requiring strength, stability, and corrosion resistance at elevated temperatures, Ti6Al4V is however, susceptible to wear and whilst it can be cold formed it can tear and gall if not

lubricated sufficiently. Due to its high tensile strength it is well suited to applications involving tensile load such as structural fasteners; this however, contrasts with its low elongation (14 %) and ductility (0.53) in its annealed state, leading to failure if forces exceed its tensile strength (AZo metals 2019).

2.3.3 Alloy Types

In order to understand the melting characteristics during the PBF process the metallurgy of Ti6Al4V needs to be considered. The alloys of Ti6Al4V can be classified into three main groups (AZo metals, 2019).

- Alpha alloys
- Alpha-Beta alloys
- Beta alloys

Alpha alloys are non-heat treatable and are generally very weldable. They have high specific strength, good notch toughness, reasonably good ductility and have excellent properties at cryogenic temperatures. Alpha or near alpha alloys offer the highest strength and oxidation resistance at high temperature hence their use in aerospace and petrochemical applications (Zhao, et al., 2015). Alpha alloys have a Hexagonal Close Packed (HCP) crystallography (AZo metals, 2019).

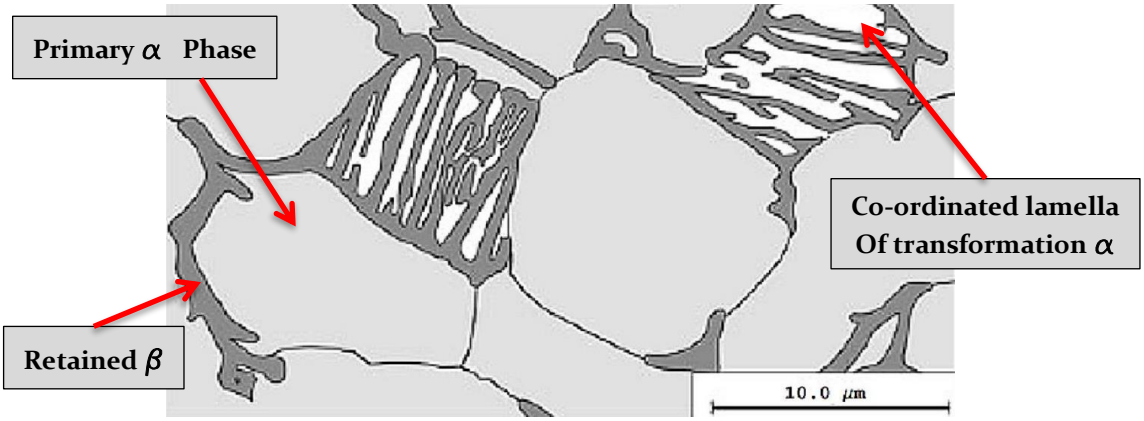

Figure 11 - Titanium 6Al-4V Grain Structure, Whittaker (2015)

Alpha-Beta alloys such as Ti6Al4V are heat treatable to varying extents as shown in Figure 11, and most are weldable with the risk of some loss of ductility in the weld area. These high strength alloys exhibit excellent combinations of ductility, strength, and fracture toughness (Qu et al., 2012, Zhang, 2016). Hot forming qualities are good but cold forming often presents difficulties (Andrade et al., 2010). Creep strength is not usually as good as in most alpha alloys (AZo metals, 2019).

Beta alloys, Beta or near beta alloys such as VT-22 and Ti-1023 are readily heat treatable, generally weldable, and offer high strength up to intermediate temperature levels. In the

solution treated condition, cold formability is generally excellent due to the beta phases increased ductility. Beta alloys have a Body Centred Cubic (BCC) crystallography and are becoming used more often for aircraft landing gear, examples being the Boeing 787 and Airbus A380 (Deshpande et al., 2018). Si, vanadium (V) and molybdenum (Mo) stabilise the beta phase of the alloys to improve strength when solution treated (Ranju, 2015).

2.3.4 Crystallographic Forms of Titanium (Ti)

The metallurgy of Ti is dominated by the crystallographic transformation which takes place in the pure metal at 882°C. Below this temperature, pure Ti has an HCP structure. Above it, the structure is BCC and termed beta (β) (Deshpande, et al., 2018). The fundamental effect of alloying additions to Ti is the alteration of the transformation temperature and production of a two-phase field in which both alpha and beta phases are present. Elements having extensive solubility in the alpha-phase characteristically raise the transformation temperature and are called alpha stabilisers (AZo metals, 2019).

2.3.5 Alpha Stabilisers

Figure 12 shows the binary phase diagram formed by the addition of an alpha stabiliser (such as Al, O_2, N_2 or C) to Ti (AZo metals, 2019). O_2 is added to pure Ti to produce a range of grades having increasing strength as the O_2 level is raised. Al is the only other alpha stabiliser used commercially and is a major constituent of most commercial alloys (Liu and Welsch 1988).

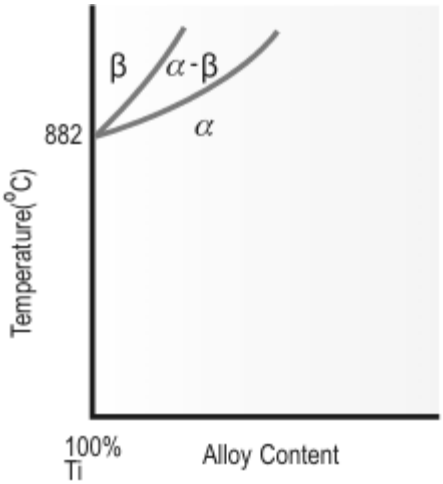

Figure 12 - Effect of alpha-stabilising elements on Ti (AZo Metals 2001).

2.4 Silicon Carbide (SiC)

SiC is the only compound of Si and C atoms. SiC occurs naturally as a mineral (Moissanite), but this is very rare. In powder form, it has been produced for abrasives for over one hundred years since 1893 as its hardness (9 – 9.5 Mohs) is only a little less

than natural Diamond (10 Mohs) and was discovered by Edward Acheson whilst attempting to create artificial Diamond. Whilst SiC is highly suited for devices working at high frequency, high temperature and high power (Eriksson, 2010), it is SiC superior ability to resist wear and its high fracture toughness that is primarily of interest within this research, where it is used as a reinforcement material within a metal matrix.

Table 5 shows a comprehensive list of physical properties for SiC giving maximum and minimum values.

Table 5 - SiC Material Properties (AZo Metals 2019)

Property	Minimum Value (S.I.)	Maximum Value (S.I.)	Units (S.I.)
Atomic Volume (average)	0.01	0.011	m^3/kmol
Density	3.1	3.15	g/cm^3
Energy Content	750	1,250	MJ/kg
Bulk Modulus	100	176	GPa
Compressive Strength	1,000	1,700	MPa
Ductility	0.01	0.4	
Elastic Limit	172	1,245	MPa
Endurance Limit	175	705	MPa
Fracture Toughness	4.6	4.6	MPa.$m^{1/2}$
Hardness (Vickers)	2,039	3,059	
Modulus of Rupture	130	1,300	MPa
Poisson's Ratio	0.35	0.37	
Shear Modulus	210	380	MPa
Tensile Strength	400	400	MPa
Young's Modulus	90	137	GPa
Latent Heat of Fusion	360	370	kJ/kg
Maximum Service Temperature	1,500	1,650	°C
Melting Point	2,650	2,950	°C
Specific Heat	670	710	$J/k^{-1}.kg^{-1}$
Thermal Conductivity	90	160	$W.m^{-1}.K^{-1}$
Coefficient of Thermal Expansion	4.5	4.5	10^{-6}/ °C
Volume Resistivity	10^3	10^5	ohm.cm

2.4.1 Mechanical Properties for SiC Key to This Research

Within this research, the mechanical properties of most significance for SiC are:

- Hardness (Vickers) 2,039-3,059
- Density 3.11 g/cm^3
- Tensile strength 400 MPa
- Melting point 2,650 – 2,950 °C
- Expansion coefficient 4.5 x 10^{-6}/ °C

These characteristics make SiC an ideal choice for applications requiring strength, stability, corrosion and wear resistance at elevated temperatures, SiC is however, susceptible to impact when in large sections having a minimum fracture toughness as low as 14 ($MPa.m^{1/2}$) in comparison with 84 ($MPa.m^{1/2}$) for Ti6Al4V. as small particles, SiC functions impressively as an abrasive resisting high compressive forces (1350 MPa) and shear stress (295 MPa) making it an ideal candidate as a reinforcement material (AZo metals 2019).

2.4.2 Crystallographic Forms of Silicon Carbide

SiC is formed in a strong 88 % covalent 12 % ionic bonded (Figure 13) tetrahedral structure (Izhevskyi, et al., 2000) that enables SiC to form other strong cryptographic structures or polytypes (Schneer, 1955) such as cubic and hexagonal.

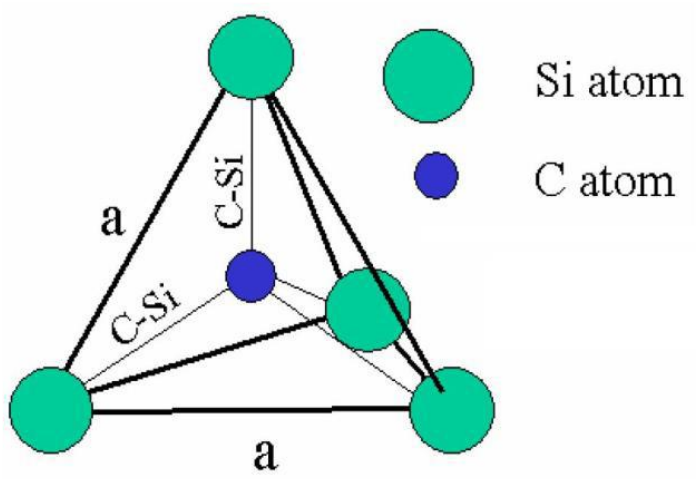

Figure 13 - SiC Structures (Eriksson, J. 2010)

In granular form, the commercially available SiC particles were angular in shape due to being manufactured by crushing they presented a strong tendency to agglomerate due to high surface energy resulting from the particles large surface area. Particle sizes used for initial experimentation was ≈10.0 µm, reduced by planetary ball milling to ≈ 2.0 µm. Further experimentation saw particle sizes further reduced, typically to around 0.5 µm as measured with a Zeiss scanning electron microscope.

Si when combined with Ti at relatively low quantities, typically below 8 percent by weight (Wt.%) form active eutectoid systems where below the eutectoid temperature the beta phase decomposes to alpha and intermetallic compounds such as $\alpha+Ti_3Si$ and $\alpha+Ti_5Si_3$, above the eutectoid temperature $\beta+Ti_3Si$ and $\beta+Ti_5Si_3$ compounds are found (Fiore, et al., 2016). As a result, controlled precipitation of the intermetallic compounds can be utilised to enhance the strength of Ti alloys. Sivakumar (2016), offered more detail

and considers the Orowan strengthening mechanism (dispersion strengthening) as the main reason for increased strength of the material. This work involved 5 %, 10 % and 15 % SiC reinforcement in Ti6Al4V, with the best results achieved at 5 % reinforcement using a 20 μm particle size, SiC reinforcement.

This mechanism of dispersion strengthening using nano particulates (Orowan strengthening mechanism) is the expected strengthening methodology for this research. In the case of this work a maximum achievable reinforcement volume of ≈ 3.81 % was calculated (see chapter 7.0) and used.

2.5 Metal Matrix Composites (MMCs)

2.5.1 MMCs introduction

The global value of the metal matrix composite market is expected to be worth $558.5 million by 2027 as a result of a 6.4 % annual growth rate (Grand view research, 2020), this is in contrast to $100 million in 1999 (Miracle, 2005). This highly specialised sector supplies components primarily to applications in aerospace, defence and the automotive industry with more applications such as lightweight vehicles, aviation and space exploration demanding exceptional mechanical properties from materials, stimulating new and further market growth.

Composite materials have existed for many years. In nature, materials have combined to produce strong, lightweight materials that unless combined would not benefit independently. For example, cellulose fibers in a matrix of lignin to form wood, independently, cellulose fibers are most commonly found in cotton and lignin is commonly found in plants, together the combination is strong enough to sustain a trees growth and be used as a construction material.

In engineering, composite materials have similarly been combined beyond base-elementals to produce a vast range of materials (Kainer, 2006), whilst these are improvements on the base materials, they are still similar in many ways and are therefore referred to as alloys rather than composites (Haghshenas, 2015).

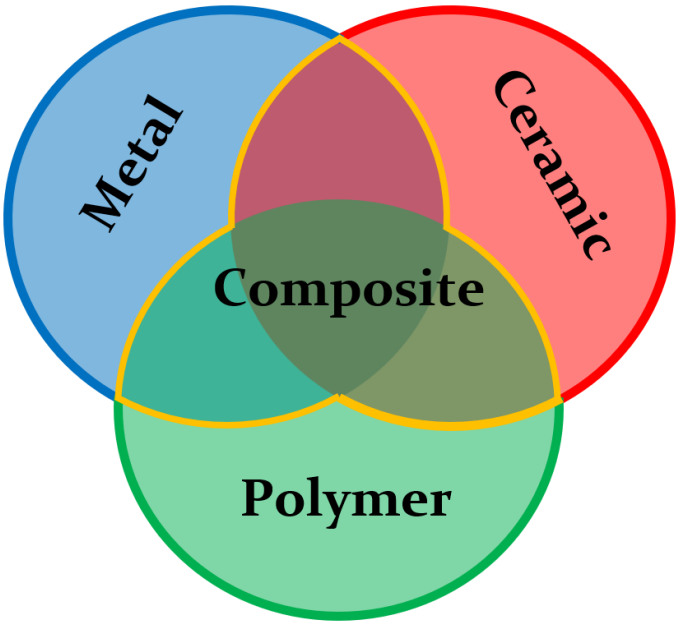

Figure 14 - Composite systems among metal-ceramic-polymers, (Haghshenas, 2015)

When developing alloys, metals are typically blended with other metals, when developing composite materials, dissimilar materials are combined such as Polymers,

metals, and ceramics (Figure 14). This is not without its difficulties. However, by exploiting combinations of these material groups, engineers can exploit their benefits bringing us a wide variety of composite materials and this has been the case since there first technological development in the 1960's (Kandpal, et al., 2014). The three composite systems are recognised as:

- Metallic materials — MMC,
- Polymer materials — PMC, and
- Ceramic materials — CMC (Kainer, 2006)

For example, through composite development, the goal of enhancing a metals mechanical property, can be achieved through the addition of nonmetallic reinforcements in the form of a ceramic. Advantages can be found in significantly improved mechanical properties including high specific strength, ductility, heat, and wear resistance in comparison to conventional blended alloys (Figure 15). Disadvantages can also be experienced within areas such as material processing, machining/material removal and fabrication.

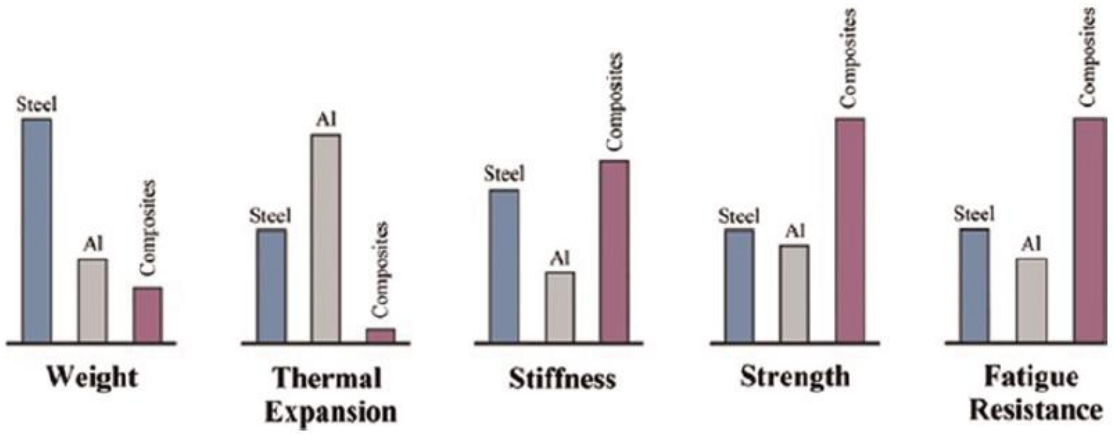

Figure 15 - Physical and mechanical properties of composites compared with two most commonly used alloys; steel and aluminium, (Haghshenas, 2015)

MMC manufacture typically aims for near-net-shape production due to difficulties on material removal post-production, but also for reasons of manufacturing efficiency.

Processes are typically classified on the basis of temperature of the metallic matrix during processing (Kandpal, et al., 2014) and fall into the following five categories:

1. Liquid-phase processes,
2. Solid–liquid processes,
3. Deposition techniques,
4. In situ processes. and
5. Two-phase (solid - liquid) processes.

Of these, the most common is liquid-phase fabrication (Jitendra, et al., 2018) and involves the incorporation of the reinforcing phase into a molten matrix metal, followed by its solidification. Specific challenges are presented in the form of homogeneity of reinforcement, wetting of the reinforcement and the complex processes involved in solidification. Within this research, liquid-phase processing is employed all-be-it on a micro-scale.

2.5.2 MMC Systems

In the 2006 book, Metal matrix composites: custom-made materials for automotive and aerospace engineering, edited by Karl Kainer, the classification of composite materials with metal matrixes is discussed with four clear classes as shown in Figure 16.

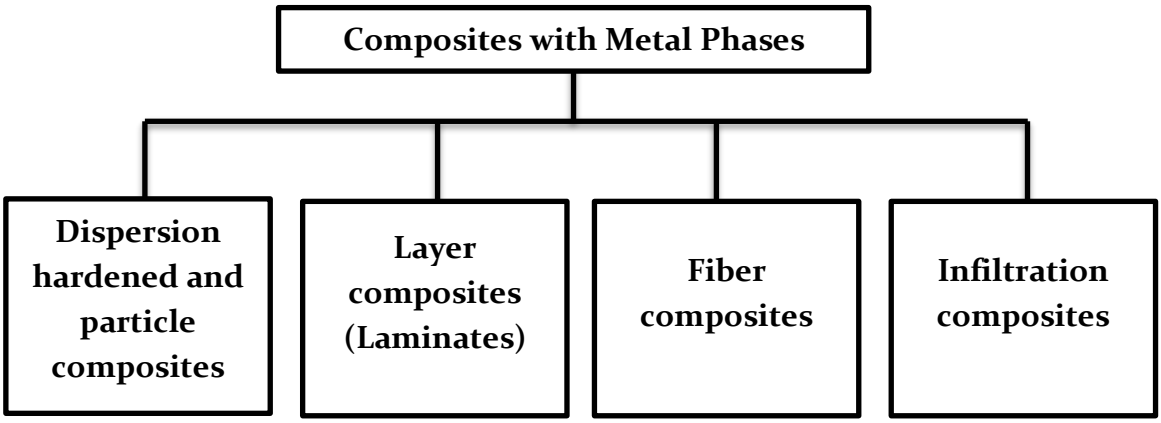

Figure 16 – Classification of Composite Materials with Metal Matrixes (Kainer, 2006)

The composite system is formed from a matrix material and a reinforcement. For a metal matrix composite and as part of this research, ceramic reinforcement material is encapsulated within a metal matrix typically a lighter or more ductile material such as aluminium or titanium. MMCs are classified by their matrix materials such as:

- Aluminium-based,
- Iron-based,
- Titanium-based,
- Copper-based,
- Magnesium-based, and
- Super Alloy-based.

By far the most used matrix material is aluminium followed by iron and titanium. Figure 17 shows a selection of other matrix materials compared by volume of usage.

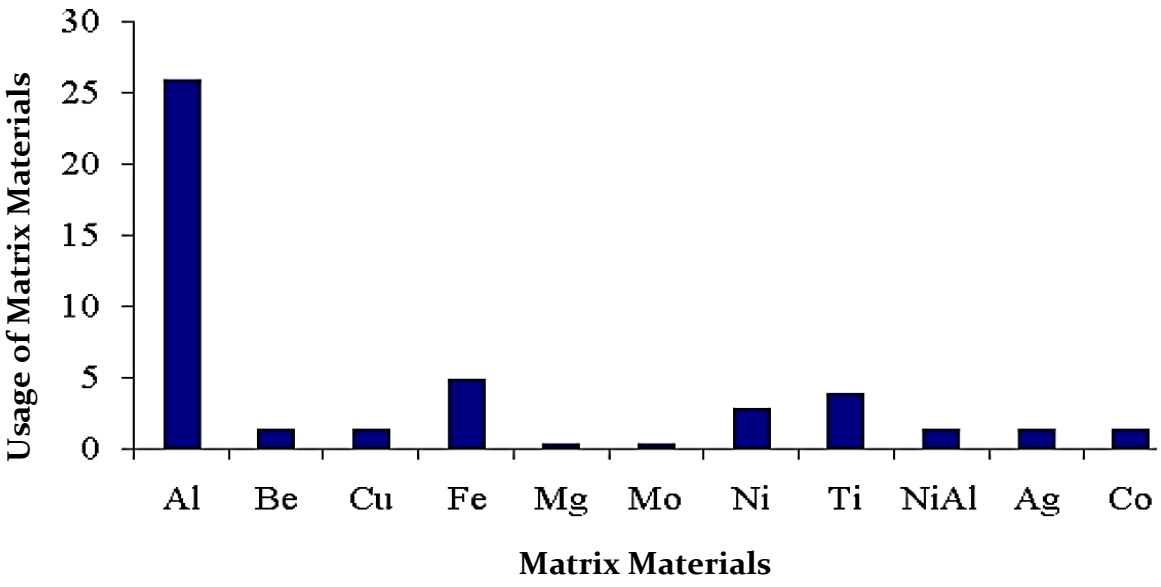

Figure 17 - Comparison of matrix materials against usage, (Adebisi, 2011)

Reinforcement materials and forms

Whilst the matrix material constitutes the bulk of the MMC, the reinforcement, either non-metallic or ceramic, makes up the rest. This is commonly a percentage by volume fraction (*F*) in one of three forms:

- Mono Filaments,
- Whisker or Short fibers,
- Equiaxed Particles (Kainer, 2006).

It is important that the volume of reinforcement is optimised to achieve the desired mechanical properties.

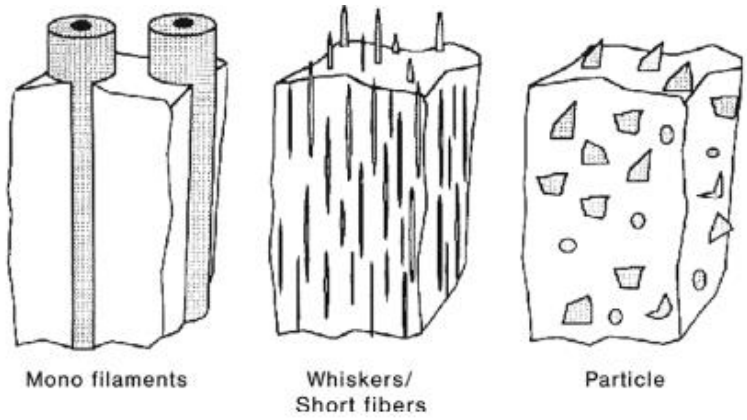

Figure 18 - Reinforcement (Kainer, 2006)

Figure 18 shows three common forms of reinforcement. In all cases, the volume of reinforcement should not exceed the super-saturation point of the matrix, at which the matrix will become discontinuous and the benefits from that material lost (Behera, et al., 2019).

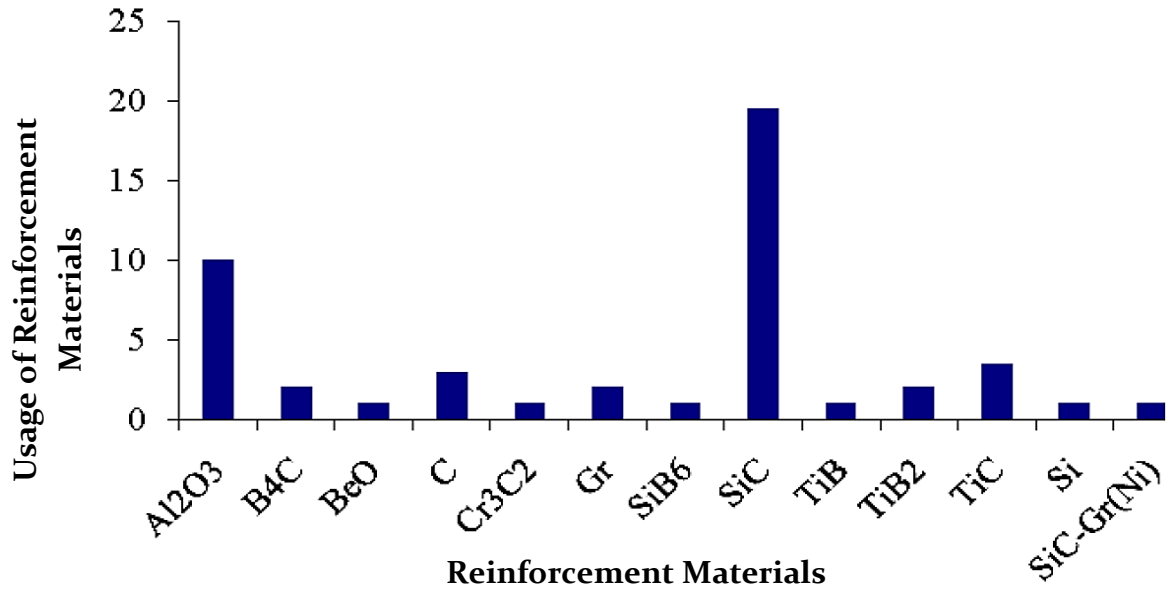

Figure 19 - Comparison of reinforcement materials against usage, Adebisi (2011)

Figure 19 shows reinforcement materials compared to use, it can be seen that SiC used twice as much as Al_2O_3. In comparison with Figure 17, it can be seen why silicon carbide reinforced aluminium is a popular choice due to its light weight and improved wear resistance (Jayaseelan, et al., 2010).

Manufacture using all three modes of reinforcement is not possible using the PBF process. Due to the nature of the feedstock delivery for PBF it is essential that a form of reinforcement is used that can be homogeneously distributed throughout the recoat and hence the powder bed layer. Filaments, whiskers, and short fibers provide better mechanical properties in terms of strength in the direction of alignment for a component produced using conventional MMC manufacturing techniques. However, due to the nature of the PBF build process it is not possible to pre-determine or influence this alignment. Authors have used short fiber reinforcement (Salazar, et al., 2014) with fiber lengths of up to 200 µm but only for Polymer printing where layer thicknesses are up to 500 µm allowing fibers to freely align naturally within the layer. This is not the case for PBF where layer thickness is much smaller i.e., 20 µm, preventing random fiber alignment. Therefore, the only option is to choose particulates as reinforcement, but homogeneous distribution still poses significant challenges (Chang, et al., 2015).

Authors Slipenyuk, et al., (2006) and Wang, et al., (2011) working with extruded MMCs, conducted work considering the effect of size and volume of reinforcement on the

mechanical properties of the MMC. The work concludes that excessive reinforcement size and volume contributed significantly to structural failure of the matrix. Furthermore, the authors were able to demonstrate that at 4.7 μm SiC particle size for the reinforcement would achieve critical content at 6.0 Wt.% and in addition a 77.0 μm SiC particle size for the reinforcement would achieve critical content at 17.8 Wt.%

It is therefore evident that with a reinforcement size of 5.0 μm, and a Wt. % of 20 % used for the initial experimentation in this work, it would suggest that the critical content percentage for the SiC reinforcement was exceeded.

Hence there are three key considerations to be focussed on:

1. Smaller reinforcement particulates (< 0.001 mm).
2. More accurate volume fraction based on maximum possible surface coverage of the matrix particles.
3. Homogeneous distribution of the reinforcement material (Chang, et al., 2015).

Whilst these classifications relate primarily to the form of the reinforcement within the matrix and the contribution made towards enhancing the matrix, it also has implications on the processing method going forward and should be considered carefully (Mistry and Gohil, 2018).

2.5.3 MMC processing methods

The composite processing route is significantly dependent on; the chosen system, matrix, reinforcement, and the reinforcement form as shown in Figure 20. This is an application focussed selection process, aiming to select and exploit the most effective combination, achieving enhanced mechanical or physical properties (Jitendra, et al., 2018). Depending on choices made at each stage, options become limited thereon due to compatibilities between matrix and reinforcement, and processing methods available.

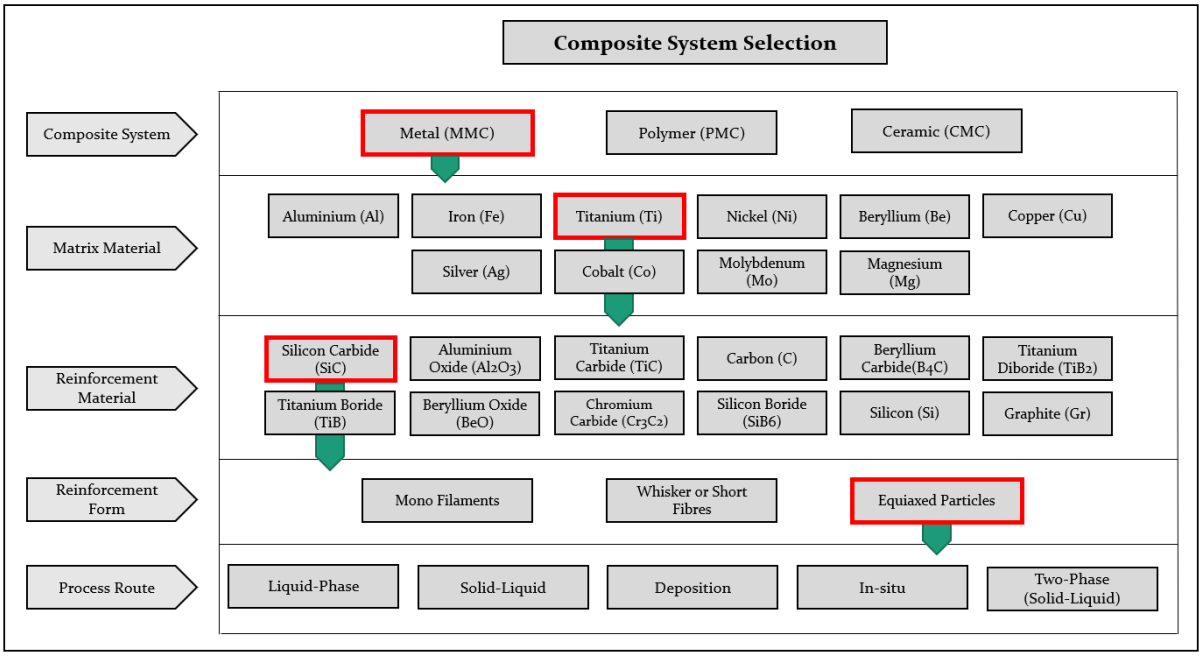

Figure 20 - Composite System Selection Route

Highlighted in Figure 20 are the composite system that forms the basis of this research is highlighted, detailing the composite system, metal, the matrix material, titanium, the reinforcement material, silicon carbide and the reinforcement form, equiaxed particles. Here the process rout is not highlighted as this will be developed through this research. Within this research the processing route would most closely follow the liquid-phase processing rout with two-phase (solid-Solid) pre-processing.

2.5.4 Liquid Phase Processing of MMCs

Liquid phase processing involves combining the matrix and reinforcement materials whilst the matrix is in a liquid state. There are typically two core methods for this (Kostikov, et al., 2014):

- Stir casting,
- Infiltration,

2.5.4.1 Stir casting

Stir casting is one of the most popular techniques for incorporating reinforcement material into the matrix. The temperature of the matrix material is raised to the casting temperature and stirred using an impeller or, in the case of magnetohydrodynamic (MHD) mixing to create a vortices in which the pre-heated reinforcement is added prior to pouring into a suitable mold (Haghshenas, 2015). By stirring the matrix, random yet homogeneous distribution of the reinforcement is achieved, and the reinforcement is primarily in the form of equiaxed particulates but shot carbon tubes have also been used. This process is most commonly used with Al matrices due to the low melt temperatures (660 °C) and the need to place mixing equipment in the melt (Singh, et al., 2020),

however, matrix's with higher melt temperatures can be used where MHD mixing is used. When forming components, gravity casting is the first choice followed by hot extrusion.

2.5.4.2 Infiltration

This process involves the infiltration of the reinforcement by permeation of the liquid matrix. Reinforcement materials are typically in a pre-form state, there are three popular processes for the manufacture of MMCs through infiltration:

- Gas pressure infiltration,
- Squeeze casting infiltration,
- Pressure die infiltration.

The variations in method is determined by the forces required for permeation, this is often a fine balance between the viscosity of the molten matrix, the size of voids and the distance of travel for the molten matrix (Kim, et al., 2017).

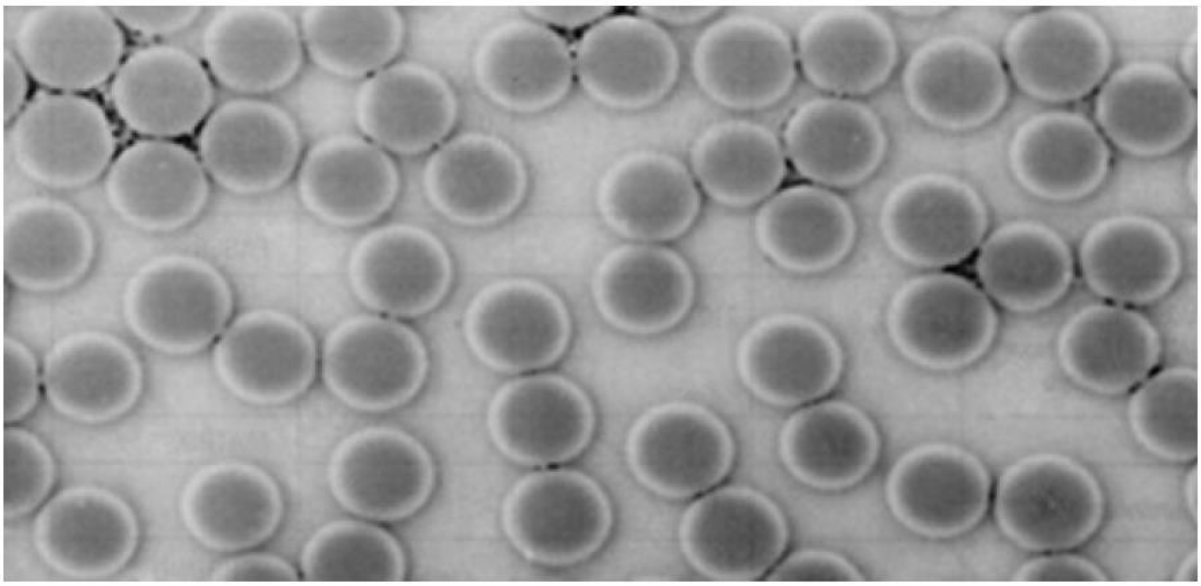

Figure 21 - Structure of a unidirectional endless fiber reinforced aluminium composite material (transverse grinding): matrix: AA 1085, 52 vol% 15-µm Altex-fiber (Al_2O_3), Haghshenas, (2015)

Unidirectional endless fibers are infiltrated by using gas pressure infiltration or vacuum (Figure 21). A lack of matrix separating fibers is clearly visible where fiber-fiber contact will result in a loss of mechanical properties. In the case of SiC monofilaments in a Ti matrix (Figure 22), the filaments are held together as a bundle in a direction suitable for increased strength and molten titanium is encouraged to infiltrate around the tubes to encapsulate them (Kainer, 2006).

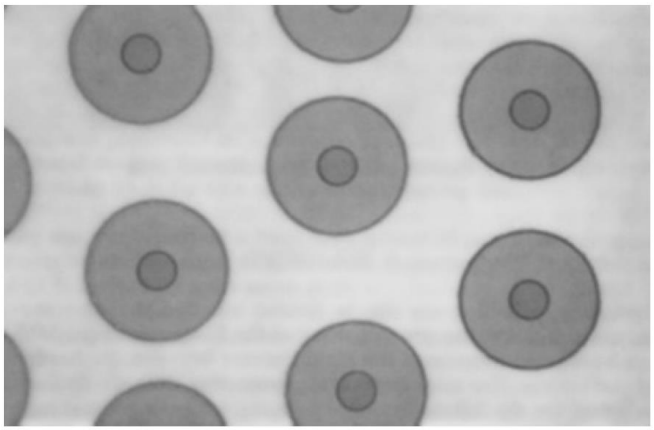

Figure 22 - Structure of a Ti matrix composite material of SiC monofilaments, Haghshenas, (2015)

2.5.5 MMC production through L-PBF

MMC materials produced by PBF is relatively new and novel. Care is needed in selecting both the matrix material and reinforcement for the PBF process, as this is significantly different to the traditional MMC manufacturing routes as discussed. Traditionally MMC materials are processed in a liquid state using stir casting, or infiltration using squeeze casting. This research focusses on metallic materials with ceramic reinforcement. Metallic materials in the main take the form of metallic bonded crystalline structures with good conductivity and ductility but are chemically unstable. Non-metallic materials have, for the better part dipolar bonds, amorphous structures, poor conductivity, are ductile at high temperatures and are chemically stable (Miracle, 2005).

Authors such as Wits, et al., (2019) have investigated Mg-SiC MMC production through L-PBF with some success, reporting however, that a system of 'simple mixing' was unreliable. Other authors in this area include, Mostafaei, et al., (2021), who looked at various matrix materials and both in-situ and ex-situ processes concluding that the technology was at an early stage, stating "*New machines designs and material options will be developed in the coming years which will rapidly drive forward this exciting technology to be used in a wider range of application areas*" this is true and more research must be conducted into volume fractions of reinforcement, homogeneity of mixing and the characterisation of the thermal behaviour within the process. Regarding Ti matrix composites produced by LPBF, Misra, et al., (2019) reported success in fabricating test samples that exhibited improved wear resistance and enhancements in mechanical properties using 5 to 15 Vol.% SiC with processing parameters representing a layer thickness from 0.2 mm to 0.4 mm and scan speeds equivalent of from 58 to 75 mm/sec, the laser spot size was reported as 0.4 mm and a hatch spacing of 0.2 was also used. The authors also reported the presence of intermetallic compounds such as TiC, Ti_3SiC_2 and TiAl with TiC being the most dominant.

2.6 Conventional Feedstock Production for PBF

Metal powder (Feedstock) is the key raw material of the PBF process. Poor quality powder equates to poor quality components and contamination in powders equates to contamination in components (Muniz-Lerma, et al., 2018). It is therefore essential to establish what constitutes good powder and how to determine this, but more specifically powder that it is "fit for purpose". There are many powder manufacturers worldwide and the industry can produce many materials in whatever particulate size range that is required. Authors such as Benson, and Snyders, (2015) developed criteria for feedstock acceptance and have demonstrated direct correlations between feedstock characteristics and part defects including density, surface finish and mechanical properties.

2.6.1 Optimum Feedstock for PBF

For optimum feedstock, the key powder characteristics are:

- Powder packing for maximum layer density and particle size distribution (PSD),
- Powder morphology,
- Powder flow behaviour for consistent feeding/spreading,
- Thermal conductivity of the powder layer,
- Particle porosity,
- Impurity levels.

The typical powder characteristics measured are summarised in Figure 23.

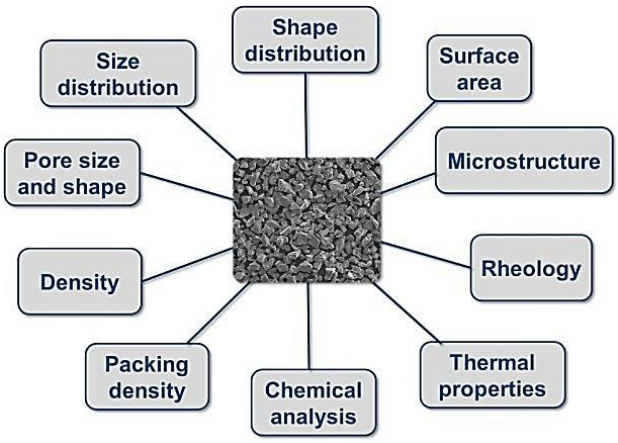

Figure 23 - Typical Powder Characterisation Parameters (Benson, and Snyders, 2015)

In combination, these characteristics and their interactions impact significantly on the PBF process. This impact is complex, as indicated in Figure 24.

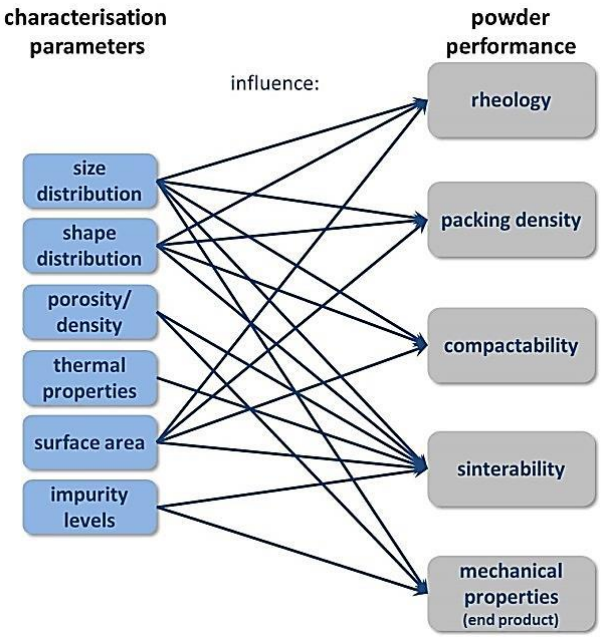

Figure 24 - Inter-Relationships of Characteristics on Powder Behaviour (Benson and Snyders, 2015)

To characterise powders for PBF, international standards are available offering requirements for bulk feedstock as shown in Table 6, taken from the international standard, ISO 17296-3: 2014 "Additive manufacturing - General principles Part 3: Main characteristics and corresponding test methods". This document provides the basic characteristics and test methods for the relevant standards within the PBF industry. In an industry, as dynamic and fast paced as PBF, these standards are continually reviewed and, Table 6 includes updates to reflect the current issue levels of standards that the document lists.

Other new standards include ASTM F3049 - 14: Standard Guide for Characterising Properties of Metal Powders Used for Additive Manufacturing Processes. The American Society for Testing and Materials (ASTM International) standard focusses not only on virgin powders but also the characterisation of used powders. This is a significant step forward for the industry as it recognises the end user's requirement for continuous monitoring of powder quality throughout the lifecycle of the powder.

Table 6 - International Standards for Powder Characterisation (ISO 17296-3 2014)

Powder Characteristic	International Standard	Year	Description
Powder Particle Size and Distribution	ISO 24497	1993	Metallic powders. Determination of particle size by dry sieving
	ISO 8130-1	2010	Determination of particle size distribution by sieving
	ISO 13319	2007	Determination of particle size distributions. Electrical sensing zone method
	ISO 13320	2009	Particle size analysis. Laser diffraction methods
Morphology	ISO 9276-6	2008	Representation of results of particle size analysis. Descriptive and quantitative representation of particle shape and morphology
Surface	ISO 9277	2010	Determination of the specific surface area of solids by gas absorption – BET method
Density (Tap and Apparent)	BS EN 23923-2 (Formerly ISO 3923-2)	1993	Metallic powders – Determination of apparent density – part 2 Scott volumeter method)
Flowability / Pourability	ISO 4490	2014	Determination of flow rate by means of a calibrated funnel (Hall flowmeter).

2.6.1.1 Powder Packing for Maximum Layer Density and Particle Size Distribution (PSD)

Powder packing refers to the amount of raw material available within a given volume, (Muniz-Lerma, et al., 2018). Also referred to as packing density or relative density, this is fundamental in providing sufficient raw material to the melt pool, insufficient material and the bead will not fully form to the desired characteristics and too much will affect the lasers ability to penetrate to the substrate. Point contact is also a key component of heat transfer between individual powder particles whilst initiating fusion (Khairallah, et al., 2016), where particle size is consistently large there are subsequently larger spaces between particles reducing the amount of point contact, this hinders fusion and

substrate penetration due to an inability to transfer energy (Spierings, 2011). Similarly, heat within the bead must be removed efficiently to facilitate solidification and conductivity between powder particles is instrumental in this process (Khairallah, et al., 2016). Research has also shown (Yadroitsev, et al., 2007, Mostafaei, et al., 2018) how small particles are consumed preferentially but are essential to the mechanics of the fusion process as it is the small particles that assist in the melting of the large particles. This can be demonstrated graphically as shown in Figure 25. It can be seen that a single particle size, either large or small reduces the maximum packing density. It is only through a combination of both large and small particles that optimal powder packing can be achieved (Rausch, 2017).

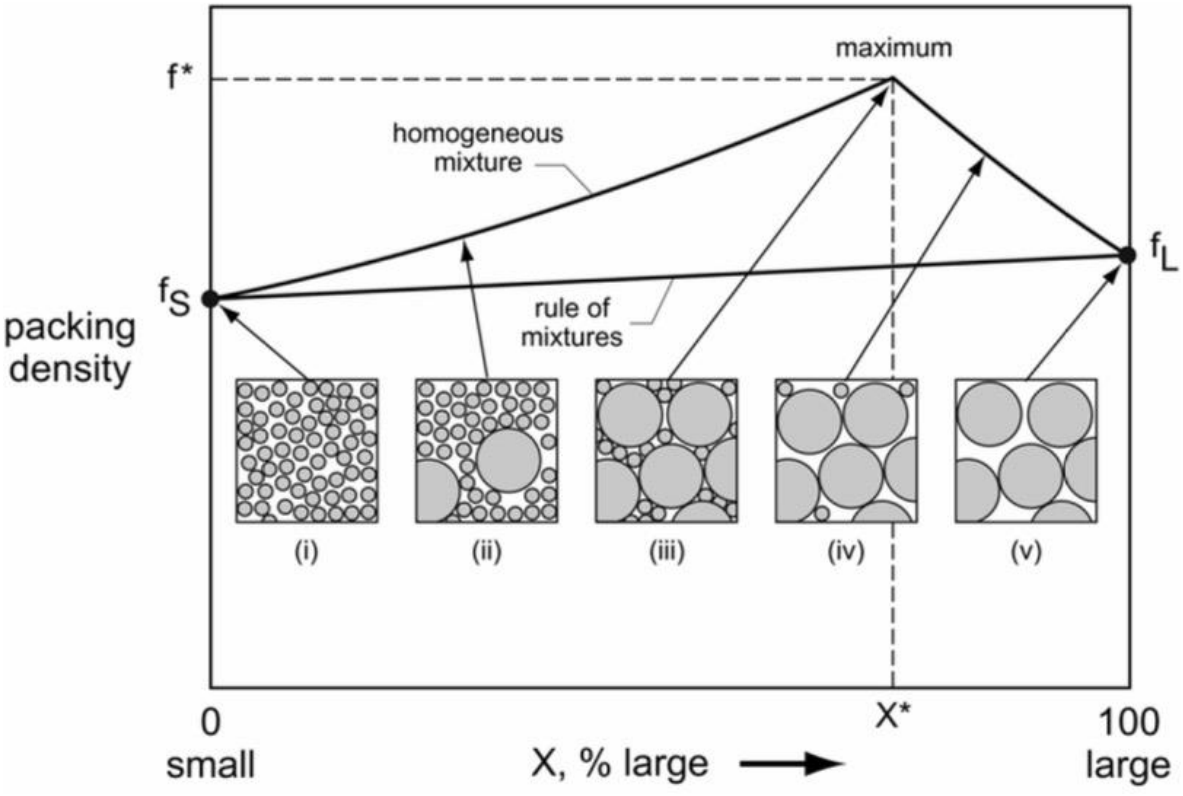

Figure 25 - Optimum Particle Size Packing, Bennett, and Smith (2001)

Referred to as Particle Size Distribution (PSD), this is a detailed measurement of not only the size range of particles within a sample but also a count of how many particles share that size. An example of a particle size distribution curve is shown in Figure 26.

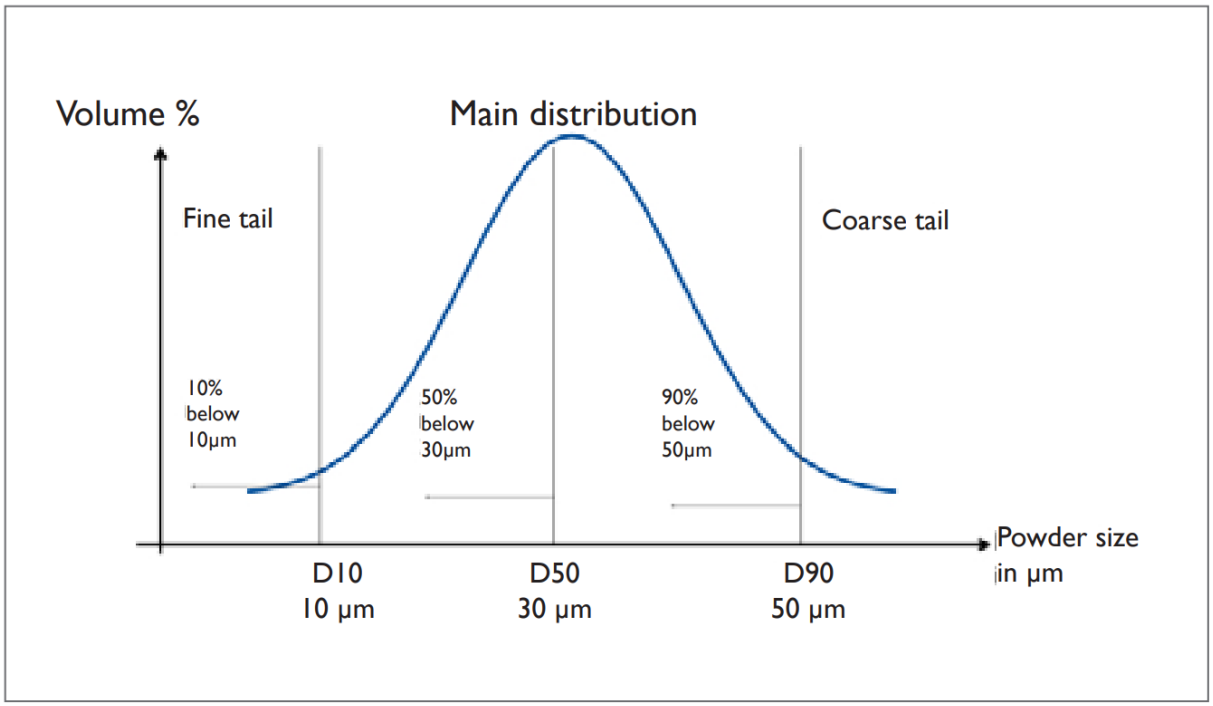

Figure 26 - Example of D10, D50 and D90 on a PSD curve for a 10-50 microns powder (EPMA, 2019)

PSD curves follow a normal gaussian distribution, typically, particle size (Xc-min) is presented along the X axis with frequency along the Y axis. Whilst the mean particle size is recorded, this is not taken as a reliable measure of the size characteristics of the sample. Therefore, a combination of three points, D10, D50 and D90 are taken along with the Calculated mean and standard deviation to provide a universally acceptable measurement of particle size distribution. Further secondary distribution characteristics can be calculated from these values (Retch 2019). As powder is used within the PBF process, a shift of this curve to the right is typically seen. This indicates that the frequency of small particles is reducing through consumption, whilst the frequency of larger particles is increasing through satelighting (Sustarsic, 2005). Values for D10 will therefore increase meaning that the number of particles below this size are now larger and there are fewer small particles in the sample, values for D90 will also increase meaning 90% of the sample is larger in size. Work by Bennett (2013), Kumar (2016) and Kong (2015) looked at a number of different PSD curves and the effect on part characteristics, concluding that the density of the powder layer (packing density) has a significant effect on the degree of densification (Bennet 2013).

2.6.1.2 Powder Morphology

Powder morphology is one of the most significant characteristics for optimised powder for PBF. Whilst it is important to establish an acceptable range of particle sizes it is also important to ensure that particles are able to pack efficiently into the space available (Mostafaei, et al., 2018). Powder morphology is the study of these particles' shapes, the

optimum shape being spherical. Spherical particles better facilitate packing density through their ability to roll and for smaller particles to fall into the gaps between larger particles on recoat (attar, 2015). This in combination with surface roughness are key parameters in achieving an optimised powder bed and are significant in powder flow behaviour (Benson, and Snyders, 2015). The most common method of particle shape analysis is by image analysis, either static or dynamic.

Static image analysis is typically by microscope, a sample of powder is dusted onto a glass slide approximately 100 mm in diameter and a microscope automatically locates each powder particle, storing an image for analysis for each. This method is relatively slow however results are accurate and reliable with the ability to return to any particle of interest based on the image recorded. Key manufactures are Malvern Panalytical (Morphologi 4-ID) and Retsch (PSA300).

Dynamic image analysis is typically by high-speed camera. Images of particles are captured whilst the samples flow past the focal point of the camera and stored for analysis. Dynamic image analysis is significantly faster with on average 300 images stored per second, accuracy and reliability is similar to that of static image analysis however, anomalous images cannot be interrogated post analysis as the sample is no longer available. Key manufactures are Sympatec GmbH (Qicpic) and Retsch (Camsizer X2).

Both methods provide information on key measurements including aspect ratio, roundness, sphericity, and sharpness. For this research, the dynamic image analysis method is used.

2.6.1.3 Powder flow behaviour for consistent feeding/spreading, rheology

As has been established, particle size and shape are both important in PBF, but it is the powders flow behaviour or rheological characteristics that delivers the maximum volume of powder to the build area layer for part manufacture. Key characteristics for rheology are:

- Particle shape,
- Surface texture,
- Inter-particulate forces of cohesion, and
- Moisture content.

Particle shape

Irregularities in particle shape effect rheological behaviour primarily through mechanical interlocking (Figure 27) but also by preventing the movement of smaller particles within the system caused by attached satellite particles (Ozbilen, 1999, Freeman technology, 2019).

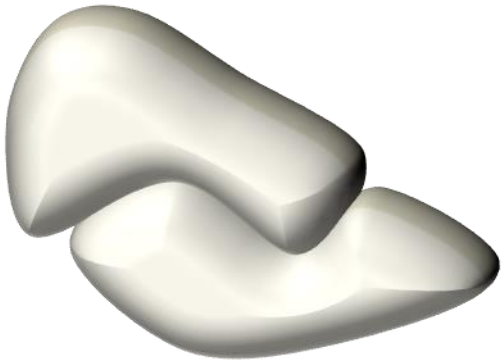

Figure 27 - Powder particle mechanical interlocking, Freeman technology (2019)

Changes in the shape of powder particles can be established and monitored using particle size analysis, particle shape analysis, Hall (ASTM B213) or Carney (ASTM B964) flow testing or angle of repose measurement (Mostafaei, 2018), providing clear insights into the degradation of the powders quality over time (Benson, 2013). If powder flow problems are indicated, costly investigations into build prep or the machine can be avoided.

Surface texture / roughness

Surface texture or surface roughness refers to the outer surface of the powder particles (Meier, et al., 2019). Surface roughness effects a particles ability to smoothly pass by other particles and the powders ability to flow consistently during recoating due to friction. Ideally, powder should be able to occupy the gap between the recoater blade and substrate efficiently with smaller powder particles falling between larger. Where powder surface texture becomes rougher, less powder is deposited within the layer but is carried across the build area to the overflow (Seyda, et al., 2012). Research by Ali, et al., 2018 concluded that part density can be reduced by up to 20% through recoat proficiency. Part built at the end of the recoat were found to be less dense than those at the beginning due to large powder particles ability to travel further with small to medium sized particles positioning sooner. It was also found that surface roughness increased over successive uses from a R_z of 91.58 to 122.71 in twelve uses for parts produced. Increased surface roughness also relates directly to an increase in surface area, therefor increasing surface energy within the powder feedstock. This increase in surface energy also contributes to attraction of particles due to inter-particulate forces (Meier, et al., 2019).

Surface roughness measurement of powder particles is particularly challenging and is typically carried out by vapor sorption analysis methods (Burnett, et al., 2011, surfacemeasurementsystems.com). Other indirect methods for the measurement of surface roughness include shear cell testing (Freemantech, 2019) or angle of repose

(Beakawi Al-Hashemi, 2018) with lessening degrees of accuracy. In this research, angle of repose was selected as the method for determining changes in surface roughness cased through the processing of powder by mechanical alloying. The powders particle's ability to lock together through mechanical interlocking and surface roughness is indicated by the change in angle of a deposited cone of feedstock powder. As powder becomes rougher and more irregular the angle of repose increases. This is a comparative methodology and relies on comparison between baseline assessments and subsequent samples taken after processing. It is a relatively inexpensive method of determining powder quality and the results represent a number of powder qualities such as: shape, roughness, surface energy and moisture content, however, for more quantifiable detail regarding these characteristics, a more detailed analysis of the individual characteristics would need to be pursued.

Inter-particulate forces of cohesion

Inter-particulate forces of cohesion are primarily caused through increases in surface energy. The existence of solid materials is due to energetically favourable conditions of low energy enabling the materials molecules to bond with each other. At the materials surface however, the molecules are in a less favourable state of higher energy being less surrounded by bulk molecules. As with conventional inter-molecular forces, powders attract other powder particles, solids, liquids, and gasses via long range van der Waals forces (dispersion forces, γ_s^d) and short-range chemical forces (polar forces, γ_s^p) (Liu, et al., 2017). These dispersive and polar forces are key to understanding optimum powder characteristics within areas such as: wettability, powder flow, agglomeration, adhesion, cohesion, and the build-up of static charge within the process. Surface free energy (SFE γ_s) for Ti6Al4V is 47.6 ± 3.5 mJ/m², (Schuster, et al., 2015) and for SiO_2 is 64.7 mJ/m² (Anupama, et al., 2019) here silicon dioxide is referenced as this is the film covering silicon carbide in most instances. As the effect of surface free energy is surface area dependent, smaller powder particles contribute considerably to the overall amount of free energy available. Inverse gas chromatography is often the preferred method for surface energy measurements, and surface energy heterogeneity.

2.6.2 Powder manufacture

A number of powder manufacturing methods have been developed for the production of feedstock for PBF, key processes such as:

- Gas Atomisation (GA),
- Vacuum Induction Melting Gas Atomisation (VIM GA),
- Plasma Atomisation (GA + Plasma),
- Plasma Rotating Electrode Process (PREP).

Figure 28 shows comparisons between powder manufacturing methods in relation to powder characteristics and powder defects. Values represented towards the centre of the diagram are considered poorer than those at the outer edge (Sun, et al., 2017).

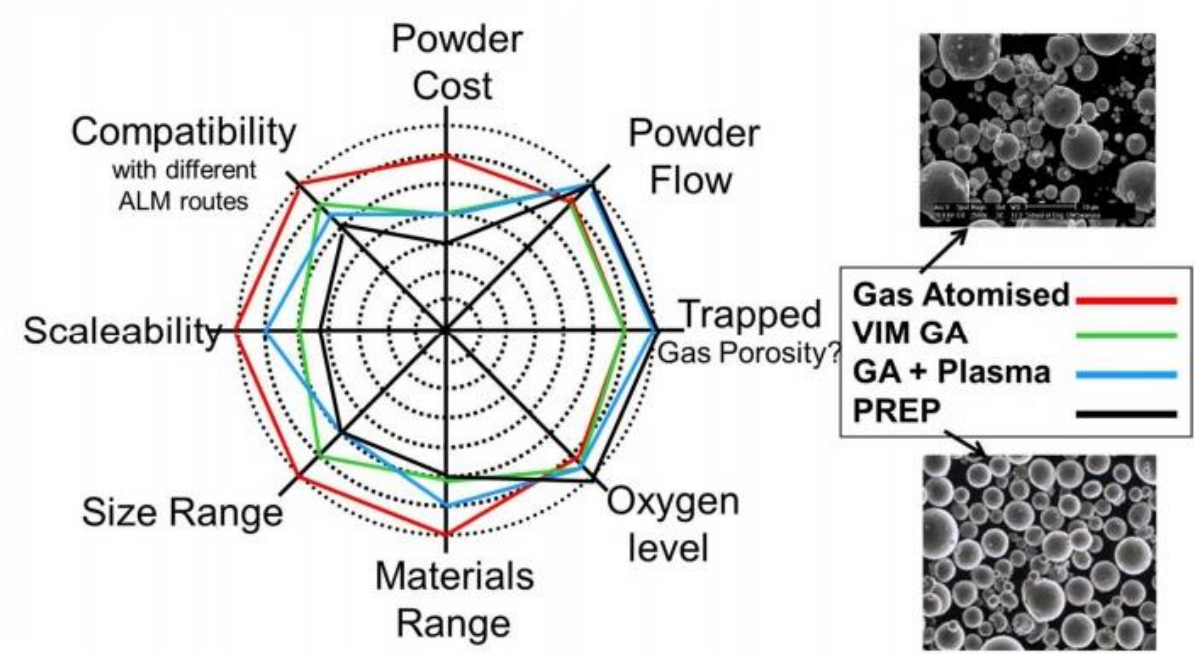

Figure 28 - PBF Powder Production Methods (Murray, Sandvik Osprey 2015)

2.6.2.1 Gas Atomisation (GA)

GA is a popular process for powder production and demonstrates good qualities in most quality categories such as size range, materials and compatibility but is limited by cost, O_2 content and trapped gasses (Figure 8). Regarding O_2 content and trapped gasses, this is problematic. In most conventional applications such as casting and powder sintering, gasses and contamination can be tolerated as they can be removed during the manufacturing process or through post processing. For PBF, trapped gasses are detrimental to the process and have deleterious effects on the part quality (Quintana, 2017).

GA involves the melting of raw material in a crucible situated at the top of the process apparatus, shown in Figure 29.

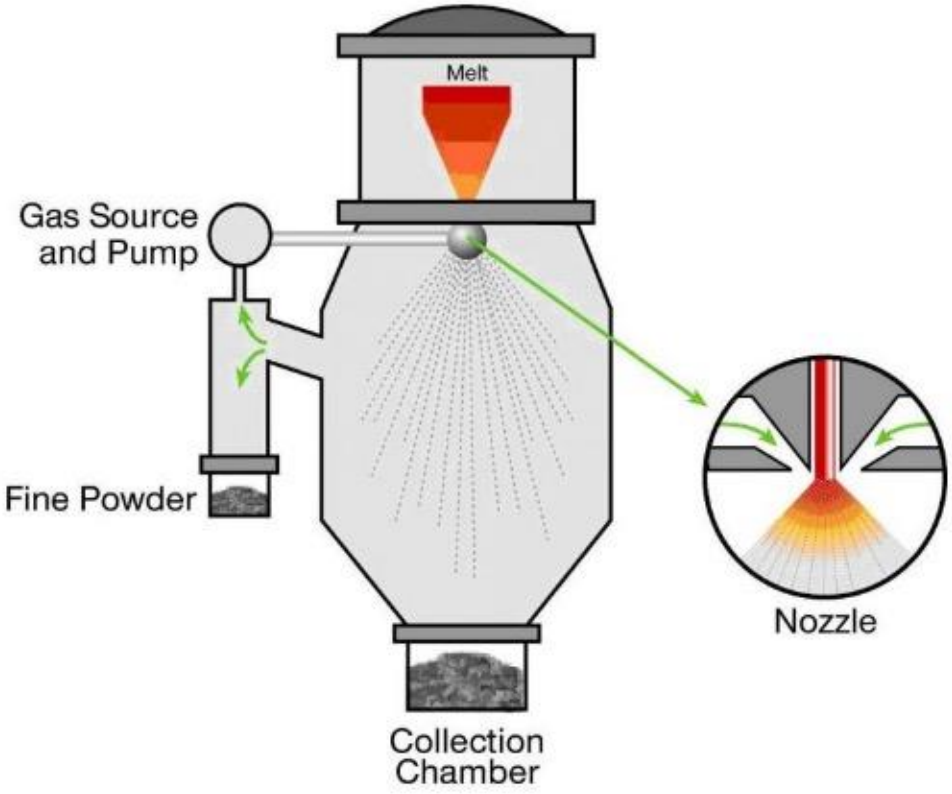

Figure 29 - Gas Atomisation process - LPW technology UK (2020)

As the material is melted, a steady flow of molten material passes through an orifice and past pressurised gas which separates particles through the nozzle. Space is provided within the collecting chamber for the particles to freely spin without contact with other particles. The height of the chamber allows particles to solidify (Phoenix Scientific Industries (PSI) Ltd (2020). The process is efficient and reliable with excellent yields in the range of 0 to 500 µm and particularly 20 to 150 µm range representing 10 to 50% of the yield (Carpenter additive, 2020), this is evident from Figure 28 as is the poor values for trapped gasses, high levels of O_2 and powder flow, these are attributed to the process environment and particle separation. Contamination is also concerning and attributed to the crucible (Jones, H. 2004).

2.6.2.2 Vacuum Induction Melting Gas Atomisation (VIM GA)

VIM GA uses a system of induction melting of the raw material in a vacuum chamber to eliminate contamination and trapped gasses (Figure 30). Raw material is melted and transferred to a tundish under vacuum where it is passed through gas jets for atomisation.

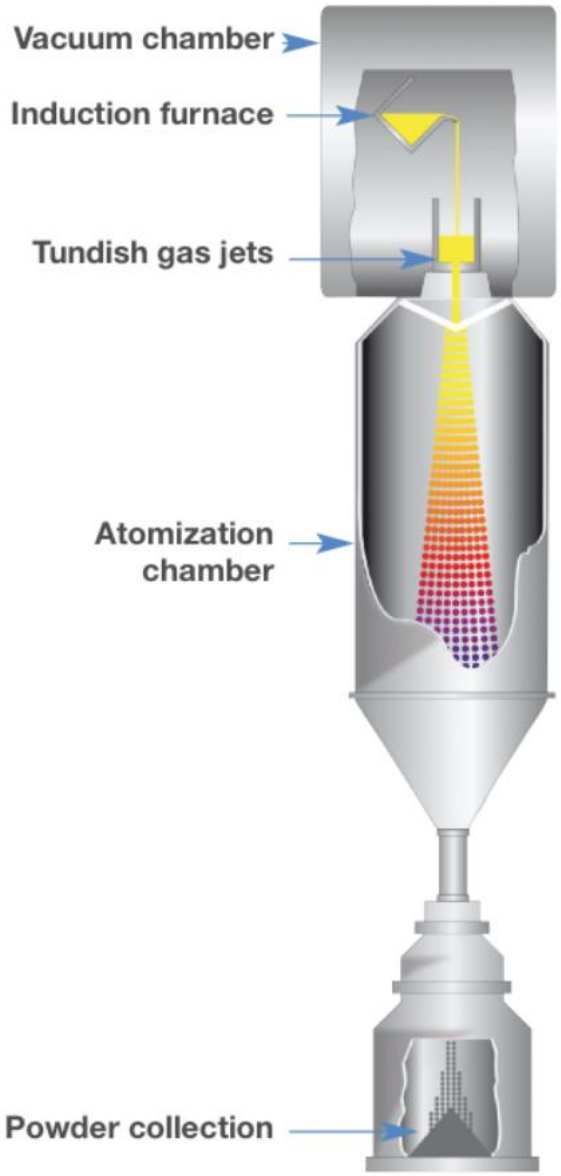

Figure 30 - VIM GA process, Erasteel France, (2020)

It is in the vacuum chamber that the raw material can be refined and degasses prior to atomisation. Whilst the process demonstrates improved powder quality in areas such as powder flow, trapped gasses and O_2 levels, it shows no significant improvements over GA. Powder yields with a typical size range from 0 to 300 µm are produced. Powder yields with a size range of 30 to 90 µm (d50) are also now being produced (ALD Vacuum Technologies GmbH, 2020).

2.6.2.3 Plasma Atomisation (GA + Plasma)

Plasma atomisation is similar in many ways to GA. Raw material is melted on-demand using plasma torches situated adjacent to the nozzle. Raw material is typically wire fed into the process allowing for an inert atmosphere to encompass the entire system.

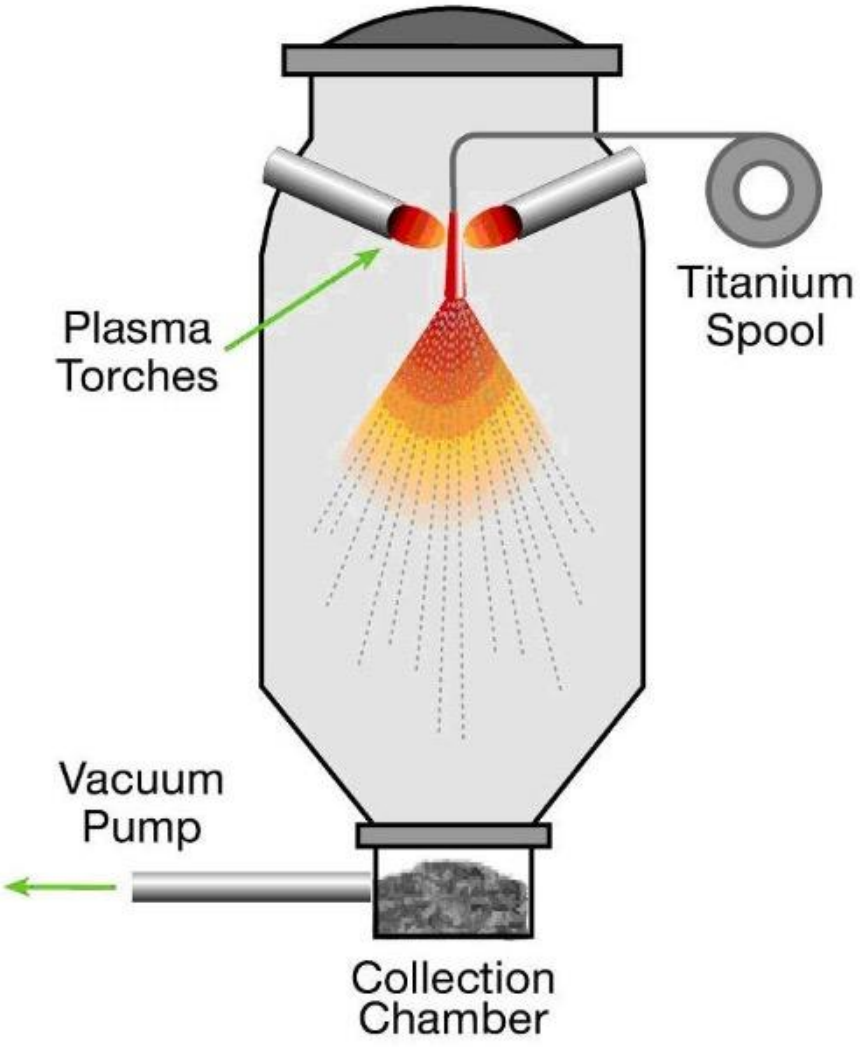

Figure 31 - Plasma Atomisation process - LPW technology UK (2020)

The process is shown here in Figure 31. Contrary to GA, Plasma atomisation demonstrates excellent performance in the areas of trapped gasses, O_2 and powder flow due to the inert atmosphere, non-contact material feed and improved surface texture and reduced satellites. However, cost is high in comparison, size range is limited typically 0 to 200 µm and the range of materials is limited to those that can be formed into wire (Ahsan, et al., 2011). Plasma atomisation is currently showing promise, with more systems being adopted with the additive industry (Carpenter additive, 2020), due to the promise of improve powder qualities.

2.6.2.4 Plasma Rotating Electrode Process (PREP)

For applications where powder flowability and trapped gasses are of significance, such as PBF, the plasma rotating electrode process PREP (PyroGenesis, Canada) offers the ability to burn off gaseous substances to produce clean spherical particles thus improving flowability and reducing trapped gas content (Clayton, 2015, Sun, et al., 2017).

In their research Ahsan, et al., (2011) found improvements in mechanical and crystallographic properties from their parts manufactured from PREP produced material in comparison to GA material-based components making this process of interest to the industry.

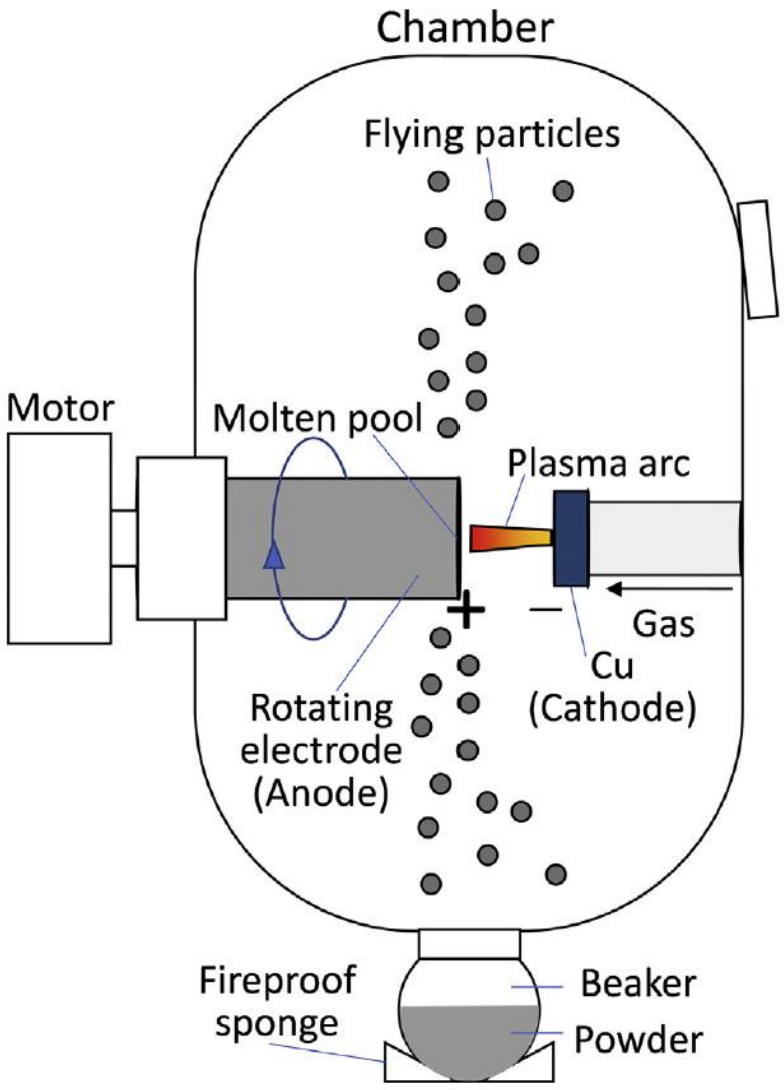

Figure 32 - Schematic of PREP atomiser, Cui, et al., (2020)

Raw material in the form of a sold bar typically 20mm in diameter is rotated at high speed circa 10,000 rev/min whilst presented to the plasma arc electrode (Figure 32). As the raw material is melted, droplets are produced that through centrifugal force are projected away and are collected within a cylindrical chamber. Atomising chambers vary in size but are around 2.5 meters in diameter (Arkon, 2020). A combination of the rotation speed and the diameter of the war materials produces increased particle spin resulting in improved sphericity and reduced contamination within the yield (Cui, et al., 2020). Rotational speeds of up to 40,000 Rev/min are now becoming possible (Arkon, 2020). Size range for a typical yield is from 50 to 500 µm. Whilst this method

demonstrates impressive characteristics for powder flow, O_2 and trapped gasses, it lacks particle sizes in the range from 0 to 50 µm required by LPBF along with minimal material range, scaleability and high cost of production means it is currently unviable as a powder production method unless for special circumstances, this challenge, however, is being addressed by researchers (Cui, et al., 2020) and powder manufacturers (Arkon, 2020).

2.6.3 Strategies for Mixing Dissimilar Powders

A crucial factor for the manufacture of an MMC is the homogeneous distribution of reinforcement within the product (Rosso, 2006). Achieving an optimal volume of reinforcement is equally as crucial. Too little reinforcement and the product will not demonstrate any benefits, with too much, the product is at risk from over saturation of reinforcement, and hence insufficient binding to hold the MMC together (Sivakumar, et al., 2016). The over saturation point of the matrix varies depending on the material and mechanical properties used for the matrix and the reinforcement materials morphology and size (Chawla, 1974). Two key factors thus present themselves: the amount of reinforcement and its homogeneous distribution throughout the matrix.

Within conventional MMC production, SC has become one of the most widely used methods employed, due to its reliability in suspending the reinforcement within the MMC. Within this research, in-situ alloying is principally employed in the formation of the MMC material, taking place continualy as the melt pool advances. It is therefore necessary to develop a method to reliably deliver the correct mix of both matrix and reinforcement materials. There are currently three possible solutions:

- Manual Mixing,
- Gas Atomising,
- Mechanical alloying.

2.6.3.1 Manual Mixing

For this research, the constituent powers could be prepared by manually tumbling or shaking of the powder mixture until the SiC would be distributed throughout the Ti6Al4V powder. This only remains so at the time of mixing. If the mixture is agitated during transportation, either to the production machine or during the process of recoating, the materials will separate through granular convection. Typically, granular convection is not reliant on gravity or effected by the mass of the objects involved but more their size. If slight movement or oscillations are produced, smaller particles are encouraged to fall between the gaps of the larger ones forcing them to appear to rise to the surface. The granular convection effect is more visible when the particles have contrasting colours as seen in Figure 33 where DM20 (EOS Direct metal 20) was mixed with tungsten (W). The DM20 has a smaller particle size than the W and has fallen beneath the W leaving it exposed.

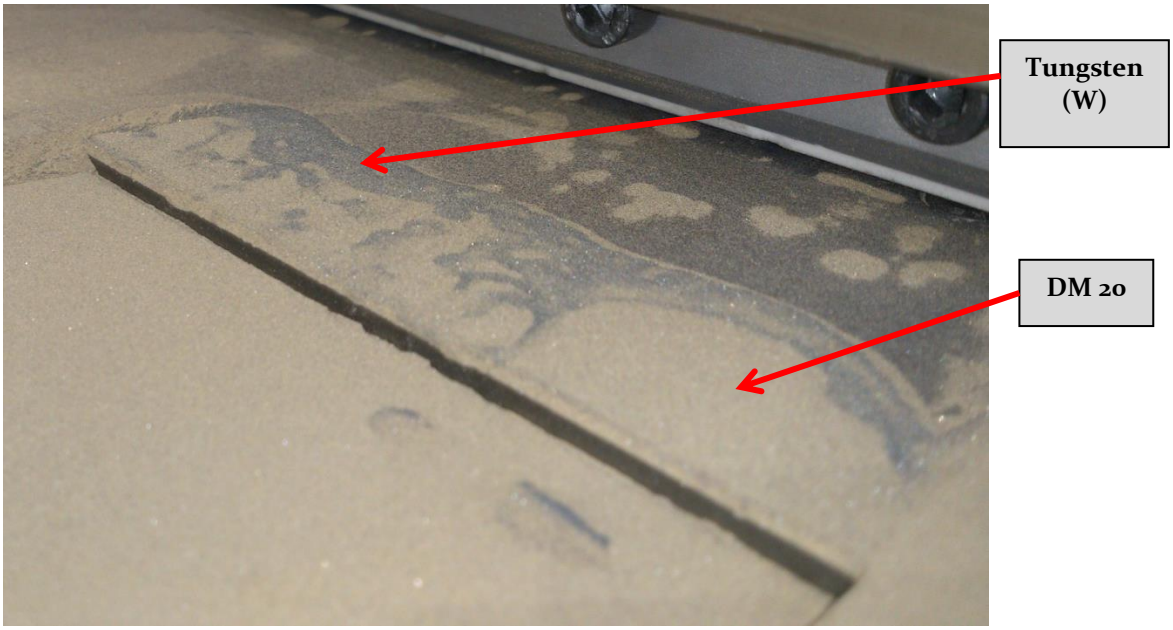

Figure 33 - EOS DM20 - Tungsten Powder Mixed by Hand

Manual mixing is therefore an unacceptable methodology due to its inconsistency and inability to produce the desired results in terms of homogeneous powder delivery.

2.6.3.2 Gas Atomisation

Gas atomisation is currently the widest spread process for the manufacture of metal powders/feedstock within the additive industry. Several producers have invested significantly in new technology such as plasma atomisation, but the industry is still undecided as to whether this produces qualities that are more desirable than gas atomised powder. Furthermore, the cost of plasma atomisation is set to be significantly higher than gas atomising at this stage due to the availability of such equipment.

With respect to PBF this is currently the most reliable production method for feedstock, producing a range of particle sizes that are subsequently sieved to achieve the desired size distribution (Tan, 2017).

Gas atomisation is a costly production process with costs usually amortised across large batches producing a cost-effective process. Small batches of powder can be produced in the region of 30kg (Minimum order), however, for research this is impractical as this minimum order will only offer one version of the powder mix ratio, should the requirement be for a varied mix ratio range of the same material for testing purposes, this cost would be significant. In this instance and as for this research MA was investigated.

2.7 Mechanical Alloying (MA)

MA is a solid-state powder processing technique harnessing high kinetic energy for the repeated cold working of material, typically in powder form. Using a high energy attrition ball mill, powder particles are flattened and cold-welded to form agglomerations of alloyed powder, over long periods of time. These agglomerates once formed, increase in size, and fracture many times to produce a refined grain structure within the resultant powder yield (ZoZ GmbH, 2018). Originally developed to produce oxide-dispersion strengthened (ODS) Ni and Fe-base super alloys for applications in the aerospace industry (Zoz, 2012), MA has now been shown to be capable of synthesising a variety of equilibrium and non-equilibrium alloy phases starting from blended elemental or pre-alloyed powders.

Commercially available MA systems vary in size, level of investment, capacity, and flexibility of use. Systems such as Drum ball mills are often the largest with a capacity of up to 20,000L of powder as opposed to a planetary ball mills being able to hold a maximum of 8L.

Chosen due to its fast-kinetic processing, and the ability for temperature and vacuum/gas control of the milling environment, the Zoz Simoloyer CM01 used for this research, provides an adequate chamber capacity (up to 400L) for small batch powder production.

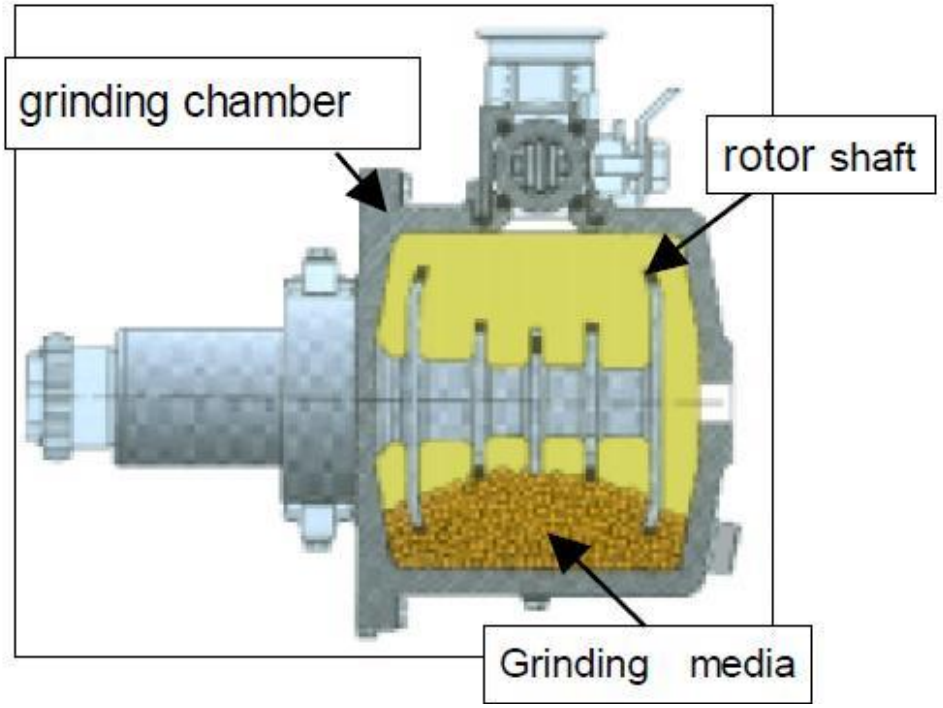

Figure 34 - High Energy Mill Sectional View (Zoz, H. Ren, H. 2008)

The Zoz Simoloyer CM01, shown in Figure 34, is an attrition ball mill having a stainless steel horizontally mounted alloying chamber. A series of steel blades can be seen mounted to the rotor shaft in the centre. While rotating, the blades force grinding media (stainless steel balls) to collide with the powder producing sufficient force to alloy the powder (Figure 35). The combined velocity of the rotor shaft and grinding media produce enough force and energy to both plastically deform the powder and induce cold welding to form agglomerated material (ZoZ, 2008).

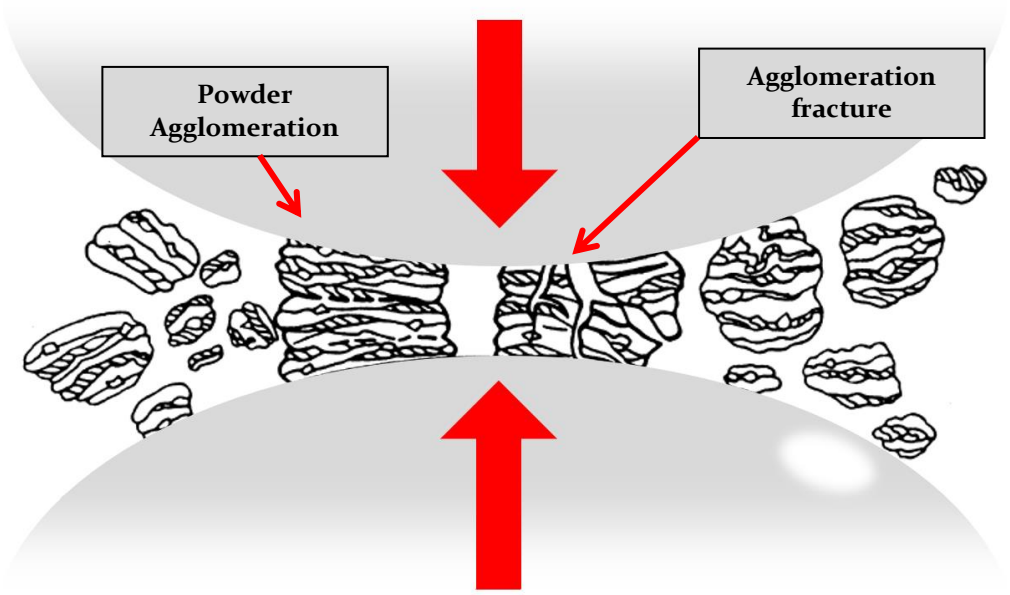

Figure 35 - Ball – powder - ball collision during mechanical alloying. Suryanarayana (2001).

Parameters significant to the process are:

- Ball to particle size,
- Ball to powder ratio,
- Chamber charge volume,
- Rotational speed (rev/min), and
- Processing time.

Typical values are shown in (Table 7).

Table 7 - Typical alloying parameter values

Operating parameter	Typical value
Ball to particle size	5, 8 or 12mm
Ball to powder ratio (BPR)	10:1
Chamber charge volume	50%
Rotational speed (rev/min)	100 to 900 rev/min
Processing time	4 to 90 hours

Ball to particle size

When selecting balls, there are no specific rules or calculations. It is important to select a size that is larger than the particle size, remembering that the particles size will increase, for fine powder particles, a small ball is favoured (Park, et al., 1992). Ball material is typically stainless steel but for harder materials, tungsten or ceramic can be chosen (Li, 2002). When developing process performance, it is noted that larger balls possess higher kinetic energy, research has also looked at the effect of processing with balls of multiple sizes (Gavrilov, 1995), reporting that the highest collision energies were achieved.

Ball to powder ratio (BPR)

Ball to powder ratio (BPR) again is maintained at a ratio of 10:1 by weight, this is rarely varied by users however, for larger systems such as an attritor, ratios of 50:1 and 100:1 have been used. Therefore, this ratio is related more to the capacity of the equipment than the effect on the powder. Suryanarayana, et al., (1992) found that formation of an amorphous phase was achieved in a Ti-Al powder mixture milled in a SPEX mill in:

- 7 h at a BPR of 10:1,
- 2 h at a BPR of 50:1, and
- 1 h at a BPR of 100:1.

It was deduced that the increase on balls in relation to the powder, increased the energy transferred into the powder particles, decreasing the alloying time.

Chamber charge volume

Chamber charge volume again is typically maintained as a constant throughout processing at around 50% of the container volume (Zoz, 2008). As the process relies on the collision of balls and powder within the chamber, space is as important as the median being processed. Should this charge ratio be lowered however, evidence shows that alloying time can also be reduced (Liang, 2009).

Rotational speed (rev/min)

Rotational speed (rev/min) of the rotor shaft is another key parameter when developing the process for individual materials. Logic dictates that a fast-rotational speed would exert more energy and therefore more force, this would also theoretically reduce the alloying time considerably. This unfortunately is not the case, at high rotational speeds, balls travel to the inner wall of the chamber where they become ineffective (Zoz, 2008). Rotational speeds are selected based on the energy required to propel balls to a position where they can drop with sufficient energy to impact together, the small amounts of powder trapped between (0.2 mg) becomes flattened and the process of effective agglomeration is achieved (Ruiz-Navas, 2006). Achieving the best speed is often

achieved through trial-and-error, however, through observation, thi9s can be determined based on the effect on samples taken and results plotted (Lu, et al., 1995).

Processing time

Processing time is the most important parameter. Due to the typical length of processing being circa twenty hours, small samples are regularly taken to establish a satisfactory time to terminate milling (Zoz, 2008).

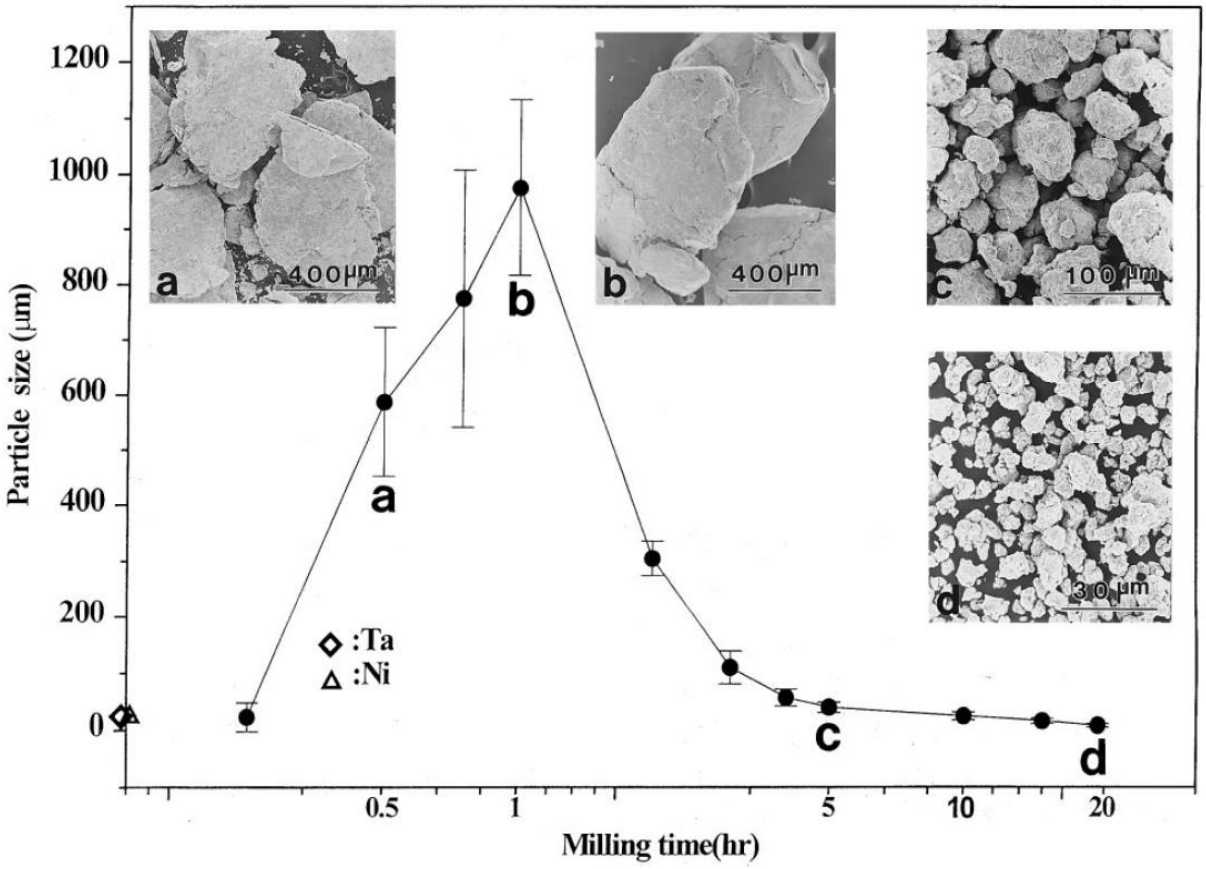

Figure 36 - Agglomeration size (μm) change over time (hr), Suryanarayana, (2001)

Milling times are chosen to achieve a steady state between cold welding and fracturing of the powder, a point can be reached over time, where particle size stabilises, and minimal change is observed. Figure 36 shows the rapid growth of agglomerations within the process in the first hour of processing. This steadily reduces over the alloying time to be similar to the original particle size. This is a good indication for the termination of the process, particle size reduction is typically around 0.1%, alloying beyond this point has been shown to introduce unwanted properties such as contamination and undesirable phases (Suryanarayana, 2001). It can also be noted from the images in Figure 36 that powder particles are significantly angular and irregular, this would be unacceptable for the LPBF process which requires spherical powders with relatively smooth surfaces. Whilst particle size is achievable, sphericity will be challenging.

Care should also be taken to consider temperature and environmental control. Due to the cold working of the powder, elevation of the materials temperature occurs rapidly and is therefore maintained at room temperature (20^{o}C) to avoid adverse effects on the material. Evidence has shown however, that by altering the temperature, control of phase transformations can be achieved (Suryanarayana, 2001) researchers have experimented with lowering the milling temperature using liquid nitrogen and increasing the temperature (Kimura, 1990) however, this is material dependent. Environmentally, due to the exposure of surfaces during the process, oxygen and other contaminates can become incorporated into the alloyed powder. This can be eliminated by milling in an inert atmosphere. Argon (Ar) or helium (H) is used to good effect (Goodwin, et al., 1996).

2.7.1 Mechanical Alloying (MA) For Laser-Powder Bed Fusion (L-PBF)

MA for L-PBF differs significantly from commercial MA. The objective here is to bind the reinforcement material to the softer matrix material for means of homogeneous transportation within the build process (Lyall, 2015) without changing the morphology of the matrix powder.

Authors; Simonelli, et al., (2018) developed a similar approach using Polyvinyl Alcohol (PVA) diluted at 2.7 % in distilled water, producing a wet mixture that was dried at 100 °C for 15 h for in-situ alloying of titanium (Ti), aluminium (Al 6 Wt.%) and vanadium (V 4 Wt.%) in exact quantities to produce Ti6Al4V material. The authors reported some minimal success, concluding that homogeneity was a key issue. Whilst this method would mix the constituent materials homogeneously it also has the potential to wash the larger particles of Al and V.

There is no need for the process to refine the grain structure of the material being processed as in conventional MA, as this will be subjected to melting during the L-PBF process. The MA processing time can therefore be reduced significantly from that of days, (4 to 90 hours) (Zoz, 2008), down to minutes, (10 to 40 mins), the duration of the MA process is enough to embed the reinforcement particles without compromising the morphology of the matrix powder.

The MA process is therefore primarily employed to embed the smaller reinforcement particulates onto the softer surface of the matrix material (Figure 37). The matrix material then becomes a reliable delivery mechanism for those smaller particles for in-situ alloying within the PBF process.

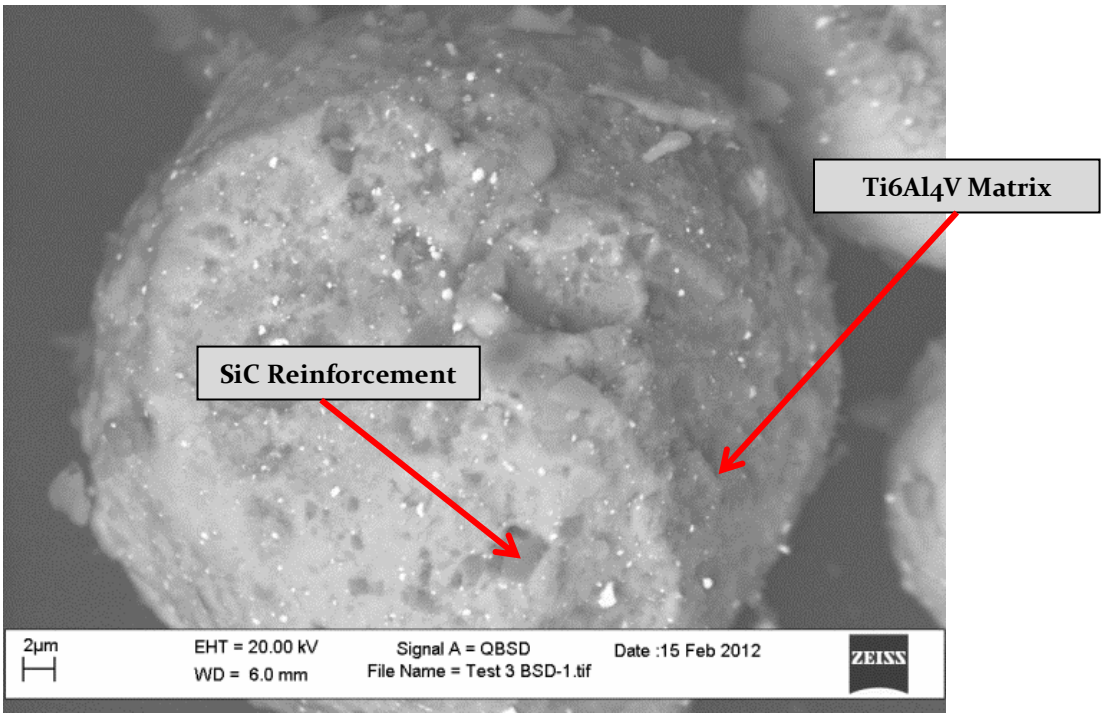

Figure 37 - SiC Reinforcement Material Embedded onto Ti6Al4V Matrix Material by MA (Lyall, 2012)

There are therefore, five key considerations to consider during the MA process:

1. Changes to particle size and size distribution during the MA process.
2. Changes in morphology during the MA process.
3. Maximum surface coverage of the matrix material possible through MA.
4. Excess reinforcement material post MA.
5. Risk of contamination during the MA process.

2.7.1.1 Changes to Particle Size and Size Distribution During the MA Process

Down-stream and in-process activities such as sieving and the mechanical recoating of powder, dictate that a specific particle size range and morphology be maintained. The particle size typically being between 10 µm to 55 µm and the morphology being as close to spherical as possible for the powder bed PBF process. Sieving fully MA feedstock could remove a significant amount of the powder base due to agglomeration. For the research done for this work it was important to take a baseline measurement of the matrix powder prior to MA and at periodic stages during the process to determine at what point the process altered the particle size and morphology of the matrix powder thus establishing a satisfactory milling time.

2.7.1.2 Changes in Morphology During the MA Process

Changes in morphology are found to be more significant due to the forces involved within the process and due to the processing equipment's tubular configuration

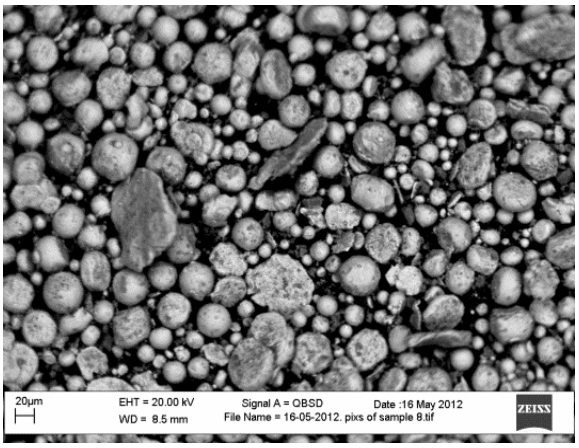

Figure 39a - Flake or Plate Like Structures Produced by Excessive MA (Lyall, 2012)

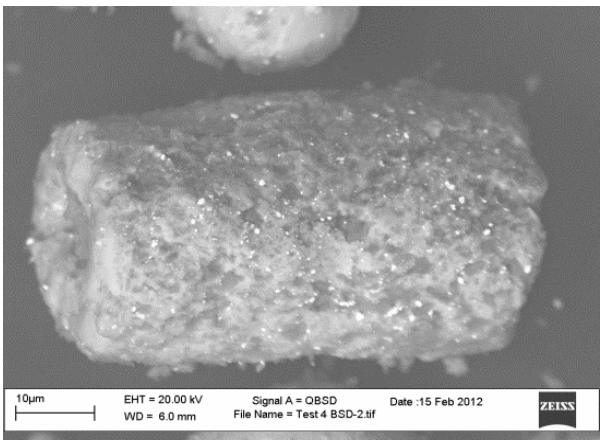

Figure 39b - Tube or Cylindrical Like Structures Produced by Excessive MA (Lyall, 2012)

(Olowofela, 2013).

The ideal particle shape for PBF due to the need to spread the powder over the powder bed is spherical (Kumar, 2016). From prolonged milling this initial spherical shape will change significantly exhibiting flake or plate like structures (Figure 39a) and tube or cylindrical like structures (Figure 39b). These particle shapes are not conducive to controlled recoating and will significantly reduce the density and predictable deposition of powder within the PBF build environment (Hentschel, 2003). Based on rheological evidence in chapter 5.2.2, the apparent density of Ti6Al4V feedstock is ~ 50.6 % that of the solid material, this being a significant contributing factor in producing a satisfactory bead. hence misshapen particles can hinder the delivery of material and lead to porosity and part failure (Attar, 2015).

2.7.1.3 Maximum Surface Coverage of The Matrix Material Possible Through MA

It can be estimated through particle analysis (Spierings, 2011) and calculation the available surface area of matrix material, to be covered by SiC. It is therefore feasible to calculate the maximum amount of reinforcement material that the matrix material can carry. Additional amounts of reinforcement material will not adhere to the surface of the matrix material and could impinge on the process. This is resolved in chapter 7.1.2.1.

2.7.1.4 Excess Reinforcement Material Post MA

Excess reinforcement material post MA is also a function of the maximum amount of reinforcement material required to coat the matrix material, exceeding this value will

result in excess reinforcement material remaining unattached within the feedstock. The risk here is that it can form areas of concentrated reinforcement within the part leading to failure due to overloading or over stressing the matrix at that point.

2.7.1.5 Contamination Risks During the MA Process

There are two main forms of contamination possible during the MA process:

- Foreign particles
- Oxygen

Foreign particles:

Whilst every effort is taken to eliminate the possibility of cross contamination between samples, it is possible to contaminate the sample with particles from the process apparatus (Zoz, 2008). In Figure 37, tungsten carbide (WC) contamination is visible as small white particles, this was contamination from a planetary ball mill (Fritsch Pulverisette 5) used to reduce the SiC in the initial experimentation (Lyall, et al., 2015). It is recommended by the manufacturer (Fritsch, GmbH) that the milling vessels are of a harder material than the material being milled thus the choice of WC lined vessels and WC balls. Most of the contamination can be eliminated by purchasing SiC within the desired size range thus eliminating the attrition between the SiC and WC equipment. Within the Symoloyer apparatus, foreign particles can be liberated from the stainless-steel paddles that form the rotator and the wall of the alloying chamber (Zoz, 2008). Prolonged processing times increase the risk of contamination from these sources (Dabhade, et al., 2007), but this is minimised when alloying for reduced cycle times as is being developed here, with MA for PBF.

Oxygen:

Risk of O_2 contamination comes from surface O_2 on the feedstock materials and from within the MA apparatus (Zoz, 2008). Submicron SiC has a large surface area and high surface energy making it susceptible to attract O_2 (Yamada, 1991), similarly Ti6Al4V also has a strong affinity for O_2 (Hidnert, 1943). During the MA process, as particles of SiC are embedded on to the surface of the Ti6Al4V matrix material O_2 can be trapped between the interfaces (Zoz, 2012), this trapped O_2 would be released during the PBF process. Therefore, during the MA process air is first removed from the chamber by vacuum and Ar gas is introduced to establish an O_2 free environment, this process is repeated two to three times before alloying the materials.

2.7.2 Process Preparation – Mechanical Alloying (MA)

With respect to the PBF process and the nature of the constituent materials it is known that delivery from the powder dispenser to the build platform area can be problematic

and a loss of homogeneity is experienced. MA is therefore used to augment the delivery of smaller particles across the build area.

Hence the main objectives for the MA phase of the research are:

- Powder / particulate selection,
- Mix ratio,
- Initial powder particle size and morphology,
- post milling powder particle size and morphology,
- Homogeneity of reinforcement,
- Degree of particle embedment,
- Contamination.

Chapter Three

3.0 Background

3.1 Initial Experimentation

Initial exploratory experimentation into MMC consisted of manually mixing 20 Wt.% SiC with Ti6Al4V powder feedstock with a view to building several small test samples as shown in Figure 40.

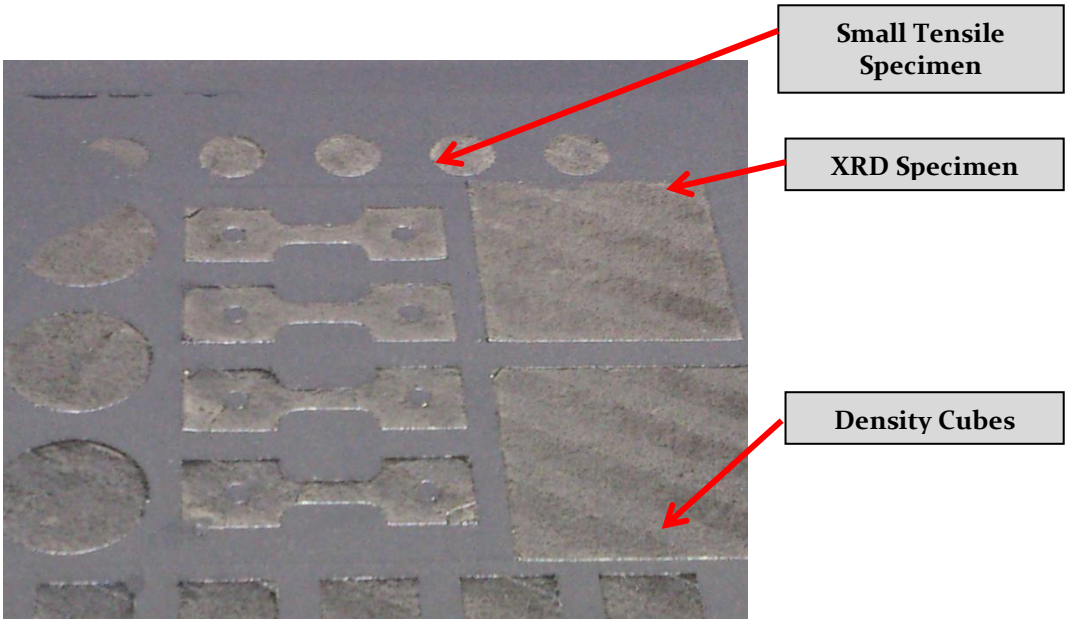

Figure 40 - Initial Test Samples. Aborted after approx. 1.5mm

The intention was to establish a baseline for further experimentation and to ascertain if the materials were compatible with the PBF process.

The test samples

Table 8) included:

Table 8 - Initial Test Samples

Quantity	Description	Size (mm)	Test
2	XDif specimen	35 x 35 x 2	X-Ray Diffraction
5	Small density specimen	Ø 10 x 5	Porosity
5	Density Cubes	12 x 12 x 5	Porosity
3	Large density specimen	Ø 20 x 5	Porosity
4	Small tensile specimen	8 x 5 x 5	Tensile

3.1.1 Feedstock Preparation

Feedstock was prepared by mixing 20 Wt.% SiC powder with a mean particle size of 10 µm (Dynamic Ceramic), into Ti6Al4V EOS standard powder with a mean particle size 39 µm (±3 µm), (EOS GmbH 2016) for a short period of time until the mixture appeared to be completely mixed.

3.1.2 Data Preparation

Slice files were prepared using PSW version 3.4 (EOS Gmbh) and files were arranged on a 120 mm x 120 mm platform, maximising the full space available (Figure 41).

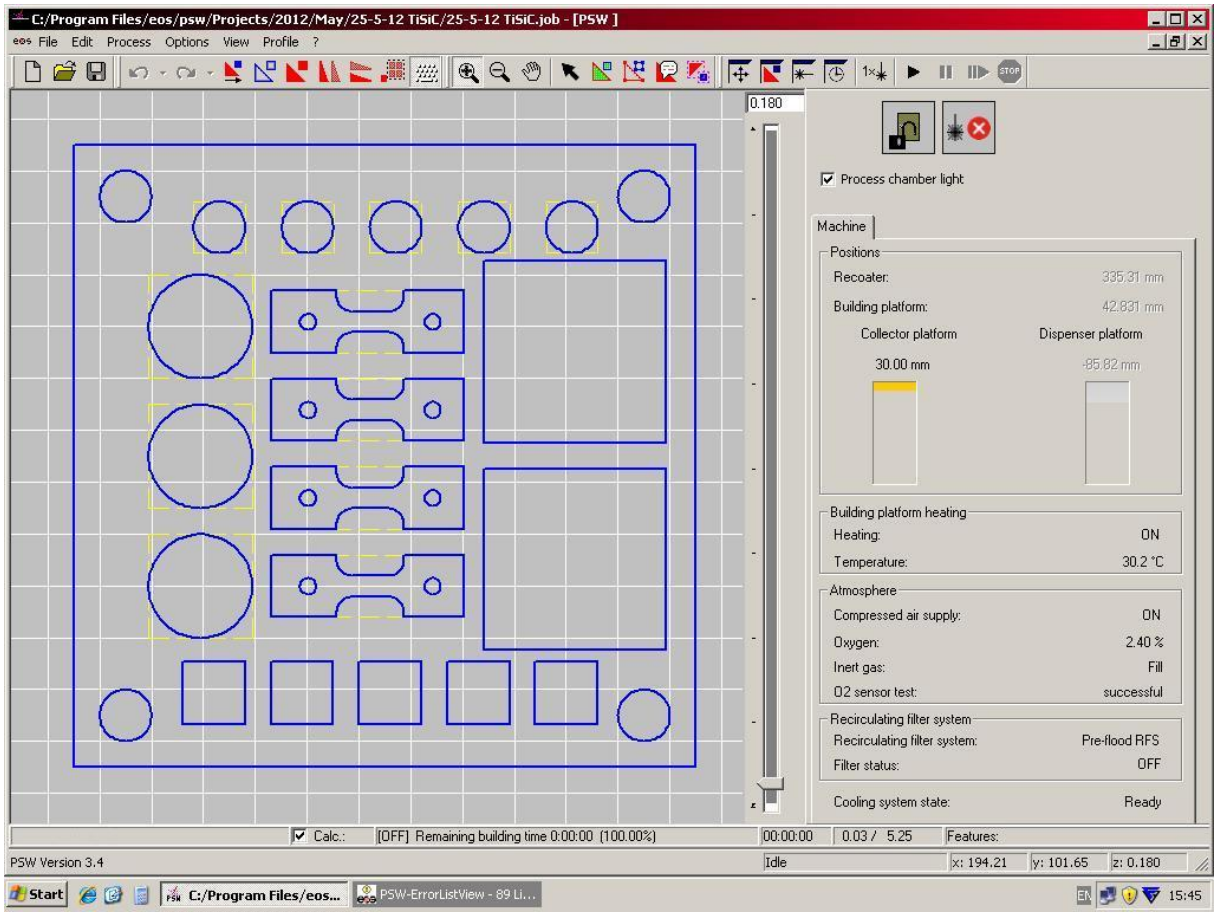

Figure 41 - PSW version 3.4 (EOS GmbH)

The material was exposed with standard EOS parameters for Ti6Al4V in 30 µm layers using an EOS M270 Machine with the following parameters (Table 9).

Table 9 - EOS M270, Ti6Al4V Standard Parameters (EOS GmbH)

Material	System	Layer Thickness	Laser Power	Scan Speed	Hatch Distance	Oxygen concentration
Ti6Al4V	M270	30 µm	175 W	1250 mm/s	0.100 mm	0.05 % to 0.13 %

A Ti6Al4V build platform was used and the build setup followed standard build preparation procedures (Figure 42) for Ti6Al4V material.

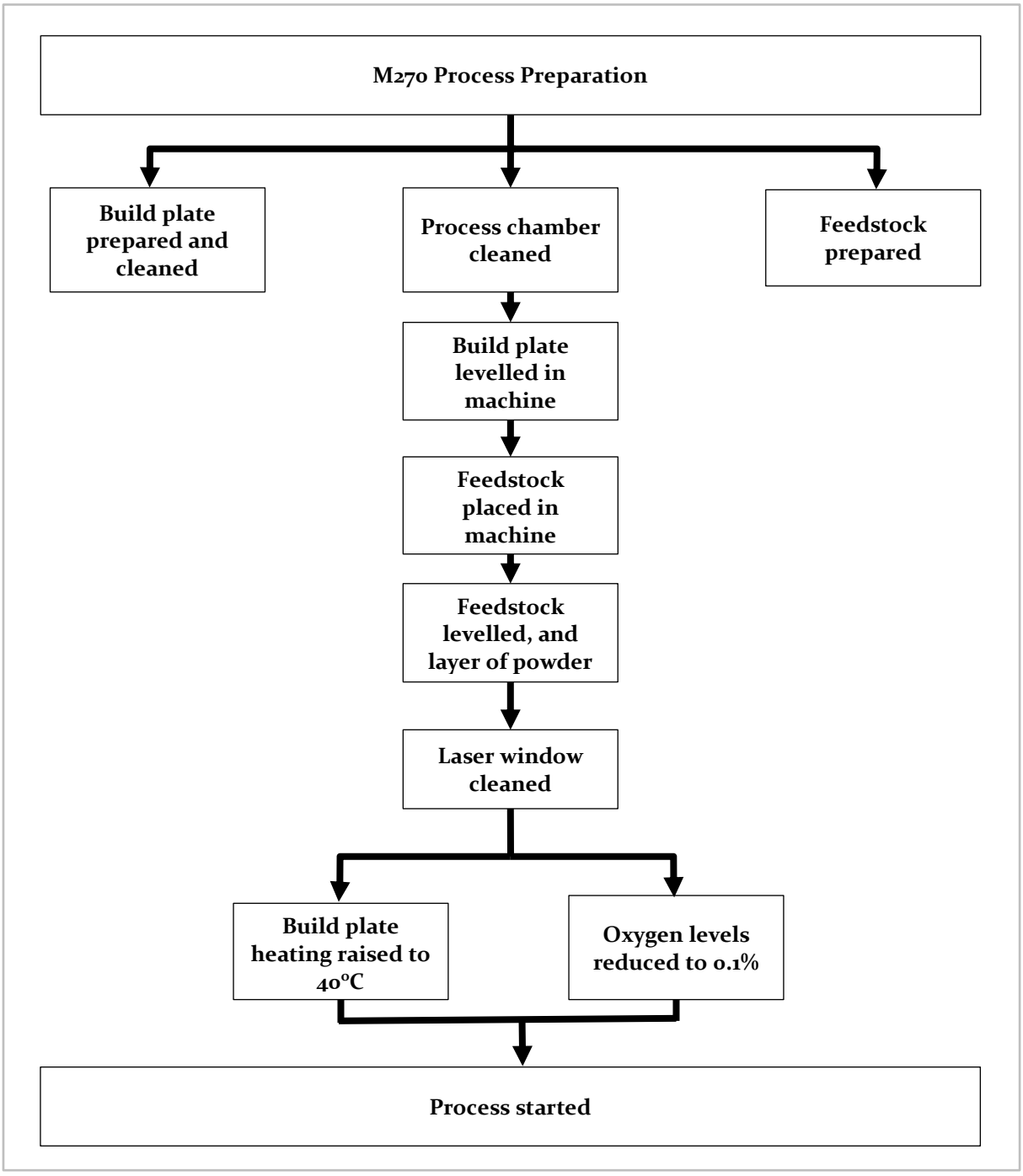

Figure 42 - EOS M270 Process Setup Flow

3.2 Observations from Initial Experimentation

By observing the initial layers of the build, it became obvious that the build would not complete. After approximately 0.3 mm (10 layers) of build height, the test samples began

to spontaneously fracture and fail structurally. In the time it took to recoat each layer the upper surfaces fractured and detached from the body of the sample leaving large voids. The experiment was terminated in view of further investigation into the cause of the phenomena. Investigation indicated that failure was due to internal stress build-up or shrinkage (Kumar Ghosh and Saha, 2011).

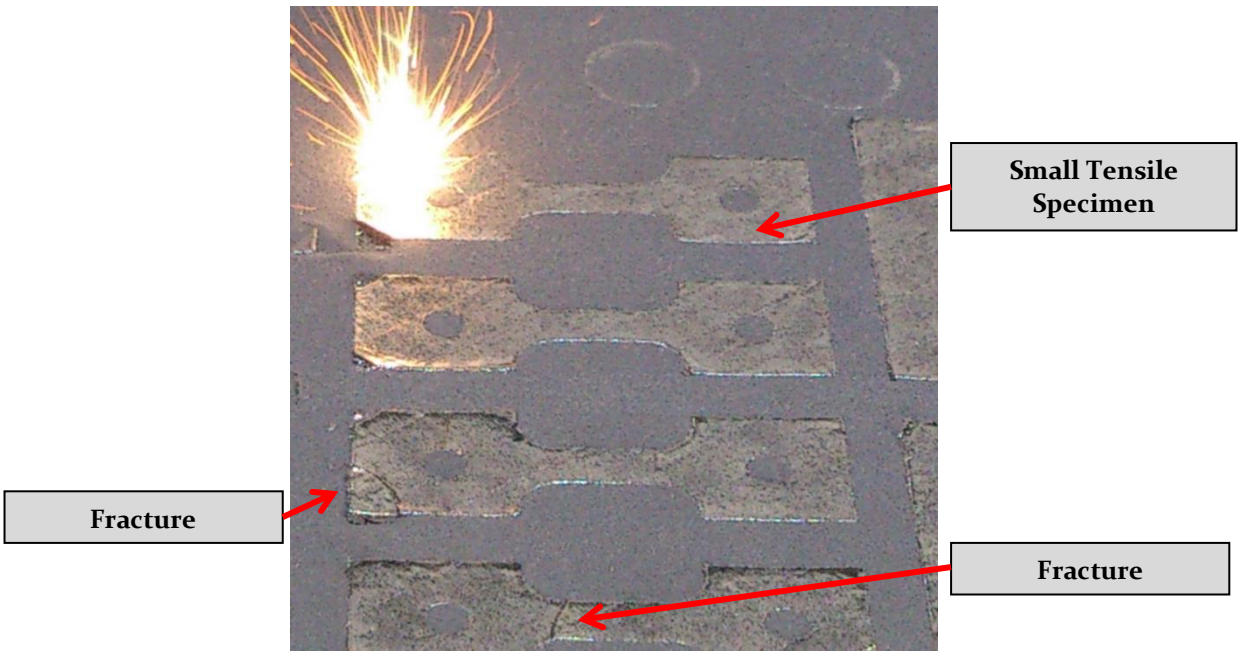

Figure 43 - In-Process Fractures

Several fractures were observed across the tensile test area of the specimen sample (Figure 43). Fractures were not exclusive to geometrically weaker areas of the test samples, as they were observed across the corners of samples and between the sample and build platform. It was also noted that these fractures were not delaminations but effected multiple layers simultaneously, indicating the materials ability to build layer by layer was not in question.

It was hypothesised that for a part to fracture so quickly the material must be undergoing rapid contraction on solidification. It is also possible that the ductility of the matrix material (Ti6Al4V) was insufficient to accommodate the changes in expansion and contraction during laser processing.

The samples produced were analysed using a scanning electron microscope (Figure 44). It was found that the fracture surfaces were populated with many round particles, 3 to 8 µm in size,

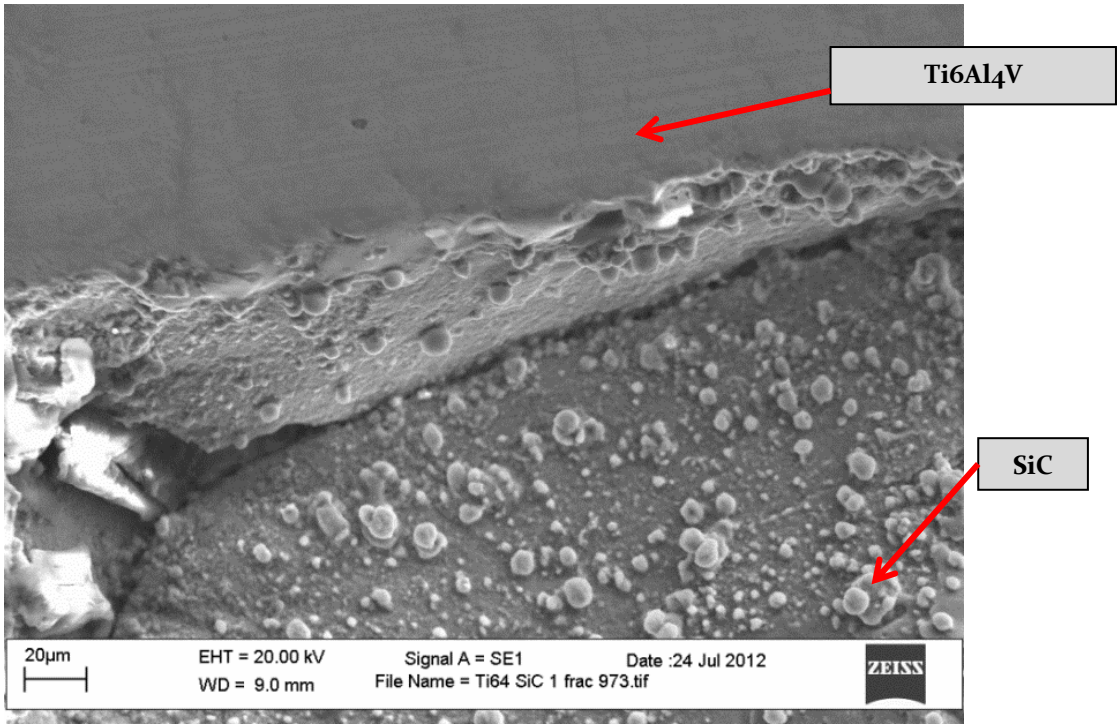

Figure 44 - MMC Fracture Surface.

On analysis of the particulates around the fracture surface, analysis by Energy-Dispersive X-ray Spectroscopy (EDS) found them to be Ti6Al4V, however, they could theoretically be particles of SiC coated in Ti6Al4V. If this were the case, they would be about the correct size. It was also noted that in comparison to a typical Ti6Al4V fracture surface (Figure 45), the fracture surface differs significantly (Yin et al., 2015).

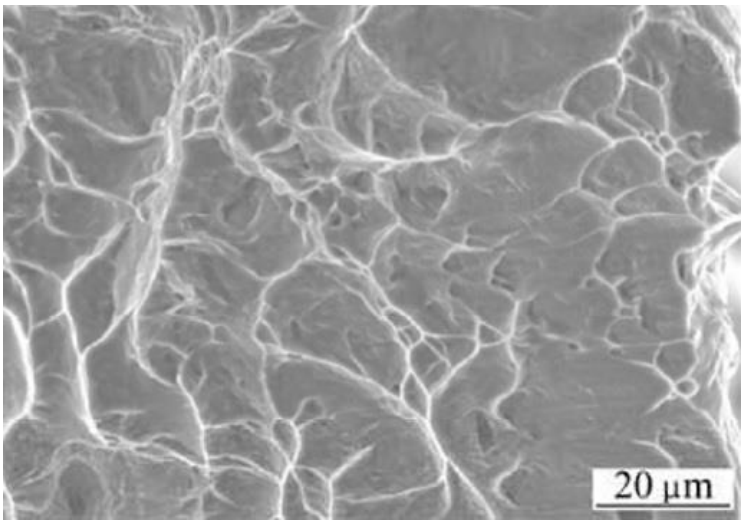

Figure 45 - Ti Fracture Surface (Yin et al., 2015)

This would suggest a concentration of SiC rather than a homogeneous distribution throughout the sample. Authors such as Patterson 2017, Yadroitsev 2016, Elambasseril 2012 and Vrancken 2013 have shown that Ti6Al4V is highly susceptible to stress

concentration during the build process and therefore it is feasible that clustered particles of SiC would act as stress raisers within the matrix by forming an area of high-saturation of SiC at this point in the matrix material (Ti6Al4V) offering a lack of continuity around the reinforcement. Figure 46 Shows the fracture surface of a fragment expelled from the test build, particulates are visible on the fracture surface. It can also be observed that the crack origin is in the centre of the sample, with a radial propagation of cracks, this would suggest that the highest concentration of stress was found at the centre of the specimen.

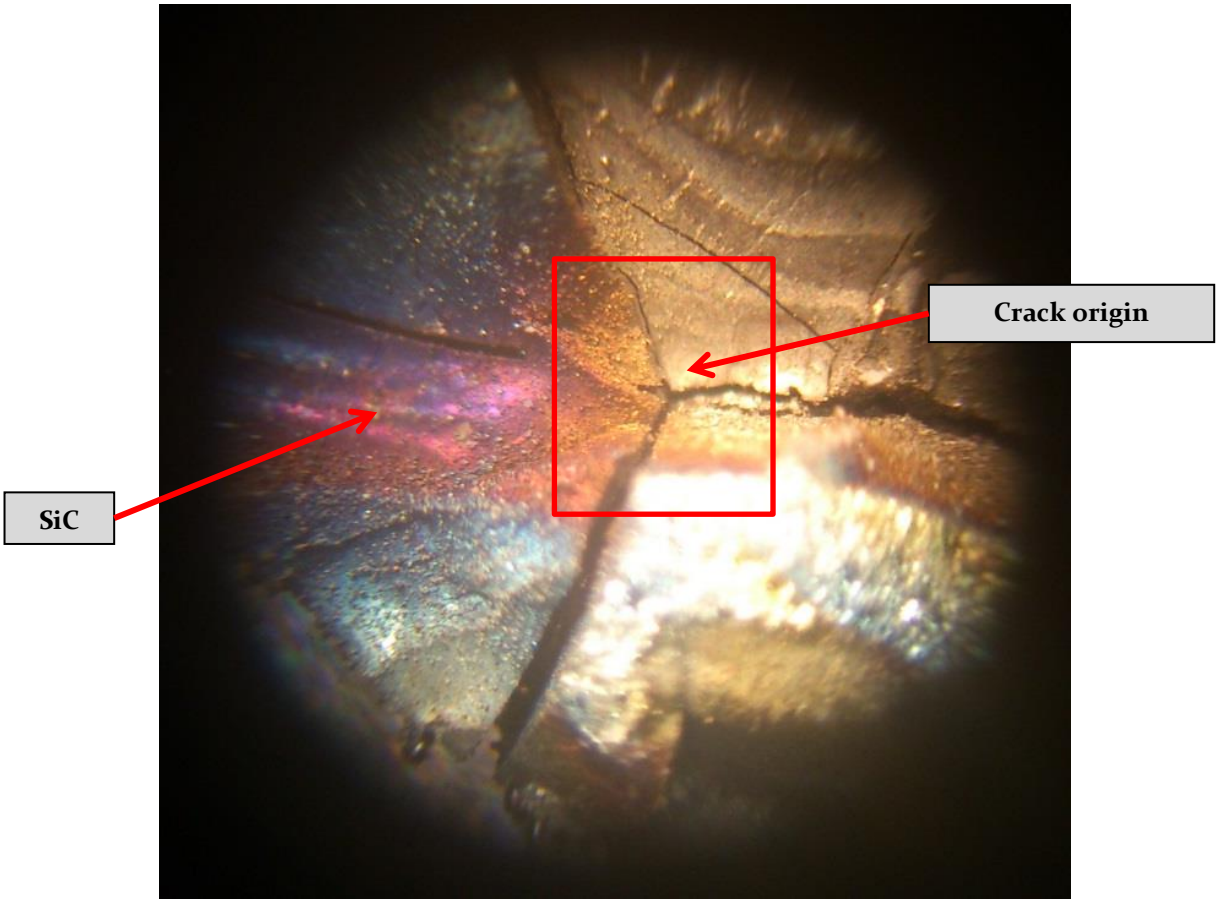

Figure 46 - MMC Fracture Surface (50 x magnification)

The initial test has highlighted complex material and process interactions taking place and has highlighted the need for further investigation into the mechanics of this interaction. Furthermore, the production of feedstock is also of concern due to the evidential lack of homogeneity.

Given the initial investigations, further work focused on:

- Feedstock production and characterisation,
- Powder bed fusion MMC material characterisation.

Chapter Four

4.0 Research Methodology

4.1 Introduction

The literature review indicated that this research would benefit significantly from experimentation and analysis to determine the most appropriate and effective characteristics of feedstock and process parameters that would offer quality processed components / material. Commercially available Ti6Al4V material sourced from EOS GmbH was used as a benchmark with which the MMC material could be compared with regards to presenting a viable effective and reliable method of validating results post the addition of SiC. It is critical that the specifications of the feedstock produced through the MA route do not fall outside that which is processable by the PBF equipment (EOS M290). The resultant feedstock was therefore benchmarked against commercially available Ti6Al4V supplied by EOS GmbH, and SiC sourced from Dynamic Ceramic, UK for powder characteristics. The processability of the subsequently manufactured MMC material was processed using the EOS M290 PBF machine over a range of energy densities to determine a processing window for the resultant MMC material.

Figure 47 shows the methodological workflow comprising eight research packages across three phases:

- Phase one considers the baseline assessment of both raw materials (Phase 1a) and Ti6Al4V scan parameters applied to a range of energy densities (Phase 1b).
- Phase two investigated the MMC feedstock manufacture by MA (Phase 2a) and the benchmarking of the feedstock against Ti6Al4V material (Phase 2b).
- Phase three determined the scan parameters and hence the processing window for the MMC material Ti6Al4V (Phase 3a-d).

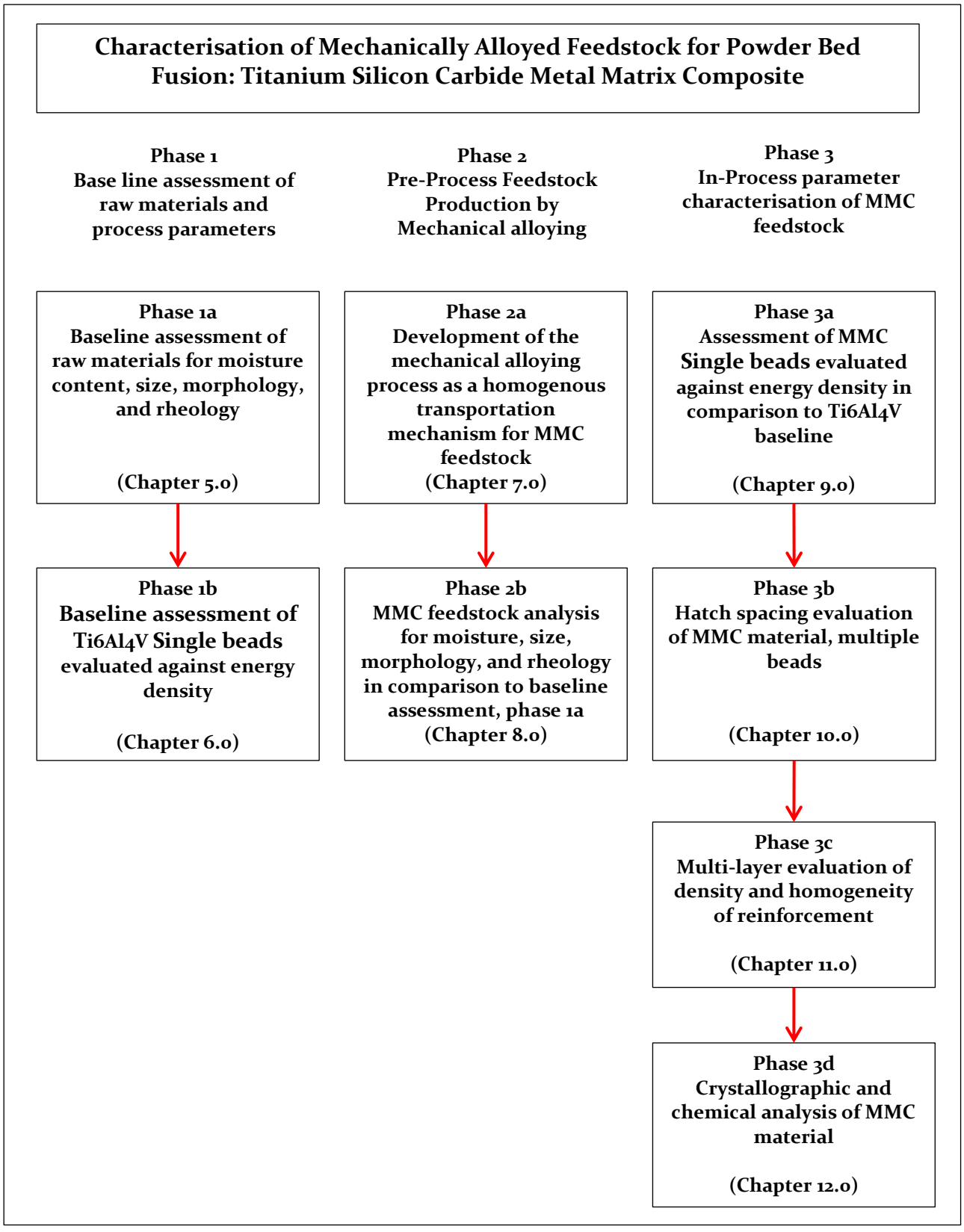

Figure 47 - Methodology Workflow.

The following chapters describe the methodology for each research package along with results, discussion and conclusions.

Chapter Five

5.0 Phase 1a Baseline assessment of raw materials for moisture content, size, morphology, and rheology

5.1 Phase 1a: Baseline Assessment of Raw Materials Methodology

5.1.1 Overview of The Experimental Design

Powder analysis techniques were used to characterise the experimental feedstock materials to verify that they were suitable for the PBF process, in so doing they were comparable to commercially available Ti6Al4V feedstock. The objective of the MA process was to embed the reinforcement on to the surface of the matrix material without significantly altering the morphology of the matrix material and to provide a transportation mechanism for the powder spreading activity for the PBF process. The analysis provided data to benchmark the experimental results against to determine that the resultant feedstock remained comparable to the source material. The component materials used were analysed individually as was the MMC feedstock at stages during and after MA. Data was gathered for the:

1. Moisture content,
2. Particle size, size distribution, and morphology,
3. Rheological characteristics.

5.1.2 Sample Sizes

In all cases, a representative sample of the raw materials was collected and analysed in accordance with the test procedures as summarised in (Table 10).

Table 10 - Powder Analysis Sample Sizes

Experiment	Equipment	Sample size (g)
Moisture content	Adam PMB53 (UK)	< 10
Particle size, size distribution, and morphology	Retsch Camsizer X2 (Retsch Gmbh)	10 to 30
Rheological characteristics	LPW Powder Flow (Carpenter additive USA)	50

Samples were tested at a temperature of 20 ^{o}C in an environment conducive with the test being carried out and all appropriate safety precautions for the handling of powders were followed. Three samples were taken for each test to provide an arithmetic mean ($\bar{x}$) to avoid the effect of anomalous results.

5.1.3 Restrictions and limitations

5.1.3.1 Moisture Content, Restrictions and Limitations

Measurement of moisture was conducted using the 'loss of mass' method (Cordova, et al., 2017) wherein the measurement of all volatiles present in the sample are measured as total loss of mass, not only water present. The method chosen was conducted under laboratory conditions and a target value of < 1 % was adopted for the chosen variable (Vluttert, 2016). Results of loss of mass were presented in the form of a percentage of the original mass.

5.1.3.2 Particle Size and Morphological, Restrictions and Limitations

A Retsch Camsizer X2 dynamic image analysis system was used to measure particle size, size distribution, and morphology. The manufacturers specified accuracy of the equipment specified an ability to measure particulates from 0.8 µm to 8 mm. The size range for the Ti6Al4V material was specified by the manufacturer (EOS GmbH) as 10 µm to 63 µm which was within the apparatus operating limits. However, the SiC material was specified as 0.6 µm to 1.0 µm which was below the operating range of the apparatus. Additional equipment in this case in the form of a Scanning Electron Microscope (SEM) (Zeiss evo 50 xvp, GmbH) was used for the measurement of particulates of 0.8 µm and smaller. Whilst this gave accurate sizes of particles it was not possible to generate a particle size distribution graph. Calibration of the particle size analysis equipment was conducted using a reticule provided by the equipment manufacturer and following the calibration routine. Calibration of the SEM was conducted annually by a qualified service engineer and before each session. The EDS system was calibrated before use using a cobalt (Co) sample (Figure 141).

5.1.3.3 Rheological Restrictions and Limitations

The methods followed were traceable to international standards where applicable (ASTM B213, ISO 4490, ASTM B964, ASTM B212 and ISO 3923-1). Angle of repose was determined using a protractor to directly measure the angle. As the same method was applied to all analysis this was not considered an issue.

The research was restricted in terms of analysis of entrapped gasses and the analysis of entrapped O_2 both on the surface and embedded within the particulate material. Every

effort was made during the handling, storage, and processing of the materials to ensure that they were not exposed excessively to O_2 ensuring that the O_2 levels would remain the same throughout. Results in terms of the role that O_2 could play in the reaction process did not form part of this research.

5.1.4 Equipment

5.1.4.1 Moisture Content

Moisture content measurement was carried out using an Adams PMB53 Moisture Analyser. Representative samples of the matrix material, reinforcement material, and mechanically alloyed feedstock were analysed to determine the levels of moisture that was present within the samples prior to analysis for particle size, morphology, or rheology. Elevated levels of moisture within the feedstock can affect its morphology, evidenced by high levels of agglomeration within the powder; when analysed, these agglomerates can give the impression that the powder is unsatisfactory. Rheologically, elevated levels of moisture within the feedstock affect its flowability and therefore directly affect its packing density and ability to coat the entire build area homogeneously. In terms of part quality, moisture in the feedstock can lead to gas entrapment in the part and the chemical dissociation of water molecule can lead to extra O_2 and H in the process (LPW Technologies 2017).

The method employed was a volumetric measurement using the loss of mass method to measure the evaporation of water and other volatiles.

Moisture levels for Ti6Al4V were typically measured at < 1.0 % for powder stored in accordance with manufacturers guidelines and used within the EOS M290 machines. This was thus taken as typical. Where levels were > 1.0 % the powder was heated at 150^{o}C for twenty minutes (Cordova, et al., 2017) and retested before conducting further analysis. Within the laboratory conditions it was accepted that environmental moisture pickup was largely unavoidable but could be minimised.

5.1.4.2 Particle Size and Morphological Characteristics

Particle size, size distribution, and morphological characterisation was carried out using a Retsch Camsizer X2, in a dry environment suspended in an air stream. Utilising two cameras, a basic camera for large particles and a zoom camera for the smaller particles, the Retsch Camsizer X2 employs dynamic image processing (ISO 13322-2) to accurately analyse the particulate capturing on average, 300 images per second.

The Retsch Camsizer X2 was used specifically to analyse the changes taking place in terms of size and morphological aspects during the MA stage of this research. It has been established that changes regarding the particulates shape and size distribution are key

factors relating to an increase of porosity within subsequent manufactured parts (Spierings, et al., 2011, and Baitimerov, et al., 2018). The MA process was conducted until the feedstock lost these properties.

5.1.4.3 Rheological Characteristics

Feedstock manufacture for PBF demands a range of tests to be adopted for the analysis of powders. Over recent years these have included many tests adopted from other industries such as the pharmaceutical industry, however, for the AM industry it is becoming increasing clear that a select few rheological tests are required. These tests apply to both the manufacturer and the end user. These include:

- Hall flow to ASTM B213 and ISO 4490 standards
- Carney flow to ASTM B964 standard
- Apparent density to ASTM B212 and ISO 3923-1 standards
- Tap density
- Angle of Repose to LPW standardized procedure.

This series of tests has been established to provide a set of standardised techniques for the characterisation of powders. The ASTM international standard was developed specifically for metal powders with the current versions being published in 1999 (B 212) and 2003 (B 213).

Table 11 summarises the rheological experimentation with respect to this research:

Table 11 - Rheological Experimentation with Respect to This Research

Test	Description	Key indicator	Value	Research relevance
Hall flow	Time taken for a mass of powder to fall through an aperture of 2.54 mm	Satellites, loss of sphericity and agglomerations causing voids within the powder bed leading to porosity in the part.	Grams per second (g/s)	Relevant in comparison between Ti6Al4V elemental powder and MA feedstock, an increase in time indicates an increase in surface roughness resulting in less feedstock per recoat.
Carney flow	Time taken for a mass of powder to fall through an aperture of 5.08 mm			
Apparent density	Volumetric measurement of loose powder in a standard volume	Volume of powder deposited per layer, as this decreases less material is available within the melt pool leading to porosity.	Grams per cubic centimetre (g/cm3)	Relevant comparison between Ti6Al4V elemental powder and MA feedstock, a decrease in apparent density indicates an increase in average particle size leading to possible part porosity.
Tap density	Volumetric measurement of compacted powder in a standard volume	Volume of powder in dispenser, powder is agitated to ensure that powder is compact to give best coverage when recoating.	Grams per cubic centimetre (g/cm3)	Assists in maximising packing density
Angle of repose	Angle at which a sloping surface of loose powder is stable	Indicator of powders ability to lock together, a low angle is preferred indicating powder will spread evenly on recoat.	Degrees	Relevant comparison between elemental powders and MA feedstock, an increase in angle indicates degradation of powder surface finish, uneven spreading may occur.

Apparent density and angle of repose were used within this research as indicators of powder acceptability using commercially available Ti6Al4V as a benchmark. Hall or Carney flow was not used due to inability to obtain satisfactory results and tap density was not used as this is only an indication of the volume of compacted feedstock.

Apparent Density

Within this research, the apparent density of mechanically alloyed feedstock was measured and compared to the same tests conducted for both the matrix material (Ti4Al6V) and the reinforcement material (SiC) to determine its suitability within the process in terms of the deliverable volume of material per layer.

The apparent density test is primarily concerned with a powders ability to occupy space, for a normal distribution within a powder sample small particle will mix freely with larger ones creating less voids between the particles and allowing more powder to occupy the same space and specifically the volume for the recoated layer (Benson, 2015). The apparent density experiment relates directly to the powder deposited during recoat. This material is mechanically positioned by the recoater with minimal force and particles can freely fall to enhance the layer density, however, as smaller fines are consumed more easily by the process the particulate size range must be monitored as more gaps form between larger particle on recoat, resulting in less material per layer (Berretta, 2013). This is detrimental to the formation of weld beads within the process due to the starvation of the melt-pool; this intern can lead to voids and porosity within the part (Yadroitsev, 2010). When the current layer is lased, the powder transitions from a loose mass to a solid and is added to the substrate, this process involves a loss of height as the recoated layer sinks marginally on solidification. In effect the powder is transitioning from apparent density to physical density, if the apparent density of the powder is 50 % that of the density of the solid material the resultant added material will be half that of the layer height, this will be made up on a subsequent recoat by a thicker layer of powder. This is accepted as necessary for the process however, by maintaining the maximum possible amount of material being available to the melt-pool, maintaining a high apparent density the risk of creating thicker layers and inconsistencies within the part are minimised (Baitimerov, et al., 2018).

Angle of Repose

Within this research, the angle of repose was measured for the mechanically alloyed feedstock and compared to both the matrix material (Ti4Al6V) and the reinforcement material (SiC) to determine its suitability within the process.

Angle of Repose was measured using the Carney flow funnel utilizing a 5.08 mm standard orifice to maintain a repeatable powder flow. A platform of known diameter (34.0 mm) is placed 25 mm beneath the funnel and powder can flow from the funnel onto the platform to form a heap. The height of the resultant heap was measured, and the angle is calculated in accordance with the manufacturer's instructions (LPW Technologies 2018).

The angle of repose is concerned primarily with the powders ability to lock together and retain position, smooth spherical particulates that flow easily, typically demonstrate a low angle of repose (Sutton, et al., 2016). However, as the powder degrades through multiple uses, satellites form on particulates and agglomeration takes place inhibiting its ability to flow as freely, this is evidenced by an increased angle of repose. A baseline angle of repose using virgin Ti6Al4V powder was established for comparison to the optimum batch of MA feedstock to determine rheological changes that could pose challenges to the PBF process.

5.1.5 Procedures and variables

5.1.5.1 Moisture Content Analysis Procedure and Variables

Lightweight aluminium weighing trays were cleaned with a solvent (isopropanol), dried and placed into the Adams PMB53 Moisture analyser and the analyser was set to zero.

Samples of <10gms of powder were distributed evenly across the weighing tray and enclosed within the Adams PMB53 Moisture Analyser. Samples were heated to 120°C for 20 minutes and the resultant percentage of moisture documented.

The sample tested was retained and the process repeated three times taking a fresh weighing tray and sample each time. This ensured that the process remained uncontaminated and that a representative sample was taken from the batch. The target moisture level was set at < 1 %, samples with an average moisture level of > 1 % were heated in an oven at 150 °C for twenty minutes then allowed to cool within the same environment, the moisture content analysis procedure was then repeated.

Table 12 shows the variables used across all moisture analysis experiments.

Table 12 - Moisture Analysis Process Variables (Adam, 2018)

Variable	Description	Parameter	Operator	Value
Test duration	Length of time the test was conducted	Minutes	min	20
Temperature range	Minimum and maximum temperatures	Degrees centigrade	°C	20 - 120

5.1.5.2 Particle Size and Morphological Analysis Procedure and Variable

Before conducting analysis, the apparatus was cleaned with a solvent (isopropanol) to remove contamination remaining from previous test samples, in accordance with the manufacturer's instructions.

A calibrated reticule was used to calibrate the instruments optics, for both the basic and the zoom cameras in accordance with the manufacturer's instructions (Retsch 2018).

A representative sample of raw material was taken from each batch and analysed.

Table 13 shows the variables measured across all particle size and morphological experiments.

Table 13 - Variables for Particle Size and Morphological Analysis (Retsch, 2018)

Variable	Description	Parameter	Operator	Value
Particle size	Refers to the particle width. The shortest distance across the particles image, that which would fall through a sieve.	$x_{c\ min}$	≥ (used to exclude unwanted data)	0.010 µm (used to exclude unwanted data)
Particle length	The longest measured element of a particle	X_{Fe} Max	-	-
Aspect ratio	The ratio between width ($x_{c\ min}$) and length (X_{Fe} Max) an aspect ratio of 1.000 AR indicates a round particle	b/l	≤ (used to exclude unwanted data)	0.850 (to calculate number of irregular shaped particles)
Sphericity	The roundness of a particle	SPHT		
Transparency	Transparency of a particle high values indicate a blurred image	Trans	≤ (used to exclude unwanted data)	0.100 (used to exclude unwanted data)
Area	The width of a circumferential boundary around a particles image, irregularities make the boundary larger.	X_{area}	µm	-

5.1.5.3 Rheological Procedure and Variables for Apparent Density and Angle of Repose

Experiments were conducted on Ti6Al4V matrix material to establish baseline characteristics and SiC reinforcement material in comparison prior to MA (Phase 1). On

completion of mechanically alloying experiments, the resultant feedstock powder was analysed and compared against the results for Ti6Al4V. Before conducting analysis, the apparatus was cleaned with a solvent (isopropanol) to remove contamination remaining from previous test samples analysed by the equipment in accordance with the manufacturer's guidelines (LPW Technologies 2017). The apparatus was calibrated against a reference material supplied by the manufacturer and in accordance with the manufacturer's guidelines (LPW Technologies 2017). Each test was conducted three times and an average taken to reduce errors found during the procedure. All tests were conducted in a temperature-controlled environment at 20°C. Table 14 shows variables used across all apparent density and angle of repose experiments.

Table 14 - Variable for Rheological Analysis (LPW Technologies 2017)

Variable	Description	Parameter	Operator	Value
Material density	Density of solid material for a fixed volume	g/cm³	P	-
Apparent density	Density of loose powder for a fixed volume, Used to calculate volume of material recoated	g/cm³	=	-
Angle of repose	Steepest angle of a sloping surface of loose material	(x)°	=	0 - 90

5.1.6 Statistical Treatment

5.1.6.1 Moisture Content

Three samples were analysed from the process and a mean ($\bar{x}$) value was calculated to determine the moisture content within the batch, along with a calculation of the standard deviation (σ) to determine the level of error in the results.

5.1.6.2 Particle Size and Morphological Analysis

Statistical treatments as part of the Retsch analytical software (Retsch 2017) were used in compiling data for analysis. Table 15 show the statistical operators used.

Table 15 - Sampling methods and Statistical treatments for Particle Size and Morphological Analysis (Retsch, 2018)

Variable	Description	Parameter	Operator	Value
Volume based distribution	Total volume of powder analysed against the measured particle variable	Q3	%	0 - 100
D10 percentiles	Particle size in the first 10 % of the total sample, 10 % of the sample is less than this size	Q3 10 %	µm	-
D50 percentiles	Particle size at 50 % of the total sample, 50 % of the sample is less than this size and 50 % is above	Q3 50 %	µm	-
D90 percentiles	Maximum particle size in 90 % of the total sample, 10 % of the sample is larger than this size	Q3 90 %	µm	-
Sample mean size	Mean particle size in the total volume of the sample, weighted; $x1, r = \Sigma\, x\, qr(x)\Delta x$	Mv3($\bar{x}$)	µm	-
Sample standard deviation	Standard deviation σ(x) from the mean value Mv3($\bar{x}$)	Sigma 3 ($\bar{x}$)	µm	-
Mean aspect ratio	The mean aspect ratio is an indication of a sample's roundness, above 0.850 $_{AR}$ would be classed as round	b/l3	-	0 - 1
volume fraction of round particles	The inverse volume of the aspect ratio at 0.850 $_{AR}$ is the percentage of particles that are rounded	1-Q3 (b/l = 0.850)	%	0 - 1

5.2 Phase 1a: Baseline Assessment of Raw Materials Results and Discussion

Within the research experimental results were compared to the standard characteristics of feedstock powders used within the industry. Analysis was conducted on the raw materials to establish a baseline for the following characteristics:

- Moisture content,
- Particle size and size distribution,
- Particle morphology,
- Rheological characteristics.

5.2.1 Phase 1a Baseline Assessment of Moisture Content

The moisture content of Ti6Al4V and SiC were measured using the loss of mass method (Cordova, et al., 2017). Three separate samples were analysed from different areas of the batch of material to establish an arithmetic mean. The results are shown in Table 16.

Table 16 - Moisture Content Results (Initial Analysis)

	Moisture Content (%)	
	Ti6Al4V	SiC
Test 1	0.59	1.88
Test 2	0.50	1.55
Test 3	0.67	1.92
Mean ($\bar{x}$)	0.59	1.78
Sigma (σ)	0.09	0.20

For Ti6Al4V the moisture levels were below the 1.0 % maximum limit (chapter 5.1.3.1) and were therefore considered acceptable. For the samples of SiC, higher than expected levels of moisture were detected, this was most likely from either the storage or handling of the powder and it was suspected that this would be attributed to surface moisture as SiC does not readily react to moisture due to its chemical inertness. Due to the particulate's submicron size and therefore increased surface area, there becomes a higher probability of surface moisture being introduced into the powder. The powder was spread on to a metal tray and heated in an oven at 150°C for twenty minutes then allowed to cool within the same environment. Once the powder was again at room temperature it was retested with the following results (Table 17).

Table 17 - Moisture Content Results After Moisture Removal Process

	Moisture Content (%)	
	SiC (initial analysis)	SiC (secondary analysis)
Test 1	1.88	0.79
Test 2	1.55	0.97
Test 3	1.92	1.13
Mean ($\bar{x}$)	1.78	0.96
Sigma (σ)	0.20	0.17

It was evident from the results in Table 17 that the moisture could be driven off using a heating process but also that over a short space of time, the SiC powder would rapidly pick up moisture again. The duration of each moisture test was 20 minutes; therefore, the powder had been away from the oven for approximately 60 minutes and the moisture levels were returning to previous levels. It was concluded therefore that the SiC powder and subsequent alloyed feedstock should be stored in a dry environment at a temperature of around 80°C prior to use and furthermore, to eliminate the risk of moisture being introduced into the powder should be processed within 60 minutes.

5.2.2 Phase 1a Baseline Assessment of Rheological Characteristics

Rheological analysis was conducted on the Ti6Al4V and SiC powders prior to MA to determine baseline values for apparent density and angle of repose. The results are shown in Table 18.

Table 18 - Rheological Characteristics for Ti6Al4V And Sic Powders Prior To MA

Rheological measurement	Ti6Al4V	SiC
Material density	4.43 g/cm^3	3.21 g/cm^3
Apparent density	2.24 g/cm^3	0.41 g/cm^3
Sigma (σ)	0.005 g/cm^3	0.0 g/cm^3
Percentage of physical density	50.6 %	12.8 %
Angle of repose	33°	48°
Sigma (σ)	0°	0°

With regard to packing density, it could be seen that the apparent density of the Ti6Al4V powder was 50.6 % in comparison to its material density, for the SiC powder this was 12.8 % demonstrating a poor packing density in comparison to Ti6Al4V. These results were measured three times and a mean value taken. For Ti6Al4v, the result of 50.6 %

was accepted as typical for the size distribution curve observed during size and size distribution analysis. The results for SiC however were considerably lower than expected. Analysis followed the same methodology as all powders and experiments were conducted three times with a mean calculated. It was therefore concluded that as with the particle size analysis, agglomerated powder prevented the material to settle withing the measuring vessel sufficiently to occupy voids. This is further supported by the values obtained for angle of repose, a steeper angle indicating that particles are more likely to lock together rather than slide across each other to move into available space. Results for the angle of repose established a baseline for Ti6Al4V of 33 degrees, for SiC this increased to 48 degrees, this was expected due to the powders angularity and lack of roundness, hence the powders ability to lock together in formation rather than freely role. Due to the Ti6Al4V powder maintained a mean angle of 33 degrees, this was taken as the baseline value to benchmark against for the MA experiments in phase 2. In combination with the SiC powder, the angle of repose was expected to increase due to an expected increase in surface roughness.

5.2.3 Phase 1a Baseline Assessment of Particle Size, Size Distribution

Using a Retsch Camsizer X2 particle size analyser a representative sample of Ti6Al4V and SiC powders were analysed to establish a baseline assessment with respect to the following characteristics:

$X_{c\ min}$ Measures the shortest width (µm) across a particles image and is taken as being representative of particle size and used as a direct correlation to sieving sizes.

X_{area} Measures the width (µm) of a circumferential boundary around a particle to include any irregularities such as satellites or agglomerations, for a round particle this would be equal to $X_{c\ min}$.

b/l Measures the aspect ratio (AR) between the shortest distance on the particle ($X_{c\ min}$) and the longest ($X_{fe\ max}$) and is a good indication of elongated particle.

5.2.3.1 Ti6Al4V Particle Size and Size Distribution Baseline Assessment

Table 19 shows results for $X_{c\ min}$ (particle size) frequency distribution curve for Ti6Al4V powder (Figure 48). The analysis showed a multi-modal size distribution from 0 µm to 75 µm with peaks at 3.5 µm, 37 µm and 44 µm.

Table 19 - Statistical Results for Ti6Al4V Particle Size and Distribution ($X_{c\ Min}$) Baseline Results

Statistical measurement	Baseline result ($X_{c\ min}$)
Q3 10 %	28.8 µm
Q3 50 %	39.9 µm
Q3 90 %	49.9 µm
Mv3($\bar{x}$)	39.7 µm
Sigma 3 ($\bar{x}$)	9.7 µm
Mean b/l3	0.851
1-Q3 (b/l = 0.850)	65 %

Table 19 shows the salient characteristics of the particle size analysis. It can be seen from the data that 50 % of the sample by volume (Q3 50 %), has a particle size of 39.9 µm and the mean particle size of the over-all sample (Mv3($\bar{x}$)) is 39.7 µm. The closeness of these two values, (within 0.2 µm), suggests a high degree of confidence in the results. The mean aspect ratio result (Mean b/l3) indicates that not all particles are spherical. Looking at the inverse statistical volume for the sample (1-Q3 (b/l = 0.850)) it can be seen that 65 % of the sample would be classed as rounded, this was further evaluated using particle image analysis.

Values for Q3 10 %, Q3 50 % and Q3 90 % are key indicators for particle size within the sample, representing sizes at 10 %, 50 % and 90 % of the total sample often referred to as D10, D50 and D90. For a normal distribution curve Q3 10 % (D10) and Q3 90 % (D90) represent the tails at either end, Q3 50 % (D50) represents the midpoint in the sample, 50 % of the sample would be less than this size. These values are universally accepted as indicators of size distribution across batches of powders.

Further analysis was conducted with the same sample, evaluating the width (µm) of the particles bounding circumference, (x_{area}) (Figure 49). Where particles have a good aspect ratio fewer satellites and agglomerations are indicated and the statistical analysis would be comparable to the values for particle size $X_{c\ min}$.

Analysis showed a multi-modal distribution with a range between 1 µm to 85 µm with peaks at 3.5 µm, 37 µm and 47 µm.

Table 20 - Statistical Results for Ti6Al4V Particle Size and Distribution, $X_{c\ Min}$ Versus X_{area} Baseline Results

Statistical measurement	Baseline result ($X_{c\ min}$)	Baseline result (x_{area})
Q3 10 %	28.8 µm	30.2 µm
Q3 50 %	39.9 µm	43.1 µm
Q3 90 %	49.9 µm	55.8 µm
Mv3($\bar{x}$)	39.7 µm	42.7 µm
Sigma 3 ($\bar{x}$)	9.7 µm	11.6 µm
Mean b/l3	0.851	0.839
1-Q3 (b/l = 0.850)	65.0 %	61.5 %

Comparison of results from $X_{c\ min}$ and X_{area} suggests that the particles measured by area are marginally larger than those measured by size, (Table 20). X_{area} evaluates the distance across a circumferential boundary around the particles image, this boundary also includes aspects of the image that are not of the particle thus the value calculated is larger than $X_{c\ min}$. Particles with more surface imperfections such as satellites and powder agglomerations exhibit a greater difference between the values of $X_{c\ min}$ and X_{area}. It is also possible for the cameras to capture images where two or more particles coexist, forming an elongated particle, these can be assessed using the image database.

Figure 50 and Figure 51 show volume-based distribution curves for Ti6Al4V baseline assessments. Volume based distribution makes it easier to compare results specific to gains or losses of a specific characteristic, in the case of $X_{c\ min}$, the minimum distance across a particles image and for X_{area}, the area of a particle within a circumferential boundary.

Figure 52 shows the volume-based analysis of the particle's aspect ratio (b/l), key indicators are presented at the aspect ratio pints, 0.150, 0.500 and 0.850, for this research the key indicator at 0.850 $\mathcal{AR}$ is used to classify the sample as rounded. Here. A result of 0.851 $\mathcal{AR}$ means the sample would be classed as rounded. By measuring the inverse volume (1-Q3 (b/l = 0.850)) we can see that 65 % of the sample's particles would be classed as rounded.

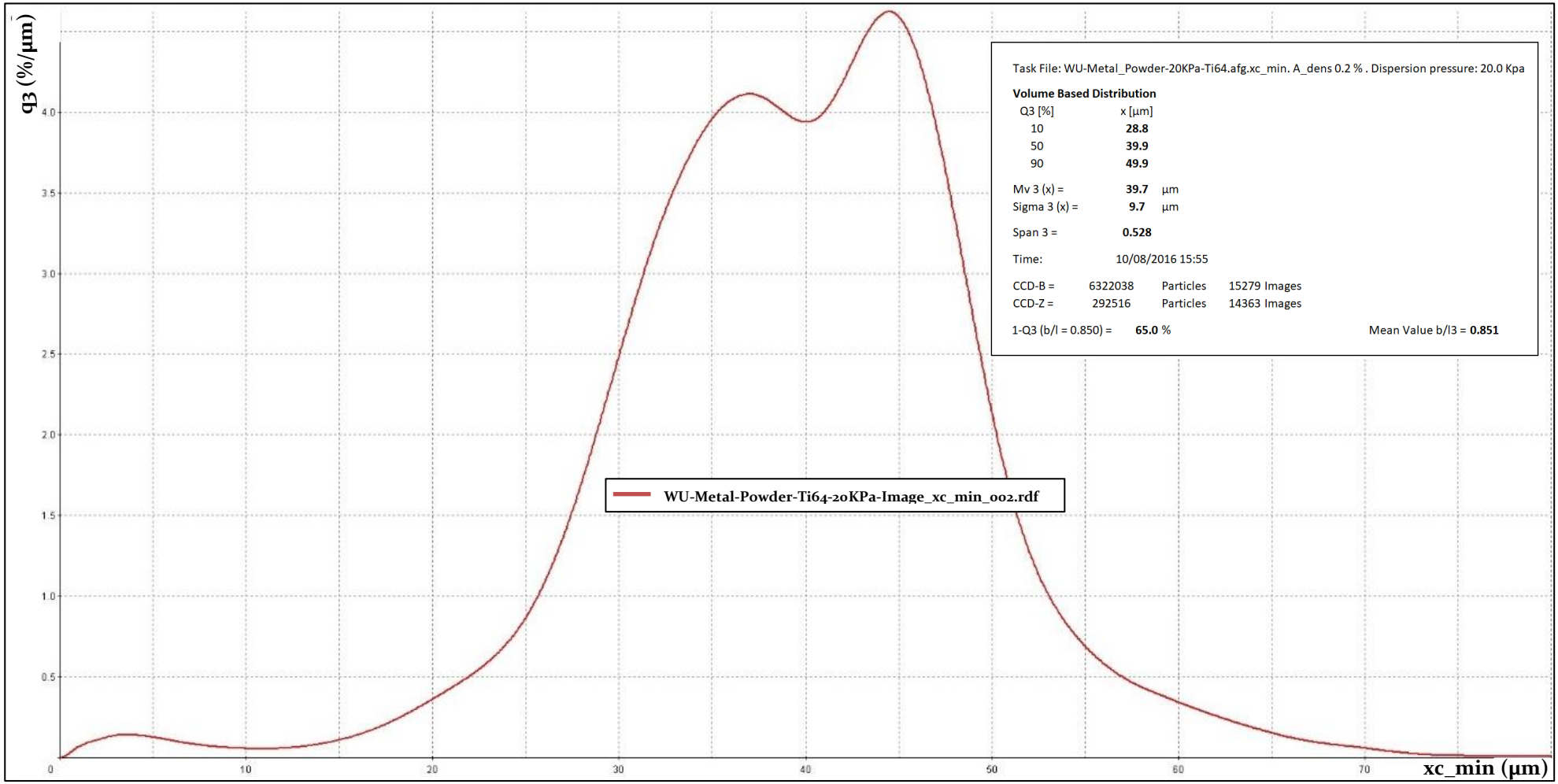

Figure 48 - Ti6Al4V Size Distribution Baseline $X_{c\ Min}$

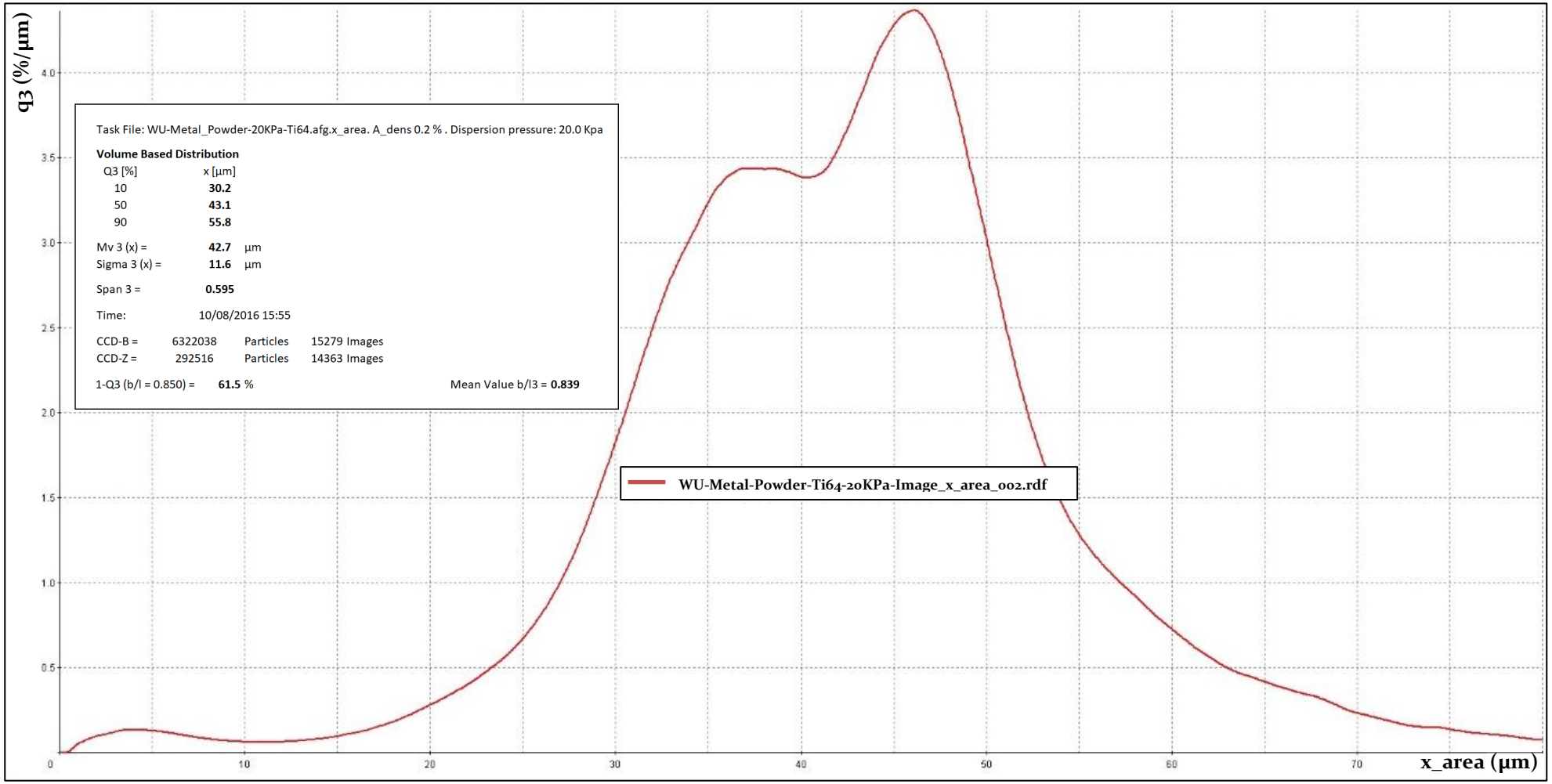

Figure 49 - Ti6Al4V Size Distribution Baseline X_{area}

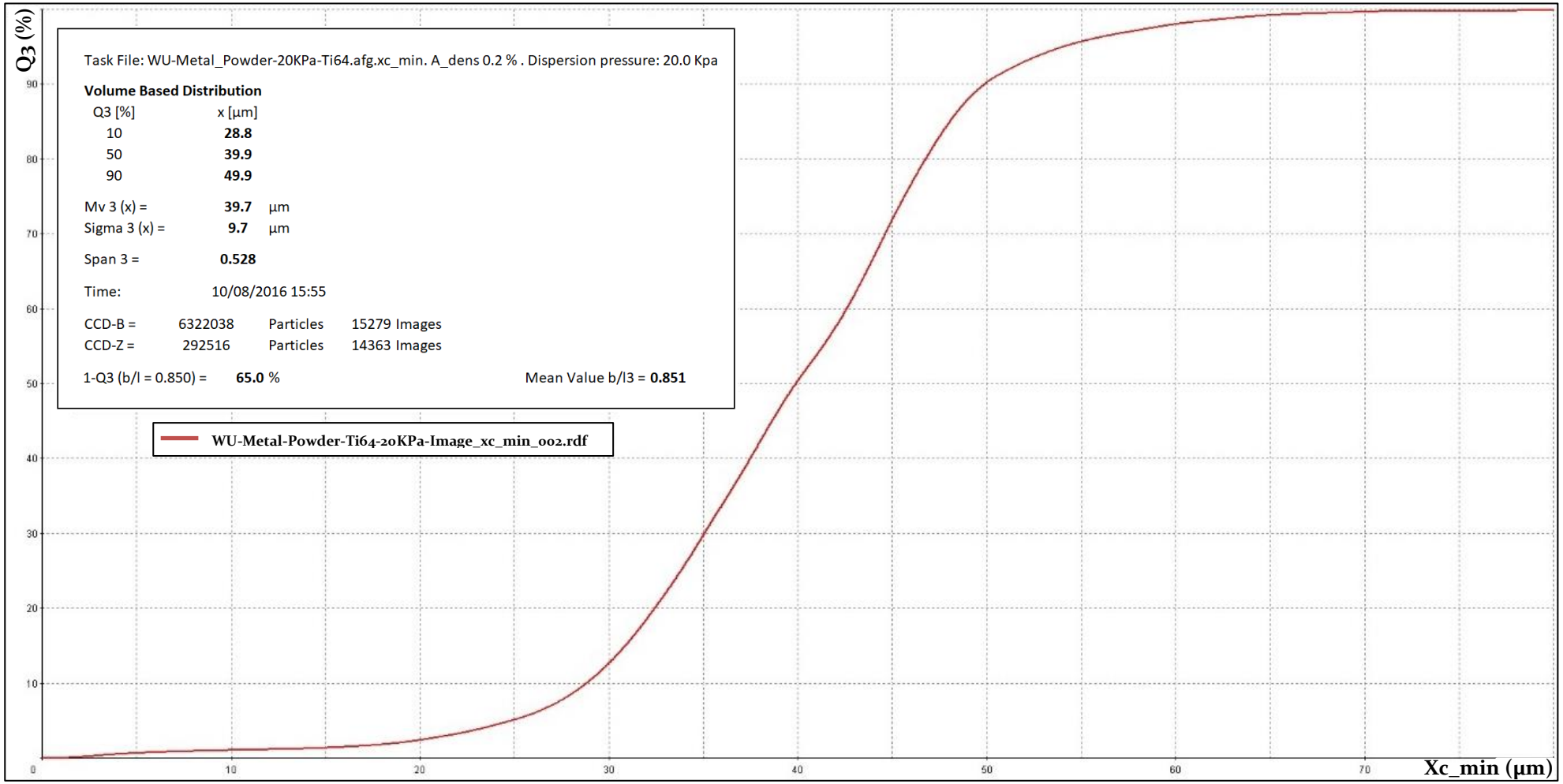

Figure 50 - Volume Based Distribution Curve Results for Ti6Al4V Baseline $X_{c\ Min}$

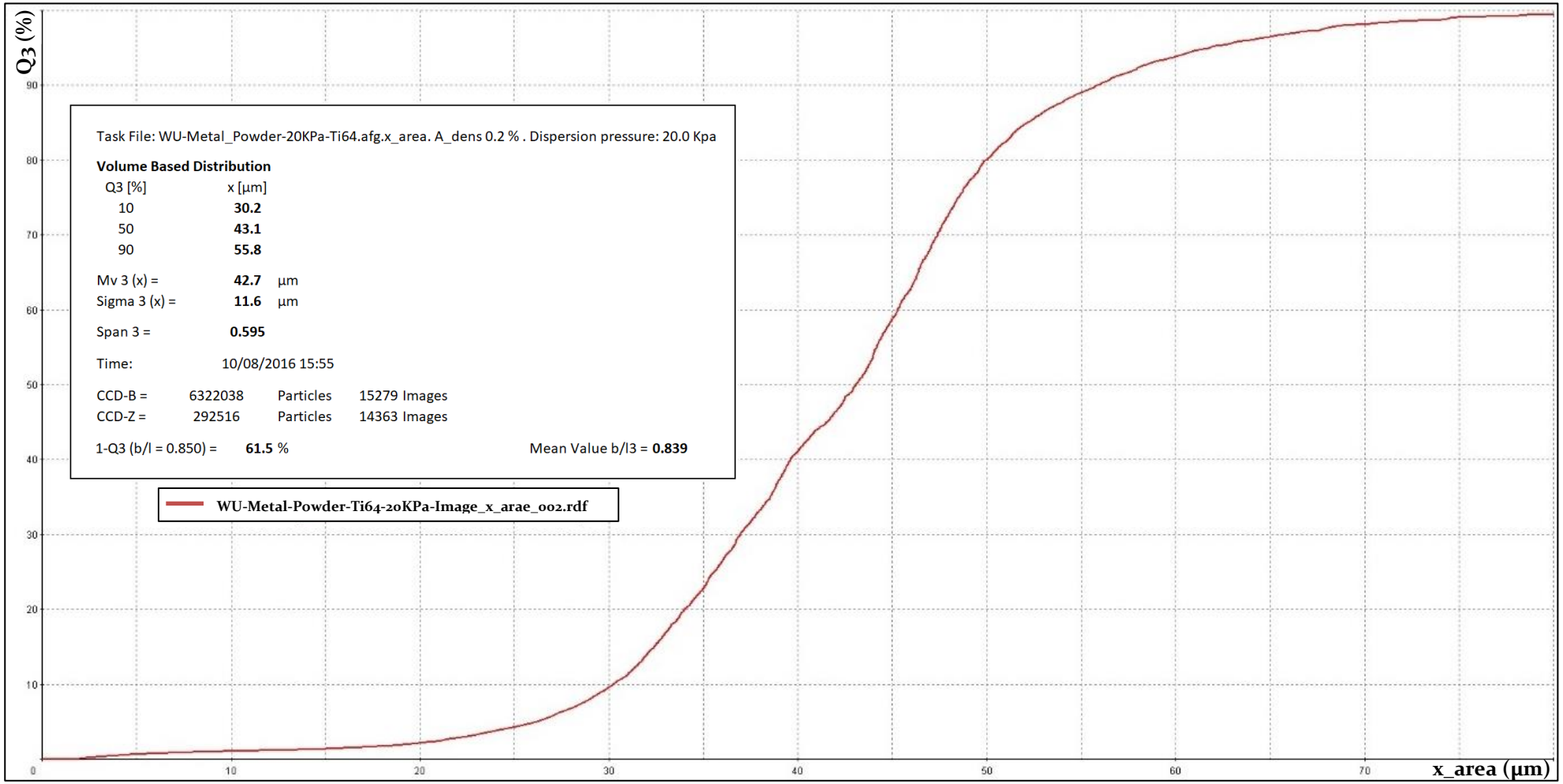

Figure 51 - Volume Based Distribution Curve for Ti6Al4V Baseline X_{area}

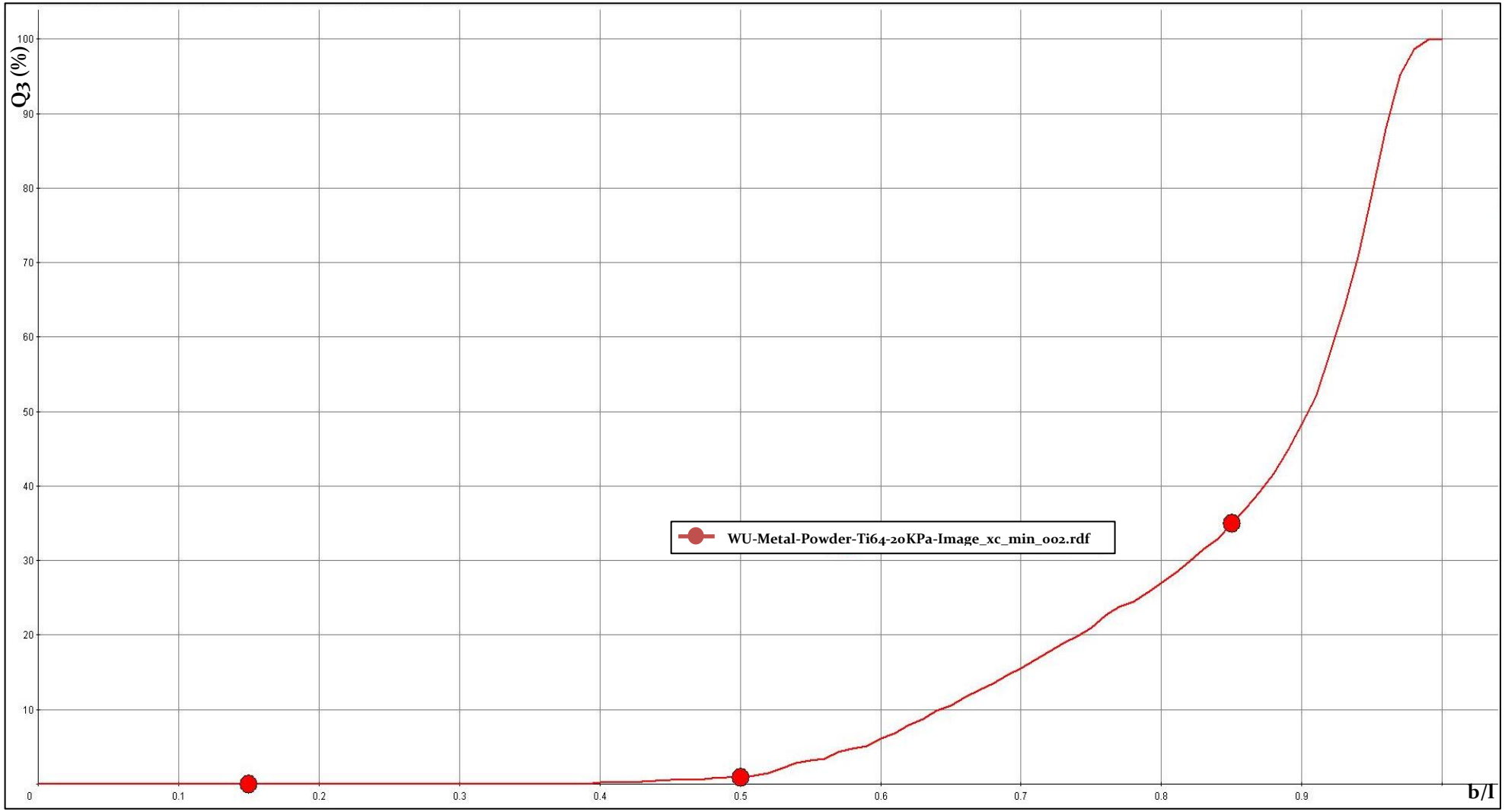

Figure 52 - Volume Based Distribution Curve for Ti6Al4V Baseline b/l

5.2.3.2 SiC Particle Size and Size Distribution Baseline Assessment

Figure 53 shows results for $X_{c\ min}$ (particle size) distribution curve for SiC powder.

Table 21 - Statistical Results for SiC Particle Size and Distribution ($X_{c\ Min}$) Baseline Results

Statistical measurement	Baseline result ($X_{c\ min}$)
Q3 10 %	7.6 µm
Q3 50 %	70.2 µm
Q3 90 %	491.9 µm
Mv3(x̄)	171.4 µm
Sigma 3 (x̄)	244.2 µm
Mean b/l3	0.762
1-Q3 (b/l = 0.850)	27.4 %

Table 21 shows the salient characteristics of the particle size analysis. It can be seen from the data that D50 (Q3 50 %) is 70.2 µm and the mean particle size of the sample (Mv3(x̄)) is 171.4 µm. As these two values are at extremes, it suggests a low degree of confidence in the results. The mean aspect ratio (Mean b/l3) result indicates that very few particles are spherical based on the relationship between the longest (X_{Fe} Max), and shortest ($X_{c\ min}$) measurements of what the system has recognised as particles. Looking at the inverse statistical volume for the sample (1-Q3 (b/l = 0.850)) it can be seen that 27.4 % of the sample would be classed as rounded, this was further evaluated using the particle images.

Further analysis was conducted with the same sample, evaluating the width (µm) of the particles bounding circumference, (X_{area}). Where particles have a close aspect ratio indicating fewer satellites and agglomerations, the statistical analysis would be comparable to the values for particle size $X_{c\ min}$.

Figure 54 shows results for X_{area} distribution curve for SiC powder

Table 22 - Statistical Results for SiC Particle Size and Distribution, $X_{c\ Min}$ Versus X_{area} Baseline Results.

Statistical measurement	Baseline result ($X_{c\ min}$)	Baseline result (x_{area})
Q3 10 %	7.6 µm	8.4 µm
Q3 50 %	70.2 µm	73.0 µm
Q3 90 %	491.9 µm	559.7 µm
Mv3(x̄)	171.4 µm	198.4 µm
Sigma 3 (x̄)	244.2 µm	290.3 µm
Mean b/l3	0.762	0.753
1-Q3 (b/l = 0.850)	27 %	25.1 %

Comparison of results between $X_{c\ min}$ and X_{area} (Table 22) suggests that the particles measured by area are once again larger than those measured by shortest distance ($X_{c\ min}$). It has been established from the baseline assessment of the Ti6Al4V powder (4.2.5) that it is possible for the cameras to capture images where two or more particles coexist; this however would not cause such a large spread of results between the D10 and D90 values. It was also established that multiple particles within an image can present as an elongated particle, once again this would not cause such a large spread of results. It was therefore, concluded that the values returned by the equipment did not relate to individual particles, but to agglomerations of the powder. Due to the large surface area and increased surface energy of the particles, the likelihood of agglomeration is significantly increased, the Camsizer X2's particle dispersion system is designed to aid separation of particles during analysis however it is evident that this was not possible for particles of this size.

The results were further confirmed using volume-based distribution Figure 55 and Figure 56.

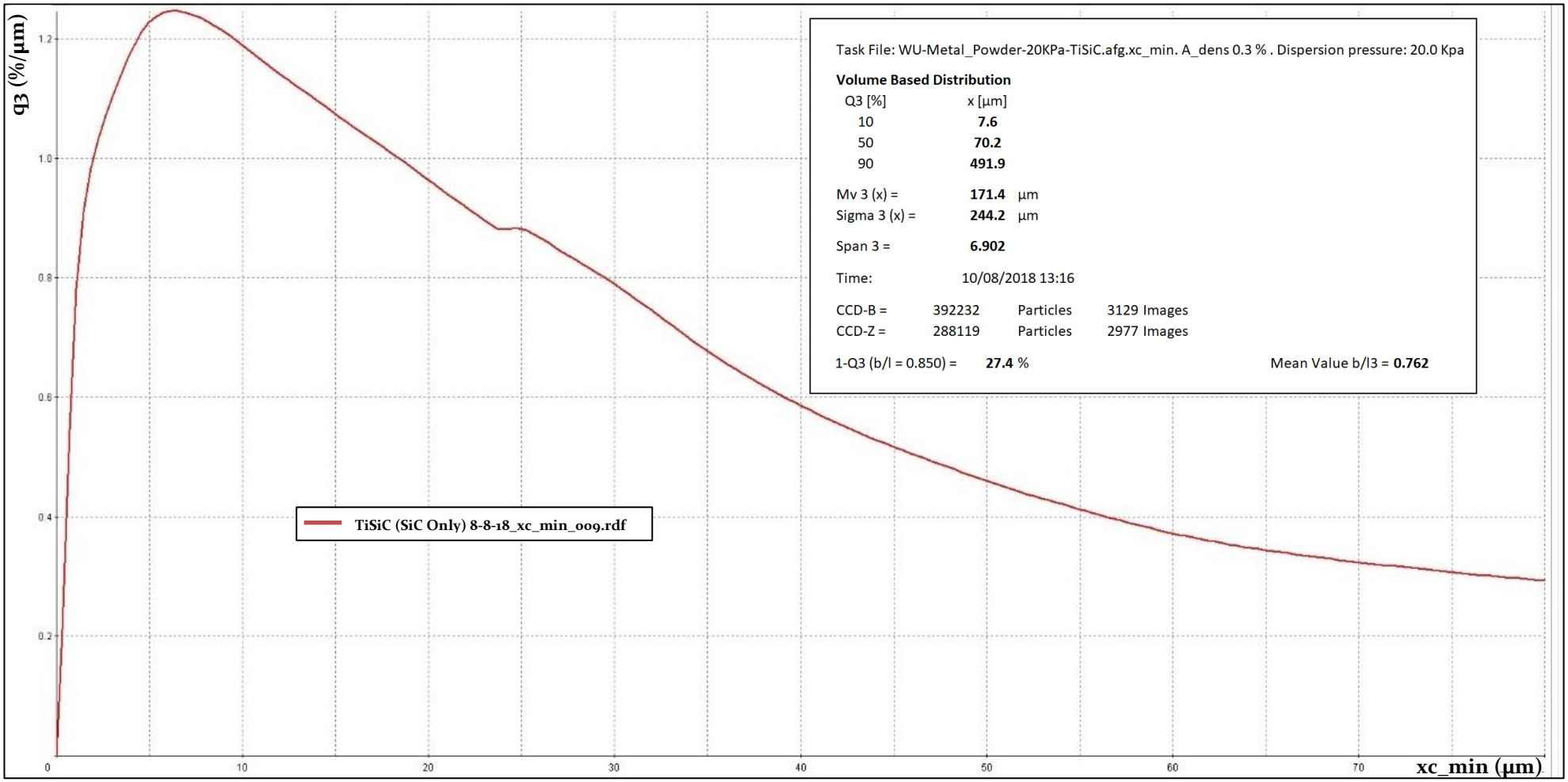

Figure 53 - SiC Size Distribution baseline $x_{c\,min}$

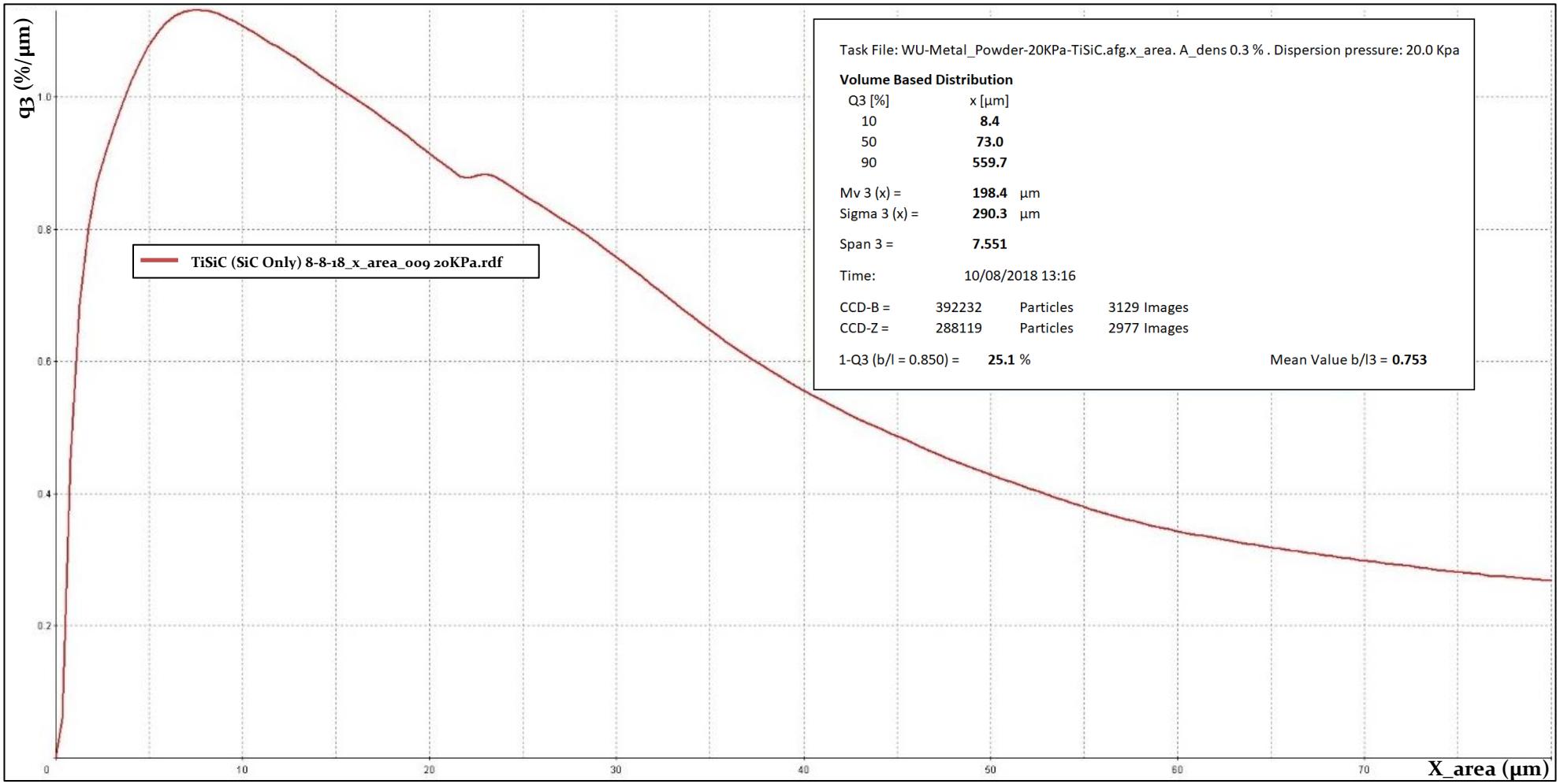

Figure 54 - SiC Size Distribution Baseline X_{area}

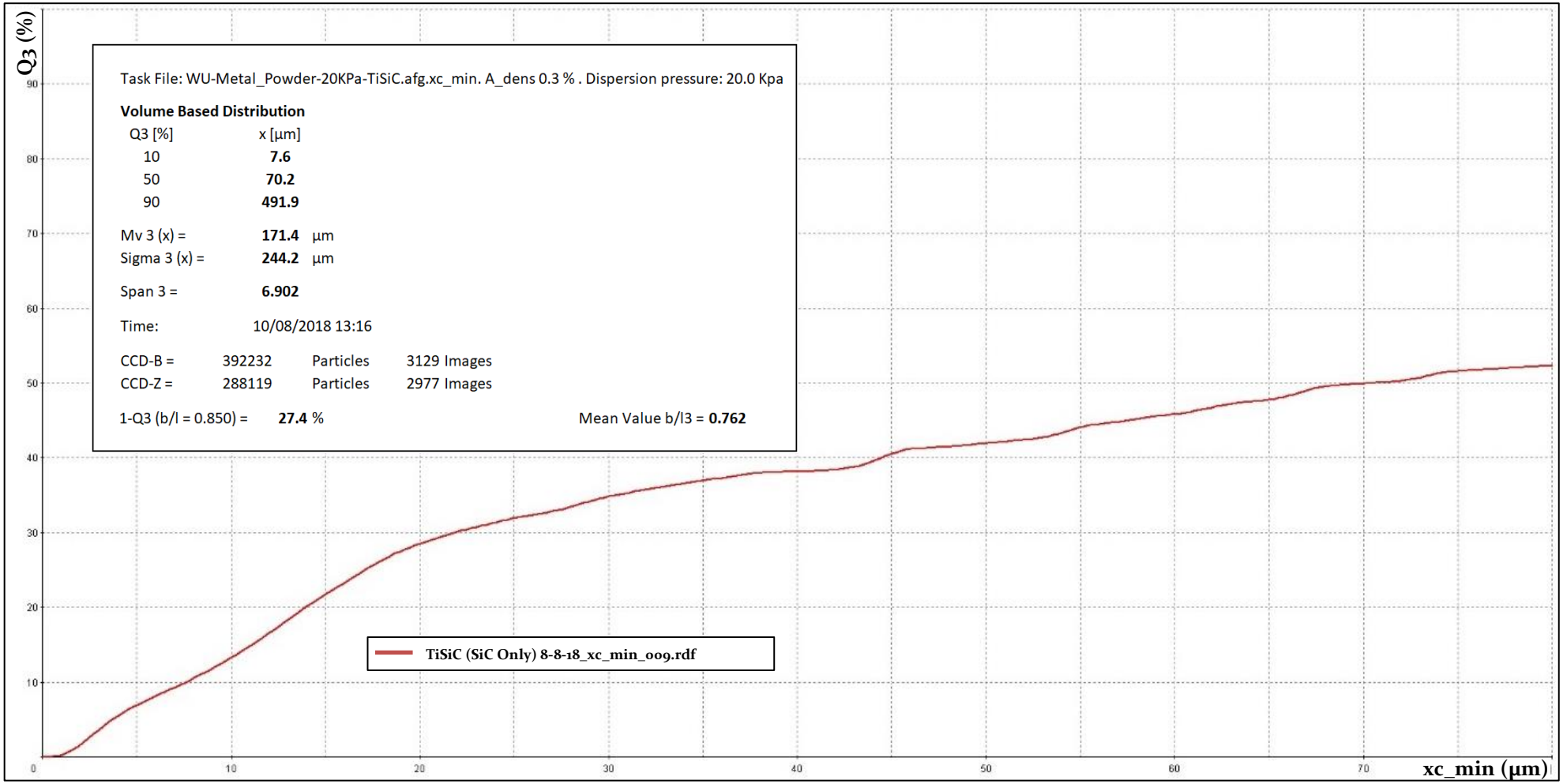

Figure 55 - Volume Based Distribution Curve for SiC Baseline $X_{c\ Min}$

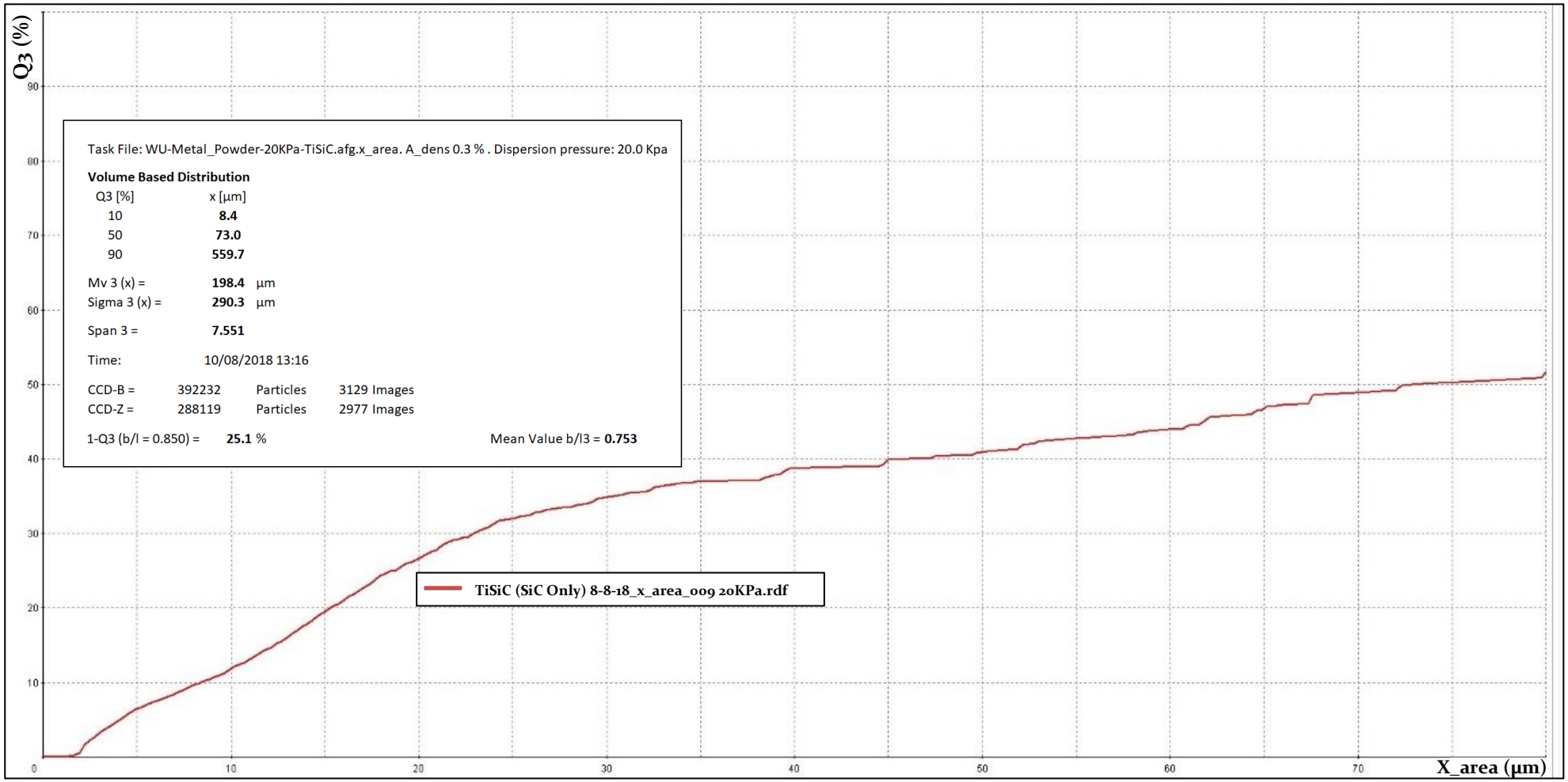

Figure 56 - Volume Based Distribution Curve for SiC Baseline X_{area}

5.2.4 Phase 1a Baseline Assessment of Ti6Al4V Particle Morphology

Further analysis of the Ti6Al4V baseline assessment results using the Camsizer X2 was carried out using the image database. Using filters to locate specific criteria such as size and aspect ratio, it could be observed that the Camsizer software had difficulty recognising some particles.

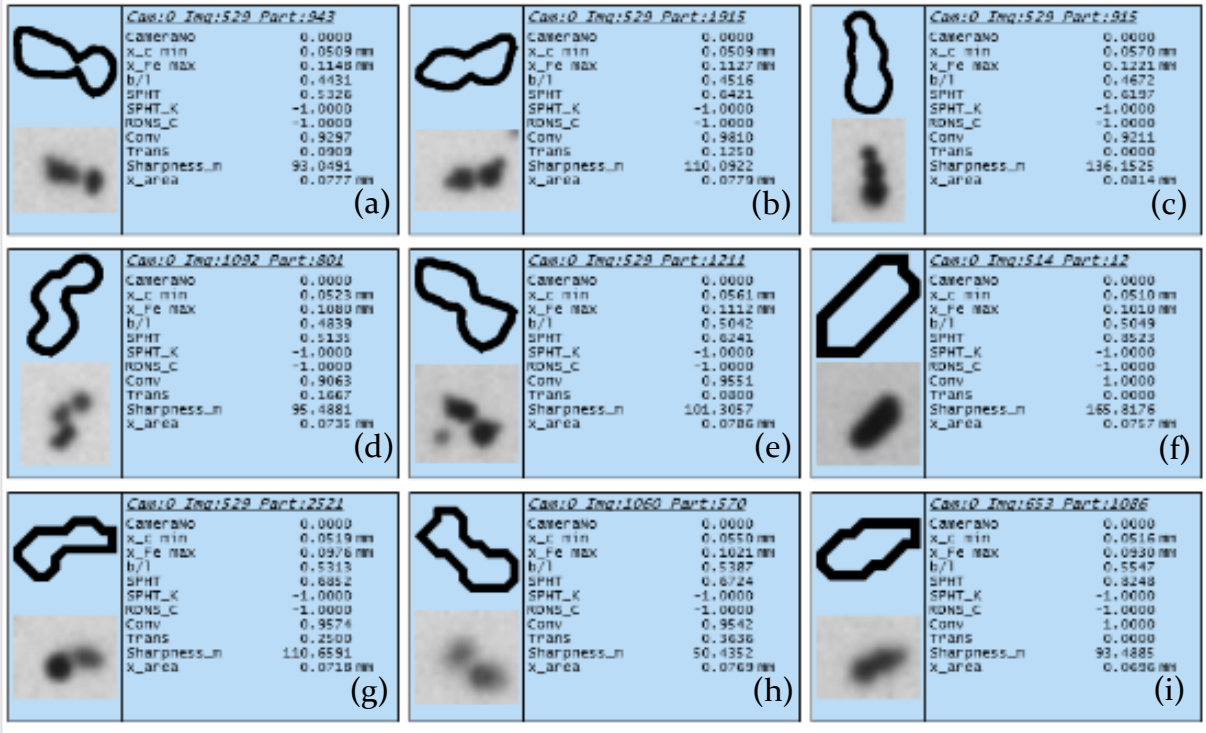

Figure 57 - Retsch Camsizer X2 Database Images of Nonrounded Ti6Al4V Particles (B/L ≤ 0.850)

Figure 57 shows a selection of images and software measurements using the Retsch Camsizer X2 database software. Elongated particles were isolated using the database filters, $X_{c\ min} \geq 0.010$ mm to filter out small fines and b/l ≤ 0.850 $\mathcal{AR}$ to capture nonrounded particles. It was evident from the images that in some cases, the software failed to distinguish between individual particles in the images. In image (a) showed two disconnected particles, one that appeared to be rounded and one that was elongated. This was also the case with image (b), two particles appeared to be present in the image but were separated, both particles also appeared to have satellites. Image (c) presented what appeared to be three particles joined together, as the focus of the three particles appeared to be the same it was concluded that this was a complete particle. For image (d) it was concluded that this was three or more particles in the same image that were not joined. Images (e) presented similarities with (b) and whilst the camera image captured a third particle the software image has discounted this. Images (f) and (i) showed particles with clearly nonrounded forms whilst the camera image (g) showed two particles with varying focus of multiple particles, this indicated that the two particles were not in the same location in terms of distance from the cameras focal point.

Image (h) two particles with poor focus, separated but possibly rounded. It was therefore deemed important to visually check the images to ensure the software had not falsely represented the particles data. Using the filters above, 285 out of 726 images were found that met the conditions, 39.3 % nonrounded.

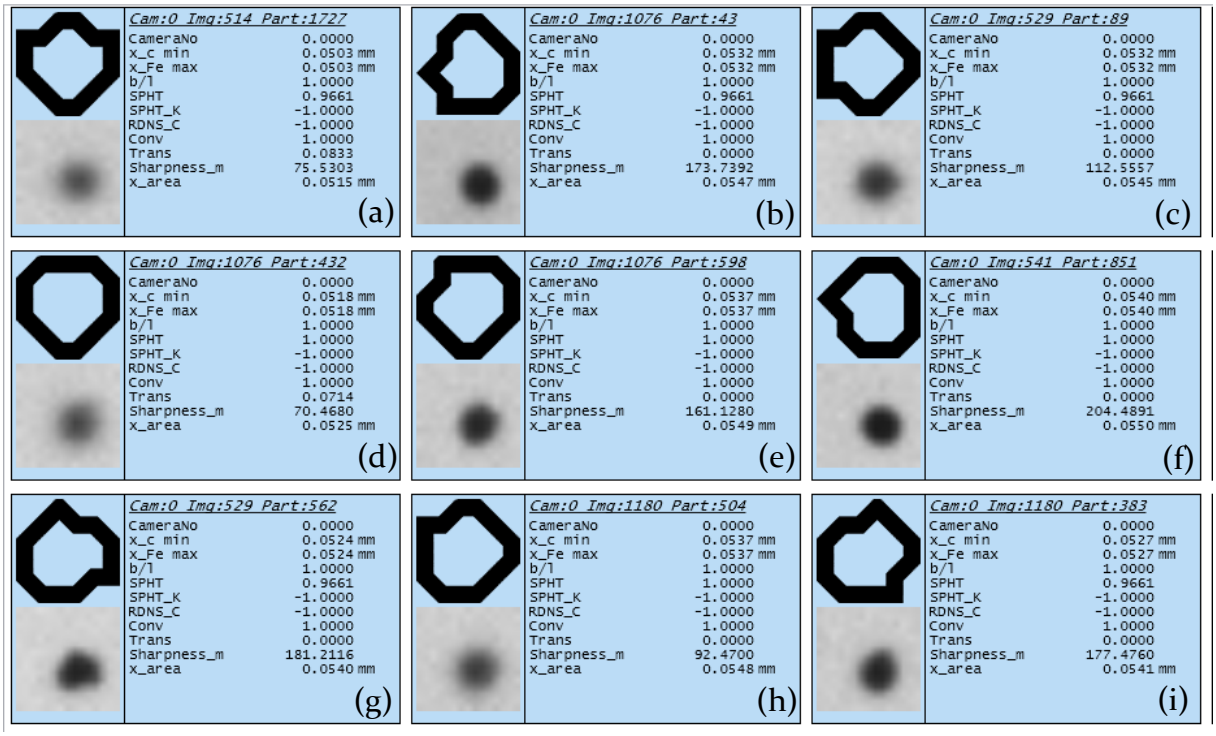

Figure 58 - Retsch Camsizer X2 Database Images of Rounded Ti6Al4V Particles (B/L ≥ 0.850)

Figure 58 shows a selection of images and software measurements showing nonrounded particles using the database filters, $X_{c\ min} \geq 0.010$ mm to filter out small fines and b/l ≤ 0.850 $\mathcal{R}$ to capture rounded particles. It was evident from the images that recognised rounded particles satisfactorily. Using the filters above, 424 out of 726 images were found that met the conditions, 58.4 % rounded.

5.2.4.1 Scanning Electron Microscopy of Ti6Al4V Powder

Following on from analysis of the database images the powders were observed using a SEM. Figure 59 shows SEM images at (a) 1,000 x and (b) 2,000 x magnifications, it was clearly observed from the images that most of the particles were spherical with a range of sizes as shown. It was also observed that several particles were elongated (c), satellited (d) and possibly agglomerated (e).

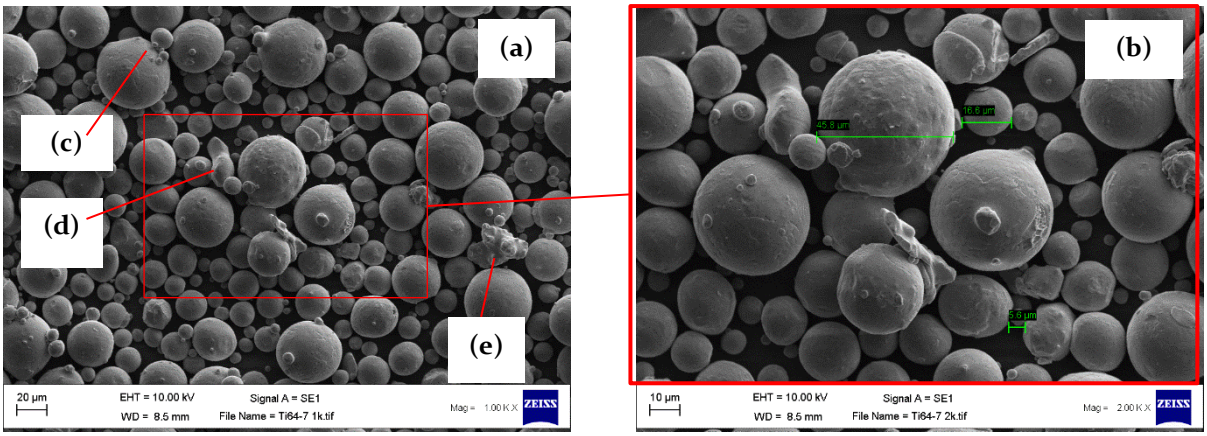

Figure 59 - Scanning Electron Microscopy of Ti6Al4V Powder (A) 1,000 X Magnification (B) 2,000 X Magnification

Figure 60 shows a Ti6Al4V powder particle at 8,000 x magnification measuring 45.8 µm. solidification patterns are visible on the surface along with columnar alpha phase.

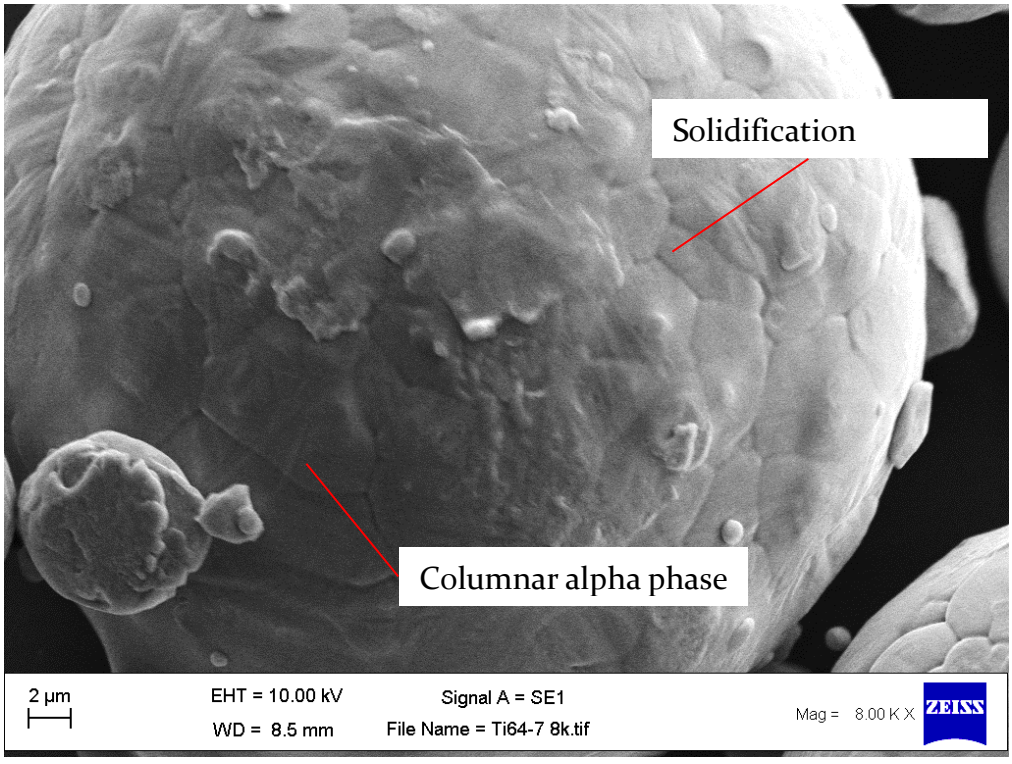

Figure 60 - Scanning Electron Microscopy of Ti6Al4V Powder 8,000 X Magnification.

5.2.5 Phase 1a Baseline Assessment of SiC Particle Morphology

Further analysis of the SiC baseline assessment results using the Camsizer X2 was carried out using the image database.

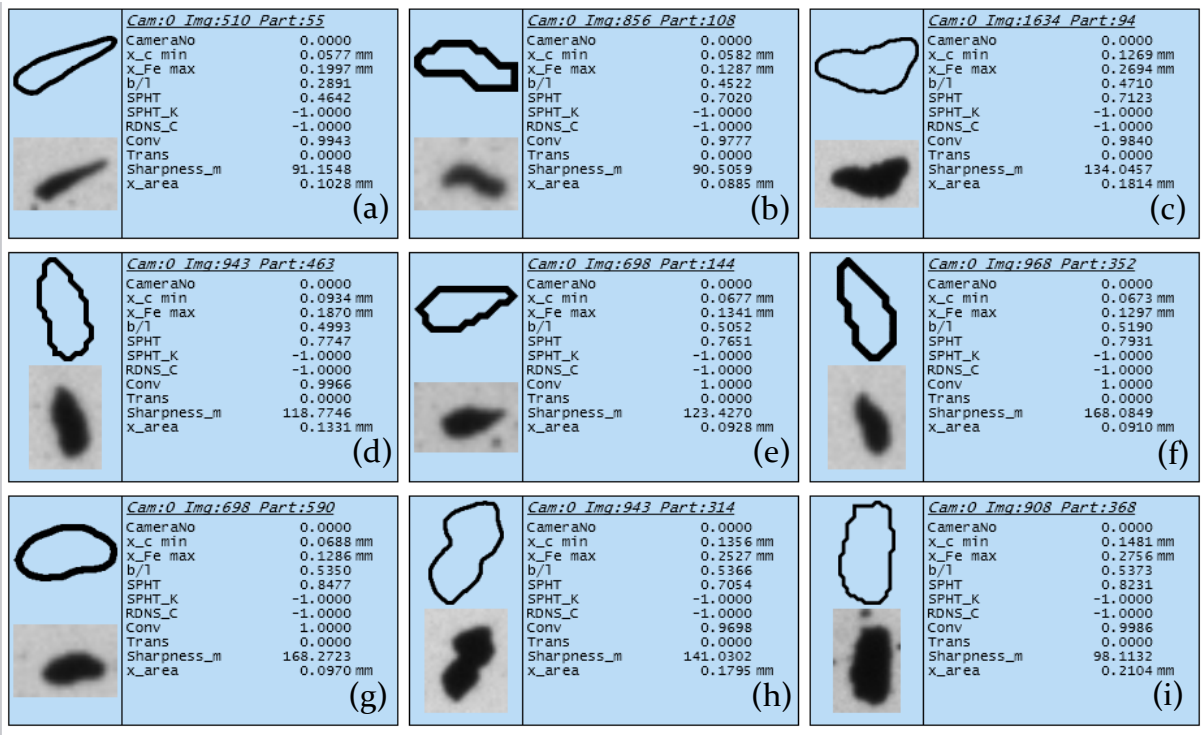

Figure 61 - Retsch Camsizer X2 Database Images of Nonrounded SiC Particles (B/L ≤ 0.600)

Figure 61 shows examples of the Retsch Camsizer X2 database images of nonrounded particles using database filters to isolate, $X_{c\ min} \geq 0.010$ mm and b/l ≤ 0.850 $\mathcal{AR}$. It was evident from the images that the software failed to distinguish between individual particles in the images. Using the filter $X_{c\ min} \geq 0.010$ mm to exclude particles smaller than 0.010 mm, should have selected no images as the largest particles are less than one micron. Images (a) to (i) exhibit minimum widths ($X_{c\ min}$) ranging from 0.057 mm to 0.148 mm.

Using the filters above, 852 out of 2631 images were found that met the conditions, this would suggest that 32.4 % of the particles are statistically rounded however, based on SEM results there is enough evidence to show that these are agglomerations.

5.2.5.1 Scanning Electron Microscopy of SiC Powder

Figure 62 shows an SEM image of SiC powder at 30,000 x magnification, it was observed from the image that the largest visible particles were approximately 0.89 µm in width whilst most of the particles were substantially smaller.

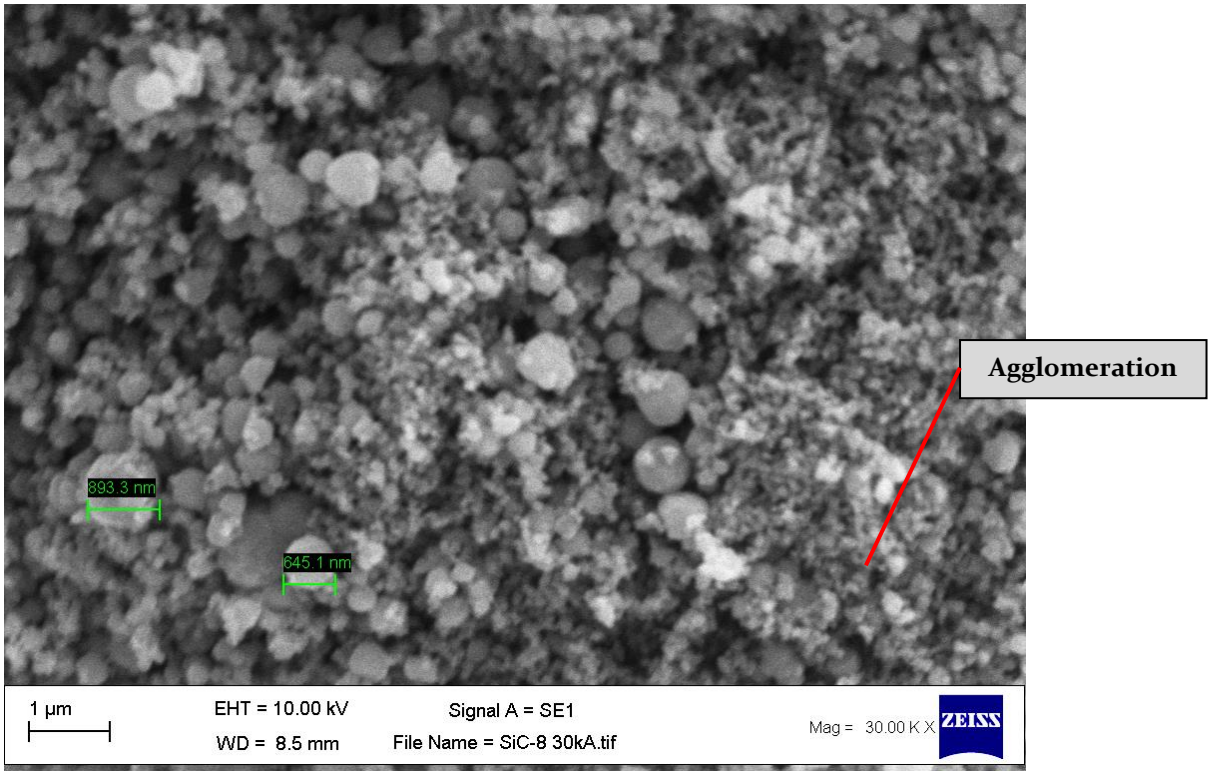

Figure 62 - Scanning Electron Microscopy of SiC Powder 30,000 X Magnification

The image showed evidence of agglomerations within the sample, whilst this posed no issues for the MA process it did present a challenge in terms of accurate size analysis.

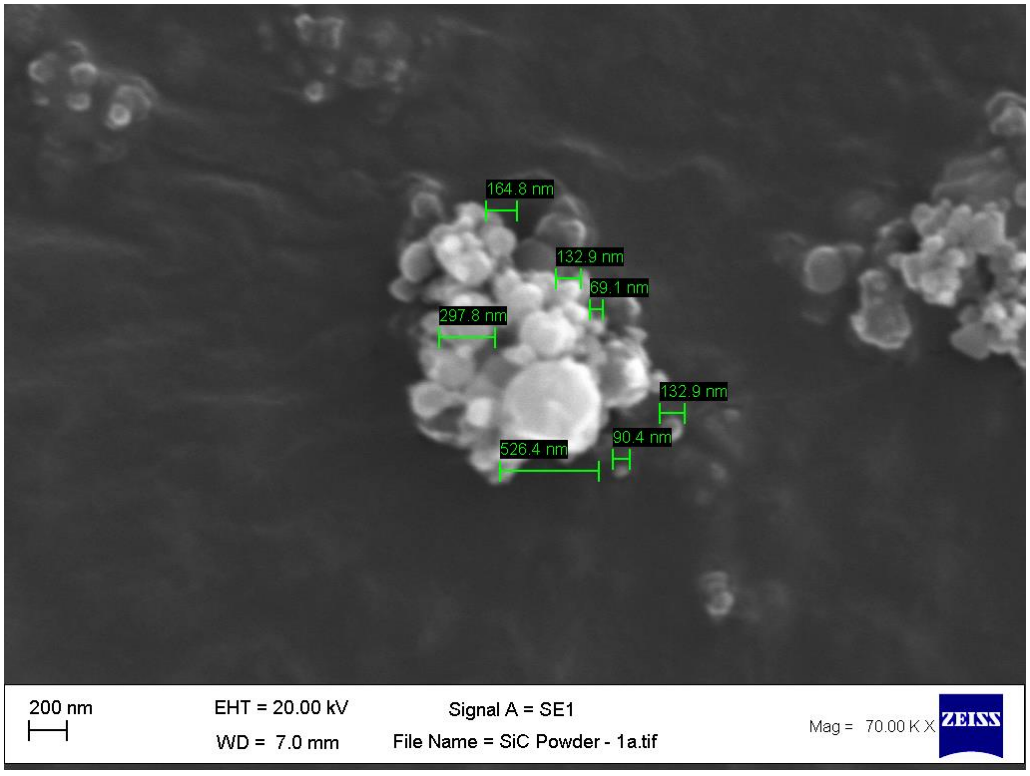

Figure 63 - Scanning Electron Microscopy of SiC Powder 70,000 X Magnification

At 70,000 X magnification, individual particles were measured at between ~0.069 µm and ~0.526 µm wide Figure 63. However, is was not possible to evaluate the frequency distribution of all particle sizes within the range.

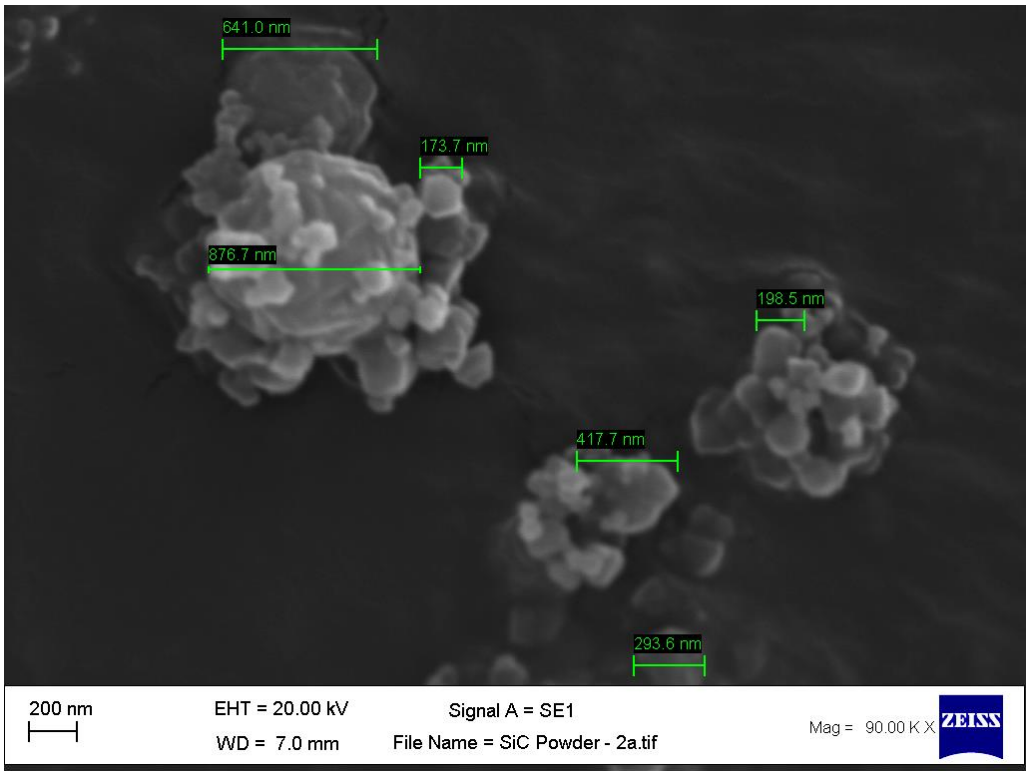

Figure 64 - Scanning Electron Microscopy of SiC Powder 90,000 X Magnification

At 90,000 X magnification, Figure 64, evidence showed SiC particles in the range of ~0.173 µm to ~0.876 µm, It was therefore concluded that whilst this is not the most accurate measurement of these particles and a bore accurate method should be sought through further research, in this instance and with the data available the particle range should be taken to be from ~0.10 µm to ~0.90 µm with an average particle size of ~0.50 µm for use with Equation 5.

5.3 Phase 1a: Baseline Assessment of Raw Materials Conclusions

5.3.1 Baseline assessment of raw materials (Ti6Al4V)

1 The moisture content of Ti6Al4V was significantly low (0.59 %), apparent density was 50.6 % that of the density of Ti6Al4V with a measured angle of repose of 33°. It was concluded that these values were typical for Ti6Al4V.

2 Size and size distribution were carried out using Retsch Camsizer X2, results showed statistically calculated results as Q3 10 % 28.8 µm, Q3 50 % 39.9 µm, Q3 90 % 49.9 µm, Mv3($\bar{x}$) 39.7 µm, Mean b/l3 0.851 with 65 % of the sample rounded (1-Q3 (b/l = 0.850)). It was concluded that these values were also typical for Ti6Al4V.

3 Morphologically, the Ti6Al4V feedstock was analysed and an image database was obtained during the measurement of size. This was used to further understand the size and size distribution results by providing additional confirmation. In conclusion, the image database was able to successfully identify images of significance although these were low, therefore providing a high level of confidence in the results.

4 The Ti6Al4V powder was found to be of good roundness with a distribution range between 3 µm to 75 µm. agglomerations were few as were satellites.

5.3.2 Baseline assessment of raw materials (SiC)

1 The moisture content of SiC was low (1.78 %), however, this was thought unacceptable within this research. After processing to remove moisture it was accepted at 0.96 %.

2 Apparent density for the SiC powder was 12.8 %. This showed an extremely low quantity of material within the volume. This was due to large agglomerations forming within the powder, thus creating voids.

3 Angle of repose was measured at 48°. It was concluded that these values were typical for SiC.

4 The SiC powder was found to be angular in shape with a distribution range between ~0.10 µm to ~0.90 µm. The material agglomerated excessively making measurement challenging.

Chapter Six

6.0 Phase 1b Baseline assessment of Ti6Al4V Single beads evaluated against energy density

6.1 Phase 1b: Baseline Assessment of Ti6Al4V Single Beads Evaluated Against Energy Density Methodology

6.1.1 Overview of The Experiment/Design

To characterise the effect of the addition of SiC reinforcement into the feedstock a series of tests were developed and were benchmarked against Ti6Al4V to investigate the MA feedstocks processability. In view of the findings from the initial experimentation (chapter 3.0), a deconstructive qualitative methodology was adopted.

The aim was to evaluate the most significant elements of the processes only, in line with the energy density equation (Equation 1) and to better understand how the new material behaves in comparison to the baseline material Ti6Al4V.

Operating conditions and parameters were kept the same as for the EOS Ti6Al4V parameter set, such as layer thickness, inert atmosphere, gas flow rate, recoat speed and recoat volume. These are categorised as attributes within this research to distinguish from variables. Depending on the findings from comparison between the MMC and

Table 23 - Energy Density Matrix (J/mm³) Using Equation 4

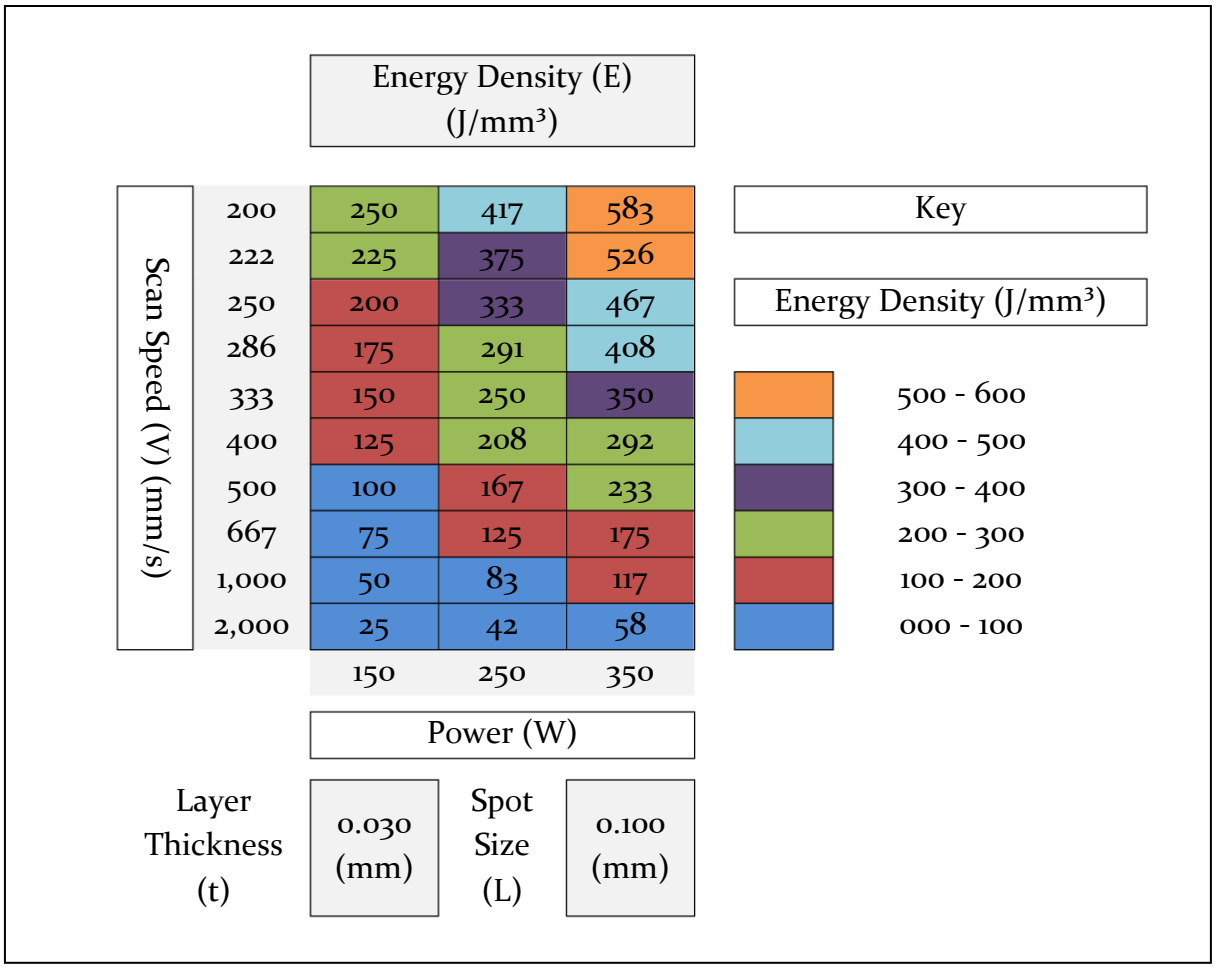

Ti6Al4V feedstocks it may be nessasay to broaden the investigatory parameters by investigating layer thickness and laser spot size.

Beginning with single beads, Ti6Al4V was exposed with a broad range of energy densities on a single layer to evaluate the materials processability, miscibility and physical characteristics. These results were used to benchmark the MMC feedstock material against in phase 2b.

An experimental population was developed to offer a matrix of energy densities across the available laser power and scan settings for the process. Table 23 shows the energy densities (*Ed*) matrix based on a laser spot size (*L*) of 0.100 mm and layer thickness (*t*) of 0.030 mm and was calculated using Equation 4. The test matrix comprises thirty single bead tests, ten in each laser power set and a variable scan speed. The matrix is formed of three laser power values, 150W, 250W and 350W to accommodate the full range of

laser power available but also to minimise the total number of samples manufactured. Scan speeds have been calculated to linearize the energy density values for better representation of results; Figure 65 graphically illustrates the energy densities shown in Table 23 for each laser power range calculated using Equation 4.

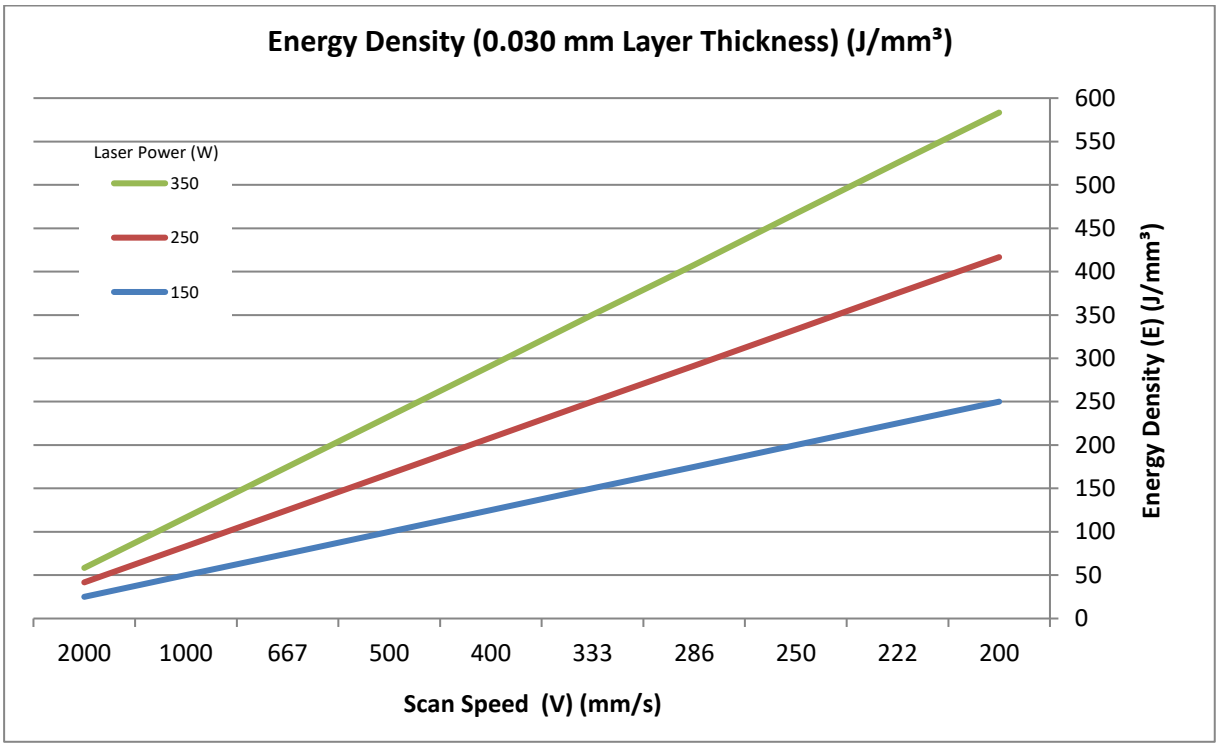

Figure 65 - Energy Density (J/mm³) Over Scan Speed (V) (mm/s)

6.1.2 Restrictions and limitations

6.1.2.1 Feedstock Availability

Due to the limited amount of feedstock produced, building sizable parts on a build platform measuring 250 mm x 250 mm was economically impractical due to the volume of powder per layer and the amount required in the dispenser. It was therefore necessary to develop a system of what became known as “mini chambers”. These mini chambers worked in conjunction with the equipment’s existing chambers but allowed for the ability to build with much less feedstock. The mini chambers build area was 120 mm x 120 mm.

6.1.2.2 Energy Density Calculations Without Hatch Distance

When using energy density calculations sometimes referred to as the Andrew Number, (Williams, et al., 1996, and Savalani et al., 2011) it is common practice to calculate the affected volume of material using Equation 1:

$$Ed = \frac{p}{s * v * t}$$ Equation 4

Where: ***Ed*** is the Laser Energy Density (J/mm^3)

P is the Laser Power (W)

s is the Spot Size (mm)

v is the Scan Speed (mm/s)

t is the Layer Thickness (mm)

For stage 1, single bead evaluation, the parameter of hatch distance (h) is substituted by the laser spot size (s) and is taken to be 0.100 mm as a constant across all calculations as shown in Equation 4 It is important to note that for Stage 2, multiple bead experimentation, the energy density equation is returned to its original format by reinstating the hatch distance variable.

6.1.2.3 Laser Power Range

The apparatus used for the experiments was an EOS M290 with a manufacturer specified laser power range of 0 – 400 W, this however is not the useable range, during the calibration of the apparatus at installation the maximum laser power was fixed at 375 W to safely manage the laser equipment. In pre-test measurements a value of 372 W was measured which was within the specified tolerance of ± 5 %. It was therefore decided not to exceed 350 W within experimentation undertaken. For experimentation, laser power values were taken as the software requested values rather than recalibrating for each test as the pre-experimentation calibration readings were within tolerance and due to the fact that the methodology involved comparison between comparative experiments, therefore the laser powers were taken as constant through all experiments within each set.

6.1.3 Equipment

Part experimentation was conducted using an EOS M290 PBF machine.

Individual parameter setups were constructed using EOSPrint version 1.5 (2017).

Due to the limited availability of feedstock, Mini platforms and chambers were used to conduct experiments (Figure 66), comprising a build area of 120 mm by 120 mm. Counter bored holes in each corner enabled the platforms to be secured to a piston-top and

levelled using 5 mm grub screws in each corner, Each platform also incorporated a two-rail system as shown (Figure 66), positioned longitudinally in the direction of re-coating. The mini platform system was developed prior to this research by the author and the two-rail system was developed by the author for this research.

6.1.3.1 The two-rail system

The two-rail system optimised the laying of the powder bed for the single bead experiments. Under normal working conditions for most materials, the first two layers are double exposed to assist with bonding to the base plate (substrate); furthermore, the amount of feedstock on the first layer would be minimal. In the case of the single bead experiments it was not possible to double expose as this would invalidate the results. Likewise, tests conducted with a less than normal layer thickness would also not be representative of the normal operating conditions of the process. Based on the apparent density measurements conducted in phase 1 of this research, it was observed that approximately 50.6 % reduction in volume occurs through the transition from powder to solid part, (chapter 5.0). This effect can also be witnessed within a build, where powder has been processed, a reduction in height occurs, on recoating this area requires a larger amount of feedstock to not only deliver a layer of 0.030 mm but also to make up the deficit to the substrate. The typical height of a bead is difficult to establish as it is dependent upon scan speed, laser power and available feedstock (layer thickness). Authors such as Kusuma, 2014, graphically showed how bead heights increased with increases in energy input. For a layer thickness of 0.070 mm and using a laser power of 194 W and scan speed of 1100 mm/s a bead height of 49.4 µm was reported. This represents approximately 30% reduction in comparison with the layer thickness. It is also understood that the range of tests use variables across layer power and scan speed which will alter the resultant bead height. Therefore, as a start point and to provide consistence across all experiments, a value of 30 µm for the powder bed layer plus an additional 12.5 µm ± 2.5 µm for a total of 42.5 µm ± 2.5 µm. Each rail was therefore cut 0.045 mm to 0.050 mm high (Figure 66). By recoating a layer of feedstock onto the build plate until the rails were cleared of feedstock an accurate and repeatable layer thickness could be achieved, this method was used for all experiments in phases 3a and 3b. Multiple layer evaluation of density and homogeneity of reinforcement (3c) was conducted on mini build plates using standard operating procedures for preparing the build platform and environment without the requirement for the two rails.

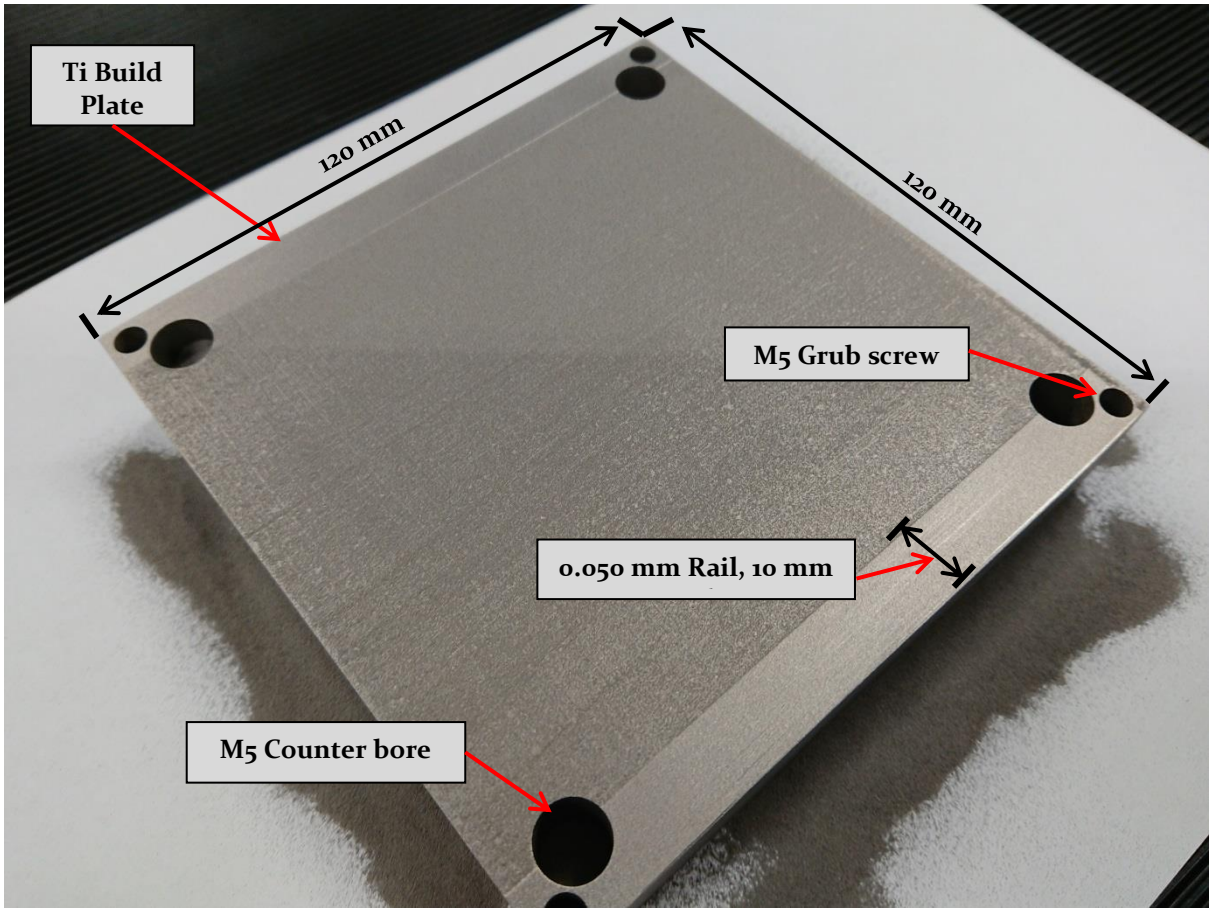

Figure 66 - Mini Platforms with Reduced Build Area for Limited Feedstock, Recoated Using 45 – 50 µm Two-Rail System.

6.1.4 Procedures

6.1.4.1 Digital Files

The digital files were prepared using EOSPrint version 1.5 (Figure 67) parts were arranged as per Table 23 and labelled for future reference. The exposure order was set to expose the parts first, working from the front of the build chamber to the rear to minimise the risk of powder contamination from previous parts. Finally, the labels were exposed.

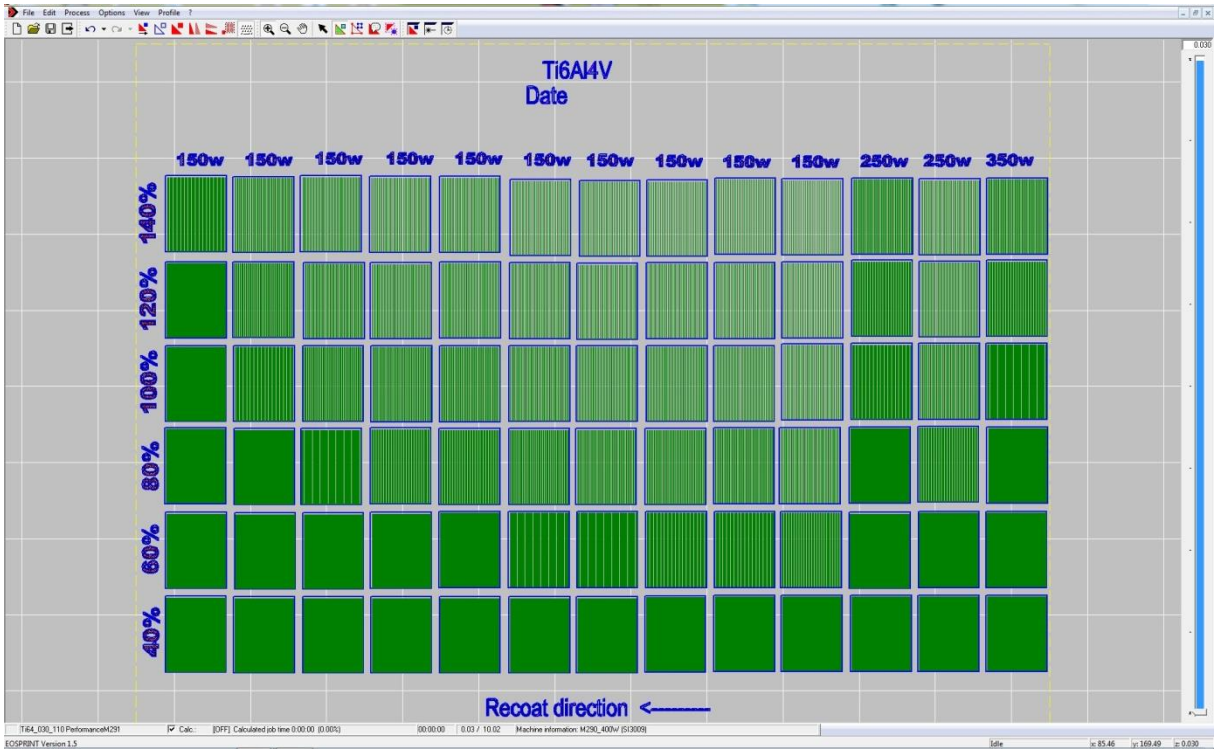

Figure 67 - EOSPrint 1.5, Layout for Ti6Al4V Phase 3b

6.1.4.2 Process Chamber Preparation

The process chamber was cleaned to ensure it was free from contamination, fitted with mini chambers and the laser power was checked using the laser power Pocket Monitor PMT 05P (Primes GmbH) Figure 68. The chamber was then purged of air/oxygen with Ar gas.

Figure 68 - Primes laser power Pocket Monitor PMT 05P

6.1.4.3 Build Platform Preparation

The 120 mm X 120 mm square build platform was secured with M5 cap head screws (x4) in each corner and Levelled with M5 grub screws (x4) using a plunger type dial test indicator mounted to the recoater arm. For phases 3a and 3b the top surface was

machined flat with 40µm to 50µm rails 10 mm wide were orientated longitudinally to the recoat direction and the build area showed no visible cutting marks or troughs such that feed stock can deposit preferentially, phase 3c build plates were prepared flat. The surfaces were mechanically abraded to produce a uniform texture capable of retaining powder deposits uniformly across the surface and was cleaned chemically with a non-water based de-greaser (ethanol, isopropanol). A deposit of powder was established on the build plate ensuring that the two rails were free from powder before inerting the build chamber.

6.1.5 Variables

6.1.5.1 Phase 3a Variables (Single Bead Evaluation Against Energy Density)

Single beads were exposed using edges parameters to produce a single bead. Variables consisted of laser power and scan speed to achieve a range of energy densities in accordance with the energy density matrix in Table 23. Table 24 shows the Scan variables for the single bead experiment.

Table 24 - Build Variables for Single Bead Experiment

Laser power (W)	Scan Speed (V) (mm/s)									
150	200	222	250	286	333	400	500	667	1,000	2,000
250	200	222	250	286	333	400	500	667	1,000	2,000
350	200	222	250	286	333	400	500	667	1,000	2,000

6.1.5.2 Phase 3a Attributes

For the software (EOSPrint 1.5) to produce single beads the following parameters were fixed for the build process (Table 25).

Table 25 - Build Attributes for Single Bead Experiment

Parameter Setting	Value
Hatch distance	0.24 mm (To enable separation of beads for analyses, not used in calculations)
Stripe width	40 mm
Pre-Contours	Off
Post-Contours	Off
Rotation	Off
X, Y	X Only (Recoat along the bead)
Alternating	Off
DMLS	Off
Pre-Exposure	Off
Up skin	Off (Thickness = 0)
Down skin	Off (Thickness = 0)
Beam expander	Automatic (Controlled by the software for Ti6Al4V)
Platform heating	35°C

6.1.6 Preparation and Evaluation of Single Beads and hatch spacing

To evaluate single beads and hatch spacing, optical microscopy was used (Olympus LEXT 3000 confocal microscope) to measure:

Table 26 - Sample evaluation (Yadroitsev et al., 2012)

Evaluated Feature	Sample view orientation	Equipment
Bead continuity,	Vertical on Z axis	Olympus microscope
Cracking and discolouration	Vertical on Z axis	Olympus microscope
(***h1***) Bead height.	Transverse section	Olympus microscope
(***h2***) Substrate penetration (depth of dilution area).	Transverse section	Olympus microscope
(***w1***) Bead width	Vertical on Z axis	Olympus microscope
(***w1***) Bead width	Transverse section	Olympus microscope
(***w2***) Width of the contact (dilution area).	Transverse section	Olympus microscope
Hatch spacing	Transverse section	Olympus microscope

An isometric view of the simple bead is shown in Figure 69, sowing the transvers sectional cut and respective directions of view required for evaluation.

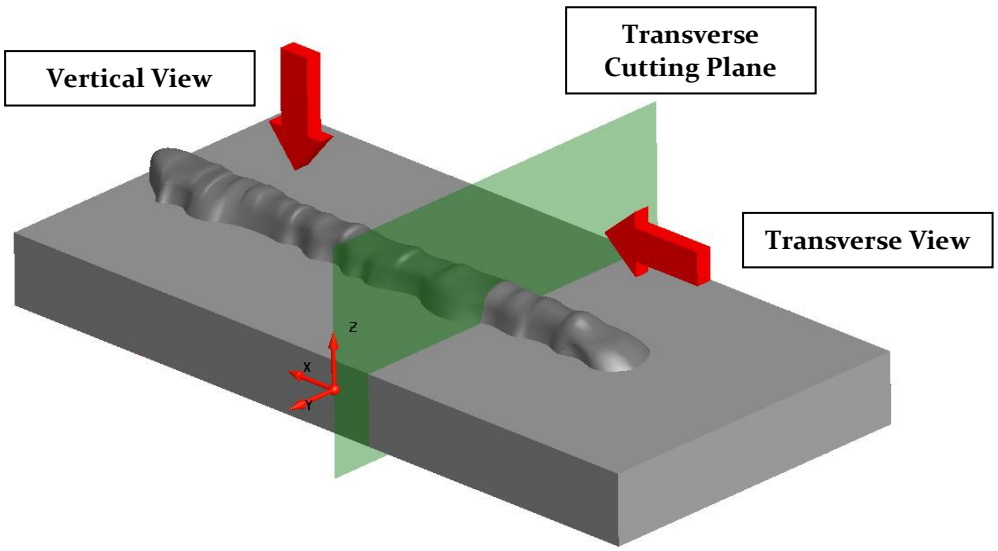

Figure 69 - Sample orientation, evaluation view and Transverse cutting plane

The Olympus LEXT 3000 confocal microscope is a confocal laser scanning system that uses a short wave 408nm violet light ray and preparatory image correction algorithms to improve reliability of sample measurement and image analysis (Olympus, 2020).

Figure 70 - Olympus LEXT 3100 confocal microscope, Olympus (2020)

Figure 70 shows the microscope and Herzan TS-150 Compact Desktop Active Vibration Control System (Herzan, USA) used to improve image accuracy and measurement confidence. Olympus LEXT-OLS software was used for the control of the microscope and the measurement of samples. The equipment was calibrated using a calibration procedure in accordance with the manufacturer's instructions and all measurements were conducted in a temperature-controlled environment at 20^{o}C. evaluation of: Bead continuity, Cracking, discolouration, and Vertical Bead width (***w1***) were conducted without additional sample preparation using 10 x magnification. Evaluation of transverse sections were carried out at 20 x magnification, after the samples were prepared by mounting and polishing.

6.1.6.1 Sample preparation for microscopy

Transverse sections of beads were cur using Wire Electro Discharge Machining (W-EDM) using an Execetek V650g shown in Figure 71, supplied by Warwick machine tools, UK.

Figure 71 - Execetek V650g, Warwick machine tools, UK (2020)

Samples were mounted in Struers PolyFast thermosetting Bakelite with carbon fibre using a Struers CitoPress-5 (Figure 72) and polished using a Struers LaboForce-100 (Figure 73) in accordance with the Struers Ti Alloys (DiaPro, Application Notes, appendix 1). Struers PolyFast was selected due to its high strength and suitability for SEM examination, samples were mounted using the following parameters (Table 27):

Table 27 - Struers PolyFast operating parameters, Struers, (2020)

Parameter	Setting
Heating temperature °C	180
Quantity (ml)	20
Heating time (min)	3.5
Heating pressure (bar)	250
Cooling time (min)	1.5
Cooling rate	high

Figure 72 - Struers CitoPress-5

Figure 73 - Struers Laboforce-100

6.2 Phase 1b: Baseline Assessment of Ti6Al4V Single Beads Evaluated Against Energy Density Results and Discussion

Samples produced using the L-PBF system were prepared and mounted, and images taken using a confocal microscope, a full set of images are presented in appendix 3. Optical microscopy proved suitable for sample measurement in this instance as SEM imaging would not have given a higher degree of accuracy, due to the nature of the test, transverse sections were taken at random positions, therefore, an alternative position would give alternative results. Results showing the width of beads viewed on the Z axis were validated by taking an average from five random positions along the bead, when plotted this presented a smoother progression of trend as opposed to the random transverse sections. It is hoped that this can be investigated with further research.

All single beads using Ti6Al4V powder exposed at 150 W showed evidence of miscibility with the substrate with good substrate penetration, along with an ability to form a continuous bead whilst maintaining a uniform width and height. The exception to this being the bead exposed at 2,000 mm/s, whilst there was substrate penetration and evidence of bead formation, it was clear that the progression of the laser produced a discontinuous bead, as shown in Figure 74. Due to the high scan speed, insufficient time is available to heat both the powder and substrate causing the molten powder to ball as described in chapter 2.2.9.

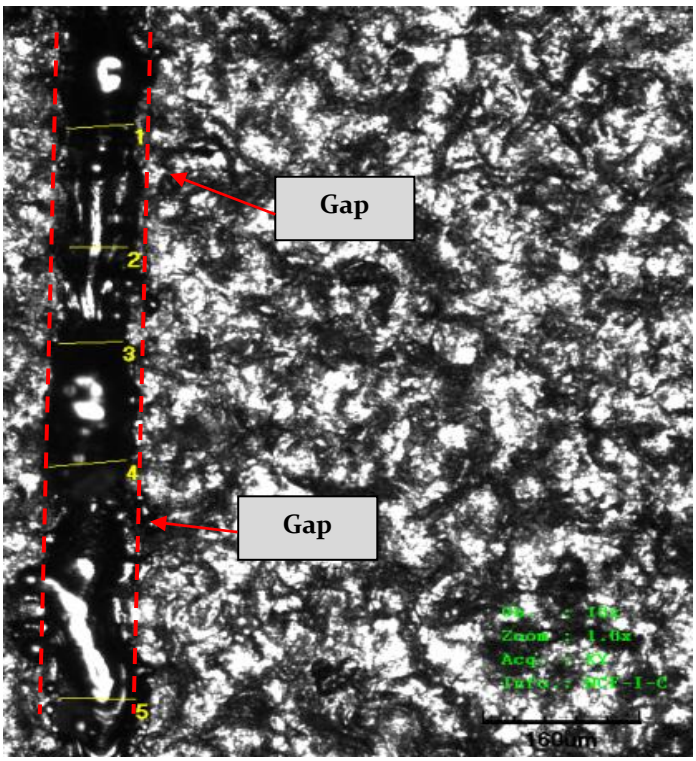

Figure 74 - Single Ti6Al4V Bead exposed at 2,000 mm/s showing evidence of sporadic exposure

it is also possible that the speed of the laser's movement could cause powder to be forced away from the meltpool (Khairallah, et al., 2016) producing the observed discontinuous bead shown in Figure 79a.

Ti6Al4V Vertical (10 x magnification)	Ti6Al4V Transverse (20 x magnification)	Results
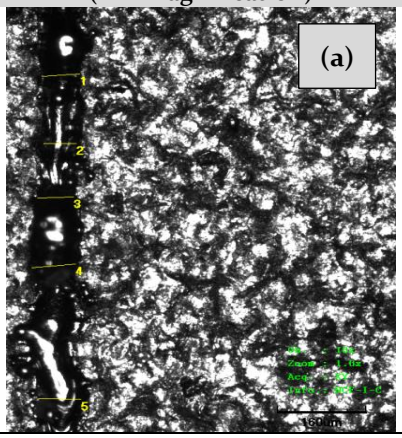	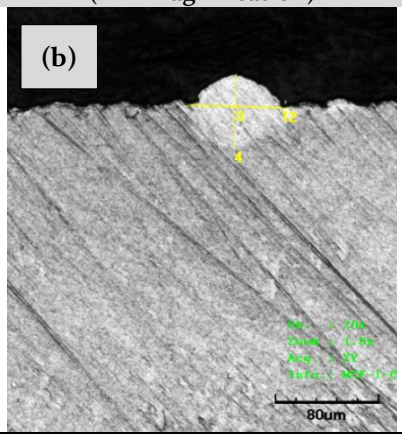	**Energy density** 25 J/mm³ **Scan speed** 2,000 mm/s **Mean bead width, vertical** 70.618 µm (σ 8.8 µm) **Bead continuity** Not continuous **Cracking and discoloration** No cracking or discoloration **h1 (Bead height)** 27.500 µm **h2 (Substrate penetration)** 33.756 µm **w1 (Bead width)** 72.543 µm **w2 (width of dilution area)** 82.521 µm

Figure 75 - Single Ti6Al4V Bead at 150 W laser power, 25 J/mm³ energy density

For single beads using Ti6Al4V powder exposed at 150 W, the best results were found in the range of 500 to 1,000 mm/s scan speed. As the scan speed increases, we can see a reduction in bead dimensions however, all bead heights were below 60 µm, there was no evidence of undercutting at the interface between the bead and substrate and levels of spatter appeared to remain similar. Figure 80 show the bead exposed at 667 mm/s scan speed with an energy density of 75 J/mm³, at this energy density level, substrate penetration is approximately twice that of the bead's height representing penetration of three previous layers approximately. Values for the mean bead with are also consistent with a standard deviation of 4.5 µm.

Ti6Al4V Vertical (10 x magnification)	Ti6Al4V Transverse (20 x magnification)	Results
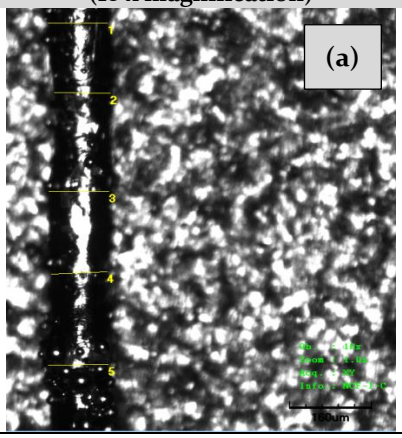	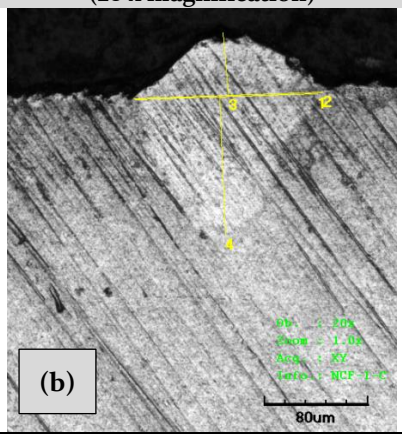	**Energy density** 75 J/mm³ **Scan speed** 667 mm/s **Mean bead width, vertical** 116.275 µm (σ 4.5 µm) **Bead continuity** continuous **Cracking and discoloration** No cracking or discoloration **h1 (Bead height)** 49.568 µm **h2 (Substrate penetration)** 108.838 µm **w1 (Bead width)** 145.066 µm **w2 (width of dilution area)** 150.085 µm

Figure 76 - Single Ti6Al4V Bead at 150 W laser power, 75 J/mm³ energy density

A full set of results can be found in appendix 3.

At 250 W, all single beads using Ti6Al4V powder showed evidence of miscibility with the substrate and ability to form a continuous bead maintaining a uniform width and height. The only exception to this being the bead exposed at 2,000 mm/s, whilst there was substrate penetration and evidence of bead formation, it was clear that the progression of the laser produced a discontinuous bead, as with those exposed at 150 W causing the balling phenomena. whilst the beads formed were acceptable they were mostly larger than the 60 µm height limit required for contact-free recoating, the exceptions to this being beads exposed at 1,000 (Figure 77) and 2,000 mm/s scan speeds (Figure 78) it can also be seen in (Figure 82a) how the bead has become discontinuous due to the elevated scan speed.

Ti6Al4V Vertical (10 x magnification)	Ti6Al4V Transverse (20 x magnification)	Results
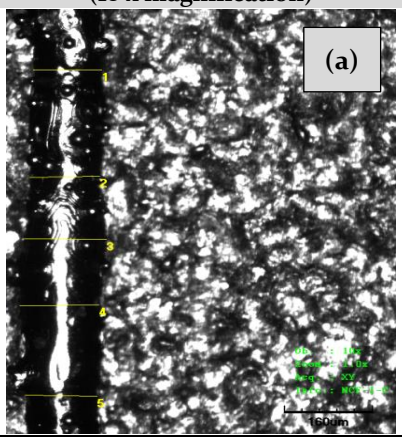	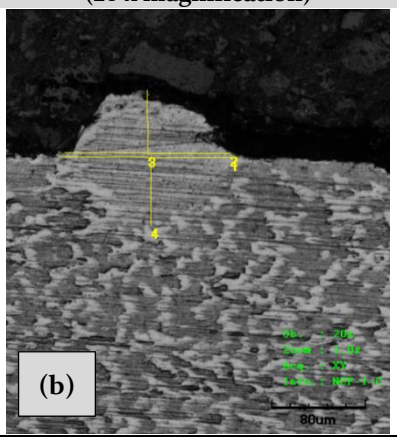	**Energy density** 83 J/mm³ **Scan speed** 1,000 mm/s **Mean bead width, vertical** 138.262 µm (σ 11.0 µm) **Bead continuity** continuous **Cracking and discoloration** No cracking or discoloration **h1 (Bead height)** 55.629 µm **h2 (Substrate penetration)** 60.625 µm **w1 (Bead width)** 150.001 µm **w2 (width of dilution area)** 145.001 µm

Figure 77 - Single Ti6Al4V Bead at 250 W laser power, 83 J/mm³ energy density

Ti6Al4V Vertical (10 x magnification)	Ti6Al4V Transverse (20 x magnification)	Results
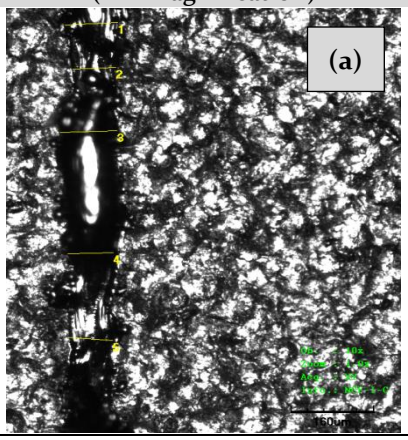	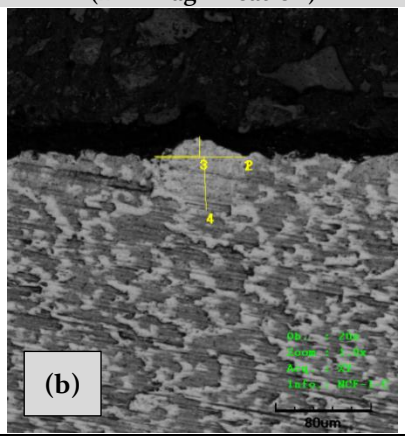	**Energy density** 42 J/mm³ **Scan speed** 2,000 mm/s **Mean bead width, vertical** 95.605 µm (σ 12.0 µm) **Bead continuity** Not continuous **Cracking and discoloration** No cracking or discoloration **h1 (Bead height)** 16.875 µm **h2 (Substrate penetration)** 45.039 µm **w1 (Bead width)** 75.003 µm **w2 (width of dilution area)** 77.503 µm

Figure 78 - Single Ti6Al4V Bead at 250 W laser power, 42 J/mm³ energy density

A full set of results can be found in appendix 4.

Exposed at 350 W, single beads using Ti6Al4V powder showed increased evidence of miscibility with the substrate and ability to form a continuous bead maintaining a

uniform width and height. Again, the only exception, being the bead exposed at 2,000 mm/s, whilst there was substrate penetration and evidence of bead formation, it was clear that the progression of the laser produced a discontinuous bead, as with those exposed at this scan speed and laser powers of 150 W and 250 W. the bead exposed at 2,000 mm/s was also the only bead capable of being lower in height than 60 µm suitable for contact-free recoating.

Across all three laser energy ranges there was evidence of spatter adhered to the surface of the beads, indicating a degree of volatility within the meltpools of subsequent beads, this however, was not excessive and therefore could be considered acceptable for this material. There was no evidence of balling around the bead, demonstrating thermal synergy between the feedstock, meltpool and substrate.

Regarding cracking, there was no evidence to show that cracks had propagated longitudinally or laterally on the beads surface. This was a clear indication that the material within the bead was sufficiently ductile to withstand the forces involved in solidification.

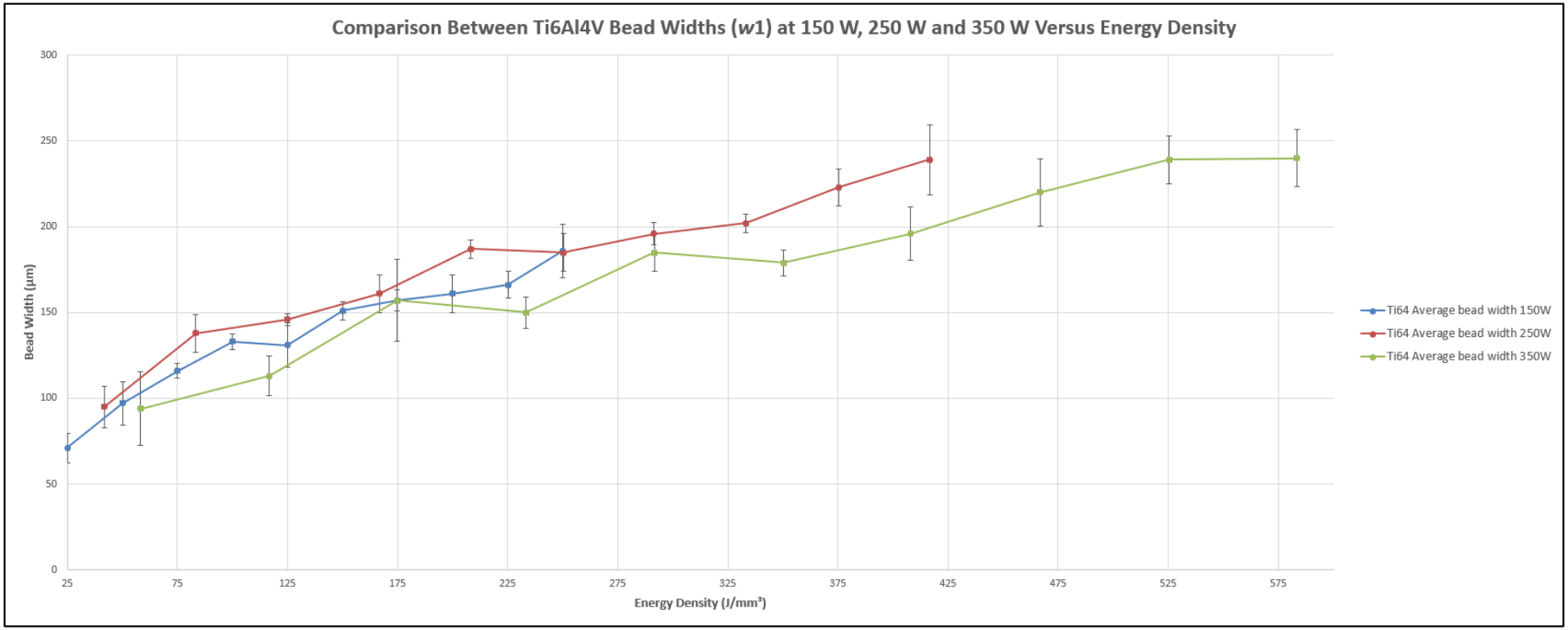

Figure 79 - Comparison Between Vertical Ti6Al4V Bead Widths (*w1*) at 150 W, 250 W and 350 W Versus Energy Density

Figure 79 shows the Comparison between Ti6Al4V Bead widths at 150 W, 250 W and 350 W versus energy density, displaying the calculated mean values from measurements taken in five places along the bead, viewed in the vertical axis with error bars representing ± 1σ. With respect to bead width, as the energy density is increased so does the width of the bead. As the range of scan speeds were identical as with layer thickness it is evident that the increase in laser power is influential in the increased consumption of feedstock thus producing a wider bead. The width of bead is unrestricted regarding how wide it can be, only influencing hatch distance, which should be calculated with bead width in mind, in order to produce the best parts (Yadroitsev, et al., 2013).

Whilst the width of bead is significant regarding its influence over hatch distance and therefore must be measured and taken into consideration when experimenting with multiple beads and multiple layers, bead height is far more crucial to processability. Due to the nature of feedstock delivery, contact-free recoating is essential. Contact with the laser melted surface results in ridges in the recoat surface from the recoat arm which become worse after each recoat leading ultimately to part failure.

Figure 80 shows comparison between Ti6Al4V bead heights (h_1) at 150 W, 250 W and 350 W versus energy density. It can be seen from the results that as with bead width, the bead height increases in size as a function of energy density. It was observed that for beads exposed at 150 W, the bead height remained below 60 µm. The value of 60 µm was chosen as a maximum cut-off value for bead height given the processes requirement for contact-free recoating. Given that the two-rail system was employed to produce beads with a layer thickness of ~45 µm to ~50 µm it would be conceivable that a bead height of ~75 µm to ~80 µm would contact the recoater blade given that the build plate would be lowered by 30 µm before recoating. A maximum bead height of 60 µm would therefore not contact the recoater blade and allow for ~20 µm variation.

Beads produced with 150 W laser power resulted in bead heights within the maximum height and could be taken forward for experimentation into hatch spacing (Phase 3c) and multiple layer evaluation (Phase 3d). as laser power is increased to 250 W and 350 W, most beads fail to remain within the 60 µm maximum due to the increased consumption of feedstock. Two values with a laser power of 250 W remained below 60 µm, having scan speeds of 1,000 mm/s and 2,000 mm/s. whilst the bead produced at 1,000 mm/s was of an acceptable quality the bead produced at 2,000 mm/s was found to have discontinuity and would therefore, not be of suitable quality. This was also found to be the case for beads exposed with a laser power of 350 W also. One bead was found to have a height of less than 60 µm, with a scan speed of 2,000 mm/s. this bead however, also exhibited evidence of discontinuity along the length of the bead.

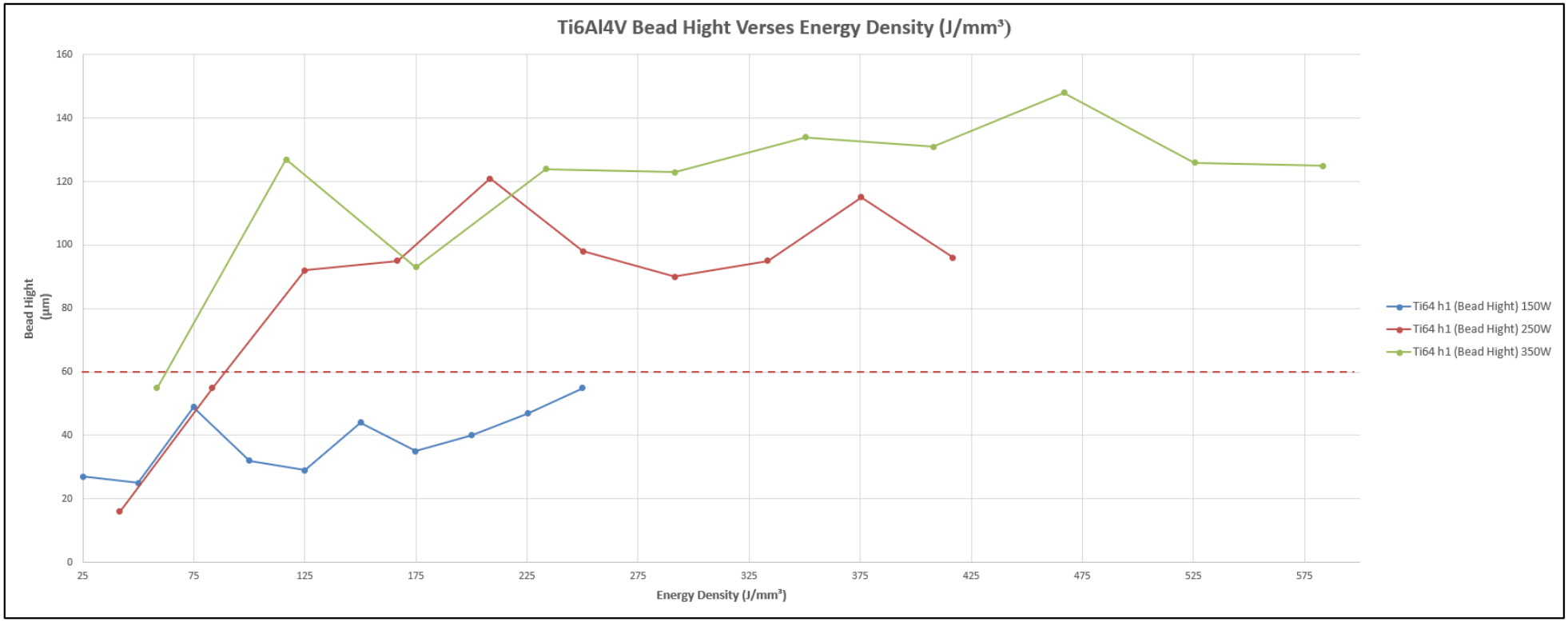

Figure 80 - Comparison Between Transverse Ti6Al4V Bead Heights (h_1) at 150 W, 250 W and 350 W Versus Energy Density

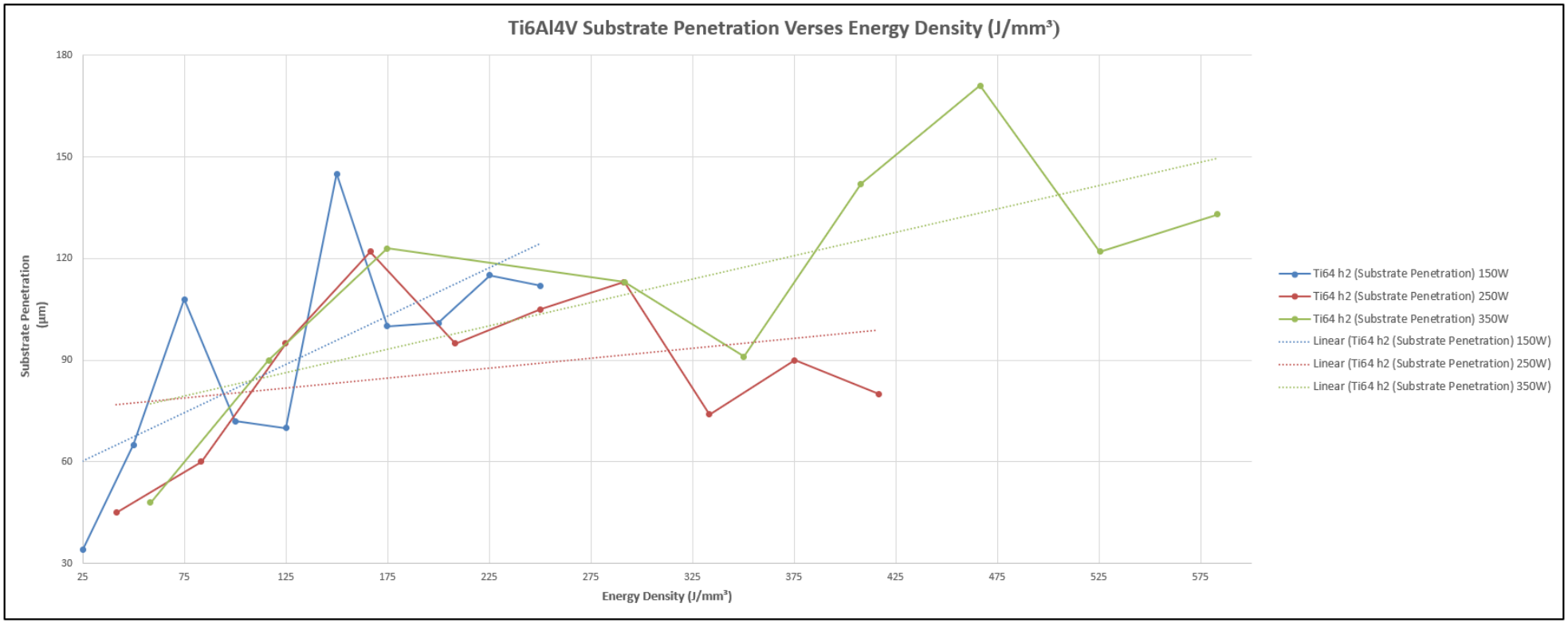

Figure 81 - Comparison Between Transverse Ti6Al4V Substrate Penetration (*h2*) at 150 W, 250 W and 350 W Versus Energy Density

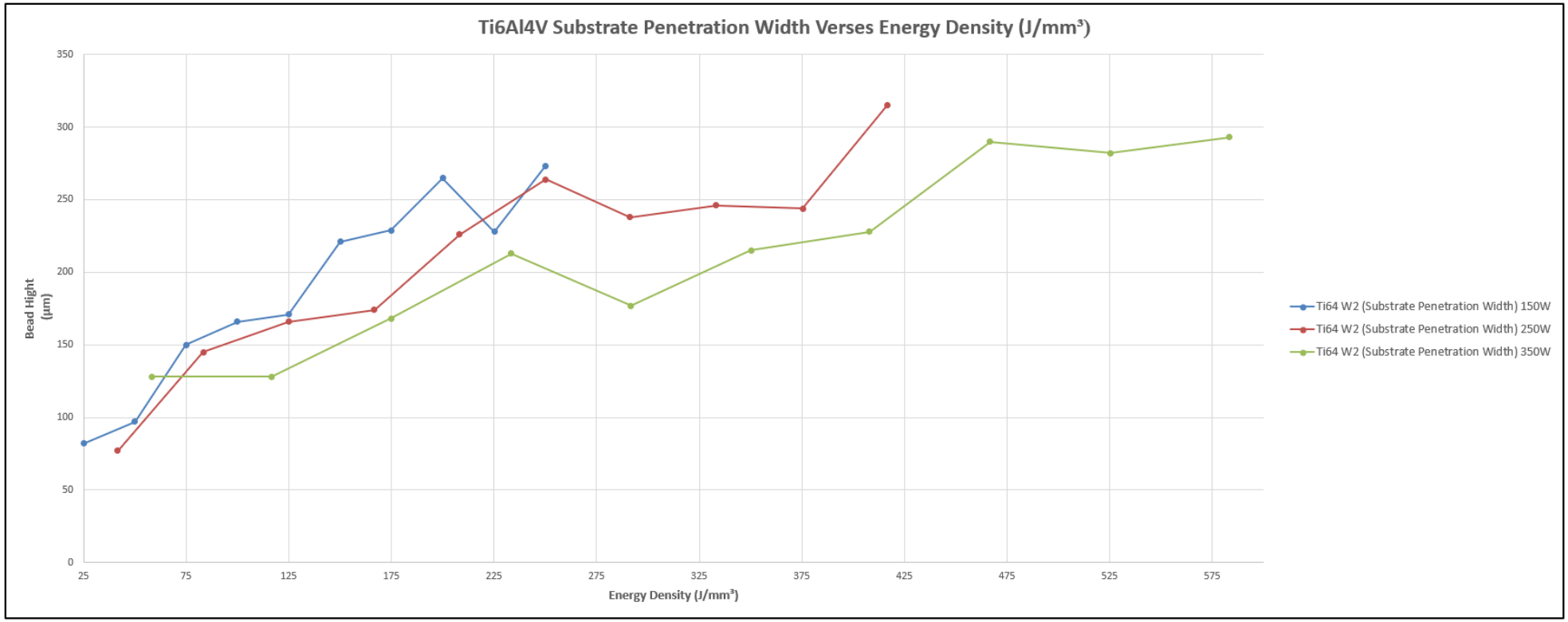

Figure 82 - Comparison Between Transverse Ti6Al4V Substrate Penetration Width (W_2) at 150 W, 250 W and 350 W Versus Energy Density

The values for substrate penetration (*h2*) shown in Figure 81, were circa 90 µm suggesting that with a laser power of 150 W the energy penetrates the substrate adequately, for a layer thickness of 30 µm this would equate to penetrating approximately three previous layers.

Increasing the laser power to 250 W had no additional effect on substrate penetration with a maximum depth of 122 µm at an energy density of 167 J/mm^3. As energy density increased from around 175 J/mm^3 to 325 J/mm^3, the depth of penetration remained between 65 µm and 100 µm deep. This suggested that the increase in energy density was having a greater effect on the surrounding feedstock and not the substrate. This is further supported by a steady increase in bead width (*w1*, Figure 79) and a marginal increase in bead height (*h1*, Figure 80). Similarly, an increase in laser power to 350 W showed a depth of penetration of 122 µm at an energy density of 176 J/mm^3 with subsequent measurements following the same trend as with a laser power of 250 W up to an energy density of 350 J/mm^3 where penetration increases to 171.893 µm. Bead height (*h1*) at these elevated energy densities remain constant, somewhat levelling off whist bead width (*w1*) maintained the same upward trend. It is therefore evident that the additional levels of energy do little to consume additional feedstock from the surrounding area, and therefore serve only to further penetrate the substrate.

Regarding the substrate penetration width (*w2*) (Figure 82) and the width of the bead (*w1,*Figure 79), it was observed that these measurements remained like each other in terms of width but also regarding trend. This suggested that by increasing laser power and therefore energy density, powder consumption around the meltpool and the width of dilution area increased simultaneously suggesting the two were interdependent. With little or no migration of the bead width beyond the dilution area it is evident that the flow of the melt pool is dependent on the molten substrate and is not free to flow across the substrate. Values used for the bead with (*w1*) were those taken from above, and the mean value used as opposed to the transvers sectional measurements that were single measurements and therefore less reliable. Values for h1, h2 and w2 were again less reliable due to challenges regarding the acquisition of multiple measurements, this is clearly evident of the erratic nature of the graphical representations. However, analysis shows clear trends that follow the increases in energy density and support the data presented. Future research will look into improved methodologies for the acquisition of multiple measurements along the bead both above and below the substrate.

6.3 Phase 1b: Baseline Assessment of Ti6Al4V Single Beads Evaluated Against Energy Density Conclusions

1 An approach for the evaluation and comparison of single beads was presented. Based across three laser power ranges (150 W, 250 W and 350 W) to evaluate a linear progression in energy density. The innovative approach enabled results to be better presented in comparison to the increased energy. In conclusion this method worked accurately and would provide a useful tool in the characterisation of new materials.

1.1 It was also concluded that this approach would work successfully on all metal platforms manufactured.

2 Mini platforms were developed and successfully utilised throughout this research, facilitating the economical use of smaller batch quantities of feedstock.

3 The two-rail system was developed to ensure that while conducting single layer characterisation, an accurate, reliable, and repeatable deposit of feedstock can be achieved, whilst this was developed for a square platform system with the recoater-arm type mechanism, the principle can be developed for all systems.

4 Results for Ti6Al4V single beads showed that as energy densities increased, so did the volume of the bead, that said however, it became evident that increased laser power contributed to a flatter bead and increased substrate penetration. Reduced scan speed contributed to a larger volume of bead with increased bead height.

4.1 It was concluded that the development of the methodology based on energy density was effective in characterising a range of energy densities that typified the feedstock investigated. Once established, the methodology was also able to successfully show the effect the main parameters had on the bead's formation for further development.

Chapter Seven

7.0 Phase 2a Development of the mechanical alloying process as a homogenous transportation mechanism for MMC feedstock

7.1 Phase 2a: Development of Mechanical Alloying Process as a Homogenous Transportation Mechanism for MMC Feedstock Methodology

7.1.1 Overview of The Mechanical Alloying Experiment / Design

MA was chosen to be explored as a method for combining reinforcement particles with matrix materials. This will allow the combined materials to be transported onto the build area for lasing using the machines recoater mechanism.

This section presents the research methodology to produce feedstock through the MA method.

Due to the forces involved during the MA process, the challenge was to embed reinforcement material onto the surface of the matrix material without significant deformation and to retain flowability, but also to achieve homogeneity within the feedstock. The feedstock was therefore, periodically evaluated and benchmarked against existing Ti6Al4V powder analysis results with respect to size and morphology.

The aim was to determine the length of mixing time required to embed the reinforcement before altering the morphology of the matrix material. The following objectives were set.

1. Embed reinforcement material onto the surface of the matrix material,
2. Minimise increase in particle size,
3. Minimise change in particles morphology,
4. Homogeneously mix the reinforcement material throughout the feedstock,
5. Avoid contamination.

7.1.2 Mechanical Alloying Variables for Surface Coverage by Reinforcement

The use of MA for AM is concerned with forcing the smaller sized particles of reinforcement material (SiC) onto the surface of the larger and softer matrix material

(Ti6Al4V). With this objective in mind, it is only theoretically possible to embed a single covering of reinforcement particles onto the surface of the matrix material before the surface becomes fully saturated, any remaining reinforcement material would therefore not become embedded but could remain present within the feedstock.

It was therefore the intention to accurately balance the volume ratio of reinforcement and matrix materials based on particle size, and to calculate an approximate value for the Maximum Volume of Reinforcement (MVR) at full saturation.

$$\mathrm{MVR} = \frac{\pi\ \mathrm{Dr}\ \mathrm{Dm}^2}{\pi\ \mathrm{Dr}\ \mathrm{Dm}^2 + \mathrm{Dm}^3}\ 100 \qquad \text{Equation 5}$$

Where: **MVR** is the Maximum Volume of Reinforcement material (%)

D_r is the average particle size ($X_{c\ min}$) of the reinforcement material (µm)

D_m is the average particle size ($X_{c\ min}$) of the matrix material (µm)

To calculate the MVR, Equation 5 was developed. The calculation expresses the total achievable percentage of reinforcement material that can be embedded into the surface area of the matrix material using the average particle sizes of the component materials.

From measurements taken, the average particle size for the matrix material (Ti6Al4V) is approximately 39.7 µm. This is atypical feedstock material currently used by the AM industry. The reinforcement material, however, can theoretically be any size. It is known from the work carried out by Tjong, Mai, (2008) and other researchers (Sivakumar, et al., 2016) that reducing the size of the reinforcement can significantly increase the strength of the composite. Tjong, and Mai, advocate the use of submicron reinforcement particulates and a reduced volume fraction of reinforcement. Much of the work within their 2008 paper used 10 vol.% (Volume by percent) reinforcement with positive results.

By using Equation 5 it is possible to determine the achievable volume of reinforcement based on average particle size.

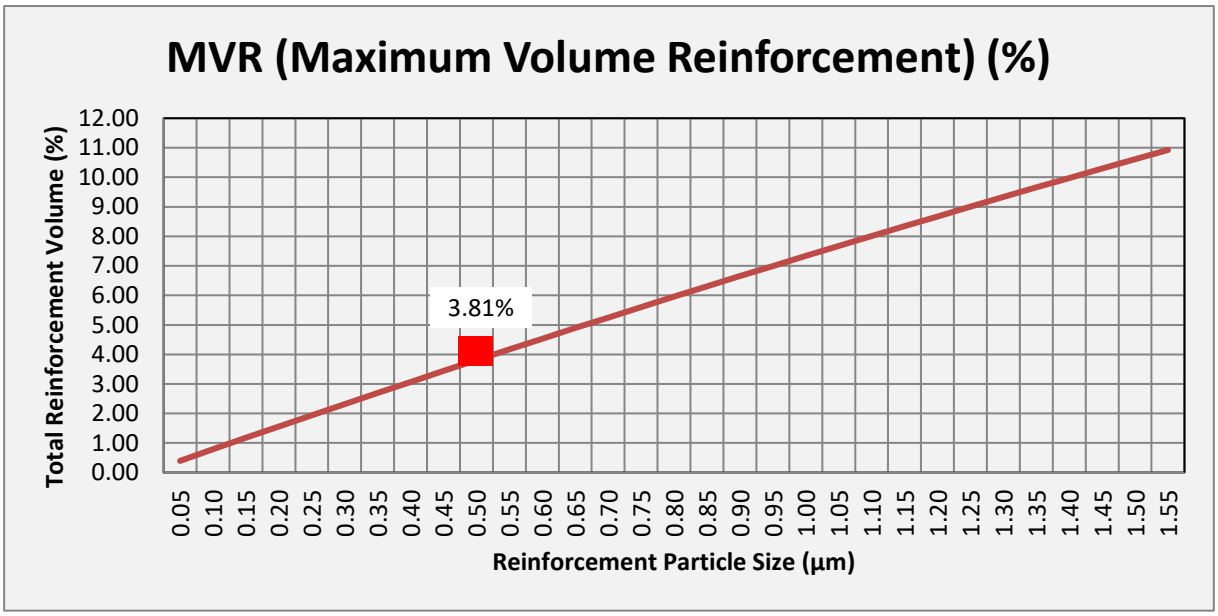

Figure 83 - MVR (Maximum Volume Reinforcement) (%)

Figure 83 shows how the size of the reinforcement particles has an impact on the final volume of reinforcement within the MMC. With an average particle size for the matrix material (D_m) of 39.7 µm and an average particle size for the reinforcement material (D_r) of 0.50 µm it was calculated using Equation 5 that 3.81 vol.% of reinforcement within the MMC could be achieved. This would be in line with Tjong and Mai's findings (Tjong, 2008).

7.1.2.1 Conversion from Volume Fraction to Weight Fraction of Reinforcement

Having calculated the volume fraction of reinforcement material (*f*) it is necessary to convert this to weight (g) to accurately measure out the materials. Firstly, the total density of the matrix material is calculated using Equation 6.

$$p = f * p_f + (1 - f) * p_m \qquad \text{Equation 6} \qquad \text{(Pilling, 2011)}$$

Where: **p** is the density of the MMC (g/cm³)

f is the Volume fraction of reinforcement material (%)

$\mathbf{p}_f$ is the density of the reinforcement (filament) material (g/cm³)

$\mathbf{p}_m$ is the density of the matrix material (g/cm³)

To accurately measure the reinforcement material (SiC) by weight it was necessary to convert the volume of reinforcement material to weight (g) using Equation 7.

$$f_w = \frac{f * P_f}{f * p_f + (1 - f) * P_m} \qquad \text{Equation 7} \qquad \text{(Pilling, 2011)}$$

Where: f_W is the weight fraction of reinforcement material (%)

f is the Volume fraction of reinforcement material (%)

$\mathbf{P}_f$ is the density of the reinforcement material (g/cm³)

$\mathbf{P}_m$ is the density of the matrix material (g/cm³)

Based on the maximum percentage of reinforcement (MVR) calculation, the calculation for quantities of component materials in relation to alloying balls can be seen in Figure 84.

Vol.% matrix (Ti6Al4V)	96.19	%	v_m	
Vol.% reinforcement (SiC)	3.81	%	v_r	f
Density of matrix material (Ti6Al4V)	4.42	g/cm³	p_m	
Density of reinforcement material (SiC)	3.21	g/cm³	p_f	
	$p = f * p_f + (1 - f) * p_m$			Equation 6
Calculated MMC Density	4.34	g/cm³	p	
weight of balls	2500	g		
Weight of powder required for milling	250	g	Balls to Powder Ratio = 10 to 1	

Convert from volume fraction of Reinforcement to weight of reinforcement

	$f_w = \frac{f * P_f}{f * p_f + (1 - f) * P_m}$			Equation 7
Wt.% reinforcement	0.02796	2.80	%	
Weight of reinforcement material	7.0	g		
Weight of matrix material	243.0	g		
Total weight of powder for milling	250.0	g		

Figure 84 - Powder Mixing Calculations

7.1.3 Mechanical Alloying Experimental Sample Size

250 g of feedstock comprising of 7.0 g of SiC powder and 243.0 g of Ti6Al4V powder was added to 2500 g stainless steel balls (4.75 mm Ø) as recommended by the equipment manufacturer (Zoz, Gmbh) to establish a ball to powder ratio of 10:1 by weight. The diameter of ball was selected due to the general size of powder particles. A rotation speed of 500 rev/min was chosen based on previous research (Lyall, et al., 2015) where samples were alloyed with rotational speed ranging from 300 rev/min up to 1200 rev/min for a fixed duration of twenty minutes. it was found that a rotational speed of 500 rev/min showed the best results for combining matrix and reinforcement materials without modification to shape characteristics. This was also found by authors Olowofela, et al., 2013 who chose a rotational speed of 450 rev/min for twenty minutes gave similar results.

Samples were alloyed for up to 40 minutes in an Ar atmosphere at a constantly maintained temperature of 20°C using the Zoz Symoloyer CM01 MA Machine supplied by Zoz GmbH.

Samples were extracted at 5 min, 8 min, 16 min, 24 min, 32 min, and 40 min intervals for analysis for size and shape.

On completion of analysis the most appropriate milling time was used to produce a full batch of feedstock for Phase 3, In process parameter characterisation of MMC feedstock.

7.1.4 Restrictions and limitations

Due to the available quantity of reinforcement material and the limited volume of material available per mill, it was only possible to take a small sample at each interval. Furthermore, this was kept to a minimum to avoid the risk of effecting the ball to powder ratio.

During processing, the Zoz Symoloyer CM01 monitored temperature but not O_2 levels, elimination of O_2 can only be achieved through the vacuum purge process and filling with an inert gas (Ar), the purge process was repeated twice in this instance.

7.1.5 Mechanical Alloying Equipment

The pre-process feedstock production equipment used is shown in Figure 85 and included the following items of equipment (Table 28):

Table 28 - MA equipment and suppliers

Equipment	Model	Supplier
Symoloyer attrition mill	CM01	Zoz GmbH
Maltoz computer software		Zoz GmbH
Haake phoenix ii chiller	C40P	Fisher Thermo Scientific
Edwards vacuum pump	RV 12	Edwards UK
Edwards vacuum meter and gauge	APG-M-NW16 Al Active Pirani vacuum gauge with AGD AIM magnetron gauge	Edwards UK
Argon gas supply	N/A	N/A
Sample containers	500 ml KF glass container	Zoz GmbH
Weighing scales	N/A	N/A

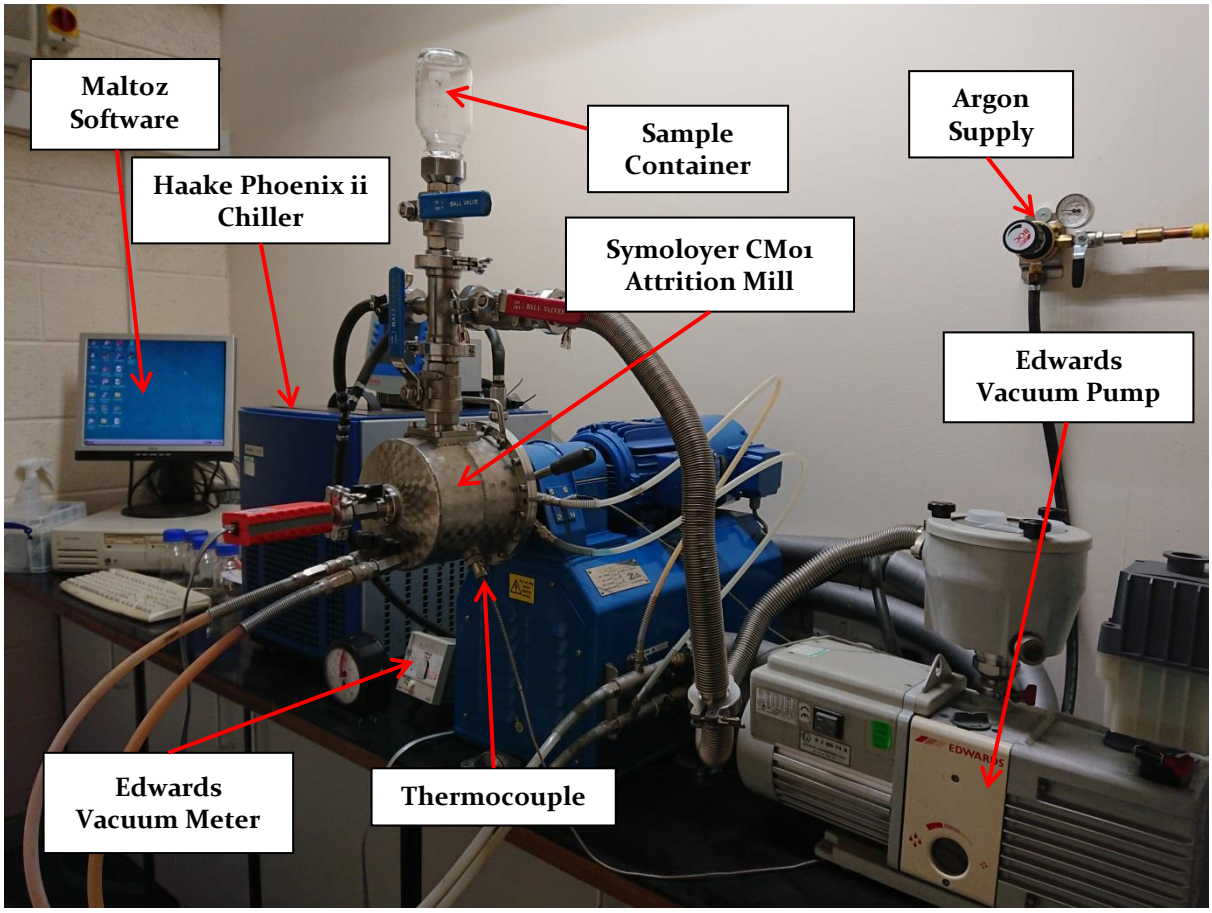

Figure 85 - Mechanical Alloying Equipment

Figure 86 shows a more detailed view of the Symoloyer CM01. The milling chamber, detailed is locked into position (as shown) during milling and can be rotated through 180 degrees to enable samples to be taken at stages during the process.

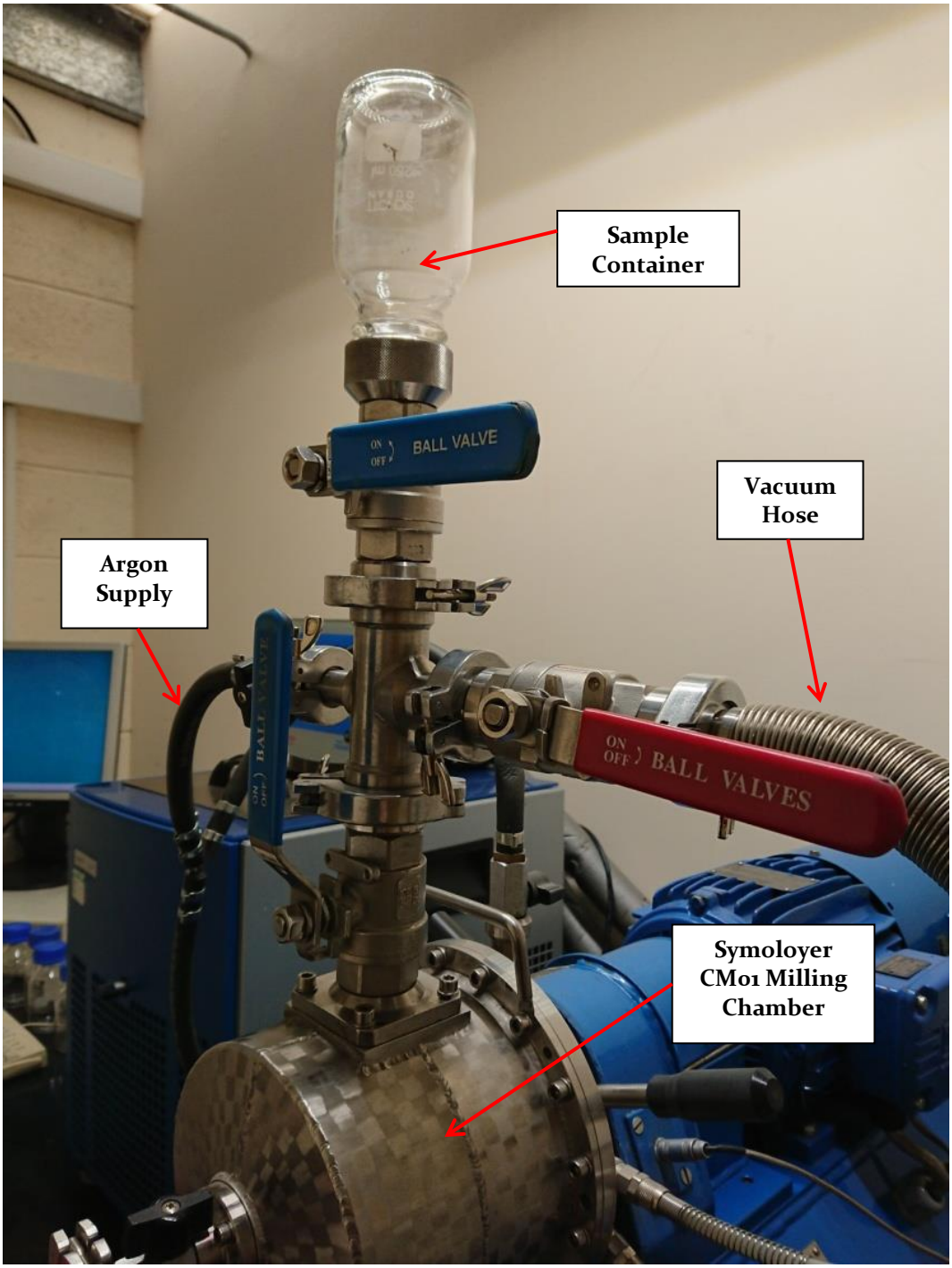

Figure 86 - Symoloyer CM01 Detailed View

Control of temperature during the milling process was carried out by the Haake phoenix ii chiller unit (Figure 87) utilising the Simoloyer's double wall system to maintain the milling environment at 20°C.

Figure 87 - Haake Phoenix ii Chiller Unit

7.1.6 MA Process Contamination Risk

Risk of contamination is high with the MA equipment due to the abrasive nature of the powders used and the prolonged processing time. MA for PBF is significantly different in that the times employed are considerably shorter and the risk of contamination is therefore reduced. The liberation of materials from the chamber walls, alloying balls, and rotor shaft still present risk of contamination though. The rotor shaft tends to mushroom on the ends where continued impacts displace material with the risk of fragmentation, this was removed and inspected for loose fragments of metal liable to detach during processing and was cleaned thoroughly as were the chamber and alloying balls.

To ensure that the atmosphere was free from O_2 whilst processing, the powders were stored in a non-humid atmosphere at room temperature. Prior to processing the chamber was purged of Air under vacuum and the atmosphere was replaced with Ar gas and the contents of the chamber was rotated at 20 rev/min to agitate and remove trapped Air. The atmosphere was again removed under vacuum and replaced with Ar before starting the process (see appendix 1).

7.1.7 Procedures

In accordance with the manufacturer's instructions, all the equipment was cleaned with isopropanol and checked for damage from previous use. The stainless-steel balls (2500 g) were cleaned and allowed to dry then placed into the milling chamber along with 250 g of feedstock comprising of 7.0 g of SiC and 243.0 g of Ti6Al4V powders.

The milling chamber was sealed and the sample container positioned vertically as shown in Figure 86, and the air was removed using the Edwards vacuum equipment, care was taken to use a low setting to avoid removing feedstock, air was removed until a vacuum reading of 10^{-3} mbar was reached measured using the Edwards AGD Pirani gauge attached to the front of the milling chamber. The chamber was then filled with Ar gas at 1 bar (14.5 PSI) the rotor shaft was then rotated at 20 rev/min for 10 seconds using the Maltoz 3.2 software. The purge process was repeated once more.

Using the Maltoz 3.2 software the equipment was run at 500 rev/min for 5 min, 8 min, 16 min, 24 min, 32 min, and 40 min intervals where upon samples were taken for analysis of size and shape at each duration.

7.2 Phase 2a: Development of Mechanical Alloying Process as a Homogenous Transportation Mechanism for MMC Feedstock Results and Discussion

MMC feedstock was mechanically alloyed in accordance with the criteria specified in chapter 7.1, with the aim to determine the length of mixing time required to embed the reinforcement before altering the morphology of the matrix material. The objectives were:

1. Reinforcement material embed onto the surface of the matrix material.
2. Minimise increase in particle size.
3. Minimise change in particle morphology.
4. Homogeneously mix the reinforcement material throughout the feedstock.
5. Avoid contamination.

Samples were extracted at 5 min, 8 min, 16 min, 24 min, 32 min, and 40 min intervals for analysis.

7.2.1 Reinforcement Material Embed onto the Surface of the Matrix Material

Using a SEM, images were analysed to determine the extent of surface coverage by the reinforcement and the degree of embedment into the surface of the matrix material in comparison to the non-mechanically alloyed Ti6Al4V material.

Using SEM images of the Ti6Al4V virgin powder for reference, (Figure 88a, c, e), images of the MA powders were compared. At 1,000 x magnification it was observed that a light coating of SiC had been deposited on to the surface of the Ti6Al4V powder particles (Figure 88b). the coverage appeared to be even across all Ti6Al4V particles within the image. However, evidence of unalloyed SiC powder was also visible.

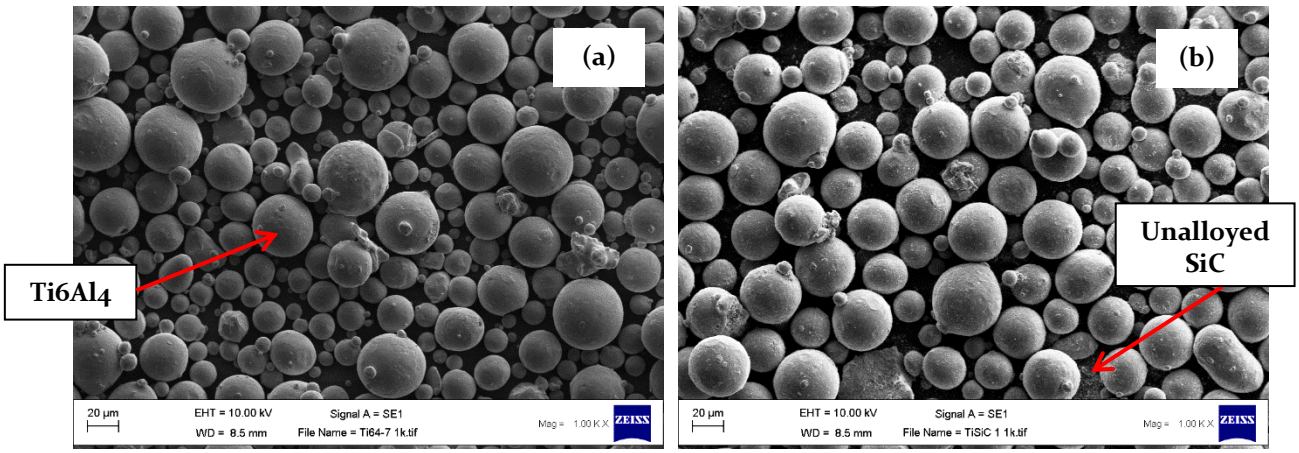

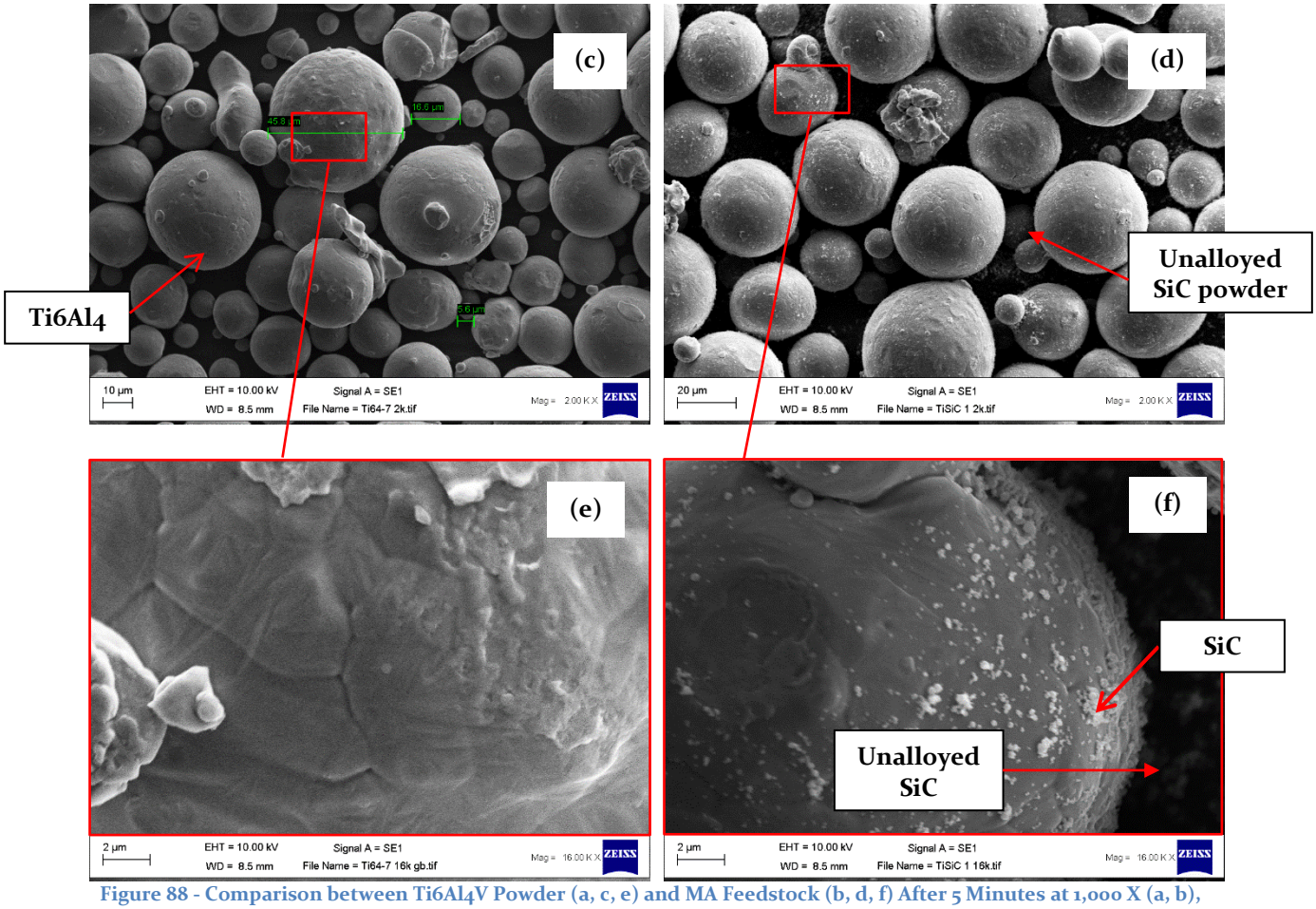

Figure 88 - Comparison between Ti6Al4V Powder (a, c, e) and MA Feedstock (b, d, f) After 5 Minutes at 1,000 X (a, b), 2,000 X (c, d) and 16,000 X Magnification (e, f).

At 2,000 x magnification (Figure 88d), it was clearer that only partial coverage of the Ti6Al4V powder particles had been achieved. This was further confirmed at 16,000 X magnification (Figure 88f). There was no evidence of changes to the morphology of the matrix particles. There was scope for further processing to increase embedded percentage.

The feedstock was mechanically alloyed for a total of eight minutes and analysed using the SEM. At 2,000 x magnification it was observed that more SiC had coated the surface of the Ti6Al4V powder particles (Figure 89a). It was further observed that the coverage of SiC was not even across all Ti6Al4V particles but appeared to be thicker on some as shown in Figure 89b. However, there was less evidence of unalloyed SiC powder, this indicated that at eight minutes of alloying the there was still a lack of homogeneity within the feedstock.

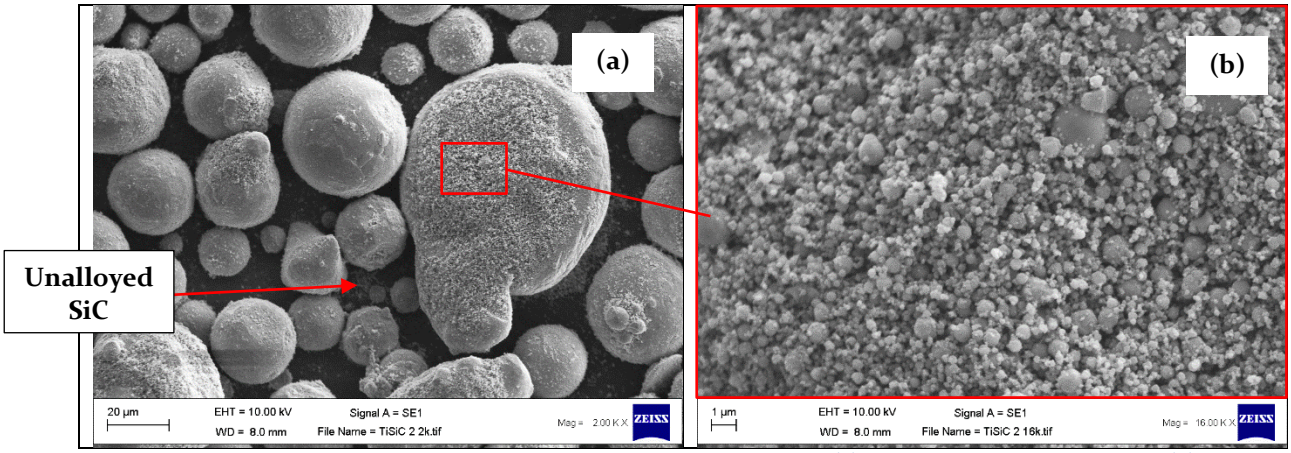

Figure 89 - MA Feedstock After 8 Minutes at 2,000 X Magnification (a) and at 16,000 X Magnification (b).

After sixteen minutes of alloying a sample was taken and analysed using SEM. At 2,000 x magnification it was observed that the coating of SiC had become more consistent and uniform on the surface of the Ti6Al4V powder particles (Figure 90a). there appeared to be a moderately high number of rounded particles remaining however, the number of agglomerated particles was now increasing and leading to flattened or flake like particles that could hinder the PBF process.

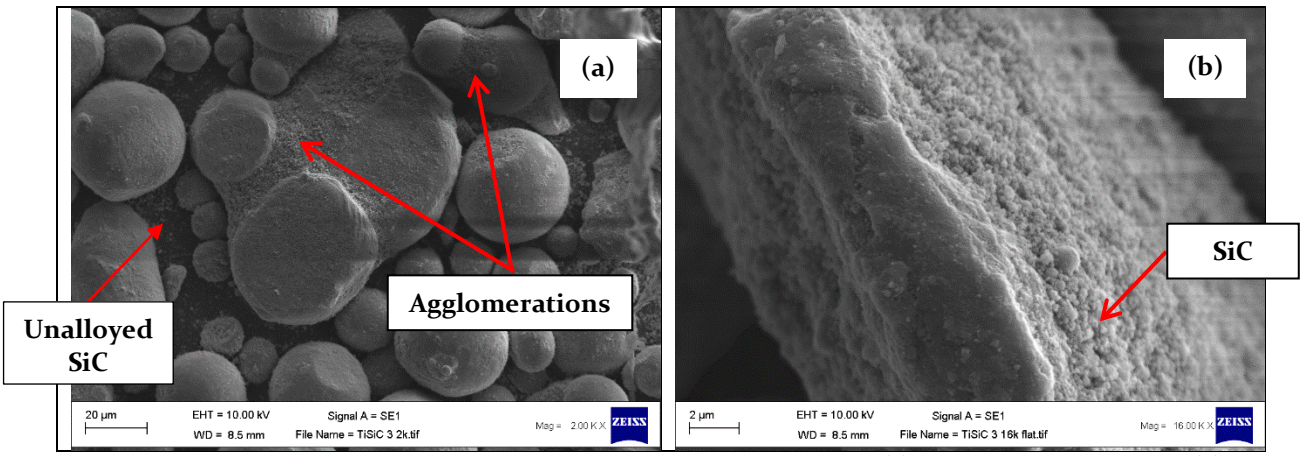

Figure 90 - MA Feedstock After 16 Minutes Compared at 2,000 X Magnification (a) and 16,000 X Magnification (b).

At 16,000 x magnification it was observed that the SiC particulates adhered to agglomerated particles around the areas where the two particles had joined. It is thought that the SiC is adhering to coarser surfaces. It was also commonly observed across such areas that the SiC particles are shielded from other larger particles, suggesting that whilst the SiC is coating the Ti6Al4V, it is subsequently being removed by impacts as particles rub together.

Figure 91a and b show the feedstock after twenty-four minutes. At 1,000 x magnification the image shows an even coating of SiC on to the surface of the Ti6Al4V powder particles. Flat or flake like deformed particles were observed along with other irregular shaped particles.

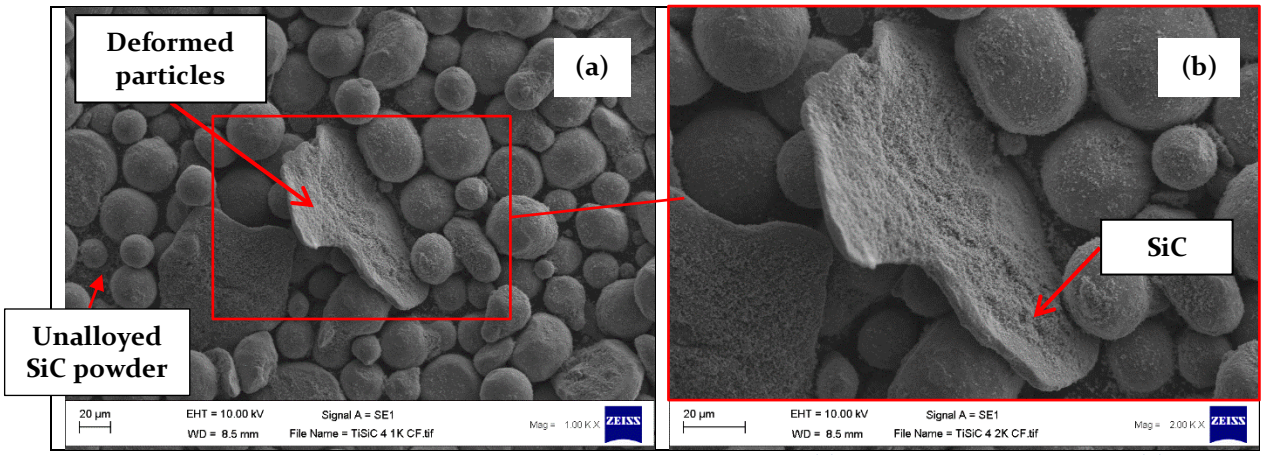

Figure 91 - MA Feedstock After 24 Minutes at 1,000 X Magnification (a) and at 2,000 X Magnification (b).

At a magnification of 2,000 x (Figure 91b), it was clearer that a better coverage of the Ti6Al4V powder particles had been achieved. There was no evidence of the SiC preferentially adhering to selective regions of agglomerates, this would indicate that the SiC had better fixation to the Ti6Al4V powder surface. This would provide a higher level of confidence that the SiC would be transported successfully within the PBF process to achieve a homogeneous distribution. At twenty-four minutes of processing, there was good evidence of successful coverage and a lack of excessive deformation.

The process was continued until thirty-two minutes to determine the effects of prolonged alloying. At 1,000 x magnification (Figure 92a), it was observed that the coating of SiC was no better than at twenty-four minutes, there was however, an increase in deformed particles in the form of cylindrical particles, flat discs, and flakes.

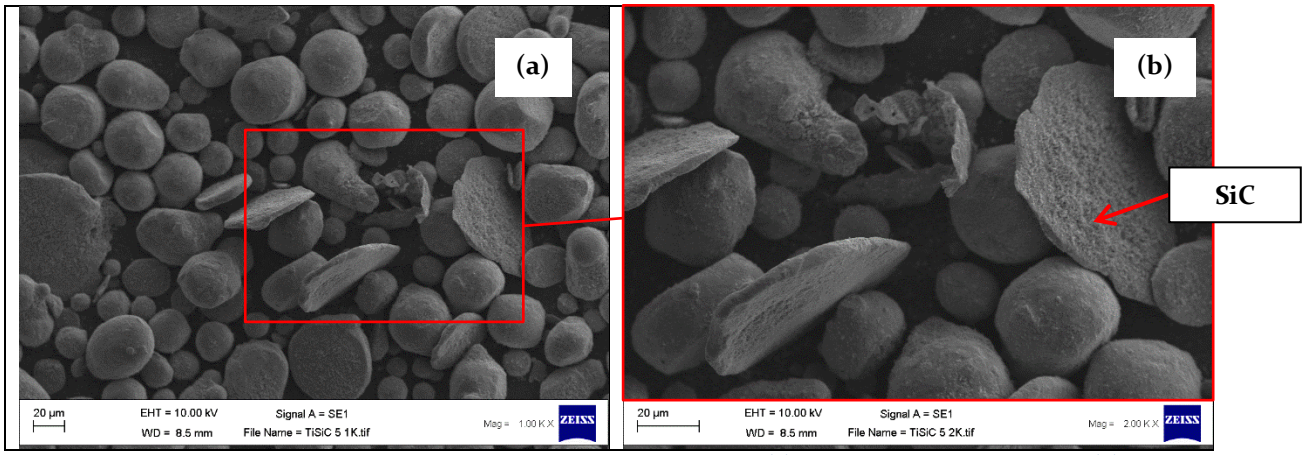

Figure 92 - MA Feedstock After 32 Minutes at 1,000 X Magnification (a) and at 2,000 X Magnification (b).

At 2,000 x magnification (Figure 92b), it was clearer that prolonged processing lead to more deformed particles whilst achieving no additional coverage of SiC.

At forty minutes of processing, visual evidence by SEM showed no increase in surface coverage of SiC and continued deformation of particles. At 1,000 x magnification (Figure 93a) it can be observed that the coating of SiC had not changed significantly since the observations taken after twenty-four minutes. The coverage of SiC and the deformed particles can be clearly seen. At 2,000 x magnification (Figure 93b), there is good evidence that there is nothing to be gained by proceeding with further alloying.

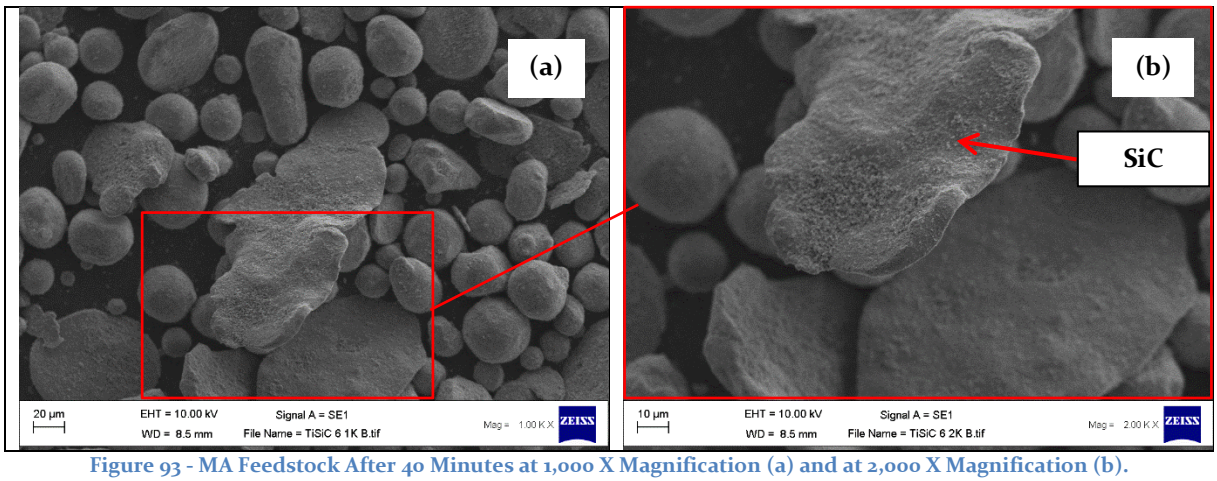

Figure 93 - MA Feedstock After 40 Minutes at 1,000 X Magnification (a) and at 2,000 X Magnification (b).

Characterisation of these particles found seven distinct shape characteristics:

1. Rounded,
2. Non-rounded,
3. Cylindrical,
4. Flattened,
5. Agglomerated,
6. Cleaved agglomerated,
7. Flattened agglomerated.

From the optical results, evidence showed that as the MA process progressed the morphology of the powder changed. Beginning with simple rounded particles, single impacts produced a non-rounded particle leading to flattened particles. Cylindrical particles were produced where particles were forced to roll in a single direction around the processing chamber, applied forces leading to cylindrical forms being produced.

7.2.1.1 Rounded Particles

All samples exhibited rounded particles (Figure 94), the degree of roundness across the sample reduced as the powder was processed for longer periods of time.

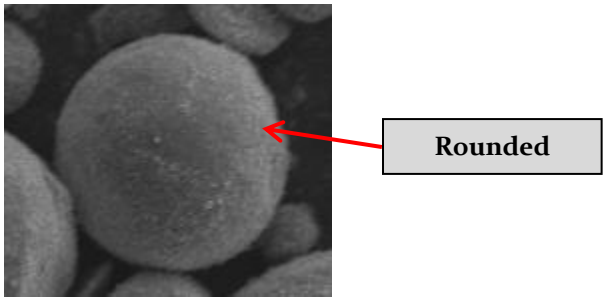

Figure 94 - Rounded Powder Particle (SEM 1,000 X Magnification, Thirty-Two Minutes Processing)

7.2.1.2 Non-rounded particles

It was evident that as the processing continues the powder particles are deformed in stages. A single impact produces a small flat area on the particle (Figure 95).

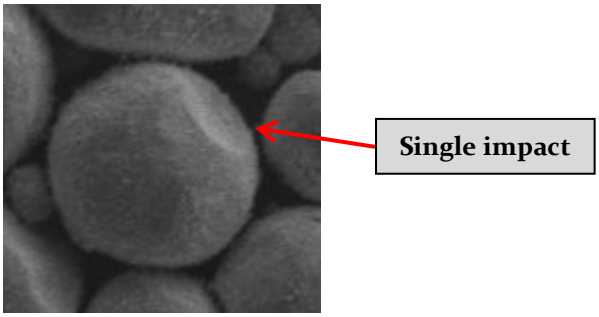

Figure 95 - Single Impact on Powder Particle (SEM 1,000 X Magnification, Thirty-Two Minutes Processing)

As these impacts multiply, particles become less rounded or non-rounded leading to become disks or flake-like in appearance.

7.2.1.3 Cylindrical Particles

Cylindrical particles were characterised as being formed by particles that are forced to travel around the processing chamber walls (Figure 96).

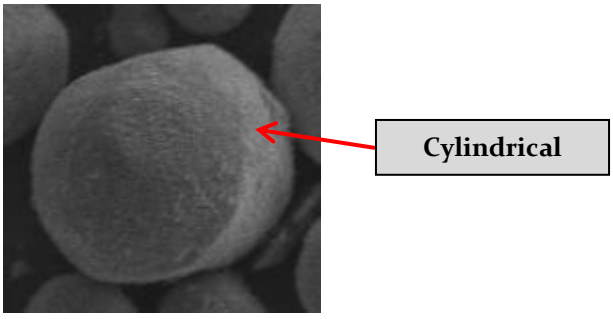

Figure 96 - Cylindrical Ti6Al4V Powder Particle (SEM 1,000 X Magnification, Thirty-Two Minutes Processing)

To maintain roundness, particles must adopt a random path with applied force to all areas of the particles surface, however, due to the configuration of the Zoz Simoloyer CM01, this is not possible for short processing times. Within the grinding chamber, the rotor shaft does not reach to the inside surface of the chamber, therefore a proportion of the powder batch can form a moving layer around the chamber wall held in place by the bulk of the powder being processed and the processing balls. This unidirectional path can produce cylindrically shaped particles (Figure 97). Prolonged processing would make this phenomenon worse. It is suggested that a short five second pauses in the process may help to randomise the chamber contents and reduce the number of cylindrical particles, this could also be achieved by changing the direction.

It is also important to note that a relatively low rotor shaft speed of 500 rev/min was selected in order to minimise centrifugal forces and reduce the likelihood of producing cylindrical particles. This is in line with previous research (Olowofela, et al., 2013 and Lyall, et al., 2015) which concluded that 500 rev/min was the maximum rotor shaft speed capable of maintaining spheroids.

7.2.1.4 Flattened Particles

The production of flatten particles marked a significant point in the MA process. At this point, particles had been produced that would not flow within the PBF process and furthermore would not pack optimally on the powder bed. The flattened particles are produced as a result of high levels of impacts from the milling balls and a direct result of prolonged processing times.

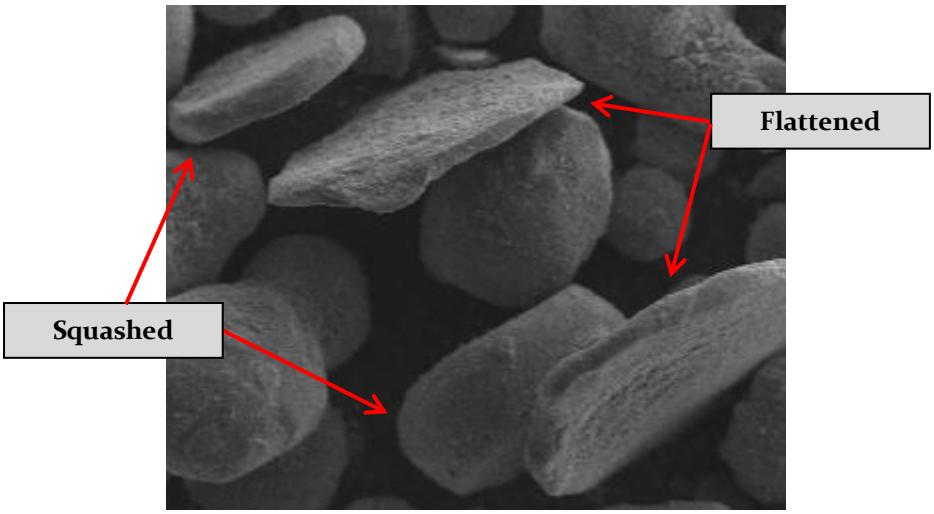

Figure 97 - Flattened Powder Particle (SEM 1,000 X Magnification, Thirty-Two Minutes Processing)

Figure 97 shows flattened particles after thirty-two minutes of processing. The particles inability to rotate within the chamber in combination with multiple impacts, firstly produced a squashed sphere, leading to flattened particles.

7.2.1.5 Agglomerated Particles.

There was a lower-than-expected level of agglomerated particles. It is thought that as the Ti6Al4V particles become coated with SiC and two particles are forced together, the SiC coating prevents them from adhering to each other and a flat surface is produced on the particles instead, evident in Figure 95.

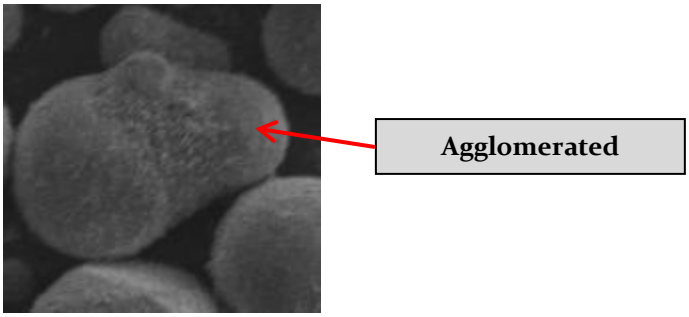

Figure 98 - Agglomerated Powder Particles (SEM 1,000 X Magnification, Thirty-Two Minutes Processing)

Figure 98 shows agglomerated particles joined prior to being coated with SiC, it is evident for samples taken at sixteen minutes processing time, that the thinner necked region of the agglomeration protected the SiC reinforcement material from being subsequently wiped from the surface by other particles.

7.2.1.6 Cleaved Agglomerated Particles

Possible fracture surfaces were also observed (Figure 99) on some particles indicating areas where particles had been cleaved apart.

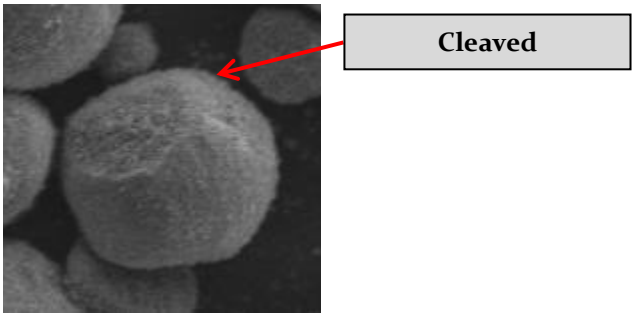

Figure 99 - Cleaved Agglomerated Powder Particle (SEM 1,000 X Magnification, Thirty-Two Minutes Processing)

This indicated that particles that had become united earlier in the processing time had become detached as a result of prolonged processing.

7.2.1.7 Flattened Agglomerated Particles

Evidence was also shown of agglomerated particles that had subsequently become flattened due to the prolonged processing time. In Figure 100 it can be seen where two additional particles of Ti6Al4V have combined to an existing particle and have subsequently become flattened over prolonged processing time.

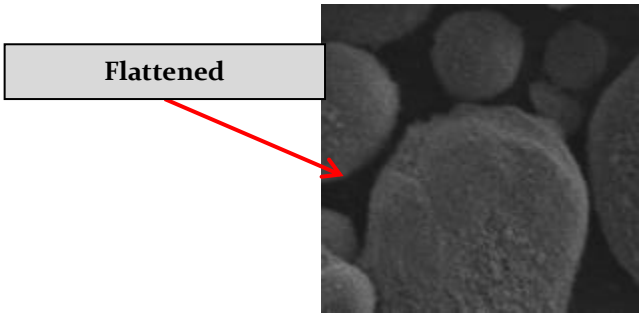

Figure 100 - Flattened Agglomerated Ti6Al4V Powder Particle (SEM 1,000 X Magnification, Thirty-Two Minutes Processing)

In conclusion, from a microscopic investigational point of view, this evidence reinforces the decision that a processing time of twenty-four minutes was adequate to embed the reinforcement material into the surface of the matrix material without excessive damage to the morphology of the matrix material. Sieving was considered as a possible solution to the removal of large particles from the feedstock however, evidence showed that these became prevalent only after twenty-four minutes of processing and should the process be halted at this time, the risk of large particles would be minimised.

7.2.2 Minimise Increase in Particle Size

To determine the effect of alloying time on particle size from the MA process, samples taken at regular intervals were analysed using a Retsch Camsizer X2. Table 29 shows results for X_c min measurements calculated for Q3 10 %, Q3 50 % and Q3 90 % with the sample mean represented by Mv3($\bar{x}$). samples were also analysed for aspect ratio (Mean b/l3) to determine whether this increased over time, indicating a loss of roundness.

Table 29 - Volume Based Distribution Analysis Comparison for MA Feedstock ($x_{c\,min}$)

Statistical measurement	Ti6Al4V Baseline	MA feedstock 5 min	MA feedstock 8 min	MA feedstock 16 min	MA feedstock 24 min	MA feedstock 32 min	MA feedstock 40 min	σ
Q3 10 %	28.8 µm	21.4 µm	22.8 µm	20.6 µm	23.5 µm	24.5 µm	21.8 µm	2.5 µm
Q3 50 %	39.9 µm	35.7 µm	37.0 µm	37.1 µm	37.7 µm	38.4 µm	36.0 µm	1.3 µm
Q3 90 %	49.9 µm	46.8 µm	48.5 µm	51.3 µm	53.4 µm	50.9 µm	49.5 µm	2.0 µm
Mv3($\bar{x}$)	39.7 µm	35.0 µm	36.6 µm	38.2 µm	39.7 µm	39.1 µm	38.5 µm	
Sigma 3 ($\bar{x}$)	9.7 µm	10.8 µm	11.3 µm	27.6 µm	20.1 µm	15.0 µm	29.8 µm	
Mean b/l3	0.851 $\overline{AR}$	0.870 $\overline{AR}$	0.859 $\overline{AR}$	0.838 $\overline{AR}$	0.819 $\overline{AR}$	0.807 $\overline{AR}$	0.825 $\overline{AR}$	

The results from Table 29 were collated as a graph shown in Figure 101.

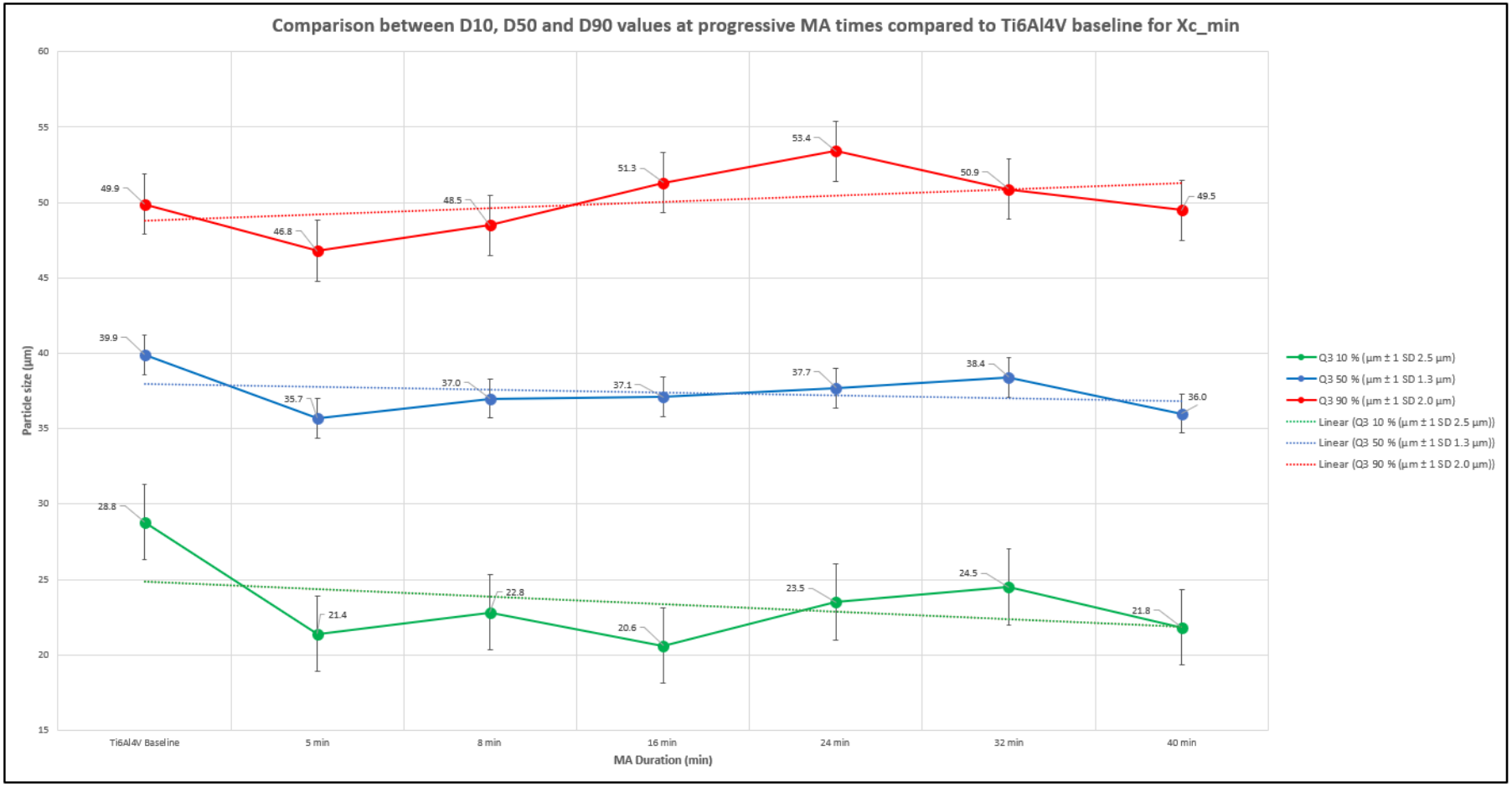

Figure 101 - Comparison between D10, D50 and D90 values at progressive MA times compared to Ti6Al4V baseline for Xc_min

It was observed from the results in Figure 101 that the MA samples all demonstrated similar values for Q3 10 % (D10), all values being less than the Ti6Al4V baseline sample, showing average particle sizes between 21.4 μm and 24.5 μm as opposed to 28.8 μm for the Ti6Al4V baseline sample. This would indicate a smaller particle size overall, indicative of non-alloyed SiC powder present within the sample. As this becomes alloyed to the larger Ti6Al4V particles this size increases, tending towards the baseline value, however, at 24 minutes this trend begins to regress once more suggesting the SiC particles are being removed. The results at 16 minutes suggest that it is at this point that SiC is successfully being bonded to the Ti6Al4V.

The Q3 90 % (D90) value is increasing above that of the Ti6Al4V baseline result, from 16 minutes indicating an increased volume of larger particles in the samples, indicating that whilst there appears to be no loss of small fines, the larger fines are increasing in size due to being coated with SiC. It has been established that the Retsch Camsizer X2 has difficulty measuring submicron particles and therefore, even though the Vol.% of small particles remains unchanged the Ti6Al4V particles are being coated. At 24 minutes the results indicate that the maximum amount of coating has been reached, further experimentation for 32 and 40 minutes showed a decrease in the values for Q3 90 % indicating that no further coating is being applied.

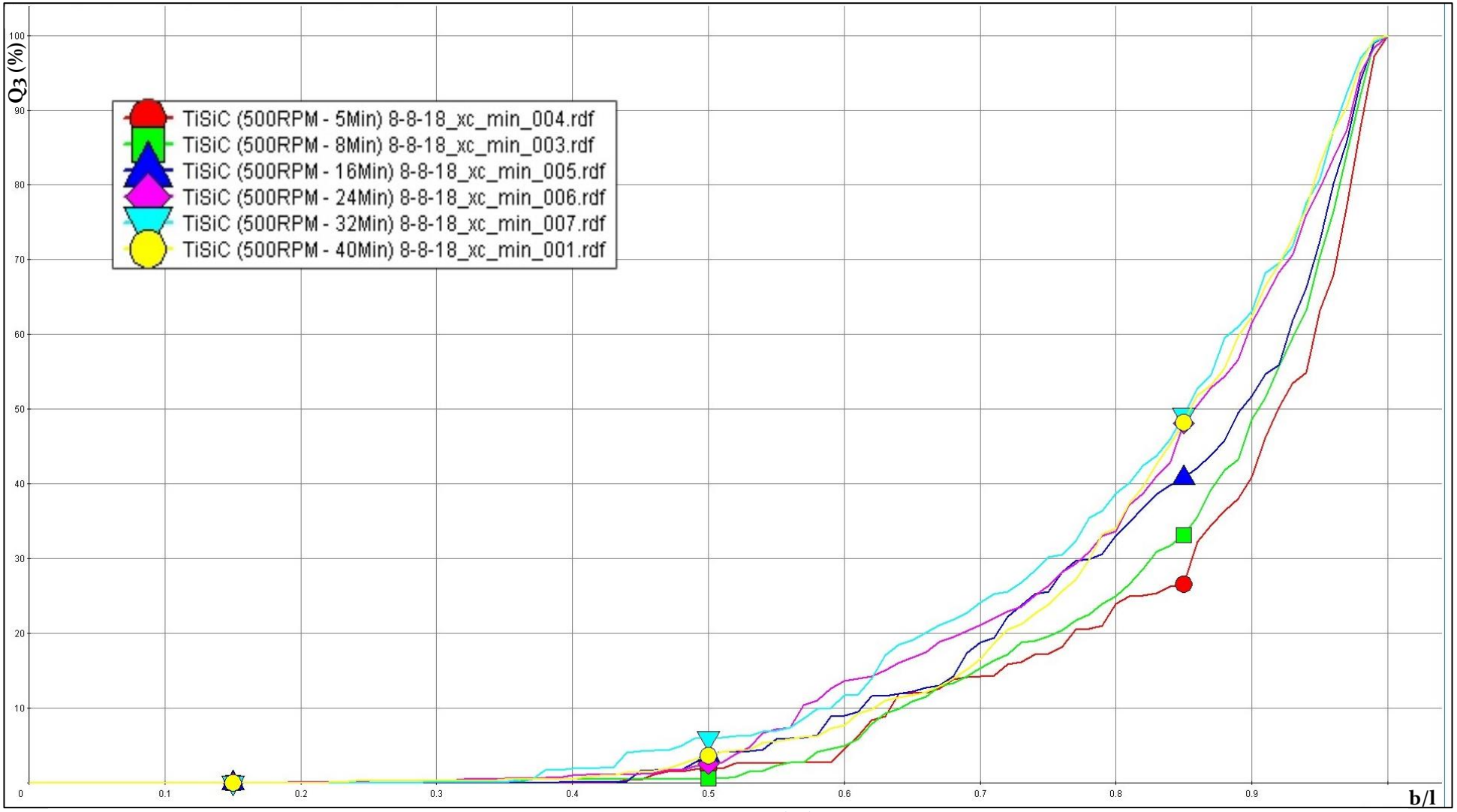

Figure 102 - Volume Based Comparison of Aspect Ratio (b/l) For Mechanically Alloyed Feedstock

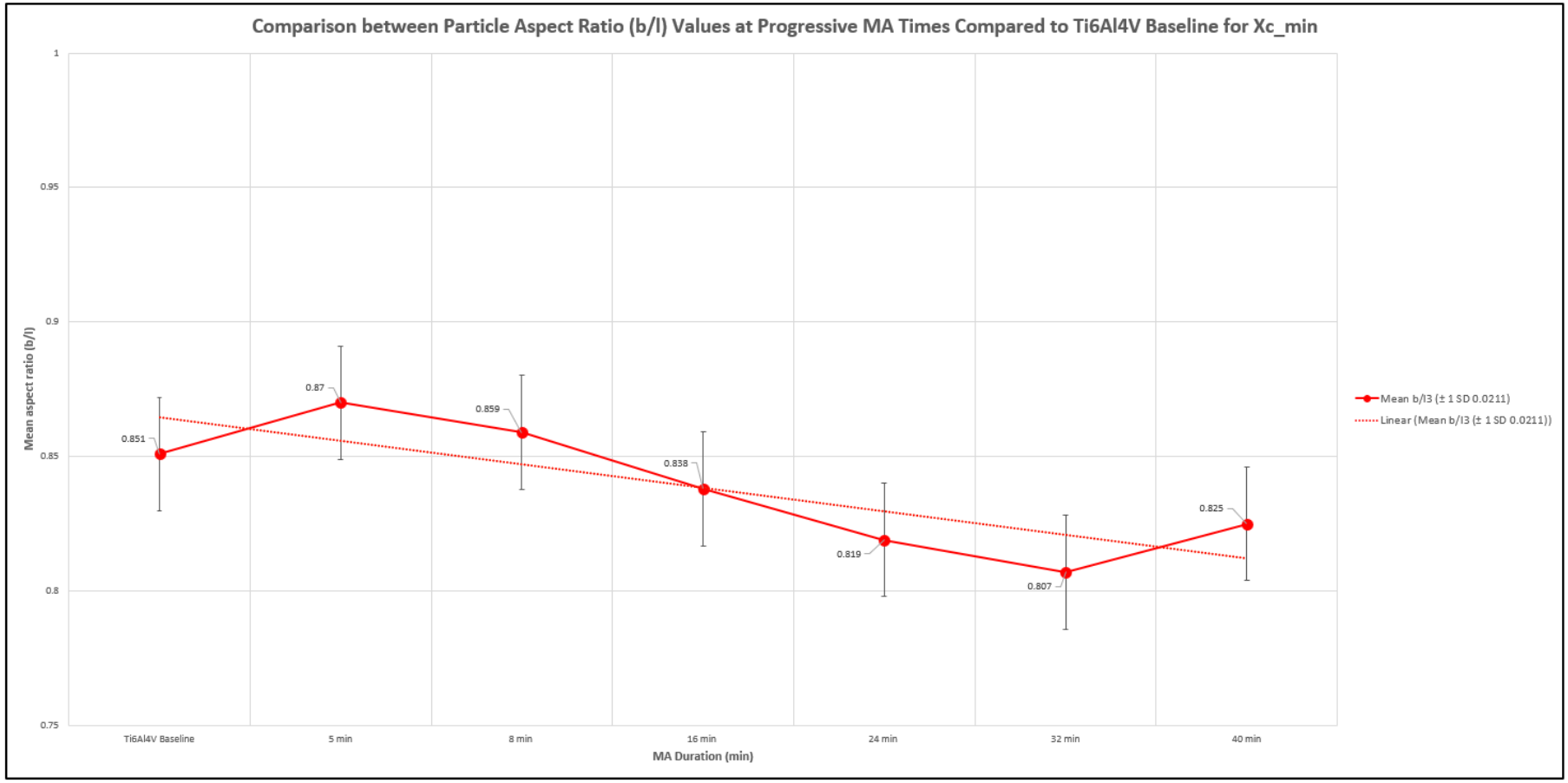

Figure 103 - Comparison between Particle Aspect Ratio (b/l) Values at Progressive MA Times Compared to Ti6Al4V Baseline for Xc_min

Figure 102 sows the accumulative percentage for aspect ratio, comparing all samples against the baseline Ti6Al4V sample. This further validates the change in SiC adhesion at 24 minutes, by demonstrating a steady decrease in the percentage of particles exhibiting an aspect ratio better than 0.850 $\mathcal{AR}$. After the first 5 minutes of alloying 73.341 % of the sample was better than 0.850 $\mathcal{AR}$, after 8 minutes this reduced to 66.871 %, after 16 minutes it reduced to 59.083 % and at 24 minutes only 50.816 % of the sample has an aspect ratio better than 0.850 $\mathcal{AR}$. Further MA for 32 (50.816 %) and 40 (51.894 %) had no further effect.

This trend can also be seen in Figure 103, whilst there is an increase on aspect ratio tending towards 1, the overall trend is towards a loss of sphericity which is at its wort at 32 minutes. Based on this evidence, an alloying duration of 24 minutes was chosen to be an optimal duration for alloying.

7.2.3 Minimise Change in Particles Morphology

It has been established that by using the Retch Camsizer X2 and by analysing changes in morphology as a function of aspect ratio, morphological changes increased over the time of the experiment. As the Camsizer X2 uses photogrammetry to determine morphological characteristics within the sample it can be open to inaccuracies due to the interpretation of the captured image. Using the Retch image analysis software, it was possible, using the database search tools, to filter out anomalous readings for manual inspection. Using the criteria: $X_{C\ Min} \geq 0.010$ mm to remove images of particles smaller than ten microns, b/l ≤ 0.600 to display images with an aspect ratio that would be far removed from the roundness acceptance limit of 0.850 $\mathcal{AR}$ in order to select particles with the worst aspect ratio and a Trans value of ≥ 0.100 to eliminate blurred or out of focus images. All samples were evaluated with these criteria individually and a selection of the results for each are presented.

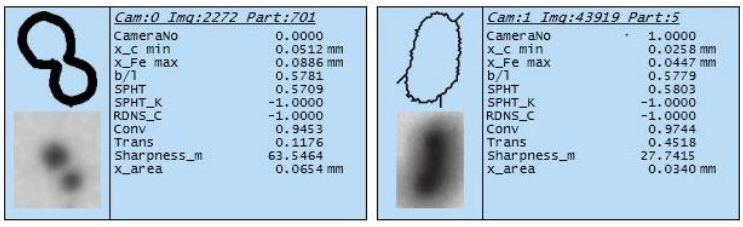

Figure 104 - Mechanical Alloying Ti6Al4V - SiC (5 Min)

Figure 104 shows image database results for powder alloyed for five minutes. The image on the left shows a particle with a size of 0.0512 mm whilst the particle to the right is half the size at 0.0258 mm, both would be acceptable. Regarding aspect ratio, both values are comparable at 0.5781 $\mathcal{AR}$ and 0.5779 $\mathcal{AR}$ respectively, there is a clear difference when viewing the images. To the right the image is elongated and could well be a single particle or small agglomeration, the image to the left, however, shows two particles that

on close inspection demonstrate individual roundedness. By using the aspect ratio term within the search criteria, it was possible to gather such images for closer inspection and whilst this data cannot be removed from the sample set and therefore remains part of the results, it assists in better understanding the images used and gain confidence in the results presented. At five minutes of alloying the search showed very few anomalous images, as was expected.

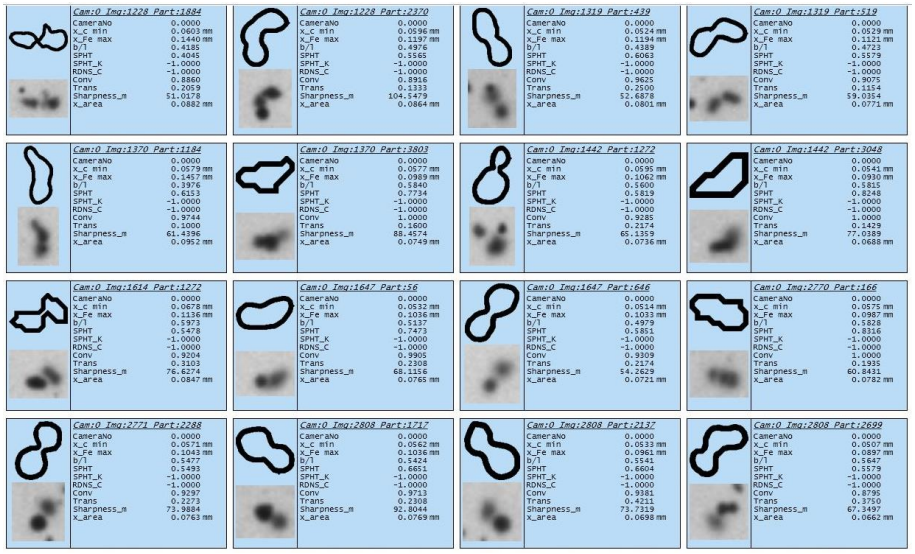

Figure 105 - Mechanical Alloying Ti6Al4V - SiC (8 Min)

After eight minutes, the search found a larger number of images fitting the criteria, Figure 105. On closer inspection of the images, again, most images are comprised of individual particle that have been captured on the same image giving rise to the result that this is an image of a large misshapen particle. Where images show multiple particles with varying sharpness to the outer edges, this would clearly indicate that the sharper particle is closer to the focal point than the other and therefore not connected. Of the sixteen images shown, all can be described as multiple particles sharing the same image. This would indicate that there is a high level of confidence in the particles still being rounded after eight minutes.

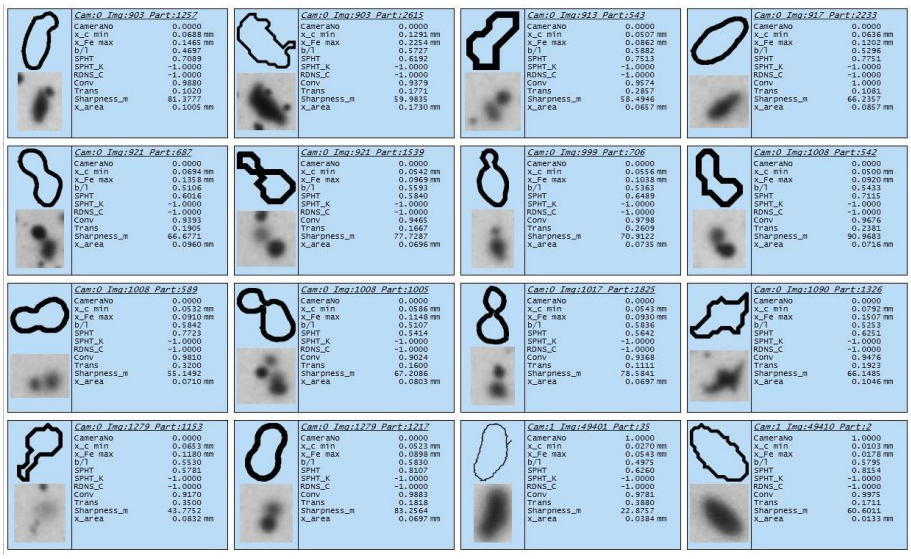

Figure 106 - Mechanical Alloying Ti6Al4V - SiC (16 Min)

At sixteen minutes (Figure 106), this characteristic continued with most images found, displaying multiple particles that had been interpreted as a single particle. However, out of the sixteen images above, six images showed particle that are either not round or agglomerations. Part 1257 shows a particle with an Xc min value of 0.0688 mm, as this constitutes a particle larger than the parent materials, this would be considered an agglomeration. This could also be the case for part 2233. Parts 2, and 35 are smaller particles that appear to be individual but nonrounded.

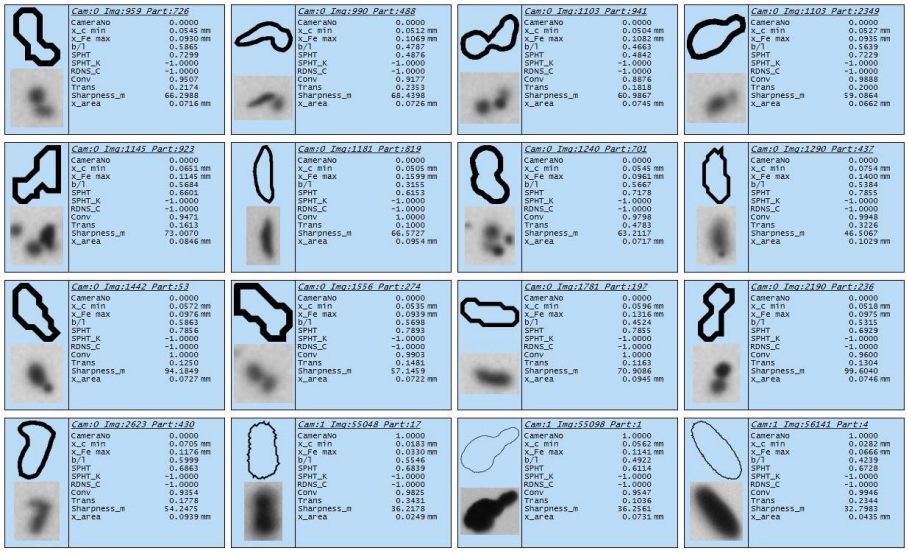

Figure 107 - Mechanical Alloying Ti6Al4V - SiC (24 Min)

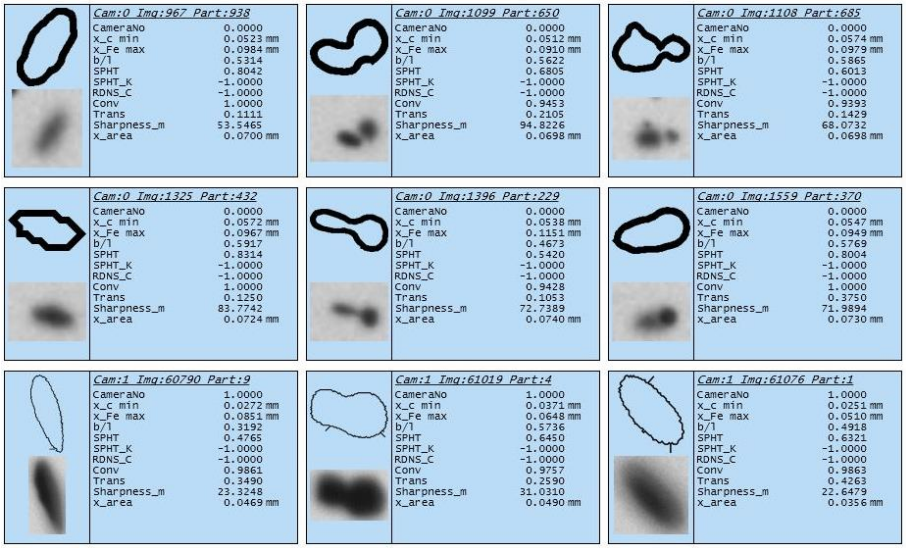

Figure 108 - Mechanical Alloying Ti6Al4V - SiC (32 Min)

At twenty-four minutes (Figure 107) and at thirty-two minutes (Figure 108), the images demonstrate similar characteristics with a mixture of coexistent particles within images, agglomerations and genuine nonrounded particles. Based on the minimal return in search results, there was no evidence to give uncertainty in the graphical results. This was also true for samples taken after forty minutes of alloying (Figure 109).

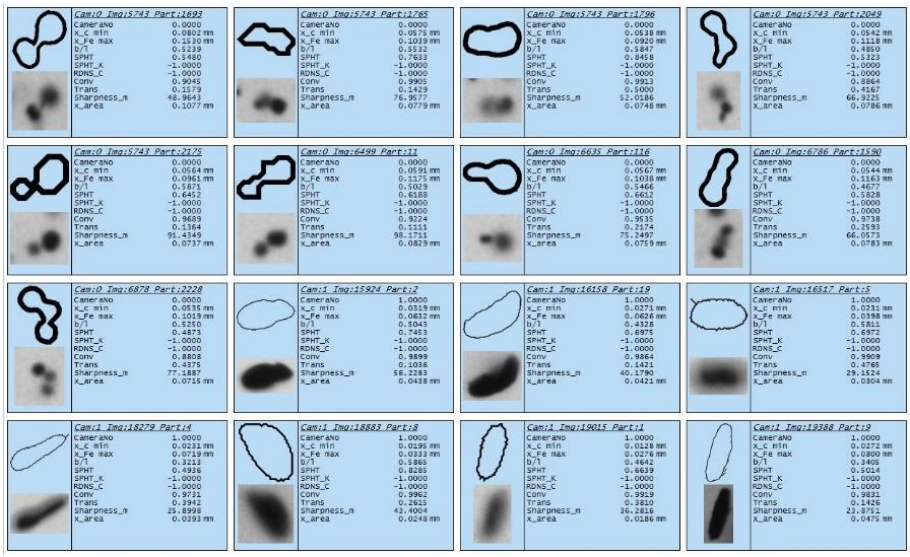

Figure 109 - Mechanical Alloying Ti6Al4V - SiC (40 Min)

In applying these search criteria across all samples, very few anomalous results were returned, demonstrating that the data presented in graphical form is reliable and that changes in particle morphology were successfully kept to a minimum.

7.2.4 Homogeneously Mix the Reinforcement Material Throughout the Feedstock

Not only was it important to achieve homogeneity of the SiC throughout the MA feedstock but also to determine whether the SiC had adhered to the surface of the Ti6Al4V powder. Where SiC had not adhered to the Ti6Al4V powder this would be evidenced by a higher concentration of small fines when graphically representing size distribution. As the smaller particles become combined with the larger Ti6Al4V particles the curve was expected to shift to the right due to an increase in size. This effect was evident in Table 29 and Figure 101 where the slope of the plots changed due to processing time, showing that as the smaller particles are combining with the larger, values for D10 reduce and values for D90 increase for samples taken at sixteen minutes and after. Images of the alloyed feedstock (chapter 7.2), also add supporting evidence in the form of unalloyed SiC powder visible in images taken after five minutes (Figure 88b) eight minutes (Figure 89a), sixteen minutes (Figure 90a) and twenty-four minutes (Figure 91a). Unalloyed SiC is not visible however, within SEM images taken after thirty-two minutes (Figure 92) and forty minutes (Figure 93). It was therefore concluded that at twenty-four minutes of MA, the SiC particles had homogeneously combined with the Ti6Al4V particles.

7.2.5 Avoid Contamination

A major consideration throughout the MA processing was the risk of contamination from materials liberated from the processing apparatus and O_2 from processing atmosphere.

Analysis for contamination was carried out on specimens manufactured from Ti6Al4V using standard parameters on the EOS M290 equipment. These samples were sectioned horizontally (Figure 110) and vertically (Figure 111) and were analysed using an area Regions of interest (ROI.

Specimen 2 from phase 3c: multi-layer evaluation, was analysed for contamination in comparison to the results shown in Figure 110 and Figure 111 to determine whether contamination from the MA process can be detected.

Samples were removed from the build platform using wire EDM, mounted in Struers ConduFast conductive acrylic resin and polished in accordance with Struers Ti alloys DiaPro application notes (Appendix 2). EDS was conducted using a voltage range of 0 KeV to 10 KeV. Multiple regions of interest (ROI) were analysed using both area and spot analysis. The optimisation element used for calibration was Co.

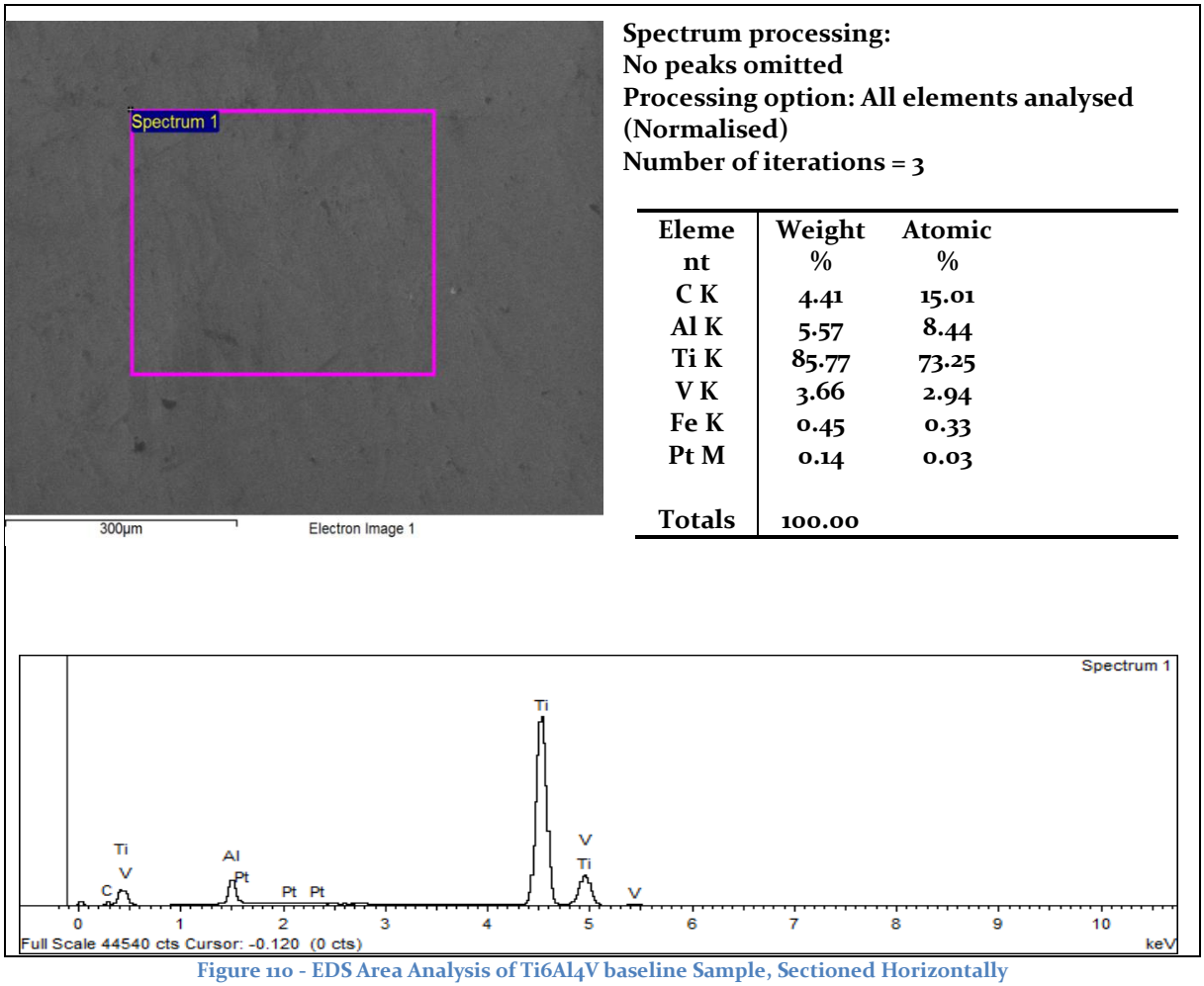

Figure 110 - EDS Area Analysis of Ti6Al4V baseline Sample, Sectioned Horizontally

Figure 110 shows an area analysis carried out on Ti6Al4V produced using standard parameters on an EOS M290 machine. The sample was produced using standard material and has not been MA, and therefore should not show evidence of contamination. The surface being analysed was in the horizontal orientation. Values for Al and V were typically around that expected with Al being 5.57 Wt. % (6.0) and V being 3.66 Wt. % (4.0) fractionally above the minimum value of 3.50 Wt. %. The bulk of the remaining elements being Ti at 85.77 Wt. %. C was also found to be present at 4.41 Wt. % along with traces of Fe, 0.45 Wt. % and Platinum (Pt), 0.14 Wt. %.

Elements of concern include C, Fe and Pt. The technical data sheet provided by EOS GmbH (Table 3) quantifies C to be a maximum of 0.08 Wt. % therefore a value of 4.41 Wt. % is unusual and would require further investigation to identify the source, at this stage it was classed as contamination. It should also be pointed out that C and other elements such as B, N_2, and O_2 elemental analysis on EDS is not always reliable, chambers in SEMs can tend to get a C coating which can add to the readings. A preferred method of analysis would be to use a LECO or similar system for C analysis using combustion analysis. Quantities of Fe at 0.45 Wt. % were approximately twice that

described in the technical data sheet (max 0.250 Wt. %) and Pt was an unexpected element and therefore classed as contamination.

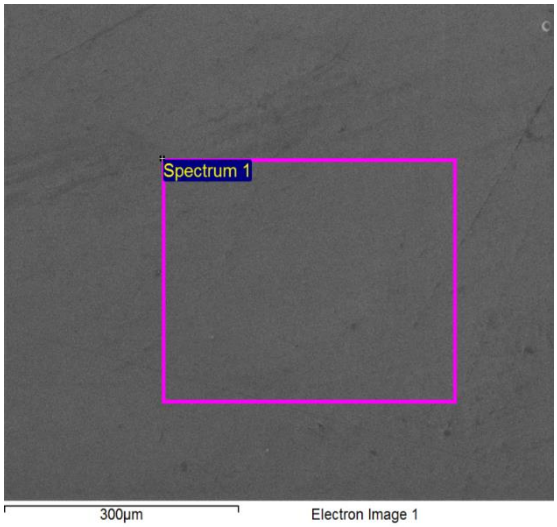

Spectrum processing:
No peaks omitted
Processing option: All elements analysed (Normalised)
Number of iterations = 3

Element	Weight %	Atomic %
C K	4.35	14.82
Al K	5.77	8.74
Ti K	86.33	73.66
V K	3.44	2.76
Pt M	0.11	0.02
Totals	100.00	

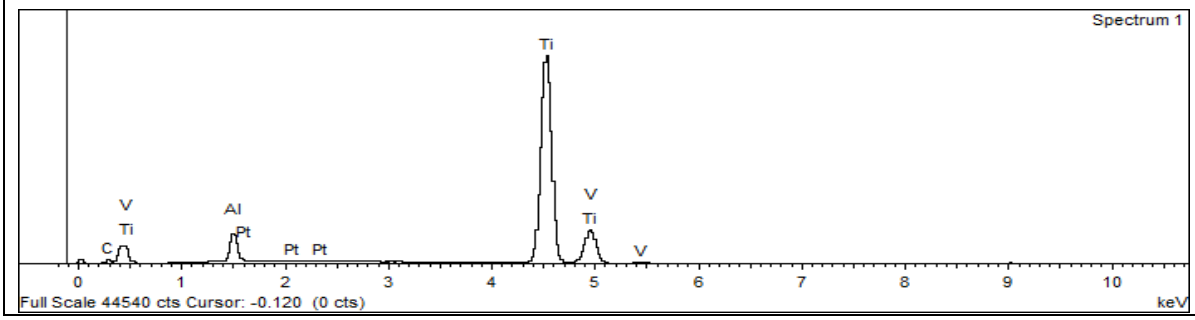

Figure 111 - EDS Area Analysis of Ti6Al4V baseline Sample, Sectioned Vertically

In Figure 111 a sample of Ti6Al4V produced using standard parameters on an EOS M290 machine was sectioned in the vertical plane, mounted, and polished. Results compared favourably with Figure 110 with the omission of Fe.

Table 30 - Ti6Al4V baseline EDS analysis between sample sectioned horizontally and vertically

Element	Ti6Al4V (Horizontal)	Ti6Al4V (Vertical)	Sigma (σ)
C	4.41	4.35	0.04
Al	5.57	5.77	0.14
Ti	85.77	86.33	0.40
V	3.66	3.44	0.16
Fe	0.45	-	-
Pt	-	0.11	-

A comparison between results can be seen in Table 30.

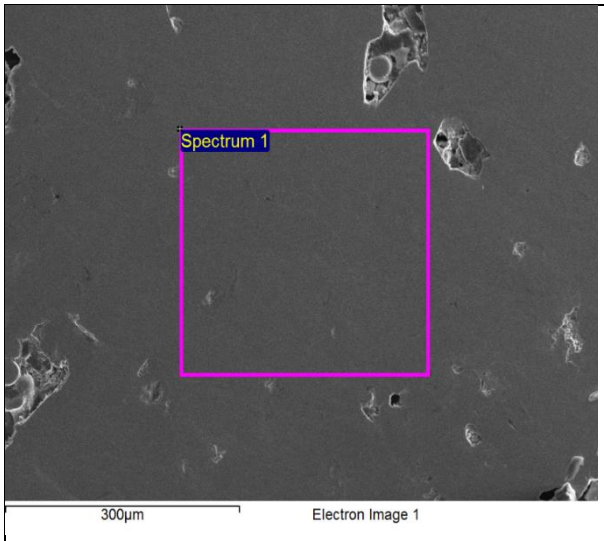

Spectrum processing:
Peak possibly omitted: 6.411 keV

Processing option: All elements analysed (Normalised)
Number of iterations = 3

Element	Weight %	Atomic %
C K	5.63	18.28
Al K	5.55	8.01
Si K	2.80	3.88
Ti K	82.83	67.41
V K	3.16	2.42
Pt M	0.04	0.01
Totals	100.00	

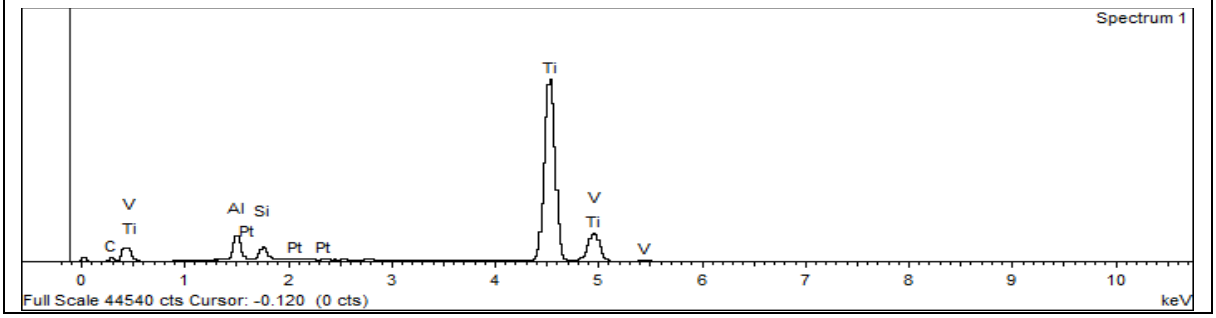

Figure 112 - EDS Area 1 Analysis of MMC Sample 3, Sectioned Horizontally

Figure 112 to Figure 114 show area analysis carried out on MA MMC sample produced on an EOS M290 machine. The surface being analysed was sectioned horizontally. The ROI sellected was such that it showed little evidence of SiC present and resembled Ti6Al4V. Values were comparable with Figure 110 and Figure 111 with the addition of Si, 2.80 Wt. %. There was an increase also in C, 5.63 Wt. % and a decrease in Pt, 0.04 Wt. %. The detection of Si and C indicating the presence of SiC.

Table 31 - EDS area analysis between Ti6Al4V baseline sample and MMC Specimen

Element	Ti6Al4V (Horizontal)	Ti6Al4V (Vertical)		TiSiC Area 1	TiSiC Area 2	TiSiC Area 3
C	4.41	4.35		5.63	4.81	8.97
Al	5.57	5.77		5.55	6.08	4.38
Ti	85.77	86.33		82.83	83.06	77.19
V	3.66	3.44		3.16	3.33	3.12
Fe	0.45	-		-	0.29	-
Pt	-	0.11		0.04	0.02	-
Si				2.80	2.40	6.34

At higher magnification, Figure 113 shows a ROI near suspected SiC deposits. Results are again comparable to Figure 112. Variation between results is attributed to the ROI positioning as indicated by Figure 113 being away from suspected SiC and Figure 114 being directly over this region. It can be seen that the ROI over the deposits exhibits lower Ti and higher Si indicating a plausible location for deposits of SiC.

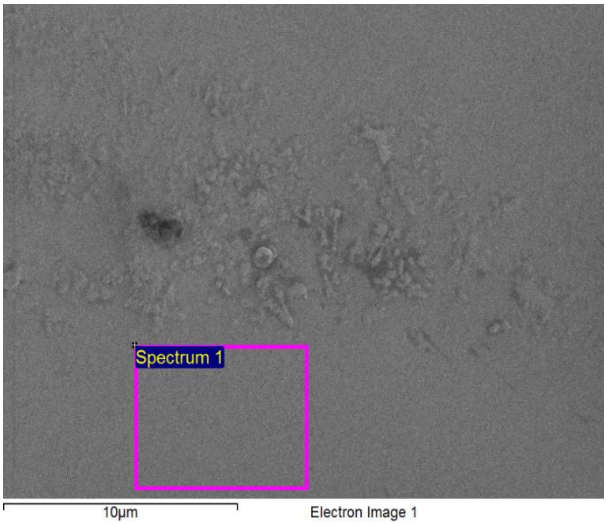

Spectrum processing:
No peaks omitted

Processing option: All elements analysed (Normalised)
Number of iterations = 3

Element	Weight %	Atomic %
C K	4.81	15.93
Al K	6.08	8.95
Si K	2.40	3.40
Ti K	83.06	68.91
V K	3.33	2.60
Fe K	0.29	0.21
Pt M	0.02	0.00
Totals	100.00	

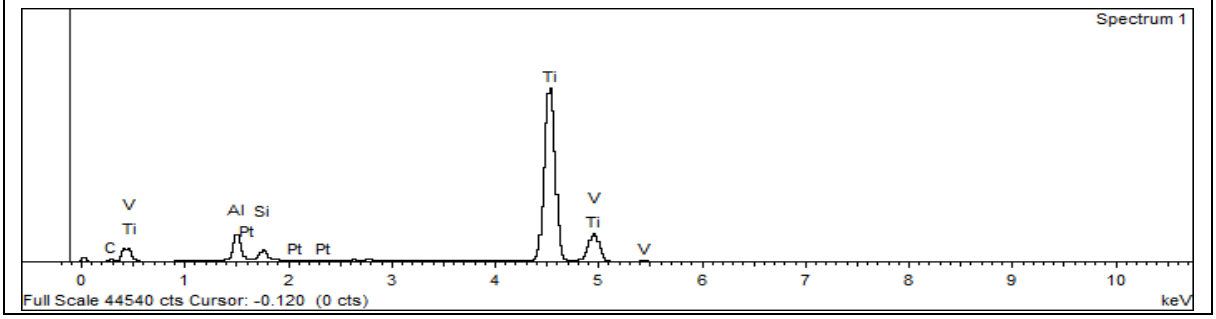

Figure 113 - EDS Area 2 Analysis of MMC Sample 3, Sectioned Horizontally

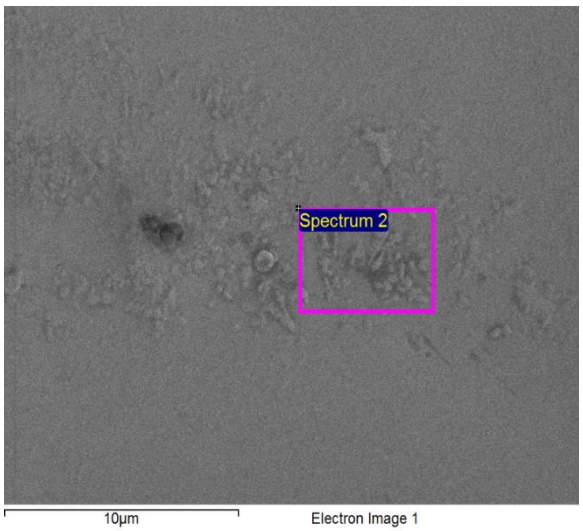

Spectrum processing:
Peaks possibly omitted: 2.780, 6.432, 9.026 keV

Processing option: All elements analysed (Normalised)
Number of iterations = 3

Element	Weight %	Atomic %
C K	8.97	26.59
Al K	4.38	5.78
Si K	6.34	8.04
Ti K	77.19	57.41
V K	3.12	2.18
Totals	100.00	

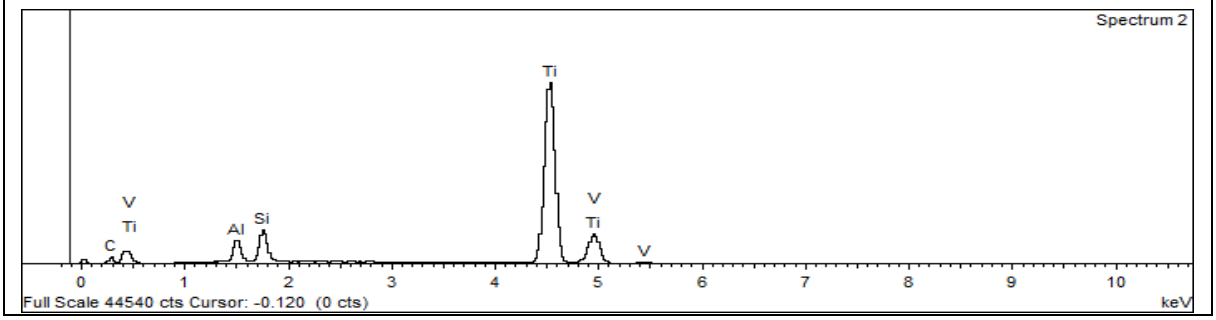

Figure 114 - EDS Area 3 Analysis of MMC Sample 3, Sectioned Horizontally

Closer analysis of the region of SiC deposits was carried out using an area ROI (Figure 114). Results showed levels of Al, 4.38 Wt. % and V 3.12 Wt. % to be typical with V below the minimum expected value as was the case throughout. Increased levels of C 8.97 Wt. % and Si 6.34 Wt. % reinforced the existance of SiC within the ROI. Further investigation was carried out by spot analysis in these areas for confirmation.

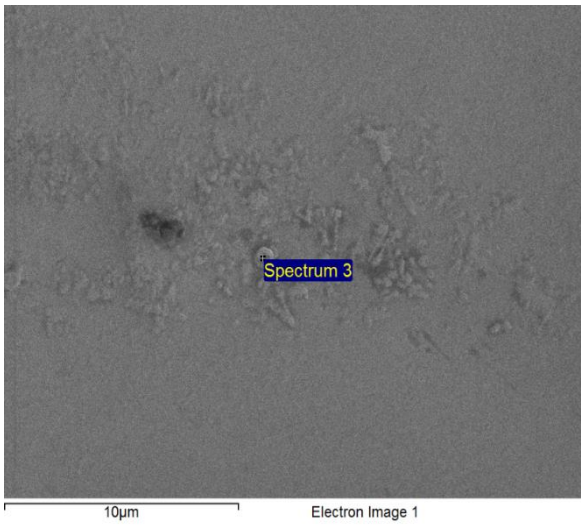

Spectrum processing:
Peak possibly omitted: 9.029 keV

Processing option: All elements analysed (Normalised)
Number of iterations = 4

Element	Weight %	Atomic %
C K	17.53	43.47
Al K	3.42	3.77
Si K	8.48	8.99
Ti K	67.85	42.18
V K	2.72	1.59
Totals	100.00	

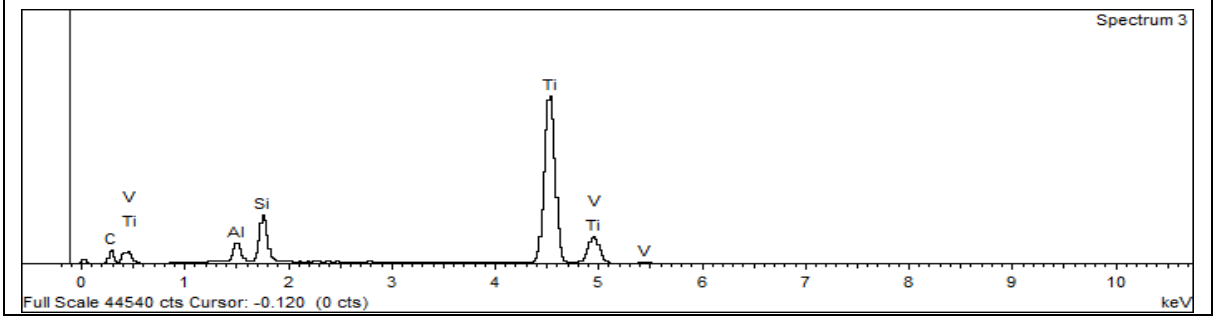

Figure 115 - EDS Spot 1 Analysis of MMC Sample 3, Sectioned Horizontally

Spot analyses were conducted on individual ROI suspected of being particles of SiC. Results confirmed high levels of C 17.53 Wt. % and Si 8.48 Wt. % (Figure 115), with T, Al and V remaining like previouse measurements.

Analysis of spot 2, (Figure 116), a darker region to the left of the image returned values of C 25.55 Wt. % and Si 24.64 Wt. %. due to the increase in both C and Si it was concluded that the ROI was a SiC particle.

Table 32 - TiSiC EDS analysis comparison between area and spot ROI

Element	TiSiC Area 1	TiSiC Area 2	TiSiC Area 3	TiSiC Spot 1	TiSiC Spot 2	TiSiC Spot 3
C	5.63	4.81	8.97	17.53	25.55	10.90
Al	5.55	6.08	4.38	3.42	1.10	3.90
Ti	82.83	83.06	77.19	67.85	45.87	75.87
V	3.16	3.33	3.12	2.72	1.64	2.82
Fe	-	0.29	-	-	-	0.33
Pt	0.04	0.02	-	-	-	
Si	2.80	2.40	6.34	8.48	24.64	6.18
O	-	-	-	-	1.10	-

In comparrison to Figure 117, the particle demonstrated characteristics of SiC with elevated readings of C 10.90 Wt. % and Si 6.18 Wt. % however not to the levels of spot 2. It is believed that the particles of SiC observed in the SEM images have a coating of TiC, the intercacial material between the Ti6Al4V and the SiC. As this material is exceptionaly wear resistant it was able to withstand the polishing stages of the sample preperation. The darker area to the left is possibly the site of a removed particle of SiC. The higher levels of C and Si detected in spot 2 confirm this hypothysis.

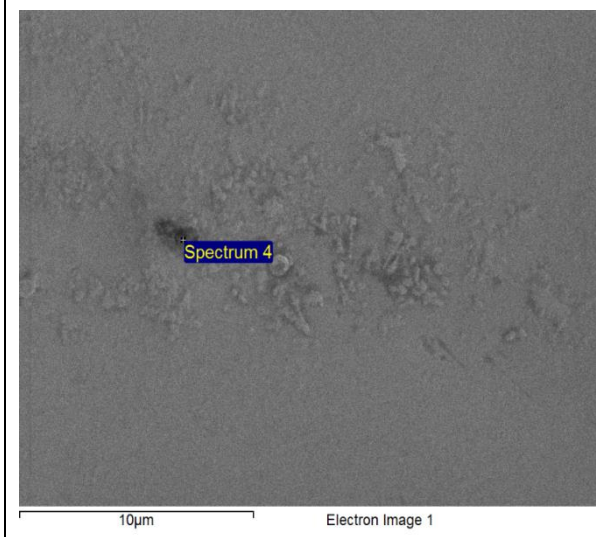

Spectrum processing:
Peaks possibly omitted: 6.260, 9.020 keV

Processing option: All elements analysed (Normalised)
Number of iterations = 4

Element	Weight %	Atomic %
C K	25.55	51.79
O K	1.10	1.67
Al K	1.20	1.08
Si K	24.64	21.36
Ti K	45.87	23.31
V K	1.64	0.78
Totals	100.00	

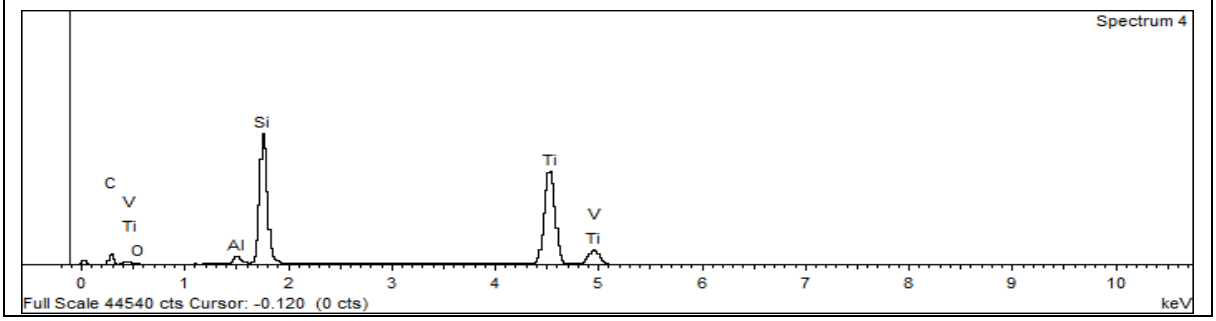

Figure 116 - EDS Spot 2 Analysis of MMC Sample 3, Sectioned Horizontally

Unexpected levels of Fe, Pt and C were present in samples one and two for Ti6Al4V, which failed to increase as a result of MA, concluding that there was no contamination from the process.

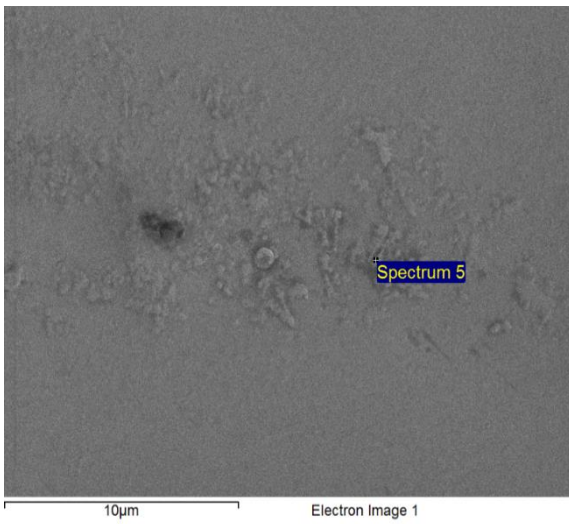

Spectrum processing:
Peaks possibly omitted: 2.761, 9.030, 9.437 keV

Processing option: All elements analysed (Normalised)
Number of iterations = 3

Element	Weight %	Atomic %
C K	10.90	31.10
Al K	3.90	4.95
Si K	6.18	7.55
Ti K	75.87	54.30
V K	2.82	1.90
Fe K	0.33	0.20
Totals	100.00	

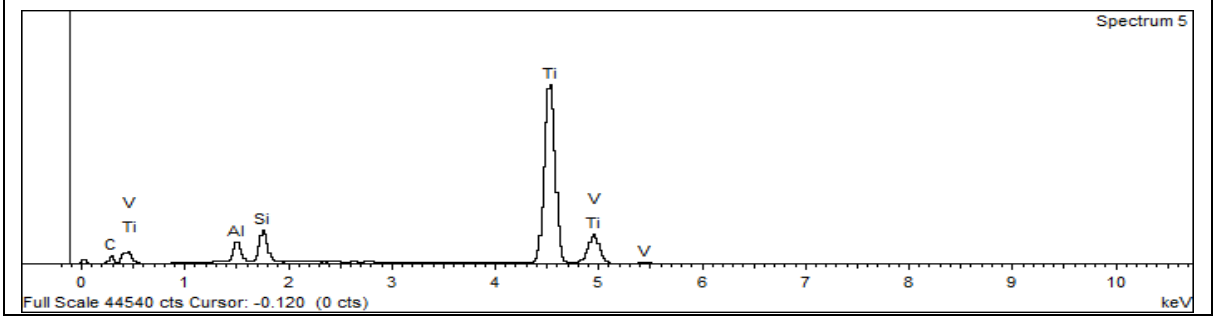

Figure 117 - EDS Spot 3 Analysis of MMC Sample 3, Sectioned Horizontally

7.2.6 Optimal MA Processing Time Summary

It is clear from the results in chapter 7.2 that it is possible to combine MMC reinforcement material in the form of particulates with matrix material using MA. Evidence shows that there is, however, an optimal point at which the reinforcement will coat the matrix material, beyond which the coating is subsequently removed, and particle shape characteristics become unusable within the L-PBF process. For this research, this point was reached after 24 minutes and may vary depending on the materials being combined. In the production of samples, it was noted that although the SiC was homogeneously mixed throughout the feedstock, distinct areas are easily distinguishable at high magnification. Whilst this may cast doubt over whether the avoidance of full MA was unnecessary, the rheological evidence does demonstrate the possibility to combine small batch materials for investigation whilst maintaining an acceptable level of powder characteristics.

7.3 Phase 2a: Development of Mechanical Alloying Process as a Homogenous Transportation Mechanism for MMC Feedstock Conclusions

1 MA was chosen as a system for combining dissimilar materials for transportation into the PBF system to overcome the effect that transportation and the powder delivery mechanism has on manually mixed powders. A new and novel equation was presented that calculated the resultant Vol.% for both matrix and reinforcement materials based on particle size. By using this equation, it was shown that whilst the MA for AM methodology was successfully able to deliver accurate quantities of reinforcement material homogeneously throughout the matrix.

2 MA results showed that at low rotational speeds (500 rev/min), and an alloying time of twenty-four minutes was optimal to produce MMC feedstock exhibiting:

- Reinforcement material embed onto the surface of the matrix material.
- Minimal increase in particle size.
- Minimal change in particles morphology.
- Reinforcement material homogeneously mixed throughout the feedstock.
- Avoided contamination.

Chapter Eight

8.0 Phase 2b MMC feedstock analysis for moisture, size, morphology, and rheology in comparison to baseline assessment, phase 1a

8.1 Phase 2b: MMC Feedstock Analysis for Moisture, Size, Morphology and Rheology in Comparison to Baseline Assessment, Phase 1a Methodology

8.1.1 MMC Feedstock Analysis Overview of Experiment/Design

Samples of mechanically alloyed feedstock were analysed to establish the adequacy of the MA method of feedstock production. Samples of the feedstock were taken at intervals of 5, 8, 16, 24, 32 and 40 minutes of alloying and analysed for size, size distribution and morphology using a Camsizer x2 (Retsch, 2017). The results were compared to those of Ti6Al4V established in phase 1a (chapter 5.0). based on the results an ideal set of MA parameters was established and a batch of feedstock was produced.

8.1.2 Sample Size

During the MA process, samples of approximately 15 to 30 grams were removed from the process and using the Retsch Camsizer x2 particle size analyser. The process was then continued until 40 minutes had elapsed.

8.1.3 MMC Feedstock Moisture and Rheological Analysis

Following successful production of a batch of MMC feedstock, moisture and rheological analysis was carried out using apparent density and angle of repose. The results were compared to those of Ti6Al4V established in phase 1a (chapter 5.0).

8.2 Phase 2b: MMC Feedstock Analysis for Moisture, Size, Morphology and Rheology in Comparison to Baseline Assessment, Phase 1a Results and Discussion

MMC feedstock processed by MA for a total of twenty-four minutes was demonstrated as being optimal, a usable quantity of feedstock was produced using the selected

parameters and the resultant batch was compared against the baseline data generated earlier.

8.2.1 Assessment of MMC Feedstock Moisture Content

The moisture content of MMC feedstock was measured using the loss of mass method. Three separate samples were analysed from different areas of the batch to establish an arithmetic mean and compared to the baseline results previously obtained (chapter 5.2.1). The results are shown in Table 33.

Table 33 - Moisture Content Results for MA Feedstock in Comparison to baseline Assessments.

	Moisture Content (%)		
	Ti6Al4V	SiC	MMC
Test 1	0.59	0.79	0.61
Test 2	0.50	0.97	1.20
Test 3	0.67	1.13	0.79
Mean ($\bar{x}$)	0.59	0.96	0.86
Sigma (σ)	0.09	0.17	0.30

For the MMC feedstock the mean moisture levels were below the 1.0 % maximum limit and were therefore considered acceptable. It was noted that the mean values for the MMC feedstock fell between the lower value for the Ti6Al4V powder (0.59 %) and the higher value for SiC (0.96 %). This was due to the percentage ratio of Ti6Al4V to SiC. It was evident from the baseline assessments that the SiC powder absorbed moisture more than the Ti6Al4V powder due to the high surface area and increased surface energy. The presence of SiC within the MMC feedstock is evident by the increased percentage of moisture however, this is not of the magnitude previously exhibited and remains within acceptable limits.

8.2.2 Assessment of MMC Feedstock Size and Morphology

Using a Retsch Camsizer X2 particle size analyser a representative sample of MMC feedstock powder was analysed in comparison to baseline assessments acquired in chapter 6.2, with respect to the characteristics: $X_{c\ min}$, X_{area} and b/l. the results were compared to the baseline data obtained for Ti6Al4V as these results best represented standard feedstock and constitute the bulk of the MMC.

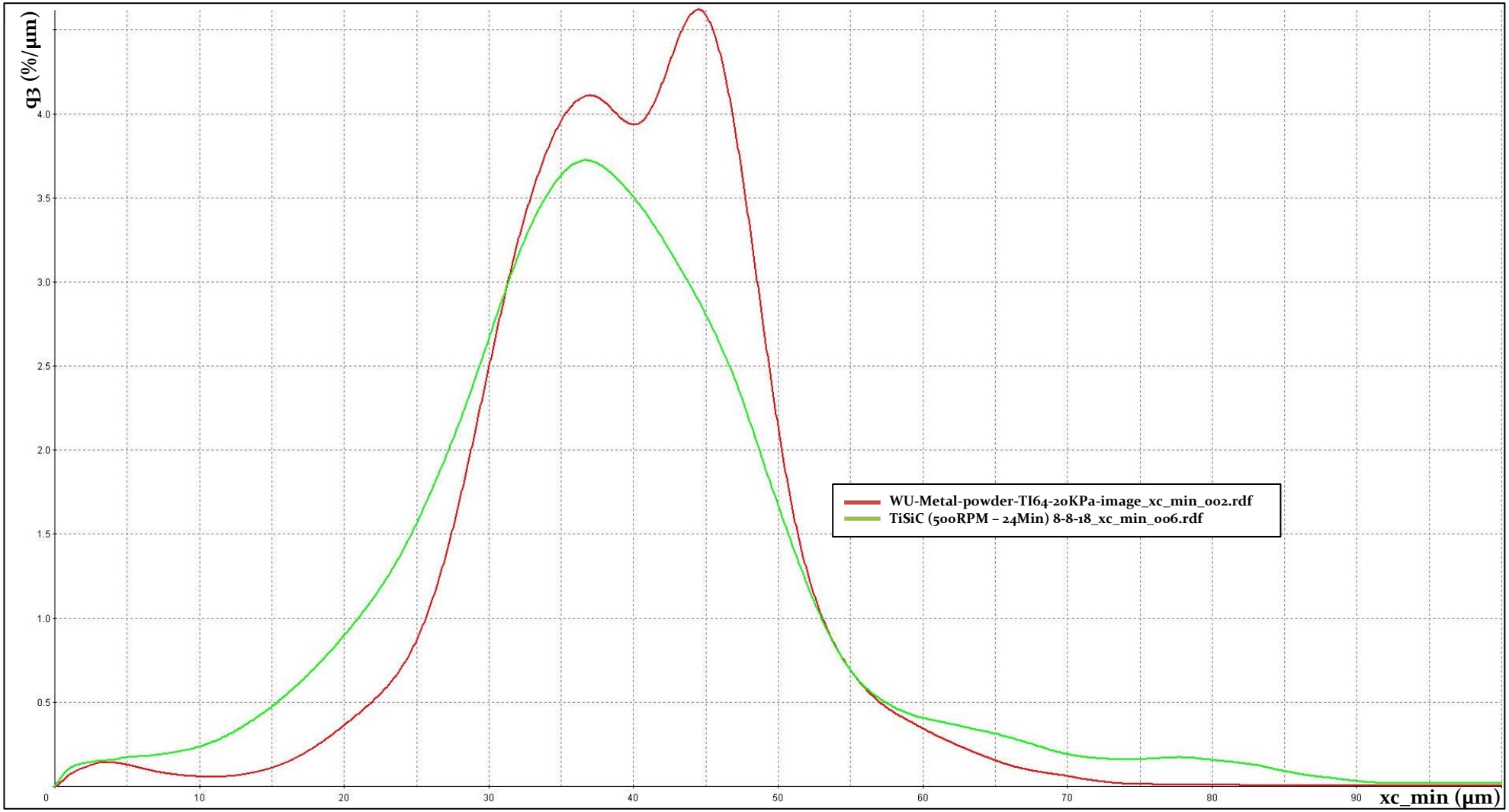

Figure 118 - $X_{c\ Min}$ Comparison Between Ti6Al4V Baseline and MMC Feedstock Alloyed for 24 Minutes

8.2.2.1 MMC feedstock Particle Size and Size Distribution Comparison

Figure 118 shows graphical results for $X_{c\ min}$ frequency distribution curve for MMC feedstock powder in comparison to Ti6Al4V powder. The analysis showed a multi-modal distribution from ~0 µm to ~75 µm for the Ti6Al4V powder (Red line), with peaks at 3.5 µm, 37 µm and 44 µm. in comparison, the MMC material shown here in green, has a normal distribution, from ~0 µm to ~100 µm with a peak at 37 µm. The distribution curve for the MMC material exhibited higher quantities of particles within the range of 0 µm to 30 µm indicating a higher quantity of small fines. Within the range of 55 µm to 90 µm this can also be seen to a lesser degree, indicating that particles within this range are larger, this was predicted as a result of the smaller SiC particles fixing to the surface of the Ti6Al4V and increasing the size.

Table 34 - Statistical Results for Ti6Al4V Particle Size and Distribution ($X_{c\ Min}$) Baseline Results

Statistical measurement	Baseline result ($X_{c\ min}$)	MMC feedstock results ($X_{c\ min}$)
Q3 10 %	28.8 µm	23.5 µm
Q3 50 %	39.9 µm	37.7 µm
Q3 90 %	49.9 µm	53.4 µm
Mv3($\bar{x}$)	39.7 µm	39.7 µm
Sigma 3 ($\bar{x}$)	9.7 µm	20.1 µm
Mean b/l3	0.851	0.819
1-Q3 (b/l = 0.850)	65 %	51.9 %

Table 34 shows the salient characteristics of the particle size analysis. It was evident For Ti6Al4V, that the volume based statistical average particle size (Q3 50 %) was 39.9 µm with a mean particle size (Mv3($\bar{x}$)) of 39.7 µm. the closeness of these two values, (within 0.2 µm), showed a high degree of confidence in the results.

In comparison, values for the MMC feedstock showed a smaller Q3 50 % size of 37.7 µm however, the mean particle size (Mv3($\bar{x}$)) was 39.7 µm, identical to that of the Ti6Al4V. Although the statistical mean for the sample was identical, it can be observed that the value for Q3 10 % was lower and the value for Q3 90 % was higher, indicating that at the lower percentile, smaller particles were detected, most likely to be SiC and that at the higher percentile larger particles were detected, likely to be Ti6Al4V coated with SiC. This data confirms the results analysed in Figure 118.

The mean aspect ratio (Mean b/l3) for Ti6Al4V was 0.851, indicating that the sample was classified as rounded. Results for Mean b/l3 for the MMC feedstock however, showed a value of 0.819. this sample would not be classified as rounded in this instance. Further comparison of the mean aspect ratio results indicated that the inverse statistical volume

(1-Q3 (b/l = 0.850)) for the Ti6Al4V sample was 65 %. In comparison, the MMC feedstock result was 51.9 %, indicating that fewer particles were rounded. This was as a result of the MA process.

Further comparisons were made between the baseline assessments and the MMC feedstock, evaluating X_{area} (Figure 119). In much the same way as results for $X_{c\ min}$, the distribution curve for X_{area} showed increases in particles sized at the lower and higher ends of the distribution with a lower count of particles within the mid-range. A more detailed analysis of this comparison was required.

Table 35 details Statistical Results for Ti6Al4V Particle Size and Distribution, $X_{c\ Min}$ and X_{area} Baseline Results Versus MMC material results.

Table 35 - Statistical Results for Ti6Al4V Particle Size and Distribution, $X_{c\ Min}$ Versus X_{area} Baseline Results

Statistical measurement		Baseline result ($X_{c\ min}$)	Baseline result (x_{area})	Percentage increase Ø		MMC result ($X_{c\ min}$)	MMC result (x_{area})	Percentage increase Ø
Q3 10 %		28.8 µm	30.2 µm	4.6 %		23.5 µm	26.0 µm	9.6 %
Q3 50 %		39.9 µm	43.1 µm	7.4 %		37.7 µm	41.4 µm	8.9 %
Q3 90 %		49.9 µm	55.8 µm	10.6 %		53.4 µm	60.3 µm	11.4 %
Mv3(x̄)		39.7 µm	42.7 µm	7.0 %		39.7 µm	44.4 µm	10.6 %
Sigma 3 (x̄)		9.7 µm	11.6 µm			20.1 µm	26.3 µm	
Mean b/l3		0.851	0.839			0.819	0.795	
1-Q3 (b/l = 0.850)		65.0 %	61.5 %			51.9 %	46.3 %	

By comparing $X_{c\ min}$ to X_{area} it is possible to better understand surface irregularities such as satellites. The closer values are, between $X_{c\ min}$ and X_{area}, the fewer surface irregularities there are. Therefore, it was observed that the percentage increase in diameter ranged from 4.6 % to 10.6 % with an increase of 7.0 % for mean b/l3, in reference to the Ti6Al4V baseline data. It has been established that the baseline material performs satisfactorily within the process and therefore these values can be considered typical. In comparison, results for the MMC material showed percentage increases from $X_{c\ min}$ to X_{area} of between 8.9 % to 11.4 % with an increase of 10.6 % for mean b/l3. This being a result of the MA processing would indicate that an increase in surface roughness and of satellites was evident. Based on the severity of difference from $X_{c\ min}$ to X_{area} for the Ti6Al4V material, the material MA for twenty-four minutes shows similar results.

Further Comparison Between Ti6Al4V Baseline and MMC Feedstock Alloyed for 24 Minutes is given in Figure 119 for X_{area}. The frequency of both smaller (less than 30 µm) and larger particles (more than 54 µm) has increased whilst particles within the range of 30 µm to 54 µm has decreased.

Figure 120 compares $X_{c\ min}$ volume-based distribution for Ti6Al4V baseline assessment with MMC feedstock MA for twenty-four minutes, it can be seen that there is a shift to the left for the green line (MMC material) in comparison to the red (Ti6Al4V), indicating that the powder is finer however the reduction in the slope angle indicates a wider spread of values. This is clarified by the results for X_{area} Figure 121.

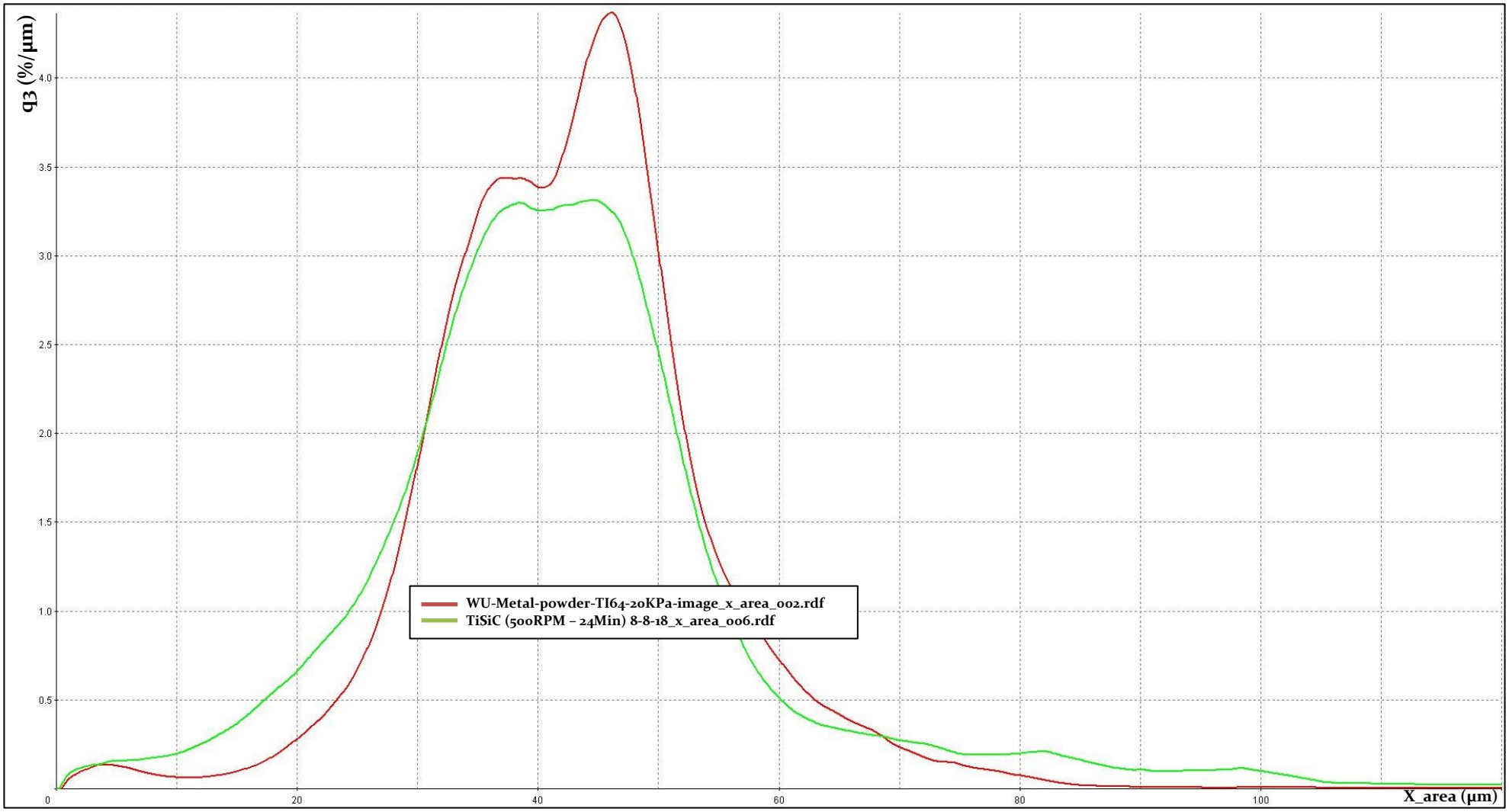

Figure 119 - X_{area} Comparison Between Ti6Al4V Baseline and MMC Feedstock Alloyed for 24 Minutes

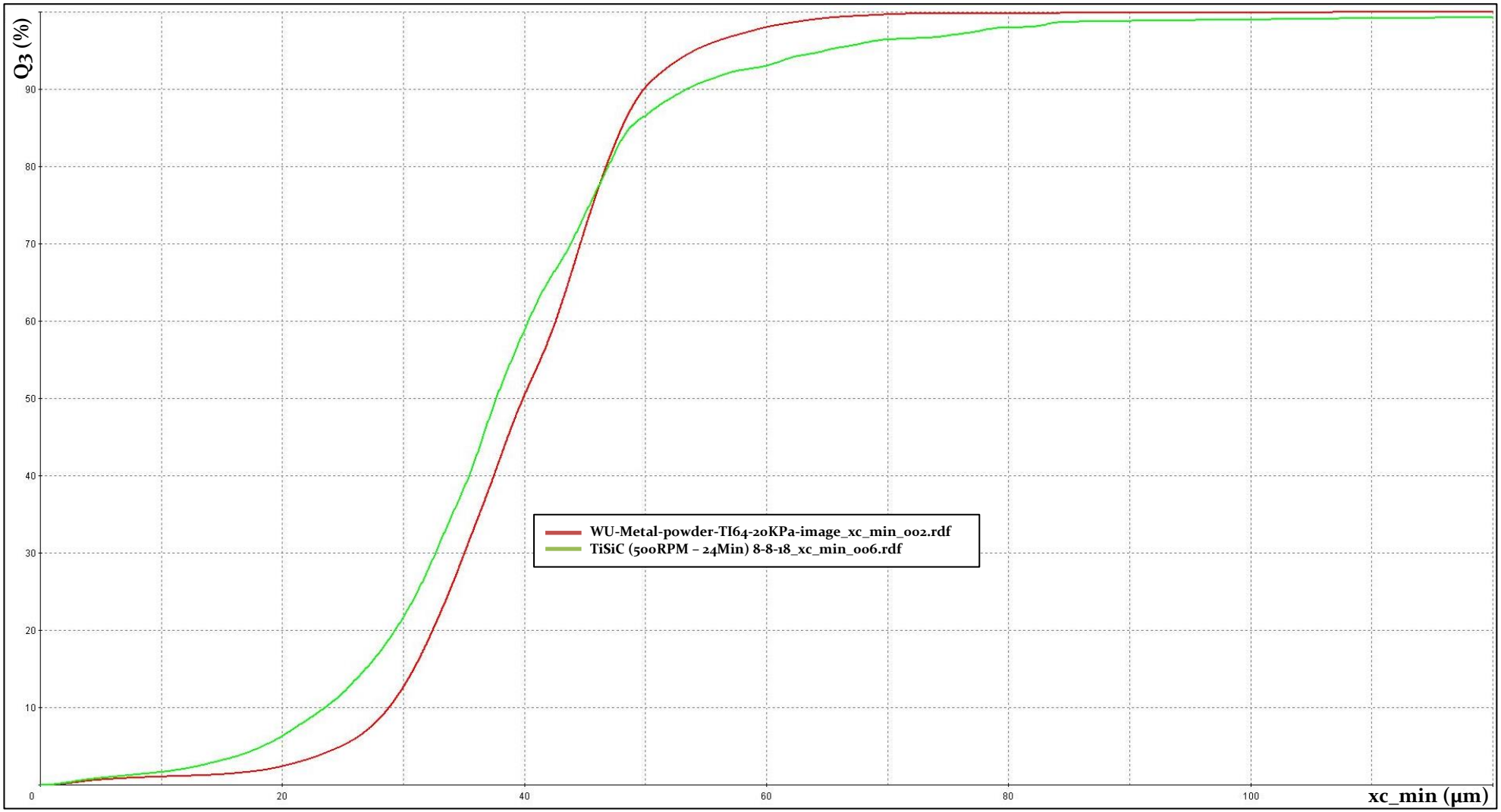

Figure 120 - $X_{c\ Min}$ Volume Based Distribution Curve Comparison Between Ti6Al4V Baseline and MMC Feedstock Alloyed for 24 Minutes.

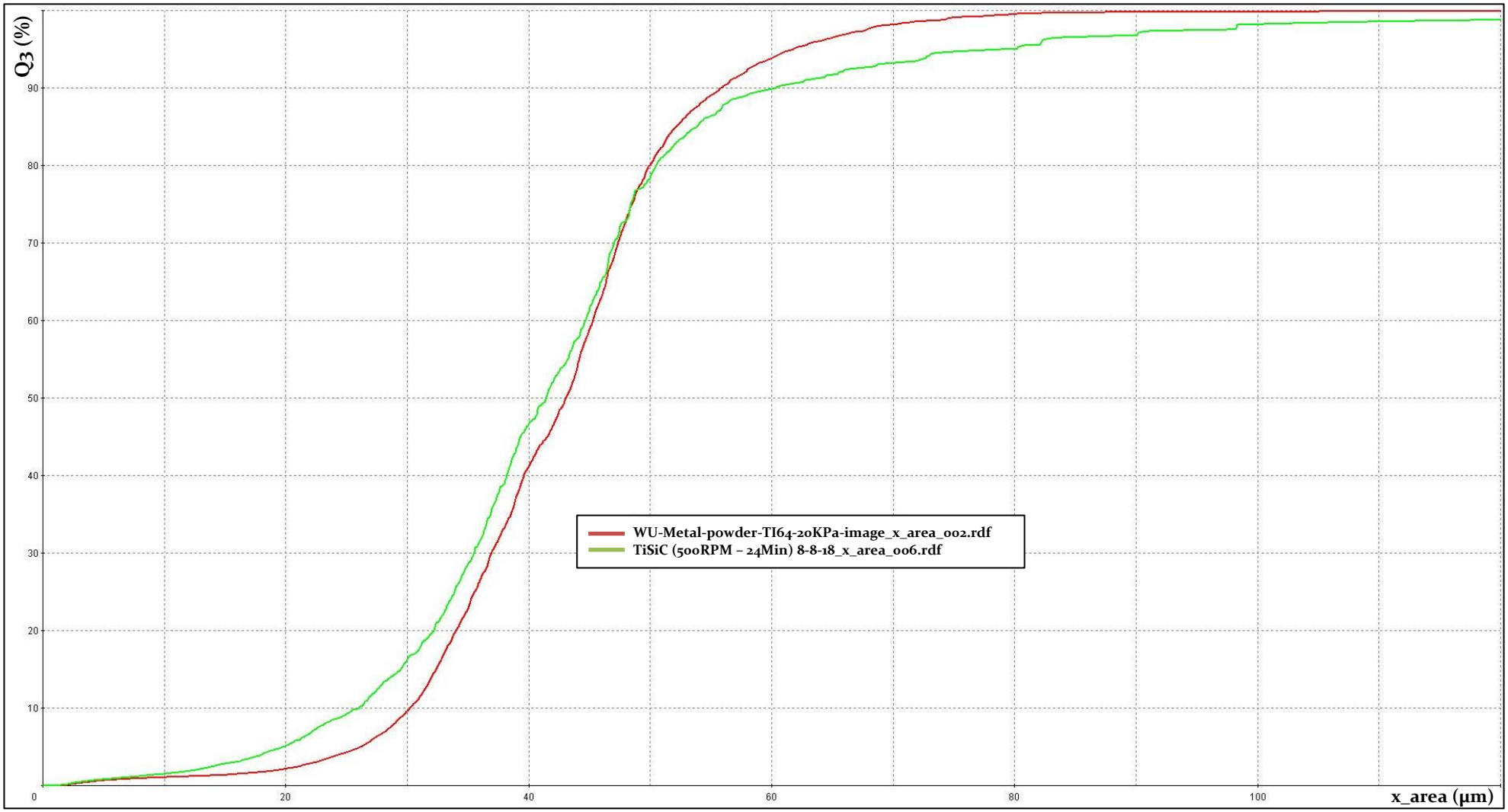

Figure 121 - X_{area} Volume Based Distribution Curve Comparison Between Ti6Al4V Baseline and MMC Feedstock Alloyed for 24 Minutes.

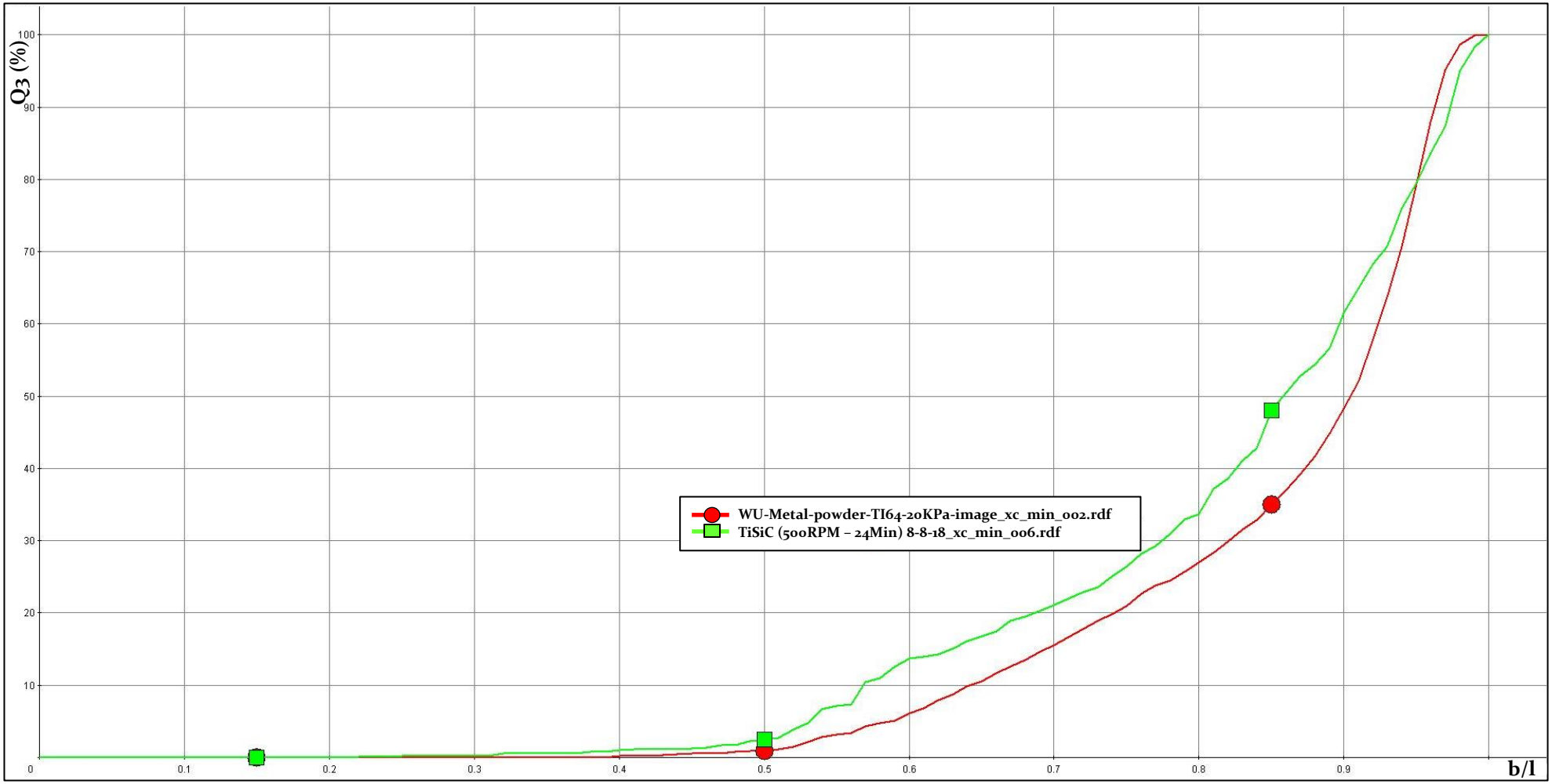

Figure 122 - b/l Volume Based Distribution Curve Comparison Between Ti6Al4V Baseline and MMC Feedstock Alloyed for 24 Minutes

Figure 122 shows b/l Volume Based Comparison Between Ti6Al4V Baseline and MMC Feedstock Alloyed for 24 Minutes, again it can be seen that the results for the MMC material (green) has shifted to the left of the Ti6Al4V material (red) , indicating that fewer particles are classed as rounded, 51.9 % in comparison to Ti6Al4V 65 %..

8.2.3 MMC Feedstock Rheology comparison against Ti6Al4V

Comparison of rheological characteristics were conducted between the MMC feedstock milled for twenty-four minutes and both the Ti6Al4V and SiC baseline results to determine the effect of the MA process. Tests included, apparent density, tap density and the angle of repose. The results are shown in Table 36.

Table 36 - Comparison of Rheological Characteristics for Ti6Al4V And MMC Feedstock.

Rheological measurement	Ti6Al4V	SiC	MMC feedstock
Material density	4.43 g/cm³	3.21 g/cm³	4.34 g/cm³
Apparent density	2.24 g/cm³	0.41 g/cm³	1.99 g/cm³
Percentage of physical density	50.6 %	12.8 %	45.8 %
Tap density	2.63 g/cm³	0.57 g/cm³	2.43 g/cm³
Percentage of physical density	59.5 %	17.8 %	56.1 %
Angle of repose	33°	48°	38°

The analysis confirmed that post MA the powder exhibited a reduction in packing and tap densities. As it is always the aim to maintain the highest apparent density, this reduction was concerning as this could lead to porosity in the parts. As tap density relates primarily to the packing density in the powder dispenser, this was not considered a problem. These reductions in packing densities indicated a loss of rounded particles and further reinforces the earlier powder morphology results.

Results for the angle of repose showed an increased angle for the MMC feedstock of 38 degrees in comparison to Ti6Al4V, 33 degrees. This was due to the MMC powder's increased surface roughness and reduced roundness, hence the steeper angle. The implications of the increased angle of repose would be that the powder may resist spreading by the recoater arm between layers. This would need to be investigated.

8.3 Phase 2b: MMC Feedstock Analysis for Moisture, Size, Morphology and Rheology in Comparison to Baseline Assessment, Phase 1a Conclusions

1 In comparison to Ti6Al4V, the moisture content of the MMC feedstock increased due to the incorporation if the SiC reinforcement, however, this was less than the upper limit established within the research and lower than SiC alone, there was no need to further process the feedstock.

2 Particle size and size distribution for the MMC material alloyed for twenty-four minutes exhibited changes in the size distribution curve with increases in small and large fines. It was concluded that an increased quantity of small fines was attributed to un-alloyed SiC and the increase in large fines was due to the SiC coating the surface of the Ti6Al4V particles. These results varied between alloying times and was optimal at twenty-four minutes.

3 Rheologically, the results for the MMC feedstock sat between those of Ti6Al4V and SiC. In comparison to Ti6Al4V, apparent density decreased from 50.6 % to 45.8 %, an indication that 4.8 % less material would be available per recoated layer. Angle of repose increased from 33° to 38° indicating that the surface of the particles was rougher and less likely to flow during recoat.

Chapter Nine

9.0 Phase 3a Assessment of MMC Single beads evaluated against energy density in comparison to Ti6Al4V baseline

9.1 Phase 3a: Assessment of MMC Single Beads Evaluated Against Energy Density in Comparison to Ti6Al4V Baseline Methodology

9.1.1 Overview of The Experiment/Design

Following the experimental methodology used in phase 1b (chapter 6.0), the successfully alloyed MMC feedstock was processed using the EOS M290 machine and followed the same procedure as in chapter 6.0, using the scan parameters from Table 23 to ensure that the material was exposed to the known energy densities. The results were compared to the phase 1b results of Ti6Al4V.

Based on the findings a selection of single beads was chosen for phase 3b.

9.2 Phase 3a: Assessment of MMC Single Beads Evaluated Against Energy Density in Comparison to Ti6Al4V Baseline Results and discussion

Using the MMC feedstock MA for twenty-four minutes, single beads were exposed. The two-rail system was used to ensure a reliable layer thickness and beads were exposed using the same variables (Table 24) and attributes (Table 25), as were used for the baseline evaluation of Ti6Al4V.

As with the baseline assessments of Ti6Al4V, measurements were taken of the mean bead width in a vertical direction along with the width of the bead ($w1$), the width of the substrate penetration ($w2$), the height of the bead ($h1$) and the depth of the substrate penetration ($h2$), from a transverse section, for comparison.

In Initial observations the MMC powder exposed at 150 W showed evidence of miscibility with the substrate and an ability to form a continuous bead whilst maintaining a uniform width and height. In comparison to Ti6Al4V, the bead formations appear to be similar, with the MMC beads having improved flow across the substrate, demonstrated as regions either side of the bead as shown in Figure 126c.

Ti6Al4V Vertical (10 x magnification)	Ti6Al4V Transverse section (20 x magnification)	MMC Vertical (10 x magnification)	MMC Transverse section (20 x magnification)
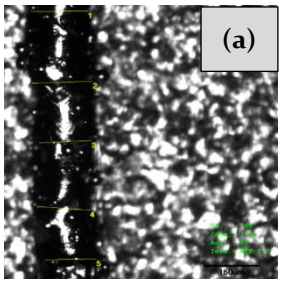	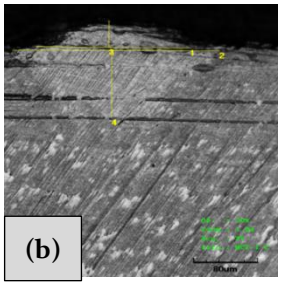	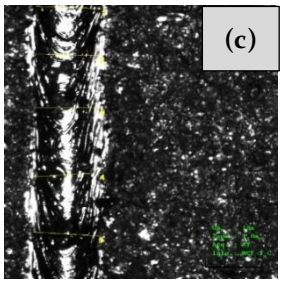	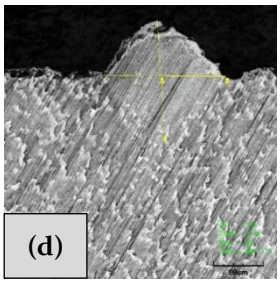
E = 200 J/mm³ **V** = 250 mm/s **Mean bead width, vertical** = 161.505 µm (σ 11.1 µm) **h1** = 40.625 µm **h2** = 101.875 µm **w1** = 196.884 µm **w2** = 265.628 µm		**E** = 200 J/mm³ **V** = 250 mm/s **Mean bead width, vertical** = 172.530 µm (σ 21.2 µm) **h1** = 86.985 µm **h2** = 91.259 µm **w1** = 198.759 µm **w2** = 200.004 µm	

Figure 123 - Single Ti6Al4V Bead at 150 W laser power, 200 J/mm³ energy density in comparison to MMC material

This is thought to be a result of lower surface tension and therefore increased fluidity of the melt pool. At lower energy density range of 25 J/mm³ to 75 J/mm³ this phenomenon is less evident. This phenomenon is also only visible within a vertical perspective, unmeasurable in the transverse sectional views meaning that this could merely be a wetting effect and not contributing to the physical bead. It is however intriguing as to why this only occurs with higher energy densities, it could also be plausible that these areas are the result of the material expanding during its liquidus stage before contracting to form the solid bead, leaving evidence behind. This would require further investigation, but if so, could demonstrate that the MMC material forms better at lower energy densities.

Ti6Al4V Vertical (10 x magnification)	Ti6Al4V Transverse section (20 x magnification)	MMC Vertical (10 x magnification)	MMC Transverse section (20 x magnification)
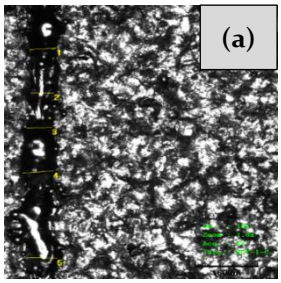	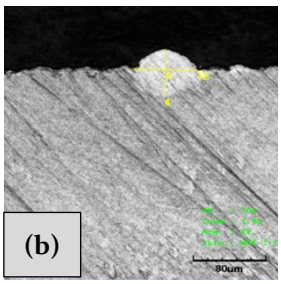	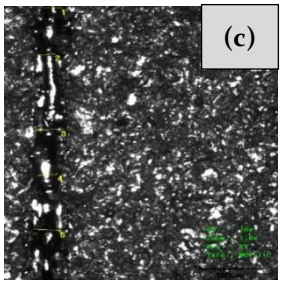	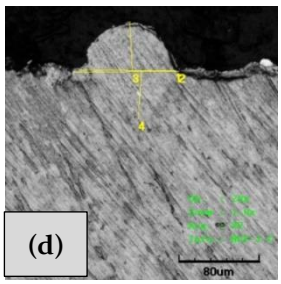
E = 25 J/mm³ **V** = 2,000 mm/s **Mean bead width, vertical** = 70.618 µm (σ 8.8 µm) **h1** = 27.500 µm **h2** = 33.756 µm **w1** = 72.543 µm **w2** = 82.521 µm		**E** = 25 J/mm³ **V** = 2,000 mm/s **Mean bead width, vertical** = 57.883 µm (σ 12.4 µm) **h1** = 50.687 µm **h2** = 48.226 µm **w1** = 96.877 µm **w2** = 108.127 µm	

Figure 124 - Single Ti6Al4V Bead at 150 W laser power, 25 J/mm³ energy density in comparison to MMC material

Beads exposed at 2,000 mm/s, displayed discontinuity within the bead due to the high velocity of the laser (Figure 124a and c). All beads showed good penetration of the substrate. There was no evidence of balling from beads other than at 2,000 mm/s, and spatter appeared to be less prominent with the MMC material than with Ti6Al4V. bead size also appeared to be larger for the MMC material in comparison to Ti6Al4V, this will be discussed further within this chapter. Full results can be found in appendix 6.

Observations the MMC powder exposed at 250 W (appendix 7), once again showed good evidence of miscibility with the substrate with continuous beads for scan speeds up to 1,000 mm/s. beads for both the MMC material and Ti6Al4V materials at 2,000 mm/s showed discontinuity.

Ti6Al4V Vertical (10 x magnification)	**Ti6Al4V Transverse section (20 x magnification)**	**MMC Vertical (10 x magnification)**	**MMC Transverse section (20 x magnification)**
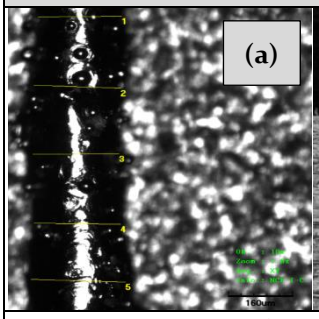	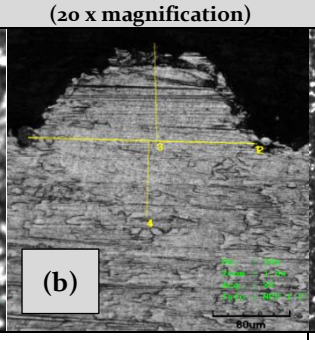	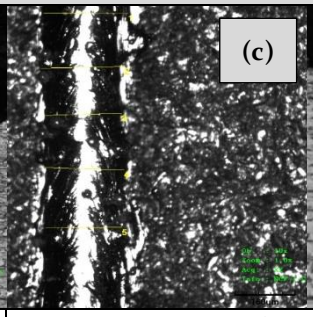	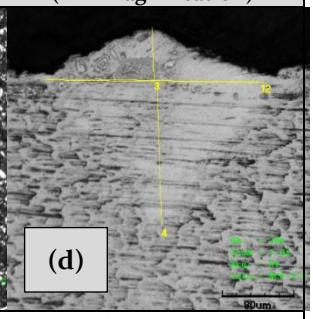
E = 375 J/mm³ **V** = 222 mm/s **Mean bead width, vertical** = 223.314 µm (σ 10.7 µm) **h1** = 115.652 µm **h2** = 90.020 µm **w1** = 240.742 µm **w2** = 243.847 µm		**E** = 375 J/mm³ **V** = 222 mm/s **Mean bead width, vertical** = 217.052 µm (σ 11.5 µm) **h1** = 60.029 µm **h2** = 166.325 µm **w1** = 243.779 µm **w2** = 255.019 µm	

Figure 125 - Single Ti6Al4V Bead at 250 W laser power, 375 J/mm³ energy density in comparison to MMC material

Comparison between Ti6Al4V and MMC beads showed similarities in bead-form without significant under-cutting. There was no evidence of balling other than with the bead exposed at 2,000 mm/s, and there was a reduction in spatter shown with the MMC material in comparison to Ti6Al4V.

The improved wettability phenomenon, once again was observed with the MMC beads having improved flow across the substrate for energy density levels from 250 J/mm³ to 417 J/mm³ demonstrated as regions either side of the bead as shown in Figure 129c.

At 350 W the visual evidence presented a similar picture to the images for both 150 W and 250 W with good bead continuity, reduced spatter with the MMC material and no evidence of balling and at all scan speeds, bead quality was acceptable except for beads produced at 2,000 mm/s. The improved wettability phenomenon was once again observed with the MMC beads having an energy density range from 408 J/mm³ to 583 J/mm³. There was no evidence to show that cracks had propagated longitudinally or laterally on the beads surface. This were clear indications that the material within both

the Ti6Al4V beads and the MMC beads were ductile. Full results can be found in appendix 8.

Figure 126 shows the Comparison between MMC and Ti6Al4V versus energy density, displaying the calculated mean values from measurements taken in five places along the bead, viewed in the vertical axis. Error bars represent ± 1σ.

Comparison between the two feedstocks showed no significant variation. However, by representing the results in the form of linear trends (Figure 127), it was possible to see that as the energy density increased, the beads produced from the MMC feedstock became wider in comparison to this produced from Ti6Al4V with the same build parameters. This indicated that the meltpool remained at a high temperature for a longer period, such that it could consume additional powder particles producing a wider bead. This would indicate that the MMC material requires less energy density as opposed to more as was originally hypothesised.

This phenomenon, however, only appears at specific energy densities for each laser power, below which the bead widths for the MMC feedstock are narrower than Ti6Al4V. For a laser power of 150 W this point was at ~ 80 J/mm^3, for 250 W the point was at ~ 262 J/mm^3, and for 350 W it was at ~ 160 J/mm^3. Whilst increased width is an indication of improved flow of the molten bead across the substrate, increased height is an indication of powder consumption, where both are observed it would indicate that the formation of the bead is consuming more feedstock than Ti6Al4V and, is remaining hotter for longer thus continuing to consume feedstock and remain more fluid. The increased depth of substrate penetration will also increase localised heat.

Figure 126 - Comparison Between Vertical MMC and Ti6Al4V Average Bead Widths (*w1*) at 150 W, 250 W and 350 W Versus Energy Density.

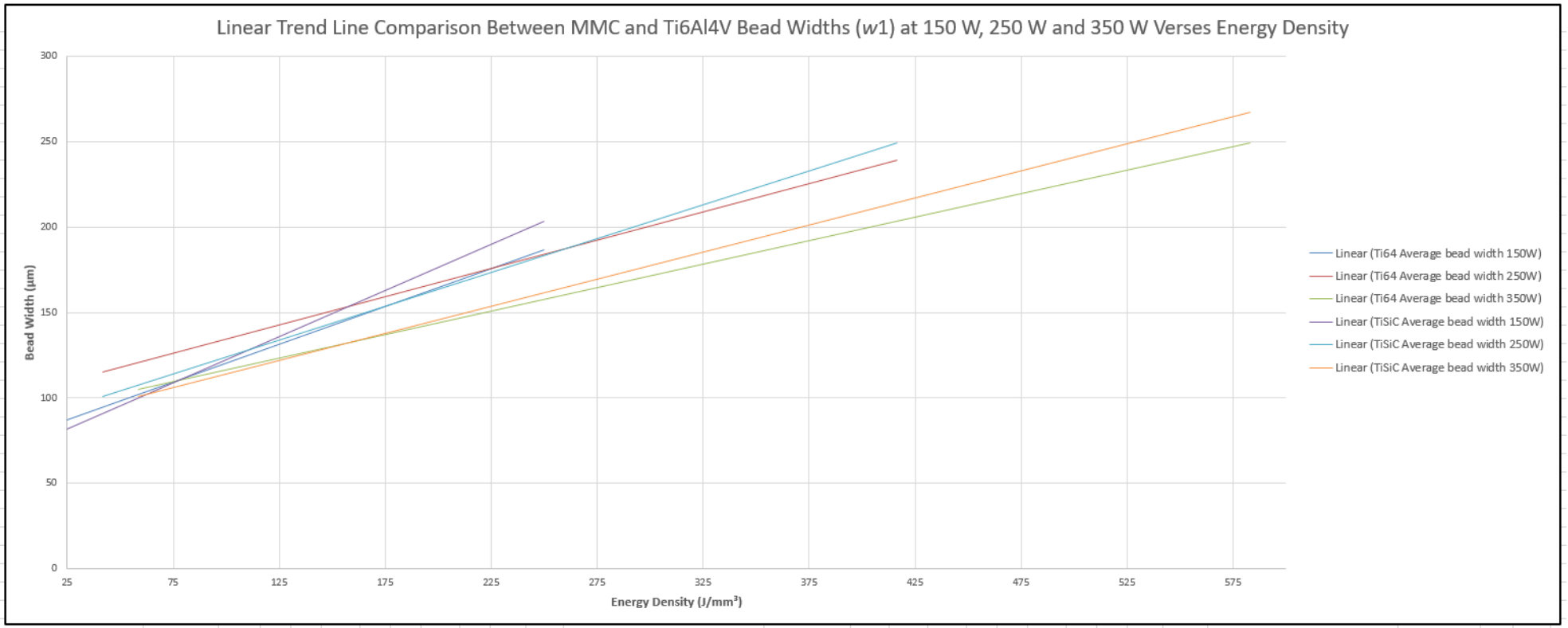

Figure 127 - Linear Trend Line Comparison Between Vertical MMC and Ti6Al4V Bead Widths (*w1*) at 150 W, 250 W and 350 W Versus Energy Density.

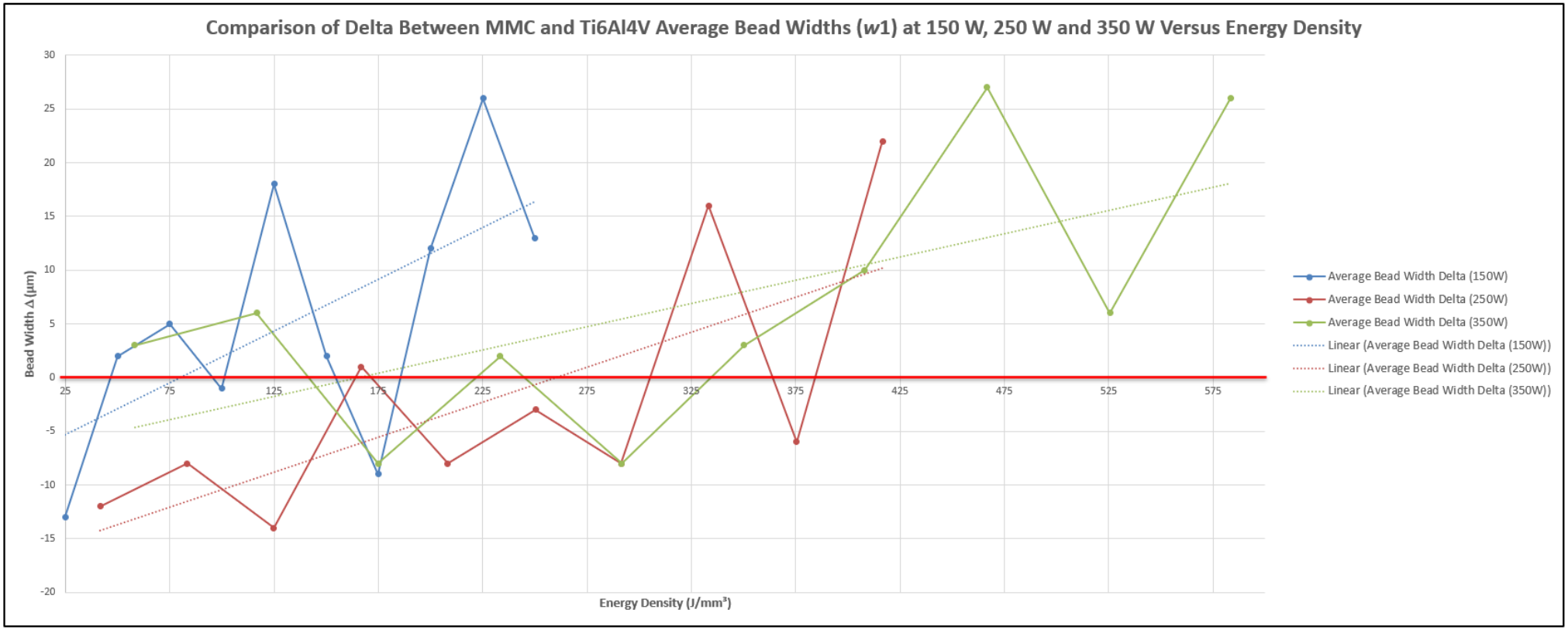

Figure 128 - Comparison of Delta (Δ) Between MMC and Ti6Al4V Average Bead Widths (*w*1) at 150 W, 250 W and 350 W Versus Energy Density.

Figure 129 shows comparison between MMC and Ti6Al4V bead height (h1) at 150 W, 250 W and 350 W versus energy density. It can be seen from the results that the bead height increases in size as a function of energy density.

In comparison between feedstock materials, for Ti6Al4V beads exposed at 150 W, the bead height remained below 60 μm, however, the bead height for the MMC material is above, only two values remained below, these being at the lower range of energy densities.

This evidence would also confirm the new hypothesis that the MMC material requires less energy.

This however was not the case for MMC beads produced with a laser power of 250W, a large proportion of the beads were lower in height than the equivalent Ti6Al4V beads. This was also the case for MMC beads produced with a 350 W laser power.

Analysis of substrate penetration (Figure 130) showed that for a laser power of 150 W, penetration remained below 90 μm, and was less than that of the Ti6Al4V material. For laser powers of 250 W and 350 W, substrate penetration exceeded that of Ti6Al4V indicating that the additional laser power, whilst demonstrating reductions in bead height, also increased the depth of substrate penetration with no benefit to the process.

Figure 131 shows comparison between MMC and Ti6Al4V substrate penetration width (w2) at 150 W, 250 W and 350 W versus energy density. As with initial observations of the baseline material, the width of substrate penetration increased as a function of energy density. Comparison between materials showed no significant change in width per energy density.

Combined analysis of all four bead characteristics showed that the beads formed using the MMC feedstock were predominately larger than those from Ti6Al4V at elevated energy densities, indicating that similar sized beads could be produced with lower energy densities. Increases in energy density, whilst still producing satisfactory bead formations, failed to improve on those produced at the lower range, beads appeared wider, flatter and substrate penetration increased excessively.

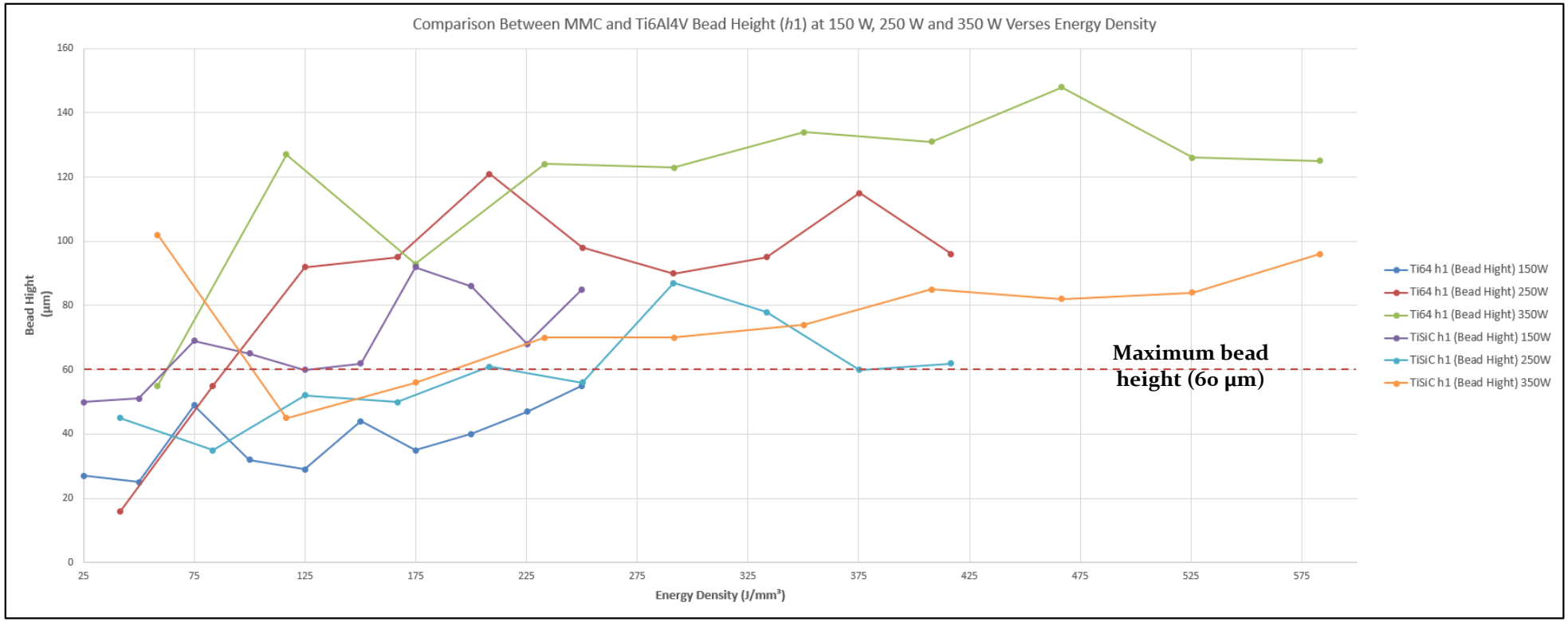

Figure 129 - Comparison Between Transverse MMC and Ti6Al4V Bead Height (h_1) at 150 W, 250 W and 350 W Versus Energy Density

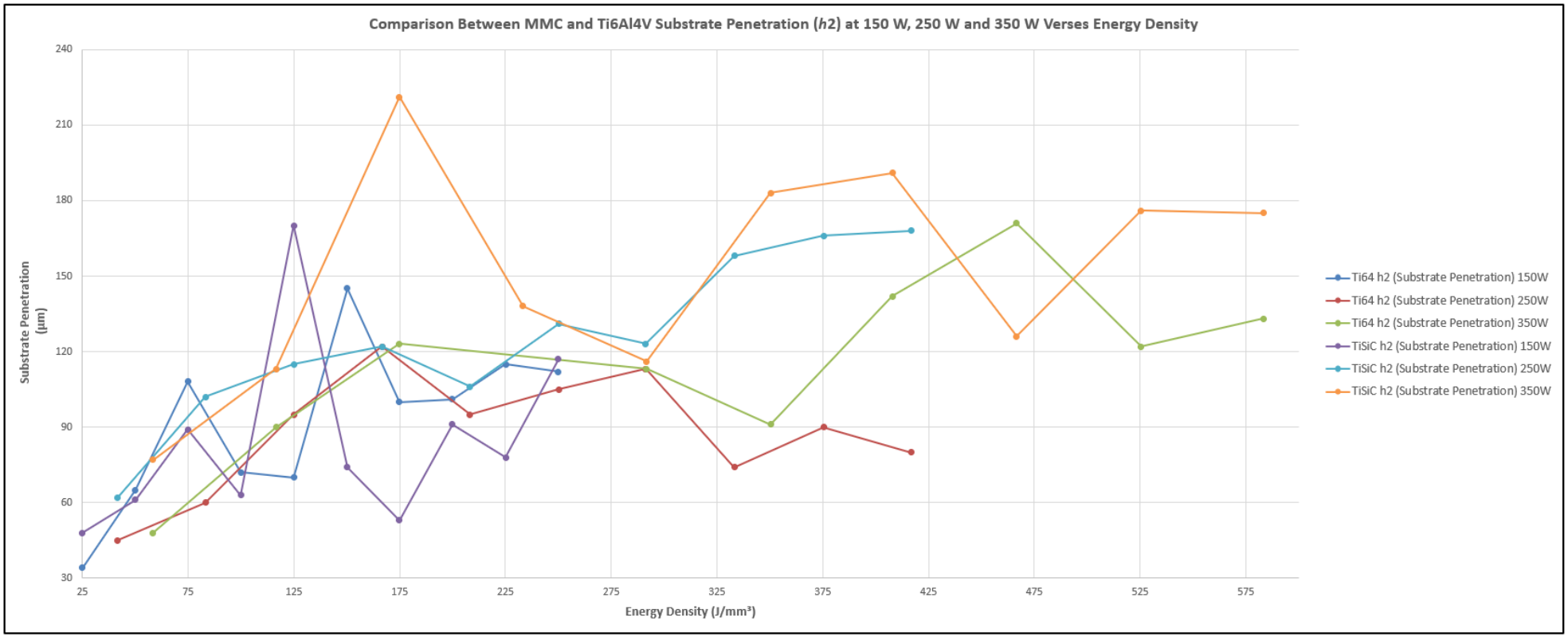

Figure 130 - Comparison Between Transverse MMC and Ti6Al4V Substrate Penetration (h_2) at 150 W, 250 W and 350 W Versus Energy Density.

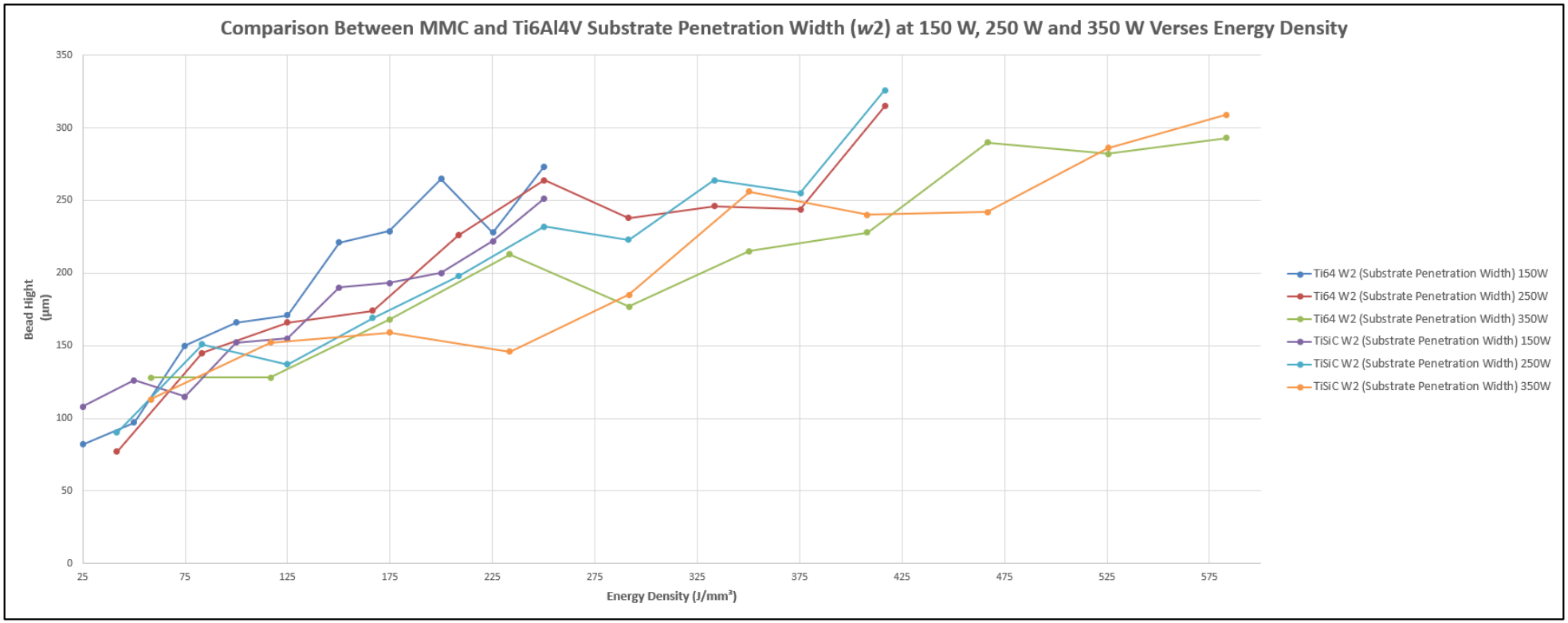

Figure 131 - Comparison Between Transverse MMC and Ti6Al4V Substrate Penetration Width (*w2*) at 150 W, 250 W and 350 W Versus Energy Density.

9.3 Phase 3a: Assessment of MMC Single Beads Evaluated Against Energy Density in Comparison to Ti6Al4V Baseline Conclusions

1 Comparison between bead form of the MMC feedstock and baseline Ti6Al4V, showed close similarities from increasing energy densities.

2 It could be seen from the graphical representations of data that the MMC feedstock required less energy to form beads of equivalent form and size. It was also established that increased energy density, produced larger beads and therefore the evidence of larger beads within the MMC data set would indicate Higher energy within the bead. Theoretically this could be due to improved absorptivity of the laser energy or a reduction in reflectivity. This was in contradiction to initial theories that increased energy was required for synthesis and would require further investigation.

Chapter Ten

10.0 Phase 3b Hatch spacing evaluation of MMC material, multiple beads

10.1 Phase 3b: Hatch Spacing Evaluation of Multiple Beads Methodology

10.1.1 Overview of The Experiment/Design

Based on the results of phase 3a, a selection of successful parameters were chosen, and the bead width was used to determine the most effective hatch spacing for phase 3b. A single layer of beads was produced with fixed scan direction, layer thickness and environmental conditions.

Table 37 - Example Hatch Spacing Calculation Form.

MMC Feedstock												
(A)					(B)							
					Hatch Spacing (*h*) (µm)Calculation							
Laser Power (W)	Scan Speed (v)	Target Energy Density (Ed) (J/mm³)	Bead height (*h*1) from phase 3a (µm)	Bead Width (*w*1) from phase 3a (µm)	40 % (*w*1)	60 % (*w*1)	80 % (*w*1)	100 % (*w*1)	120 % (*w*1)	140 % (*w*1)	
150	1,000	50	51	0.099	0.040	0.059	0.079	0.099	0.119	0.139	(*h*)

Using the example shown above in Table 37, each successful set of parameters from phase 3a, highlighted (A), was built with the hatch spacing intervals ranging, highlighted in (B), from 40 % of the measured bead width (*w*1), up to 140 % as shown in the example. Bead selection was based initially on bead height. Beads with a height exceeding 60 µm will adversely affect mechanical recoating (Yadroitsev, and Smurov, 2010). This was measured from transverse sections using an Olympus LEXT 3100 confocal microscope (Olympus, UK). Beads were also assessed for bead continuity, beads with high scan speeds but low energy density exhibited gapping along the bead and were rejected. This was also observed using an Olympus LEXT 3100 confocal microscope (Olympus, UK). Finally beads that exhibited poor adhesion to the substrate or lacked substrate penetration were rejected as these were indications of unsatisfactory parameters, falling outside the processability window (Dadbakhsh, et al., 2012). This was also measured

from transverse sections using an Olympus LEXT 3100 confocal microscope (Olympus, UK).

Beads on or close to the build platform are characteristically wider than those in the build due to differences between the volume of the build platform material and the part, surface finish of the build platform where a lower roughness promotes wetting and flowability, and initial temperature of the first few layers of build. It was therefore decided to begin with a hatch spacing 40 % of the W1 measurement (Figure 9 - Dimensioned transverse sectioned 316L stainless steel single beads (Yadroitsev, et al., 2012) Yadroitsev, et al., 2012), with the proceeding bead increasing in 20 % increments up to 140 % of the *w1* measurement. A value of 100 % giving a hatch spacing equal to that of the bead (*w1*).

10.1.2 Determination of successful hatch spacing

Successful hatch spacing was determined by measurement of transverse sections from the samples exposed in accordance with Table 38, it is well understood that the spacing between beads is important to successful part manufacture (Taylor, et al., 202). Beads that are closer than the beads with exhibit minimal form due to insufficient feedstock as the process is occurring within the powder consolidation zone. Conversely, beads that are further apart than required exhibit uniform bead form due to adequate supply of feedstock, however, un-fused powder remains between beads, this has been sown to lead to porosity in parts (Yadroitsev and Smurov, 2011). From the range of samples produced, measurements were taken using Olympus LEXT 3100 confocal microscope (Olympus, UK).

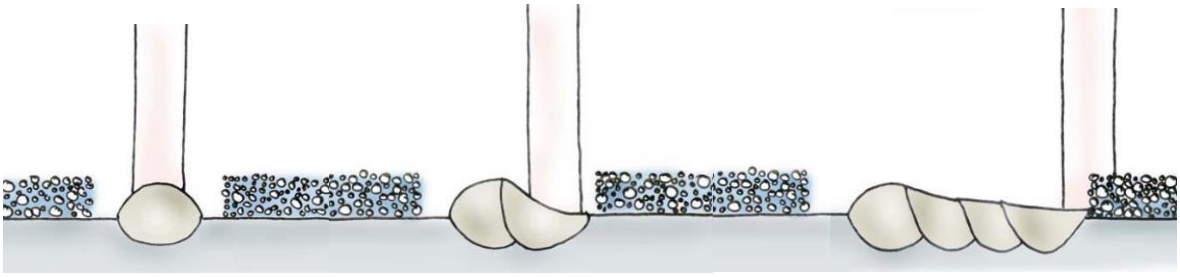

Figure 132 - Scheme of consecutive reduction of the powder consolidation zone, Yadroitsev (2011)

Yadroitsev and Smurov in their 2011 paper discussed the effects of hatch spacing and shared observations of bead formation on the first layer in the build, pointing out the deleterious effect of scans within the consolidation zone (Figure 132), the reduced incident energy absorption in comparison to loose powder and the decrease in melted material in proportion to decreased hatch distance concluding that "*Analysis of the influence of the hatch distance on forming the first layer from metal powder showed that the value of the maximum shift distance should not exceed average width of the continuous track*" (Yadroitsev and Smurov, 2011).

10.1.3 Phase 3b Variables

Multiple beads were exposed for a single layer using the two-rail method of build plate to establish a 45 µm to 50 µm layer thickness.

Variables consisted of laser power and scan speeds as calculated in Table 23, to achieve the same range of energy densities but to also evaluate the effect of hatch distance. It is at this point that the energy density equation used for calculations for single beads, Equation 4 can revert to the use of the hatch spacing term (h) instead of spot size (s) as in Equation 1.

Based on the findings from phase 3a (single beads) only beads of a height less than 60 µm were taken forward to phase 3b, in order to maintain contact-free recoating.

As an initial starting point, rather than selecting a fixed hatch distance a range of distances were used based on the measured bead widths from phase 3a as shown in Table 39.

10.1.4 Phase 3b Attributes

For the software (EOSPrint 1.5) to produce multiple beads in the same direction, the following parameters were set for the build process (Table 38).

Table 38 - Build Attributes for Hatch Spacing Experiment

Parameter Setting	Value
Hatch spacing	See Table 39
Stripe width	40 mm
Pre-Contours	Off
Post-Contours	Off
Rotation	Off
X, Y	X Only (Recoat along the bead)
Alternating	Off
DMLS	Off
Pre-Exposure	Off
Up skin	Off (Thickness = 0)
Down skin	Off (Thickness = 0)
Beam expander	Automatic
Platform heating	40°C

10.2 Phase 3b: Hatch Spacing Evaluation of Multiple Beads Results and discussion

Beads were selected from phase 3a based on bead height giving eleven suitable beads in total. At this stage it is unclear whether these parameters will produce fully dense parts, it is however known that the single beads produced, achieved satisfactory shape, substrate penetration and were lower than 60 µm in height. Based on the width of the bead, the hatch spacing was calculated in accordance with Table 37. To further filter selected beads, those scanned at 2,000 mm/s were discounted on the basis that these were outside the processability window, were discontinuous and balling in nature. The remaining hatch spacing calculations are found in Table 39.

Table 39 - Hatch Spacing Calculation.

MMC Feedstock											
Laser Power (W)	Scan Speed (v)	Energy Density (*E*d) (J/mm³)	Bead height (h_1) from phase 3a (µm)	Bead Width (w_1) from phase 3a (mm)	Hatch Spacing (*h*) (mm) Calculation						
					40 % (w_1)	60 % (w_1)	80 % (w_1)	100 % (w_1)	120 % (w_1)	140 % (w_1)	
150	1,000	50	51	0.099	0.040	0.059	0.079	0.099	0.119	0.139	(*h*)
250	1,000	83	35	0.130	0.052	0.078	0.104	0.130	0.156	0.182	(*h*)
	667	125	52	0.132	0.053	0.079	0.106	0.132	0.158	0.185	(*h*)
	500	167	50	0.162	0.065	0.097	0.130	0.162	0.194	0.227	(*h*)
	333	250	56	0.182	0.073	0.109	0.146	0.182	0.218	0.255	(*h*)
350	1,000	117	45	0.119	0.048	0.071	0.095	0.119	0.143	0.167	(*h*)
	667	175	56	0.149	0.060	0.089	0.119	0.149	0.179	0.209	(*h*)

Tests were conducted in accordance with the methodology, transverse sectional samples were obtained using wire electro discharge machining (WEDM), polished using Struers polishing equipment and following the Struers polishing application notes appendix 2. Samples were observed using an Olympus LEXT 3100 confocal microscope (Olympus, UK) and measurements were taken between the bead's centrelines. Results are shown below.

Measurements were taken between peaks and compared with the calculated hatch spacings shown in Table 39. It can be seen from the images presented that determining

the centreline of the individual beads was challenging. In these cases, no result was recorded. Similarly, the accuracy of measurements can be questioned on the grounds that the true centre or peak of a bead has a degree of randomality associated. This is true and the transvers sections are also random to avoid bias in the results. Where peaks are indistinguishable it can be evidence that the beads are unacceptably close, and the result should be discounted due to fusion taking place within the denuded zone.

Figure 133 shows transverse sectional Views of Hatch Spacings ranging from 40 % of the bead's original width ($w1$), up to 140 %. Laser power was 150 (W), scan speed was 1,000 mm/s (v) and the layer thickness remained at 0.030 mm (t). the two-rail system was used to ensure an accurate layer of feedstock.

At 150 W, beads can be clearly seen, and the measurements taken are comparable with those calculated. All spacings appear to be equal with a consistently level progression is seen, demonstrating uniform use of feedstock. Preferred hatch spacings from these tests would be those at 100 % (Figure 133d) and 120 % (Figure 133e) of $w1$, based on the beads being neither too close nor too far apart, therefore a hatch spacing of between 0.099 mm to 0.119 mm would be recommended.

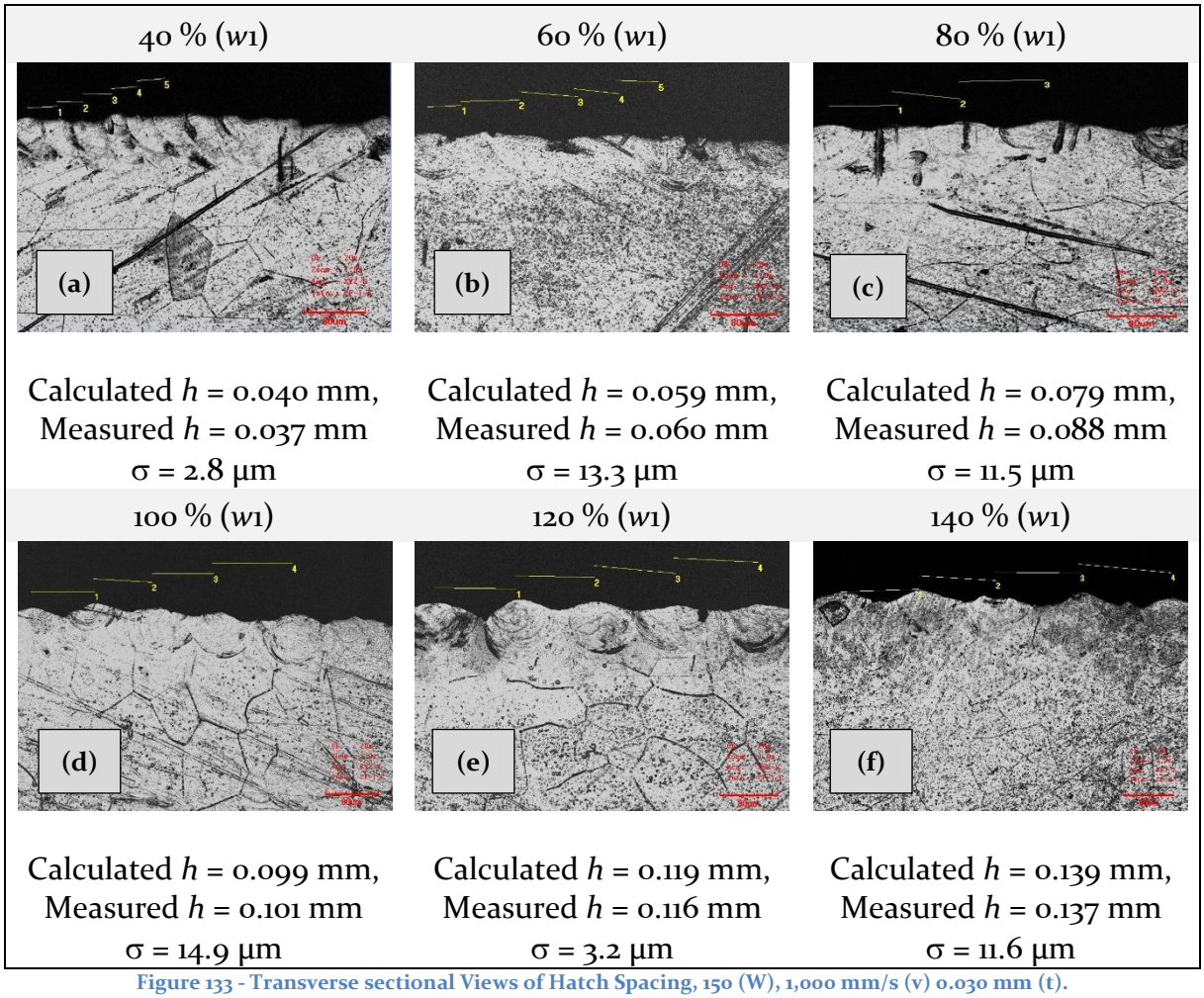

Figure 133 - Transverse sectional Views of Hatch Spacing, 150 (W), 1,000 mm/s (v) 0.030 mm (t).

In Figure 134 laser power was 250 (W), scan speed was 1,000 mm/s (v) and the layer thickness remained at 0.030 mm (t). Beads are more challenging to distinguish and measure, at 40 % of *w*1 (Figure 134a), there appears to be a flat surface, substrate penetration can be seen. At 60 % *w*1 (Figure 134b), individual beads can be seen, however, these do not correlate with the calculated hatch spacing and therefore would not be accurate in this case. This would indicate that beads created with a hatch spacing of 40 % (Figure 134a) or 60 % (Figure 134b) merely re-melts the existing structure. Measurements taken for hatch spacings of 80 % *w*1 (Figure 134c) and 100 % *w*1 (Figure 134d), compared accurately with calculated values, as did the hatch spacing at 140 % (Figure 134f). At 120 % *w*1 (Figure 134e), difficulties in determining points to measure, resulted in inaccurate measurements. This is unfortunate as this may prove to be a good spacing. At 100 % *w*1, the beads overlap resulting in a minor gap between the fourth and fifth peaks. This is due to insufficient feedstock. Similarly, it could be argued that the hatch spacing for 140 % *w*1, is too far apart, all beads are similar in shape indicating that they received equal quantities of feedstock, however, this spacing could result in porosity within parts produced. This said, the preferred hatch spacings from these tests would be those at 100 %, 120 % and 140 % of *w*1 (Figure 134d, e & f), based on the beads being neither too close nor too far apart, therefore a hatch spacing of between 0.130 mm to 0.182 mm, would be chosen.

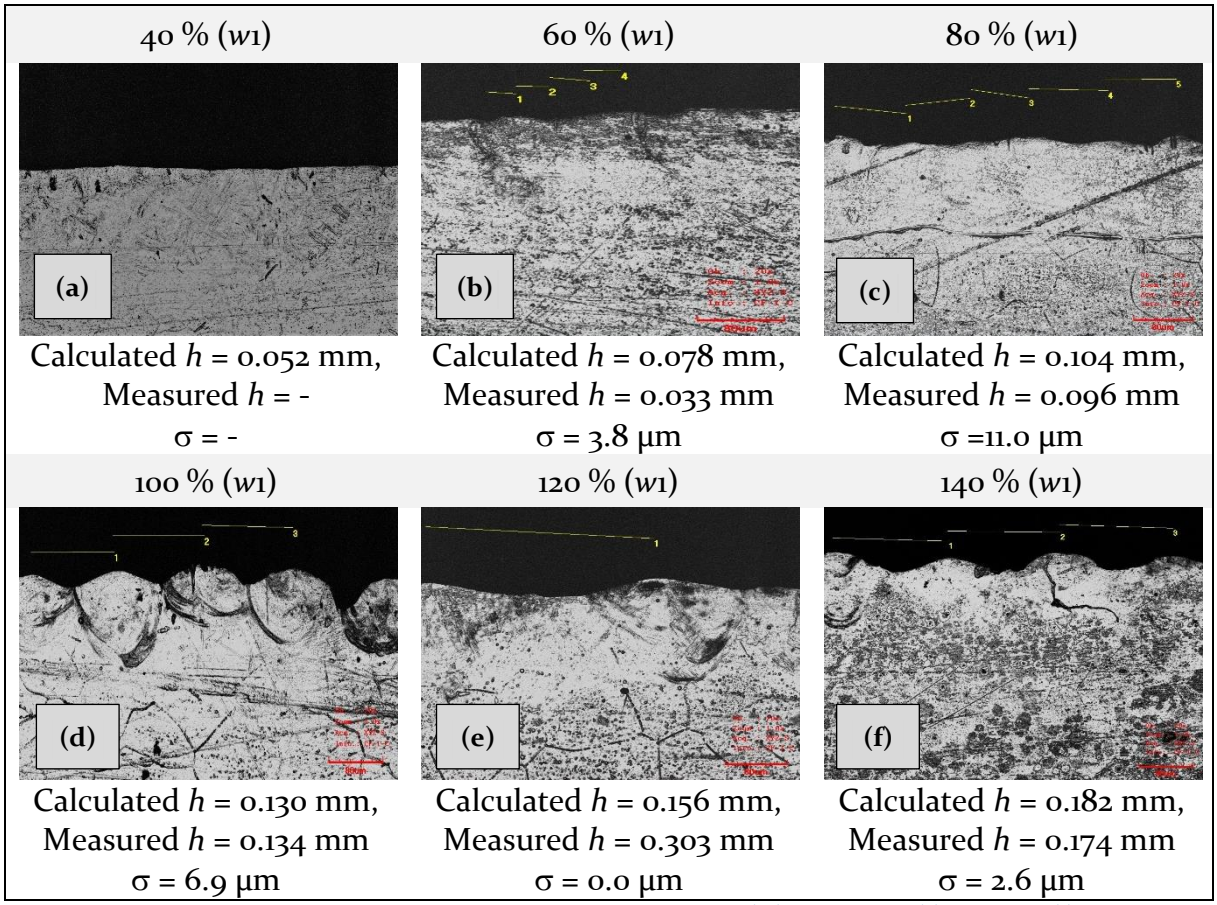

Figure 134 - Transverse sectional Views of Hatch Spacing, 250 (W), 1,000 mm/s (v) 0.030 mm (t).

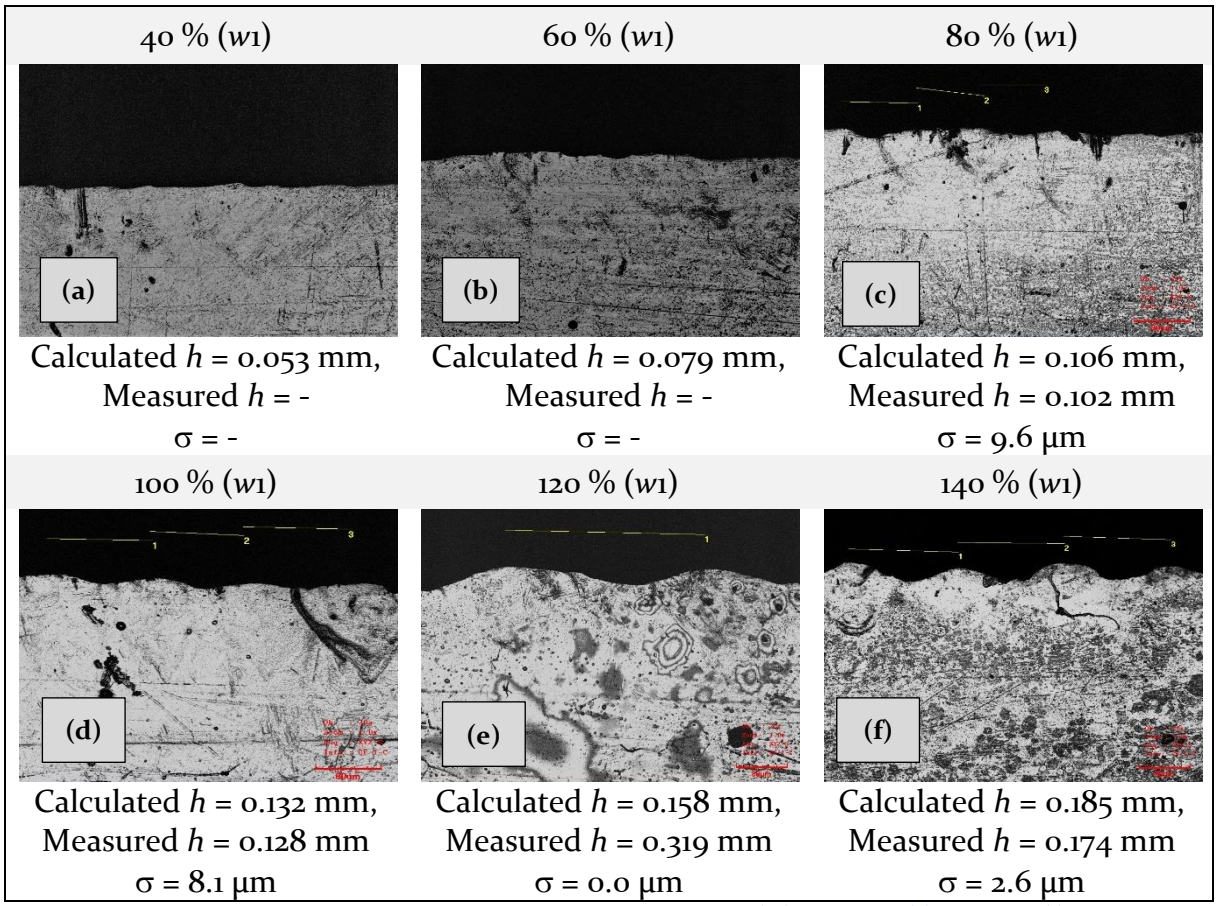

Figure 135 - Transverse sectional Views of Hatch Spacing, 250 (W), 667 mm/s (v) 0.030 mm (t).

In Figure 135 laser power was 250 (W), scan speed was 667 mm/s (v) and the layer thickness remained at 0.030 mm (t). Beads are again challenging to distinguish and measure, at 40 % (Figure 135a) and 60 % of *w*1 (Figure 135b), where the surface appears flat. At 80 % *w*1(Figure 135c), the shape of individual beads can be seen, and the measured values correlate with the calculated values, as do those at 100 % (Figure 135d) and 140 % of *w*1 (Figure 135f). Beads measured at 120 % *w*1 (Figure 135e) were inappropriate owing to the indistinguishability of the peaks. This again is due to the manner in which the feedstock is consumed, due to the energy density levels, the single bead consumes excessive amounts of feedstock from the surrounding area, the subsequent hatch spacing is therefore too small to encounter sufficient feedstock and is therefore smaller than required, the next bead is then produced in an area of sufficient feedstock and the bead is once again the correct size. It can also be seen that at 100 % *w*1 (Figure 135d), the profile is relatively flat, however, the substrate penetration is large (~ 80 µm), this would indicate that rather than producing a satisfactory bead, the process is removing feedstock from the area and the energy is going into the substrate. Therefore, based on the evidence, the selected hatch spacing would be around 0.185 mm (140 % *w*1, Figure 135f).

This phenomenon is similar in Figure 136 with hatch spacings at 40 % (Figure 136a) and 60 % of *w*1 (Figure 136b) producing near flat surfaces, hatch spacings of 80 %, 100 % and 140 % of *w*1 (Figure 136c, d & f) producing measurements comparable with those calculated and a hatch spacing of 120 % *w*1 (Figure 136e) demonstrating evidence of feedstock deficiencies. The hatch spacing of 100 % of *w*1 (Figure 136d) can be seen to overlap marginally, this would prove inefficient during production and could lead to higher residual stress levels. Therefore, for a laser power of 250 W and a scan speed of 500 mm/s, the chosen hatch spacing should be approximately 0.227 mm (140 % *w*1, Figure 136f).

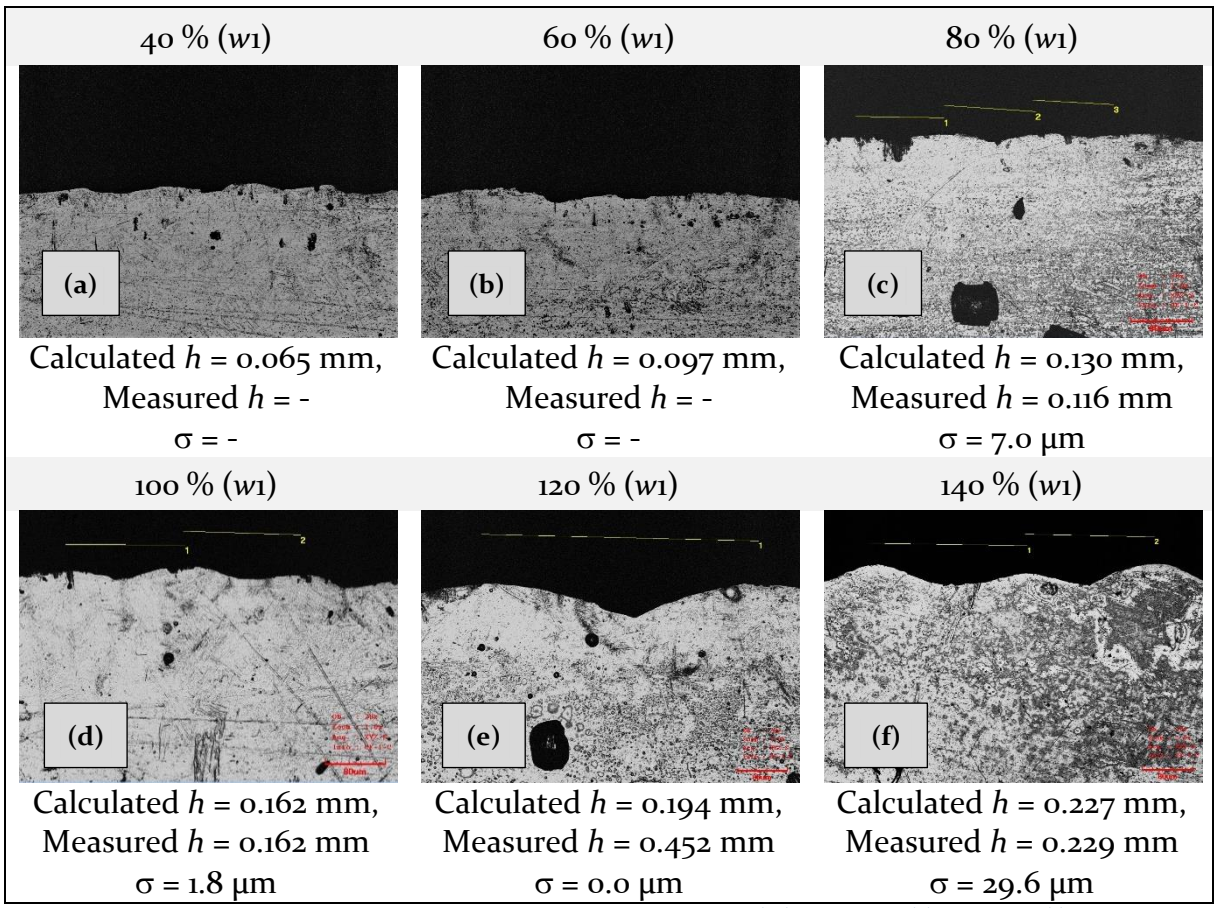

Figure 136 - Transverse sectional Views of Hatch Spacing, 250 (W), 500 mm/s (v) 0.030 mm (t).

From Figure 137 with a laser power of 250 W and a scan speed of 333 mm/s, similar observations can be made to Figure 136. A hatch spacing of 0.255 mm would be chosen based on the evidence (140 % *w*1, Figure 137f).

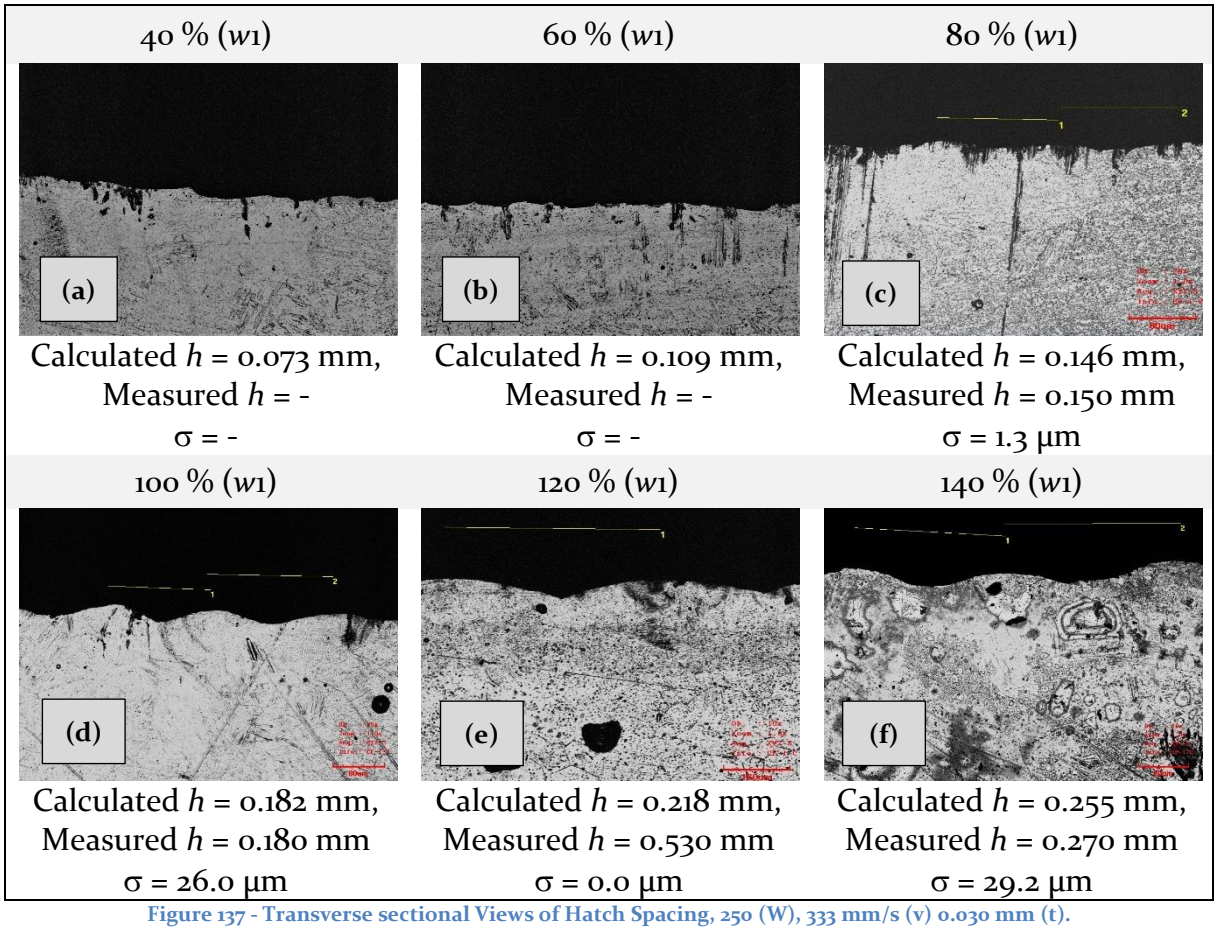

Figure 137 - Transverse sectional Views of Hatch Spacing, 250 (W), 333 mm/s (v) 0.030 mm (t).

Samples analysed from transverse sectional views of hatch spacings produced at 350 W, with a scan speed of 1,000 mm/s are presented in Figure 138. Hatch spacings from 40 % to 100 % of w1 (Figure 138a-d) are largely flat, whilst it appeared possible to obtain measurements at 80 % w1 (Figure 138c), this was not comparable with the calculated value. Similarly, measurements taken at 100 % w1 (Figure 138d) were accurate but showed excessive overlapping of the beads. At 120 % w1 (Figure 138e), individual beads can be seen however, these are twice that of the calculated hatch spacing, indicating that feedstock is being consumed preferentially, leaving gaps in the hatch spacing sequence. At 140 % w1 (Figure 138f), the measured hatch spacing correlates with that calculated, however, the surface is excessively rough and would be problematic during production. Therefore, there would be no hatch spacing selected from Figure 138.

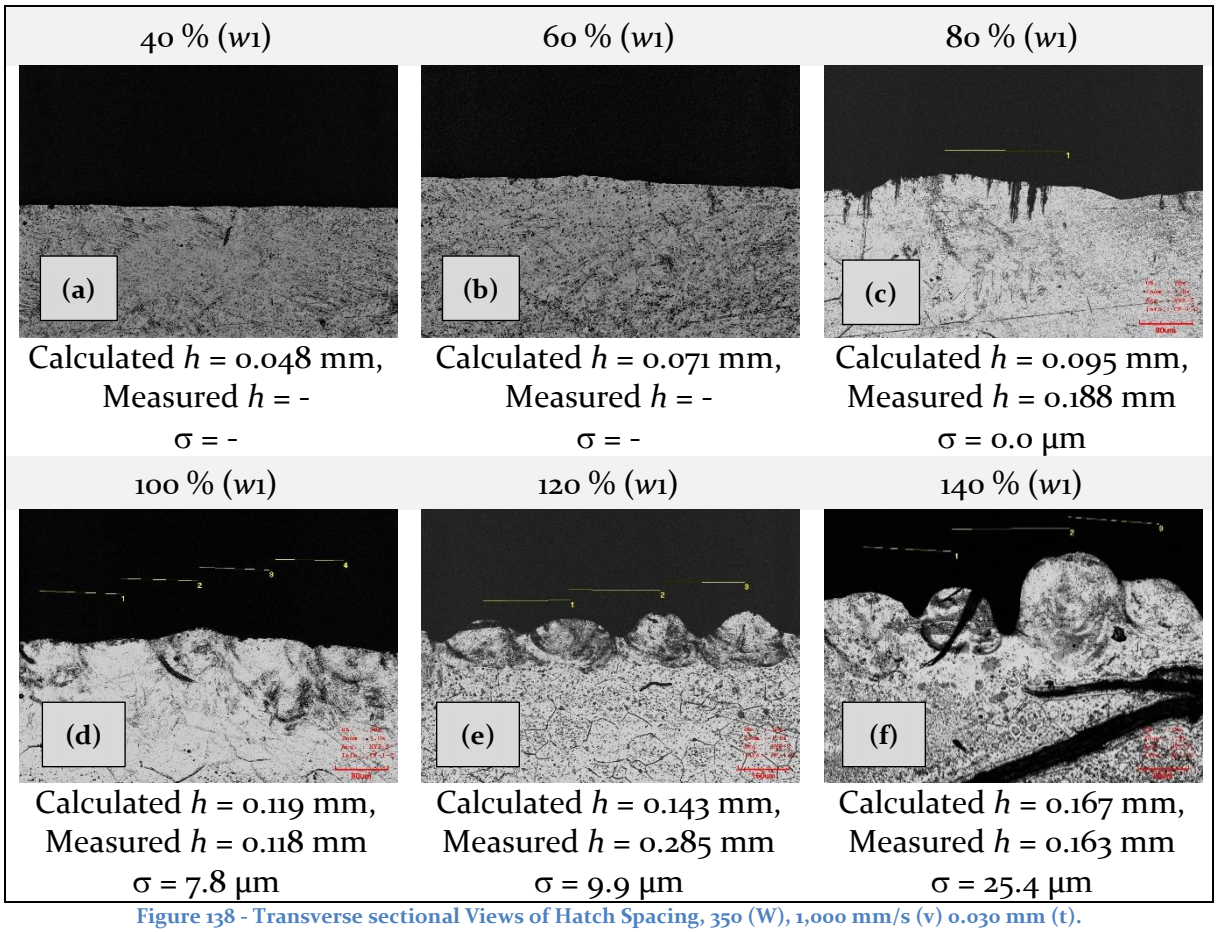

Figure 138 - Transverse sectional Views of Hatch Spacing, 350 (W), 1,000 mm/s (v) 0.030 mm (t).

This would also be the case for hatch spacings produced at 350 W and a scan speed of 667 mm/s (Figure 212). Due to the excessive energy density, surfaces produced are either devoid of feedstock, predominately substrate penetration or excessively rough. This would not be conducive with acceptable part production.

In summary, based on the evidence presented in Figure 133 to Figure 138, the following build parameters were chosen as acceptable for multiple layers experimentation (Table 40).

Table 40 - Phase 3c Build Parameters

Phase 3c Build Parameters				
	laser power	Scan speed	Hatch spacing	layer thickness
Figure 133	150	1,000	0.109	0.03
Figure 134	250	1,000	0.156	0.03
Figure 135	250	667	0.185	0.03
Figure 136	250	500	0.227	0.03
Figure 137	250	333	0.255	0.03
Figure 138	350	1,000	-	0.03
Figure 212	350	667	-	0.03

10.3 Phase 3b: Hatch Spacing Evaluation of Multiple Beads Conclusions

1 Single beads with appropriate characteristics (bead height and substrate penetration) were selected and the characteristics of multiple beads was evaluated. Transverse sections of the beads were analysed to determine efficient use of feedstock in the formation of multiple beads. It was concluded that at higher laser powers (250 W and 350 W), beads became flat and substrate penetration increased. Five sets of build parameters were selected:

Table 41 - Selected Build Parameters from Phase 3b.

Phase 3c Build Parameters				
	laser power	Scan speed	Hatch spacing	layer thickness
Figure 133	150	1,000	0.109	0.03
Figure 134	250	1,000	0.156	0.03
Figure 135	250	667	0.185	0.03
Figure 136	250	500	0.227	0.03
Figure 137	250	333	0.255	0.03

Chapter Eleven

11.0 Phase 3c Multi-layer evaluation of density and homogeneity of reinforcement

11.1 Phase 3c: Multiple-Layer Evaluation of Density and Homogeneity of Reinforcement Methodology

11.1.1 Overview of the Experiment/Design

Based on the results of phase 3b, successful hatch spacing's were processed to determine the effect of building multiple layers. Multiple layers were produced within a 10 mm by 10 mm cube with scan direction, layer thickness and rotation as for normal scan parameters used with Ti6Al4V on an EOS M290 machine. To alleviate the effect of the build platform, parts were built to a height of 4.0 mm before terminating the process. Parameters for contouring, UpSkin and DownSkin were not activated to ensure that the cubes produced would only contain beads scanned with the developed parameters, other features would be optimised through further research.

11.1.2 Phase 3c Variables

Multiple layers were exposed using laser power, scan speed and hatch distances successful from phase 3b.

11.1.3 Phase 3c Attributes (Multiple Layer Evaluation of Density and Homogeneity of Reinforcement)

For phase 3c the software (EOSPrint 1.5) was returned to standard parameters for exposing parts, the following parameters were set for the build process (Table 42) except for UpSkin and DownSkin that remained off, as in previous experiments. Laser power, scan speed and hatch spacing were those chosen from the results of phase 3b.

Table 42 - Build Attributes for Multiple Layer Experiment

Parameter Setting	Value
Hatch spacing	See Table 24 (Successful results from phase 3b)
Stripe width	100 mm
Pre-Contours	Off
Post-Contours	Off
Rotation	On
X, Y	On
Alternating	On
DMLS	On
Pre-Exposure	On
Up skin	Off (Thickness = 0)
Down skin	Off (Thickness = 0)
Beam expander	Automatic
Platform heating	35°C

11.1.4 Phase 3c Statistical Treatment

Due to the limitations on feedstock the builds were exposed once only however the analysis was conducted at multiple points to establish a statistical range.

11.2 Phase 3c: Multiple-Layer Evaluation of Density and Homogeneity of Reinforcement Results and Discussion

Whilst multi-layer structures were produced as part of the research (Figure 139), it was clear that this was an area that would require further investigation in order to optimise the parameters developed throughout this research.

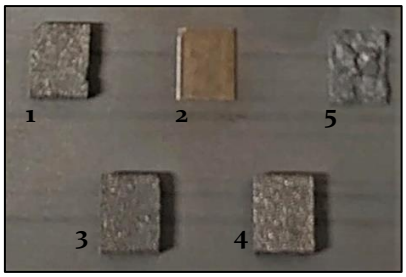

Figure 139 - Multiple Layer Evaluation of Density and Homogeneity of Reinforcement.

It was evident from the cubes produced that there was still research to be done in terms of parameter optimisation. Cracks were found in all parts with increasing severity from sample one to sample five, this was due to increases in internal stress caused by excessive

differences between the coefficient of linear expansion for the matrix and reinforcement materials and the thermal gradient on solidification resulting in cracking and catastrophic failure of sample five. Sample two has been removed for analysis. The density of the samples was not evaluated as it was visually evident that there was still work required to improve the density of the samples, therefore, measurements would provide little meaning.

11.3 Phase 3c: Multiple-Layer Evaluation of Density and Homogeneity of Reinforcement Conclusions

1 Five test samples were produced with the selected build parameters (Table 41), evidence showed that internal stresses were significantly high leading to catastrophic failure in sample five owing to a laser power of 250 W and a scan speed of 333 mm/s. the most successful sample was processed at 250 W with a scan speed of 1,000 mm/s and a hatch spacing of 0.156 mm. this produced a sample with no visible cracking. It was concluded that a scan speed circa 1,000 mm/s was acceptable but a lower laser power, circa 50 W may produce better parts.

Chapter Twelve

12.0 Phase 3d Crystallographic and chemical analysis of MMC material

12.1 Phase 3d: Crystallographic and Chemical Analysis of MMC Material Methodology

12.1.1 Overview of The Experiment / Design

Transverse sections of single bead samples produced from the MMC feedstock were chemically etched using Kroll's reagent 187, a 2:1 HF/Nitric acid mixture in an aqueous solution. The solution was prepared in order to make the microstructure more visible during optical microscopy.

Analysis of chemical composition was conducted using Energy Dispersive X-Ray Spectroscopy (EDS) for the detection of individual elements and X-Ray diffraction (XRD) for the detection of crystallography and chemical compounds.

12.1.2 Phase 3d Variables

12.1.2.1 Chemical etching Variables

Specimens were immersed for 15s to 20s then washing with distilled water for several minutes to ensure the removal of all chemicals. Ethanol was finally used to ensure specimens were clean and dry.

12.1.2.2 X-Ray Spectroscopy (EDS) Variables

EDS was performed using Oxford Instruments INCA software and a X-max N X-ray detector. Regions of interest were analysed using spot and area analysis, to obtain a fair result from various places across the samples. The EDS system was calibrated before use using cobalt (Co) (Figure 141).

Figure 140 - SEM Zeiss EVO50 Scanning Electron Microscope (SEM), Carl Zeiss Microscopy, GmbH, (2020)

The SEM used is a Zeiss EVO50 (Figure 140) and the images were taken with the SE (secondary electron) detector on a high vacuum setting. The accelerating voltage was 10kV and the beam current was 100 microamps.

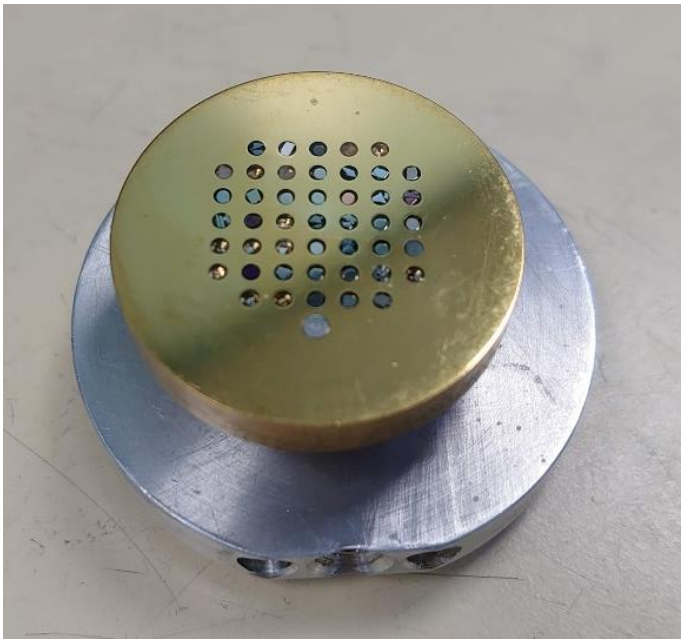

Figure 141 - EDS Co Calibration Sample

12.1.2.3 X-Ray Diffraction (EDX) Variables

EDX was carried out using Panalytical Empyrean EDX apparatus (Figure 142) supplied by Malvern Panalytical UK, using the following variables:

- Anode material Copper,
- Step size 0.013 (°2Th.),
- Step time 8.670 (s)
- Generator settings 40 mA, 40 KV.

The sample was set to spin.

Figure 142 - Panalytical Empyrean EDX apparatus

12.1.3 Phase 3d Attributes

12.1.3.1 Chemical etching Attributes

For metallographic analysis Kroll's reagent was used, consisting of:

- 5 ml of HNO_3
- 10 ml of HF (48 % concentration)
- 85 ml H_2O

12.2 Phase 3d: Crystallographic and Chemical Analysis of MMC Material Results and Discussion

It has been seen from the EDX analysis in chapter 7.2.5, concentrated areas of SiC were observed and the results from area and spot analysis confirmed the presence of SiC in the quantities predicted by equation 5. In terms of characterisation, concentrations of the SiC reinforcement material inhabited regions along the grain boundaries as seen in Figure 143, and appeared to favour β-phase regions. Further analysis would be required, beyond this research.

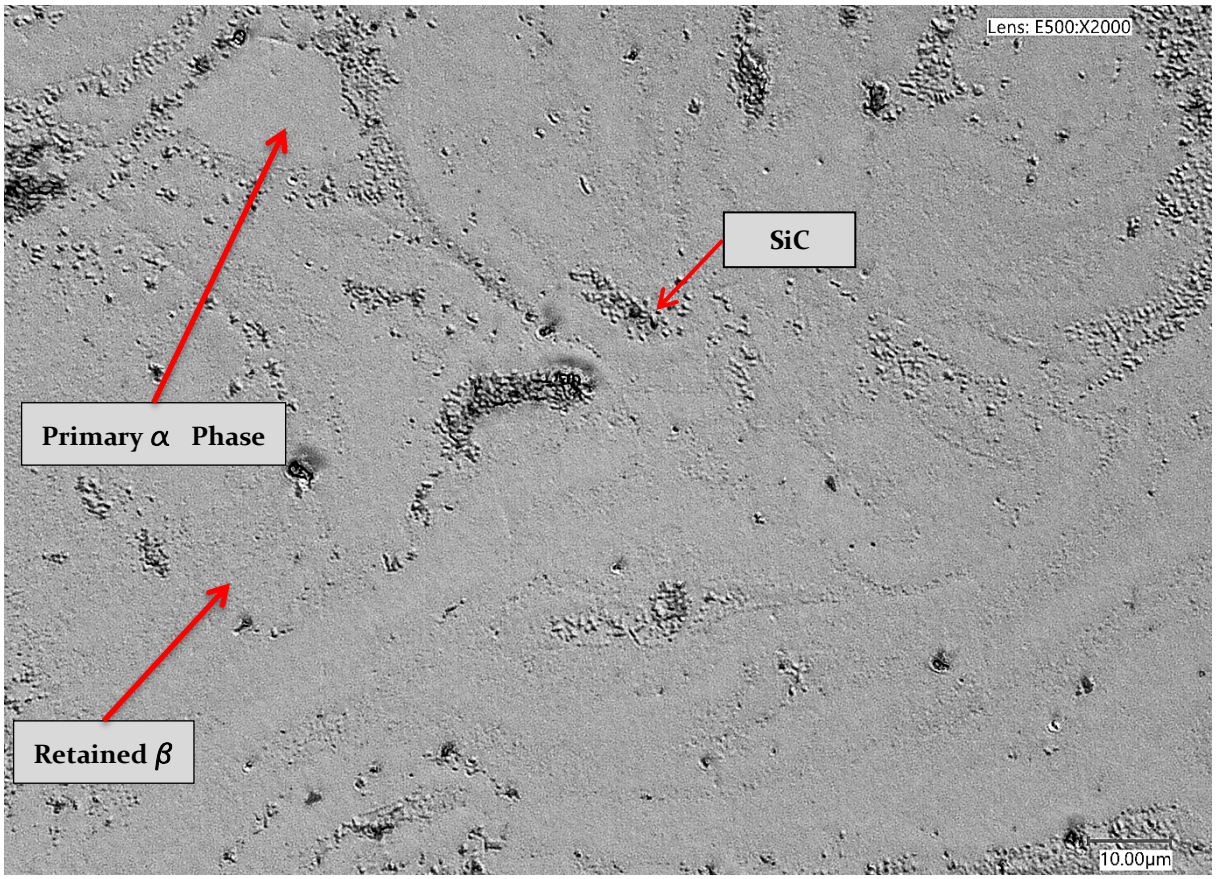

Figure 143 - Optical microscopic view of MMC material (2K x magnification)

EDX analysis detected three primary compounds:

- Silicon Carbide C_1Si_1 Hexagonal
- Titanium Silicide Ti_5Si_4 Orthorhombic
- Silicon Oxide O_2Si_1 Anorthic

The detection of SiC was due to the remaining presence of the reinforcement material, unaffected by the process. The analysis reported a high level of confidence in this result with a score of 45. Silicon oxide had a score of 37, with Ti_5Si_4 silicide scoring 32. Whilst evidence of Ti_5Si_4 is encouraging, it does further explain issues of cracking within the

structures. Ti_5Si_4 is known to be brittle with poor fracture toughness, cracks are often found because of the different coefficients of thermal expansion of Ti_5Si_4 in different crystal directions, Therefore, tensile stresses and crack initiation occur.

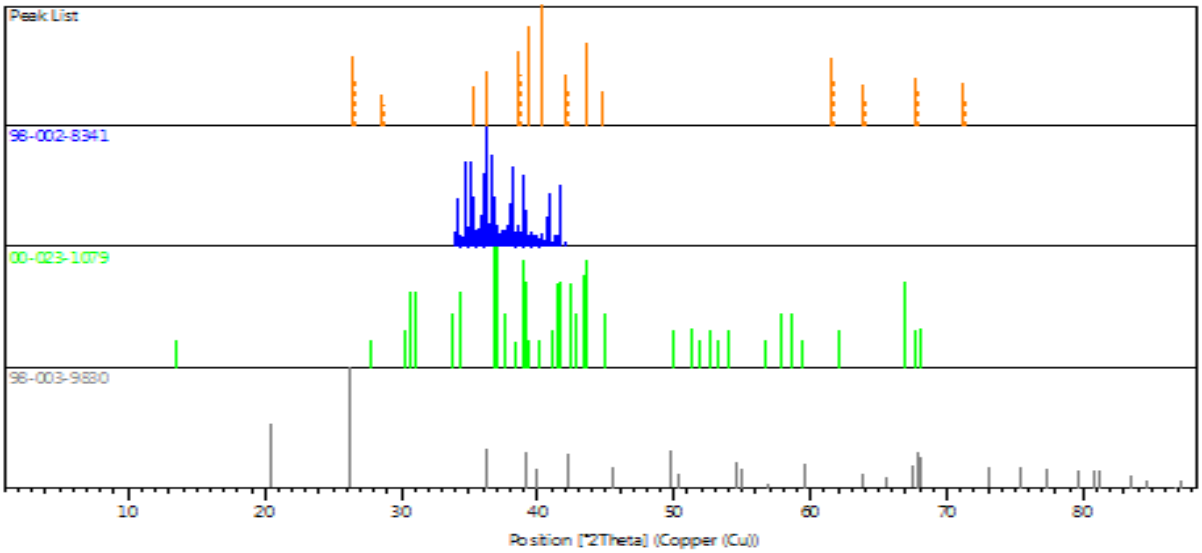

Figure 144 - XRD Stick Pattern (98-002-8341 C_1Si_1, 00-023-1079 Ti_5Si_4, 98-003-9830 O_2Si_1)

Figure 144 shows the XRD stick patterns in isolation showing the three primary compounds. Figure 145 shows the original diffractogram.

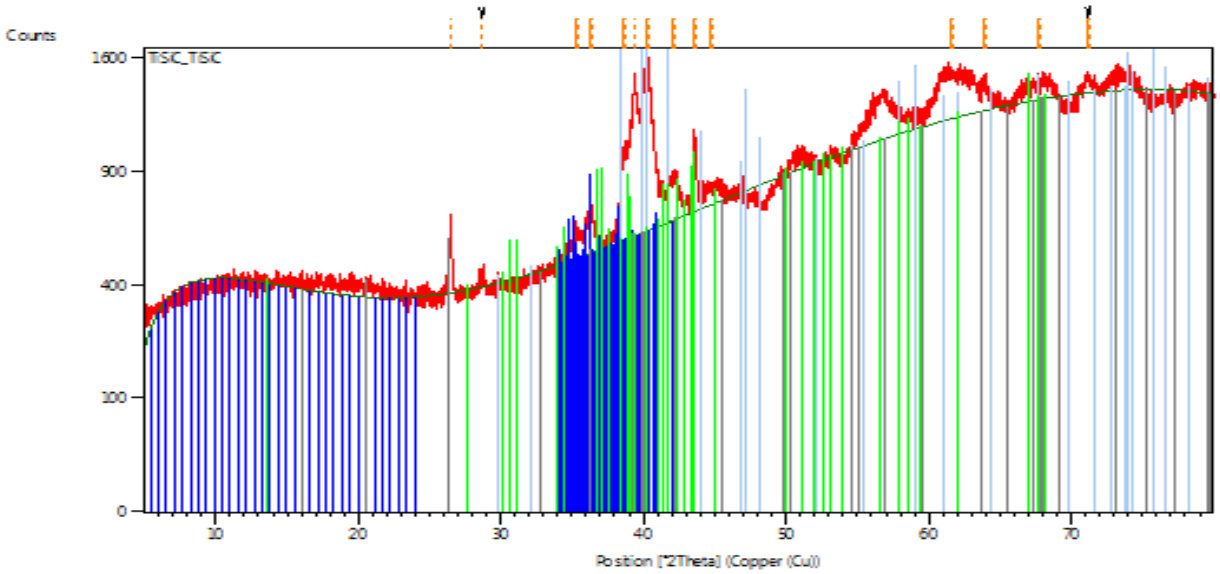

Figure 145 - XRD Diffractogram (C_1Si_1 green, Ti_5Si_4 Blue, O_2Si_1 Grey)

Full results can be found in appendix 3.

12.3 Phase 3d: Crystallographic and Chemical Analysis of MMC Material Conclusions

1 Cryptographically, samples analysed exhibited homogeneity of reinforcement indicating the robustness of the methodology.

2 Chemical analysis found SiC, SiO_2 and Ti_5Si_4. Silicon oxide was an unexpected chemical composition as there had as yet been no evidence of O_2 present within the system, SiC was expected, not only due to the addition as a reinforcement, but also as this was not expected to chemically dissolve into the system but remain as precipitates to improve wear resistance. Ti_5Si_4, whist predicted could be synthesised, was unexpected at large quantities, this will have implications for the printing of semiconductors.

3 It was concluded that the evidence of cracking within the samples was primarily due to incompatibilities in linear expansion coefficients between the matrix and reinforcement and temperature gradients during the build process.

Chapter Thirteen

13.0 Recommendations for future work.

Within the research a complete and comprehensive methodology has been developed and presented for the MA of small batch feedstock for experimentation and material development specifically within the PBF industry. Rigorous analytical methods have also been presented and demonstrated to yield reliable and confident results. There are, however, many areas that warrant further investigation and research to further the scientific understanding.

1 Develop the energy density-based methodology to include 50 w laser powers.

2 Development of the multiple bead experiment to better understand the correlation between the single and multiple beads.

3 Analysis of mechanical properties (tensile strength, fracture toughness, hardness) of the MMC material.

4 Synthesise materials with similar linear expansion coefficients such as TiB_2 and TiC.

5 In chapter 7.2.5, higher than expected values for C (4.41 Wt. %) were detected and require further investigation.

6 further research would benefit from the investigation of temperature gradients during the build process and the effect on the samples by monitoring the meltpool.

7 It was also noted in chapter 9.2, that an unexplained area was visible either side of the melt bead at higher energy densities for the MMC beads but not the Ti6Al4V beads. This may prove difficult to investigate but could add additional insights into the process after the addition of SiC.

8 Future research will look into improved methodologies for the acquisition of multiple measurements along the bead both above and below the substrate to provide a more statistically accurate representation of bead formation against energy density.

9 The analysis of the locations of the SiC particles under SEM were far from conclusive and would benefit from further research to look at their location and detection.

10 Whilst new compounds were found, and an elevated percentage of C further analysis would be recommended.

11 Additional crystallographic analysis of phases is recommended.

12 The Ti6Al4V to SiC interface of the MMC material would benefit from further investigation.

13 The author also wishes to investigate other combinations of materials for in-situ alloying either through MA or similar processes. Whilst this research investigated the combining of hard particles on-to soft, that could be referred to as a 'hard-soft' combination, the issues surrounding soft-soft and soft-hard combinations for small batch production require further work.

14 Measurement of the sub-micron SiC particles proved challenging within this research and further investigation into better measurement of particle size, size distribution and morphology should be investigated.

Chapter Fourteen

14.0 Contribution to knowledge

1 Evaluation of linear progression in energy density enabling better comparison between Ti6Al4V and the MMC material results of single beads. The addition of SiC altered bead formation in terms of size and wettability. This method demonstrated that a theory requiring additional energy within the melt-pool was incorrect and that further work should focus on lower energy levels.

2 The two-rail system was developed for single layer characterisation to better guarantee an accurate, reliable, and repeatable deposit of feedstock for single layer experimentation and is recommended for research in this area.

3 Mechanical Alloying (MA) was chosen as a method to combine dissimilar materials for subsequent in-situ alloying within the L-PBF process. Contrary to classical MA processing techniques, a methodology was developed involving a minimal rotational speed of 500 rev/min and an alloying duration of 24 minutes was found to effectively coat the surface of the Ti6Al4V particles with SiC.

4 A processing window for the Ti6Al4V – SiC MMC material was found as shown in Table 43.

Table 43 - Phase 3c Build Parameters

Phase 3c Build Parameters			
laser power	Scan speed	Hatch spacing	layer thickness
150	1,000	0.109	0.03
250	1,000	0.156	0.03
250	667	0.185	0.03
250	500	0.227	0.03
250	333	0.255	0.03

It was clear however that further work was required.

References

3T RPD. AM Reduces production steps, lead time and cost. Case studies.

A basic guide to particle characterisation. Malvern instruments worldwide. WWW.malvern.com/contact 2012.

Adam Equipment Ltd, Maidstone Rd, Kingston, Milton Keynes MK10 0BD 01908 274 545

Adebisi, A. A. Maleque, M. A. and Rahman, M. M (2011) metal matrix composite brake rotors: historical development and product life cycle analysis, *International Journal of Automotive and Mechanical Engineering (IJAME)* Volume **4**, pp. 471 – 480.

Agius, D. Kourousis, K.I. and Wallbrink, C. (2017) A Review of the As-Built SLM Ti-6Al-4V Mechanical Properties towards Achieving Fatigue Resistant Designs, *Metals* **8**, 75.

Ahsan, M. N. Pinkerton, A. J. Richard Moat, J. Shackleton, J. (2011) A comparative study of laser direct metal deposition characteristics using gas and plasma-atomized Ti–6Al–4V powders, *Materials Science and Engineering* **A** (528), pp. 7648 - 7657.

ALD Vacuum Technologies GmbH, Otto-von-Guericke-Platz 1, 63457 Hanau Phone +49 6181 307 0, info@ald-vt.de

Algardh, J. et al., (2017) State of the art for additive manufacturing of metals. RAMP-UP; Roadmap for research and innovation to industrialize additive manufacturing of metals in Sweden (2016-03898).

Alman, D.E. and Hawk, J.A. (1999) The abrasive wear of sintered titanium-ceramic particle reinforced composites, *Wear*, 225-229, pp. 629 - 639.

Al-Shemmeri, T.T. (2010) Engineering thermodynamics. Ventus publishing Aps.

Al-Shemmeri, T.T. (2012) Engineering thermodynamics solutions manual. Bookboon.com: Ventus publishing Aps.

AM-Power https://am-power.de/tools/metal-additive-manufacturing/ 2020

Andrade, A. Morcelli, A. Lobo, R. (2010) Deformation and fracture of alpha-beta titanium alloy, Revista Matéria. **15**(2), pp. 364 - 370.

Anish, R. Robert Singh and Sivapragash, M (2012) Techniques for processing metal matrix composite; A survey, *Procedia engineering* **38**, pp. 3846 - 3854.

Ansari, J. Nguyen, D. Hong, S. P. (2019) Investigation of SLM Process in Terms of Temperature Distribution and Melting Pool Size: Modeling and Experimental Approaches, Materials, **12**, 1272.

Arkon Ltd. https://arkon3d.ru/en/ 119121, Moscow, Smolenskaya st. 7 Tel: 07499 350 4772 info@arkon3d.ru

Arjunan, A. Demetriou, M. Baroutaji, A. Wang, C. (2020) Mechanical performance of highly permeable laser melted Ti6Al4V bone scaffolds, *Journal of the Mechanical Behavior of Biomedical Materials* **102,** 103517.

Arjunan, A. Singh, M. Baroutaji, A. Wang, C. (2020) Additively manufactured AlSi10Mg inherently stable thin and thick-walled lattice with negative Poisson's ratio, *Composite Structures* **247,** 112469.

Asgari, H. Baxter, C. Hosseinkhani, K. Mohammadi, M. (2017) On microstructure and mechanical properties of additively manufactured AlSi10Mg 200C using recycled powder, *Materials Science & Engineering* **A** (707), pp. 148 - 158.

Atazadeh, N. Heydari, M.S. Baharvandi, H.R. and Ehsani, N. (2016) Reviewing the effects of different additives on the synthesis of the Si3SiC2 MAX phase by mechanical alloying technique. Int. *Journal of refractory metals and hard materials*, 61, pp. 67 - 78.

Attar, H. Calin, M. Zhang, L.C. Scudino, S. and Eckert, J. (2014) Manufacture by selective laser melting and mechanical behaviour of commercially pure titanium. *Journal of materials science and engineering* **A** (593), pp. 170 - 177.

Attar, H. Prashanth, K. G. Zhang, L. C. Calin, M. Okulov, I. V. Scudino, S. Yang, S. Eckert, J. (2015) Effect of Powder Particle Shape on the Properties of In Situ Ti–TiB Composite Materials Produced by Selective Laser Melting, *Journal of Materials Science & Technology* 31, pp. 1001 - 1005.

Axelsson, S. (2012) Surface characterization of titanium powders with x-ray photoelectron spectroscopy, Masters Diploma, Chalmers University of Technology.

Azeem, M.A. and Dye, D. (2014) In situ evaluation of the transformation behaviour of NiTi-based high temperature shape memory alloys. *Intermetallics*, 46, pp. 222 - 230.

Azom. (2004) Titanium Silicocarbide (Ti3SiC2) Titanium Silicon Carbide – Properties and Applications, https://www.azom.com/article.aspx?ArticleID=2363

Bao, Y. Newkirk, J. Ruan, J. Sparks, T.E. and Liou, F. (2008) Effect of mechanical surface treatments on Ti-6Al-4V direct metal deposition parts, *Journal of manufacturing processes*, 10, pp. 56 - 60.

Banerjee, S. (2008) Simple derivation of Young, Wenzel and Cassie-Baxter equations, and its interpretations, Surface Physics Division, Saha Institute of Nuclear Physics, 1/AF Bidhannagar, Kolkata 700 064, India.

Bandyopadhyay, D. (2004) The Ti-Si-C System (Titanium-Silicon-Carbon). *Journal of Phase Equilibria and Diffusion*, **25**(5).

Barsoum, M.W. (2000) The Mn+1AXn phase: a new class of solids; Thermodynamically stable nanolaminates, *Prog Solid St Chem*, **28**, pp. 201 - 281.

Baitimerov, R. Lykov, P. Zherebtsov, D. Radionova, L. Shultc, A and Gokuldoss Prashanth, K. (2018) Influence of Powder Characteristics on Processability of AlSi12 Alloy Fabricated by Selective Laser Melting. Materials **11**, (742).

Baufeld, B. Van der biest, O. and Gault, R. (2010) Additive manufacturing of Ti-6Al-4V components by shaped metal deposition: microstructure and mechanical properties. Materials and Design **31**, pp. s106 - s111.

Baufeld, B. Brandl, E and Van der biest, O. (2011) Wire based additive layer manufacturing: Comparison of microstructure and mechanical properties of Ti-6Al-4V components fabricated by laser-beam deposition and shaped metal deposition. Journal of materials processing technology **211**, pp. 1146 - 1158.

Behera, M. P. Dougherty, T and Singamneni, S (2018) Conventional and additive manufacturing with metal matrix composites: a perspective, 14th Global congress on manufacturing and management (GCMM-2018) *Procedia Manufacturing* **30**, pp. 159 – 166.

Bennett, J. P. and Smith, J. D (2001) Fundamentals of refractory technology. *Ceramic transactions, American chemical society* volume **25.**

Benson, J.M. and Snyders, E. (2015) The need for powder characterisation in the additive manufacturing industry and the establishment of a national facility. *South African Journal of Industrial Engineering*, **26**(2), pp. 104 - 114.

Bergstrom, D. Powell, J. Kaplan, A. F. H. (2007) The absorptance of steel to Nd:YLF and Nd:YAG laser light at room temperature. *Applied surface science* 253(11), pp. 5017 - 2028.

Berretta, S. Ghita, O. Evans, K.E. Anderson, and Newman, C. (2013) Size, Shape and flow of powders for use in selective laser sintering (SLS)

Beuth, J. (2017) Additive manufacturing challenges for the gas turbine industry. Next Manufacturing centre, Carnegie Mellon University,

Biffi, C.A. Figini, A. Tuissi, A. (2014) Influence of compositional ratio on microstructure and martensitic transformation of CuZr shape memory Alloys, *Intermetallics* **46**, pp. 4 - 11.

Bourell, D. Kruth, J. P. Leu, M. Levy, G. Rosen, D. Beese, A. Clare, A. (2017), Materials for additive manufacturing. *CIRP Annals - Manufacturing Technology* **66**, pp. 659 - 681.

Brandl, E. Greitemeier, D. (2012) Microstructure of additive layer manufactured Ti-6Al-4V after exceptional post heat treatments. *Materials Letters* **81**, pp. 84 - 87.

Buvanashekaran, G. Shanmugam, S.N. Sankaranarayanasamy, K. and Sabarikanth, R. (2009) A study of laser welding modes with varying beam energy levels, Proceedings of the Institution of mechanical engineers, part C: *journal of mechanical engineering science* **223**, pp. 1141 - 1156.

CAM2 Centre for additive manufacturing – metal, ChSLMers University of Technology, SE-412 96 Gothenburg, Sweden. +46 (0)31-772 10 00 www.chSLMers.se

Cao, X. Jahazi, M. Immarigeon, J.P. and Wallace, W. (2006) A review of laser welding techniques for magnesium alloys, *Journal of materials processing technology* **171**, pp. 188 - 207.

Carl Zeiss microscopy Deutschland GmbH, Carl Zeiss Strasse 22, 73447 Oberkochen, Germany. Tel +49 7364 20 3800.

Carpenter Technology Corporation, 1735 Market Street, 15th Floor, Philadelphia, PA, 19103, United States. Tel: +1 610 208 2000.

Chalabyan, Avetik. Jänsch, Elena. Niemann, Tom. Otto, Tobias. Zeumer, Benedikt. Zhuravleva, Ksenia. How 3-D printing will transform the metals industry. McKinsey and Company. 2017.

Chang, F. Gu, D. Dai, D. Yuan, P. (2015), Selective laser melting of in-situ Al4SiC4 + SiC hybrid reinforced Al matrix composites: Influence of starting SiC particle size, *Surface & Coatings Technology 272*, pp. 15 - 24.

Chawla, K. K. (1974), On the Applicability of the "Rule-of-Mixtures" to the Strength Properties of Metal-Matrix Composites. *Revista Brasileira de Física*, Vol. 4, N.° 3, pp. 411 - 418.

Chen, B. Shi, T.L. Li, M. Yang, F. Yan F. and Liao, G.L. (2014) Laser welding of annealed Zr55Cu30Ni5Al10 bulk metallic glass, *Intermetallics* **46**, pp. 111 - 117.

Chen, X. and Bei, G. (2017) Toughening mechanisms on nanolayered MAX phase ceramics – A review, Materials 10, 366. www.mdpi.com/journal/materials

Chun, S. Noh, J Yeom, J. Kim, J and Nam, T (2014) Martensitic transformation behaviour of Ti-Ni-Ag alloys, *Intermetallics* **46**, pp. 91 - 96.

Citim-am (2016)**Error! Hyperlink reference not valid.**. *Metal additive manufacturing* Springer, Vol. 2 No, 1, pp. 15.

Clayton, J. (2014) Optimising metal powders for additive manufacturing, Metal Powder Report, September-October 2014, Vol.69 (5), pp. 14 - 17. info@freemantech.co.uk

Condliffe, J. (2015). A new manufacturing technique cold finally make titanium cheaper. Gizmodo, 26/2/2015.

Cooksongold 2016, Cooksongold launches platinum metal powder for the jewellery industry, *Metal additive manufacturing* Springer, Vol. 2 No, 1, pp. 10.

Cordova, S. Campos, M. Tinga, T. (2017) Assessment of moisture content and its influences on laser beam melting feedstock.

Cordova, S. Campos, M. Tinga, T. (2019) Revealing the Effects of Powder Reuse for Selective Laser Melting by Powder Characterization, JOM, Vol. 71, No 3, pp. 1062 – 1072.

Criales, L, E. Arısoy, Y, M. Lane, B. Moylan, S. Donmez, A. and Özel, T (2017) Laser powder bed fusion of nickel alloy 625: Experimental investigations of effects of process parameters on melt pool size and shape with spatter analysis, *International Journal of Machine Tools & Manufacture* **121**, pp. 22 – 36.

Cui, Y. Numata, H. Bian, H. Wako, K. Yamanaka, K. Aoyagi, K. Zhang, C and Chiba, A (2020) Effects of plasma rotating electrode process parameters on the particle size distribution and microstructure of Ti-6Al-4 V alloy powder. *Powder Technology* **376**, pp. 363 – 372

Dadbakhsh, Hao, S. L. Jerrard, P. G. E. Zhang, D. Z (2012) Experimental investigation on selective laser melting behaviour and processing windows of in situ reacted Al/Fe2O3 powder mixture. *Powder Technology* **231**, pp. 112 – 121.

Dadbakhsh, S. and Hao, L. (2014) Effect of layer thickness in selective laser melting on microstructure of Al/5 wt.%Fe2O3 powder consolidated parts, *The scientific world journal*, Volume 2014 Article ID 106129.

Deshpandea, A. Manda, P. Vanitha, C. and Singh, A. K. (2018) Microstructural Characterization of Metastable Beta Titanium Alloys in Hot Rolled and Solution Treated condition, Materials Today: *Proceedings* **5**, pp. 3657 - 3663

Dickens, P. Minshall, T. (2015) UK National strategy for additive manufacturing; Update report 2. www.amnationalstrategy.uk

Dimitrov, D. Becker, T.H. Yadroitsev, I. and Booysen, G (2016) On the impact of different system strategies on the material performance of selective laser melting – manufacturing Ti6Al4V components, *South African journal of industrial engineering* **27**(3), pp. 184 - 191.

Dingal, S. Pradhan, T.R. Sarin Sunder, J.K. Roy Choudhury, A. and Roy, S.K. (2008) The application of Taguchi's method in the experimental investigation of the laser sintering process, *International journal of advanced manufacturing technology* **38**, pp. 904 - 914.

Dolinsek, S. (2005) Wear Characteristics of laser sintered moulding tools, *Wear* **259**, pp. 1241 - 1247.

Dybdahl Hede, P. (2006) Fluid bed particle processing. Bookboon.com: www.ventus.dk

Dynamic Ceramic, Crewe Hall Enterprise Park, Weston Road, Crewe, CW1 6UA, England +44(0)1270 501000, info_crewe@coorstek.com.

Edwards, Innovation Drive, Burgess Hill, West Sussex, RH15 9TW, UK. Tel: 08459 212 223.

El-Raghy, T. Barsoum, W. (1999) Processing and mechanical properties of Ti3SiC2: Reaction path and microstructure evaluation, *Journal of American ceramic society* **82**(10), pp. 2849 - 2854.

EOS GmbH (2016) Material data sheet, EOS Titanium Ti64, EOS GmbH Electro optical systems, Robert Stirling Ring 1, D-82152 Krailling Munchen.

EOS GmbH Electro optical systems, Robert Stirling Ring 1, D-82152 Krailling, Munchen, Germany.

Eriksson, J. (2010) Transport properties at 3C-SiC interfaces PhD in Nanoscience, Scuola Superiore of the University of Catania, 2010.

Esmaeilizadeh, R. Ali, U. Keshavarzkermani, A. Mahmoodkhani, Y. Marzbanrad, E. Toyserkani, E. (2019) On the effect of spatter particles distribution on the quality of Hastelloy X parts made by laser powder-bed fusion additive manufacturing, *Journal of Manufacturing Processes* **37**, pp. 11 - 20.

European additive manufacturing group (EAMG)

European powder metallurgy association (EPMA), epma.com

EPMA, Introduction to Additive Manufacturing Technology, 3rd Eddition

Eustathopoulos, N. Voytovych, R. (2016), The role of reactivity in wetting by liquid metals: a review, J Mater Sci 51, pp. 425 - 437.

Fiore, M. Neto, F.B. Azevedo, C. R. (2016) Assessment of the Ti-Rich corner of the Ti-Si phase diagram: the recent dispute about the eutectoid reaction. *Materials Research*. **19** (4), pp. 942 - 653.

Falmbigl, M. Romaka, V.V. Grytsiv, A and Rogl, P. (2014) Formation and stability of the clathrate-I structure in the systems Sr-(Ni, Cu, Zn)-Ge based on experimental and DFT studies, *Intermetallics* **46**, pp. 185 - 189.

Fisher Scientific, Bishop Meadow Road, Loughborough, Leicestershire, LE11 5RG

Fogagnolo, J.B. Ruiz-Navas, E.M. Robert, M.H and Torralbs, J.M. (2003) The effects of mechanical alloying on the compressibility of aluminium matrix composite powder, *Materials science and engineering* **355**(A), pp. 50 - 55.

Foratirad, H. Baharvandi, H and Maraghe, M.G. (2017) Effect of excess silicon content on the formation of nano-layered Ti3SiC2 ceramic via infiltration of TiC preforms, *Journal of the European ceramic society* **37**, pp. 451 - 457.

Freeman Technology, 1 Miller Court, Severn Drive, Tewkesbury, GL20 8DN, United Kingdom. Tel: 01684 851 551 info@freemantech.co.uk

Fukuda, A. Yoshikawa, T. Tanaka, T. (2009) A fundamental approach for the measurement of solid-liquid interfacial energy, *Journal of Physics: Conference Series* **165**.

Gavrilov, D. Vinogradov, O. Shaw, W.J.D (1995) In: Poursartip A, Street K, editors. Proc. Inter. Conference on Composite Materials, ICCM-10, vol. **III**. Woodhead Publishing, pp. 11.

Gharbi, M Peyre, P. Gorny, C Carin, M. Morville, S. Le Masson, P. Carron, D and Fabbro, R (2013) Influence of various process conditions on surface finishes induced by the direct metal deposition laser technique on a Ti-6AL-4V alloy, *Journal of materials processing technology* **213**, pp. 791 - 800.

Goodwin, P.S. Mukhopadhyay, D.K. Suryanarayana, C. Froes, F.H. Ward-Close, C.M. (1996) In: Blenkinsop, P. et al., editors. Titanium '**95** (3). London: Institute of Materials. pp. 2626 - 33.

Grand view research, 2020 www.grandviewresearch.com

Griggs, J. Lang, A.C. Gruber, J. Tucker, G.j. Taheri, M.L and Barsoum, M.W. (2017) Spherical Nanoindentation, modelling and transmission electron microscopy evidence of ripplocations in Ti3SiC2, *Acta Materialia* **131**, pp. 141 - 155.

Gu, D. Chen, H. (2018) Selective laser melting of high strength and toughness stainless steel parts: The roles of laser hatch style and part placement strategy, *Materials Science & Engineering* **A** 725, pp. 419 - 427.

Gu, D. Hagedorn, Y. Meiners, W. Meng, G. Batista, R.J.S. Wissenbach, K and Poprawe, R (2012) Densification behaviour, microstructure evolution, and wear performance of selective laser melting processed commercially pure titanium, *Acta Materialia* **60**, pp. 3849 - 3860.

Gu, D and Ma, C (2018) In-situ formation of Ni4Ti3 precipitate and its effect on pseudoelasticity in selective laser melting additive manufactured NiTi-based composites, *Applied surface science* **441**, pp. 862 - 870.

Gu, D. Meiners, W. Li, C and Shen, Y. (2010) In situ synthesized TiC/Ti5Si3 nanocomposites by high-energy mechanical alloying: microstructural development and its mechanism, *Materials Science and Engineering* **A** 527, pp. 6340 - 6345.

Gu, D.D. Meiners, W. Wissenbach, K and Roprawe, R. (2012) Laser additive manufacturing of metallic components: materials, processes and mechanisms, *International materials review* **57**(3), pp. 133 - 164.

Gu, D. Shen, Y and Xiao, J (2008) Influence of processing parameters on particulate dispersion in direct laser sintered WC-Cop/Cu MMCs, *International journal of refractory metals and hard materials* **26**, pp. 411 - 422.

Gu, D. Wang, Z. Shen, Y. Li, Q and Li, Y. (2009) In-situ TiC particle reinforced Ti-Al matrix composites: powder preparation by mechanical alloying and selective laser melting behaviour. *Applied surface Science* **255**, pp. 9230 - 9240.

Gu, H. Gong, H. Pal, D. Rafi, K. Starr, T and Stucker, B (2013) Influence of energy density on porosity and microstructure of selective laser melted 17-4PH stainless steel, 24TH

Annual international solid freeform fabrication symposium, University of Texas, Austin, Texas, 12-14 August. pp. 474 - 489.

Gupta, M. (2017) 3D printing of metals, (editorial) Journal of Metals 7, Department of mechanical engineering, national university of Singapore, 9 engineering drive 1, Singapore 117576, Singapore: mpegm@nus.edu.sg pp. 402 - 403.

Haghshenas, M. (2015) Metal-Matrix composites *University of Waterloo, Waterloo, ON, Canada.*

Hanzel, P. Zetek, M. Baksa, T and Kroupa, T (2015) The influence of process parameters on the mechanical properties of SLM Parts, *Procedia engineering* **100**, pp. 1405 - 1413.

Hentschel, M.L and Page, N.W (2003) Selection of descriptors for particle shape characterization. *Particle & Particle Systems Characterization*, **20**(1), pp. 25 - 38.

Hidnert, P. (1943) Thermal expansion of titanium, Journal of research of the national bureau of standards, Volume **30**, pp. 101 - 105, National bureau of standards.

Ho-Duc, L.H. (2002) Synthesis and characterisation of the properties of Ti3SiC2/SiC and Ti3SiC2/TiC composites. Master of science thesis, Drexel University.

Holt John M. (Tim), Technical Ed; C. Y. Ho, Ed. Structural Alloys Handbook, 1996 edition, CINDAS/Purdue University, West Lafayette, IN.

Hu, B and Richardson, I.M (2006) Mechanism and possible solution for transverse solidification cracking in laser welding of high strength aluminium alloys, materials science and engineering **A** 429, pp. 287 - 294.

Hu, L. Kothalkar, A. Proust, G. Karaman, I and Radovic, M (2014) Fabrication and characterisation of NiTi/Ti3SiC2 and NiTi/Ti2AlC composites, *Journal of alloys and compounds* **610**, pp. 635 - 644.

Herzan LLC, 23042 Alcalde Drive, Suite E, Laguna Hills, CA 92653 Tel: (949) 363-2905

Hung, Y.C and Withers, P.J (2012) Fibre bridging during high temperature fatigue crack growth in Ti/SiC composites, *Acta Materialia* **60**, pp. 958 - 971.

http://www.lindegas.ru/en/applications/laser_technologies/gases_for_laser_welding.

Innovate UK-NEDO Meeting (2016) New manufacturing technology – metal additive manufacturing.

Izhevskyi, V.A. Genova, L.A. Bressiani, J.C & Bressiani, A.H.A. (2000) Review article: Silicon Carbide. Structure, properties and processing. *Ceramics* **46**(297) pp. 4 - 13.

Jabbar, H. Monchoux, J.P. Thomas, M. Pyczak, F and Couret, A. (2014) Improvement of creep properties of TiAl alloys defined by spark plasma sintering. *Intermetallics* **46** pp. 1 - 3.

Jandl, I. Boero, F. Ipser, H and Richter, K.W. (2014) Phase equilibria and structural investigations of the general NiAs-type in the ternary systems Ni-Sn-Te, *Intermetallics* **46**, pp. 199 - 210.

Jayaseelan, V. Kalaichelvan, K. Kannan, M and Ananth, S. V (2010) Extrusion Characterizes of Al/Sic by different Manufacturing Process, *international journal of applied engineering research*, dindigul Volume **1**, No 1,

Jing, S. Lian, G. (2001) Dispersing SiC Powder and improving its Rheological behaviour, *Journal of the European Ceramic Society* **21**, pp. 2447 - 2451.

Jing, W. Peijie, L. Guangbao, M. Yuexian, Z. (2010) Microstructural evaluation caused by electromagnetic stirring in superheated AlSi7Mg alloys, Journal of materials processing technology **210**, pp. 1652 - 1659.

Jitendra M. Mistry and Piyush P. Gohil (2018) Research review of diversified reinforcement on aluminium metal matrix composites: fabrication processes and mechanical characterization, Sci Eng Compos Mater, **25** (4), pp. 633 – 647.

Jones, H. (2004) Gas-atomised aluminium alloy powders and their products: an update 1996–2001. Materials Science and Engineering A pp. 104 – 110.

Jordan, J.L. Sekine, T. Kobayashi, T. Li, X. Thadhani, N.N. El-Raghy, T. and Barsoum, M.W. (2003) High pressure behaviour of Titanium-Silicon Carbide (Ti3SiC2), *Journal of applied physics* **93**, pp. 9639 - 9643.

Jung, Y.I. Parl, J.H. Kim, H.G. Park, D.J. Park, J.Y and Kim, W.J. (2016) Effect of Ti and Si interlayer materials on the joining of SiC ceramics, *Nuclear engineering and technology* **48**, pp. 1009 - 1014.

Kandpal, B. C. Kumar, J. and Singh, H (2014) Production Technologies of Metal Matrix Composite: A Review, *IJRMET Vol.* **4,** Issue 2, Spl - 2 May - October 2014.

Kainer, K.U. (2006) Basics of metal matrix composites. Germany: Wiley-VCH Verlag GmbH & Co.

Khaing, M.W. Fuh, J.Y.H and Lu, L (2001) Direct metal laser sintering for rapid tooling: processing and characterisation of EOS parts, *Journal of materials processing technology* **113**, pp. 269 - 272.

Kim, C. Cho, K. Manjili, M. H and Nazafati, M (2017) Mechanical performance of particulate-reinforced Al metal-matrix composites (MMCs) and Al metal-matrix nanocomposites (MMNCs), *Journal of materials Science*, pp. 1 – 31.

Kimura, H. Kimura, M. (1990) In: Clauer, A.H. deBarbadillo, J.J. editors. Solid state powder processing. Warrendale, PA: TMS. pp. 365 - 77.

King, W. E. Anderson, A. T. Ferencz, R. M. Hodge, N. E. Kamath, C. Khairallah, S. A. and Rubenchik, A. M. (2015) Laser powder bed fusion additive manufacturing of metals; physics, computational, and materials challenges, *Applied Physics Reviews* **2**,

Klicpera, M. Javorsky, P. Cermak, P. Rudajevova, A. Denis, S. Brunatova, T. Cisarova, I (2014) Crystal Structure and its Stability in CeCuAl3 Single crystal, *Intermetallics* **46**, pp. 126 - 130.

Knowles, C.R. Becker, T.H and Tait, R.B (2012) Residual stress measurements and structural integrity implications for selective laser melted TI-6AL-4V, *South African journal of industrial engineering* **23**(3), pp. 119 - 129.

Kong, C. Y. Carroll, P. A. Brown, P. Scudamore, R. J (2007) The Effect of Average Powder Particle Size on Deposition Efficiency, Deposit Height and Surface Roughness in the Direct Metal Laser Deposition Process. Paper presented at 14th International Conference on Joining of Materials, Sunday 29 April - Wednesday 2 May, Helsingør, Denmark.

Körner, C. Attar, E. Heinl, P. Mesoscopic simulation of selective beam melting processes, *Journal of Materials Processing Technology* **211**, pp. 978 – 987.

Kosnikov, G. A. Figovsky, O. L and Eldarkanov, A. S (2014) Liquid Phase Production Technologies of Metal Matrix Composites (Review), *International Letters of Chemistry, Physics and Astronomy* **25**, pp 69 – 77.

Krakhmalev, P. Yadroitsev, I. Yadroitsava, I. and de Smidt, O. (2017) Functionalization of Biomedical Ti6Al4V via In Situ Alloying by Cu during Laser Powder Bed Fusion Manufacturing, *Materials* **10**, 1154

Krinitcyn, M. Fu, Z. Harrsi, J. Kostikov, K. Pribytkov, G.A. Greil, P and Travitzky, N (2017) Laminated object manufacture of in-situ synthesized MAX-phase composites, *Ceramics international* **43**, pp. 9241 - 9245.

Kruth, J.P. Froyen, L. Van Vaerenbergh, J. Mercelis, P. Rombouts, M and Lauwers, B. (2004) Selective laser melting of iron-based powder, *Journal of materials processing technology* **149**, pp. 616 - 622.

Kruth, J.P. Leu, M.C. Nakagawa, T (1998) Process in additive manufacturing and rapid prototyping, Keynote paper Annals of the CIRP **47**(2), pp. 525 - 540.

Kruth, J. P. Levy, G. Klocke, F. Childs, T. H. C. (2007) Consolidation phenomena in laser and powder-bed based layered manufacturing. Annals of the CIRP **56**(2), pp. 730 - 759.

Kumar Ghosh, S and Saha, P (2011) Crack and wear behaviour of SiC particulate reinforced aluminium-based metal matrix composite fabricated by direct metal laser sintering process, Materials and design **32**, pp. 139 - 145.

Kumar Ghosh, S. Saha, P and Kishore, S (2010) Influence of size and volume fraction of SiC particulates on properties of ex situ reinforced Al-4.5Cu-3Mg metal matrix composite prepared by direct metal laser sintering process, *Materials science and engineering* **A** 527, pp. 4694 - 4701.

Kumar, V. Fang, Z. Z. Wang, H and Shetty, D. K. (2016) Geometric model of sintering of unequal-sized particles. *Powder metallurgy* **59**(3), pp. 170 - 181.

Kurzynowski, T. Chlebus, E. Kuźnicka, B. Reiner, J. (2012) Parameters in Selective Laser Melting for processing metallic powders. SPIE 8239, High Power Laser Materials Processing: Lasers, Beam Delivery, Diagnostics, and Applications, San Francisco, California, USA

Kusuma, C. (2014) The Effect of Laser Power and Scan Speed on Melt Pool Characteristics of Pure Titanium and Ti-6Al-4V alloy for Selective Laser Melting, Kakatiya University.

Lecoanet, A. Ivey, D.G. and Henein, H. (2014) Simulation of the temperature profile during welding with COMSOL Multiphysics® software using Rosenthal's approach. COMSOL Conference in Boston.

Le Razer, B. and Kilburn, P. (2009) Rapid manufacturing of dental and medical parts using DMLS. TCT Seminar 20/10/09.

Leuders, S. Thone, M. Riemer, A. Niendorf, T. Troster, T Richard, H.A. and Maier, H.J (2013) On the mechanical behaviour of titanium alloy TiAl6V4 manufactured by selective laser melting: fatigue resistance and crack growth performance, *International journal of fatigue* **48**, pp. 300 - 307.

Li, H.T. Xia, M. Jarry, P.H. Scamans, G.M and Fan, Z (2011) Grain reinforcement in an AlZnMgCuTi alloy by intensive melt shearing: a multi-step nucleation mechanism, *Journal of crystal growth* **314**, pp. 285 - 292.

Li, J.F. Matsuki, T. and Watanabe, R. (2002) Mechanical-alloying-assisted synthesis of Ti3SiC2 powder, *Communications of the American ceramic society* **85**(4), pp. 1004 - 1006.

Li, R. Liu, J. Shi, Y and Jiang, W. (2011), Balling behaviour of stainless steel and nickel powder during selective laser melting process, *The international journal of advanced manufacturing technology*, **59**, pp. 1025 - 1035.

Liang, B. Han, X. Zou, Q. Zhao, Y. and Wang, M. (2009) TiC/Ti3SiC2 Composite prepared by mechanical alloying. Int. *Journal of refractory metals and hard materials* **27** pp. 664 - 666.

Lin, Z.J. Zhuo, M.J. Zhou, Y.C. Li, M.S. and Wang, J.Y. (2006) Microstructural Relationship between compounds in the Ti-Si-C system, *Scripta Materialia* **55**, pp. 445 - 448.

Linde Group, The. info@linde.com. Additive manufacturing and powder metallurgy

Liu, D. Hu, P. and Min, G. (2015) Interfacial reaction of cast Wu particulate reinforced titanium metal matrix composites coated by laser processing, *Optics and laser technology* **69** pp. 180 - 186.

Liu, L. Bhatia, R. Webster, T. J. (2017) Atomic layer deposition of nano-TiO_2 thin films with enhanced biocompatibility and antimicrobial activity for orthopaedic implants. *International Journal of Nanomedicine* **12**, pp. 8711 – 8723.

Liu, Z. Welsch, G. (1988) Literature Survey on Diffusivities of Oxygen, Aluminum, and Vanadium in Alpha Titanium, Beta Titanium, and in Rutile, *Metallurgical Transactions* A, **19**(4), pp. 1121 - 1125.

Locker. Metal 3D Printer Guide – All About Metal 3D Printing, 2018.

Lu, L. Lai, M.O. Zhang, S (1995) Modeling of the mechanical-alloying process. *Journal of Materials Processing Technology* **52**, pp. 539 – 546.

Lu, X.H. Yang, Y.Q. Huang, B. Luo, X and Liu, Y.C. (2006) Reaction diffusion in continuous SiC fibre reinforced Ti matrix composites, *Transactions of nonferrous metals society of China* **17**, pp. 27 - 34.

Lyall, I. Stanford, M. Kibble, K. and Lister, P A. (2015) Reliable manufacture of Additive Layer Manufacturing feedstock for the Selective Laser Melting process via Mechanical Alloying. *FAIM, Flexible Automation and Intelligent Manufacturing*, Wolverhampton, UK, 23rd – 26th June 2015.

Maeda, K and Childs, T.H.C. (2004) Laser sintering (SLS) of hard metal powders for abrasion resistant coatings, *Journal of materials processing technology* **149**, pp. 609-615.

Makoana, N.W. Moller, H. Burger, H. Tlotleng, M. Yadroitsev, I. (2016) Evaluation of single tracks of 17-4PH Steel manufactured at different power densities and scanning speeds by selective laser melting. *South African Journal of industrial engineering* **27**(3), pp. 210 - 218.

Malvern Panalytical Ltd, Enigma Business Park, Grovewood Road, Malvern, WR14 1XZ, UK. Tel: 01684 892 456

Malvern instruments worldwide (2012) A basic guide to particle characterisation.

Manickavasagam, K. Atzeni, E. Riccardo, C. Calignano, F. Diego, M. Ambrosio, E. P. and Iuliano, L. (2014). On the effect of process parameters on properties of AlSi10Mg parts produced by DMLS. *Rapid Prototyping Journal*, Vol. **20**(6), pp. 449 - 458.

Mattern, A. Huchler, B. Staudenecker, D. Oberacker, R. Nagel, A and Hoffmann, M.J (2004) Preparation of interpenetrating ceramic-metal composites, *Journal of European ceramic society* **24**, pp. 3399 - 3408.

Meier, C. Weissbach, R. Weinberg, J. Wall, W. A and Hart, A. J (2019) Modeling and characterization of cohesion in fine metal powders with a focus on additive manufacturing process simulations. *Powder Technology* **343,** pp. 855 – 866.

Melendez, I.M Neubauer, E. Angerer, P. Danninger, H and Torralba, J.M (2011) Influence of nano-reinforcements on the mechanical properties and microstructure of titanium matrix composites, *Composites science and technology* **71**, pp. 1154 - 1162.

Mikli, V. Kaerdi, H. Kulu, P and Besterci, M. (2001) Characterization of powder particle morphology. *Proceedings of the Estonian Academy of Sciences: Engineering (Estonia),* **7**(1), pp. 22 - 34.

Mistry, J. M. Gohil, P. P (2018) Research review of diversified reinforcement on aluminium metal matrix composites: fabrication processes and mechanical characterization, *Sci Eng Compos Mater*, **25**(4), pp. 633 – 647

Miracle, D. B. (2005) Metal Matrix Composites – From Science to technological significance, *Composite Science and Technology* **65**, pp. 2526 - 2540

Montealegre, I. Melendez. Neubauer, E. Angerer, P. Danninger, H and Torralba, J.M (2011) Influence of nano-reinforcements on the mechanical properties and microstructure of titanium matrix composites, *Composites Science and Technology* **71**, (2011) pp. 1154 – 1162.

Morgan, R. Papworth, A. Sutcliffe, C. Fox, P and O'Neill, B (2001) Direct Metal Laser Re-Melting of 316L Stainless Steel Powder Part 2: Analysis of Cubic Primitives, Solid freeform fabrication symposium, Austin Texas USA.

Mostafaei, A. Hilla, C. Stevens, E. L. Nandwana, P. Elliott, A. M. Chmielus, M. (2018) Comparison of characterization methods for differently atomized nickel-based alloy 625 powders. *Powder Technology* **333,** pp. 180 - 192.

Muniz-Lerma. J. A, Nommeots-Nomm. A, Waters, K. E and Brochu, M (2018) A Comprehensive Approach to Powder Feedstock Characterization for Powder Bed Fusion Additive, Manufacturing: A Case Study on AlSi7Mg, *Materials* **11,** 2386.

Murr, L.E. Gaytan, S.M. Ceylan, A. Martinez, E. Martinez, J.L. Hernandez, D.H. Machado, B.I. Ramirez, D.A. Medina, F. Collins, S and Wicker, R.B (2010) Characterization of titanium aluminide alloy components fabricated by additive manufacturing using electron beam melting, *Acta Materialia* **58**, pp. 1887 - 1894.

Murray, K. (2016) Developments in metal powders for additive manufacturing (Presentation) Sales and marketing manager – EMEA,

Negi, S. Dhiman, S and Sharma, R.K (2013) Basics, Applications and Future of Additive Manufacturing Technologies: A Review, *Journal of manufacturing technology research* **5**(1/2), pp. 75 - 97.

Nelson, M. Agne, M.T. Anasori, B. Yang, J and Barsoum, M.W (2017) Synthesis and characterisation of the mechanical properties of Ti3SiC2/Mg and Cr2AlC/Mg alloy composites, *Materials science and engineering* **A** 706, pp. 182 - 188.

Olowofela, H.O. Lyall, I. Stanford, m. Zhang, L. and Obuoza, C. (2013) Mechanical alloying (MA) of composite materials for the laser melting (LM) process, Faim 2013,

Olympus Europa, Olympus Europa SE & Co. KG, Amsinckstraße 63, 20097 Hamburg.

Olympus UK, KeyMed (Medical & Industrial Equipment) Ltd. KeyMed House Stock Road Southend-on-Sea, Essex SS2 5QH, UK. Tel: 0170-261-6333

Ozbilen, S (1999) Satellite formation mechanism in gas atomised powders. *Powder metallurgy* Vol **42**, No 1, pp. 70 – 79.

Park, Y. H. Hashimoto, H. Watanabe, R. Mater Sci Forum (1992) 88 - 90: 59 - 66.

Pavlov, M. Doubenskaia, M and Smurov, I (2010) Pyrometric analysis of thermal processes in SLM technology, *Physics procedia* **5**, pp. 523 - 531.

Phoenix Scientific Industries (PSI) Ltd. Apex Business Park, Hailsham, East Sussex, BN27 3JU, UK. Phone: 01323 449001. Email: info@psiltd.co.uk Website: www.psiltd.co.uk

Pilling, J. Professor of Materials Science and Engineering, Michigan Technological University, 1400 Townsend Dr, Houghton, MI 49931, USA. (https://sites.google.com/site/compositematerialsdesign/home/weight-and-volume-fractions)

Prashanth, K. G. Scudino, S. Maity, T. Das, J. & Eckert, J. (2017), Is the energy density a reliable parameter for materials synthesis by selective laser melting? *Materials Research Letters,* **5:6**, pp. 386 - 390.

Primes GmbH, Max-Planck-Str. 2, 64319 Pfungstadt, Germany, T +49 6157 9878 0

PyroGenesis 1744, William St., Suite 200, Montréal, Qc H3J 1R4, CANADA T +1 514 937 0002

Quintana, O.A. Tong, W. (2017), Effects of Oxygen Content on Tensile and Fatigue Performance of Ti-6Al-4 V Manufactured by Selective Laser Melting. JOM 69, pp, 2693 - 2697

Rausch, A. M. Küng, V.E. Pobel, C. Markl, M and Körner, C (2017) Predictive Simulation of Process Windows for Powder Bed Fusion Additive Manufacturing: Influence of the Powder Bulk Density, Materials Basel, Switzerland, Vol.10 (10)

Renishaw PLC. Industrial applications of Renishaw metal additive manufacturing technology.

Retsch GmbH, Retsch-Allee, 1-5, 42781 Haan, Germany. Tel: +49 2104 2333-100.

Robinson, J. Stanford, M. Arjunan, A. (2020) Stable formation of powder bed laser fused 99.9 % silver. *Materials Today Communications* **24** 101195.

Robinson, J. Stanford, M. Arjunan, A. (2020) Correlation between selective laser melting parameters, pore defects and tensile properties of 99.9 % silver. *Materials Today Communications* **25** 101550.

Rosso, M. (2006) Ceramic and metal matrix composites: Routs and properties, *Journal of materials processing technology* **175**, pp. 364 - 375.

Ruiz-Navas, E.M. Fogagnolo, J.B. Velasco, F. Ruiz-Prieto, J.M and Froyen, L. (2006) One step production of aluminium matrix composite powders by mechanically alloying, *Composites part A* **37**, pp. 2114 - 2120.

Rutkowski, P. Huebner, J. Kata, D. Lis, J. Grabos, A and Chlubny, L (2018) Lasert initiated Ti3SiC2 Powder and coating synthesis, *Ceramics international* **44**, pp. 10883 - 10890.

Savalani, M. M., Chung, C. C., Poon, C. and Yeung, W. (2011) Selective laser melting of Aluminium and its alloys. New Zealand Rapid Product Development Conference. Auckland University of Technology, Auckland 7 - 8 February.

SSLMinen, A. Piili, H and Purtonen, T (2010) The characteristics of high-power fibre laser welding, *Journal of mechanical engineering science* **224**, pp. 1019 - 1029.

Salazar, A. Rico, A. Rodríguez, Segurado Escudero, J. Seltzer, R. Martin de la Escalera Cutillas, F (2014) Fatigue crack growth of SLS polyamide 12: Effect of reinforcement and temperature, *Composites*: Part B 59, pp. 285 - 292

Sampedro, J. Perez, I. Carcel, B. Ramos, J.A and Amigo, V (2011) Laser cladding of TiC for better titanium components, *Physics procedia* **12**, pp. 313 - 322.

Saunders, N. (1996) Modelling of phase equilibria in Ti-alloys, Titanium 95: science and technology.

Sevcik, S. How 3D Printing Is Shaping the Future of Manufacturing. VP of Manufacturing Solutions at Stratasys.

Seyda, V. Kaufmann, N and Emmelmann, C. (2012) Investigation of aging processes of Ti-6Al-4V powder material in laser melting. *Physics Procedia* **39,** pp. 425 – 431.

Schniedenharn, M. Wiedemann, F. Schleifenbaum, J. H. (2018) Visualization of the shielding gas flow in SLM machines by space-resolved thermal anemometry. *Rapid Prototyping Journal* **24**/8, pp. 1296 - 1304

Schoinochoritis, B. Chantzis, D. Salonitis, K. (2015) Simulation of metallic powder bed additive manufacturing processes with the finite element method: A critical review, Proceedings of the Institution of Mechanical Engineers Part B *Journal of Engineering Manufacture*, pp. 1 – 22.

Sculpteo. (2015) The state of 3d printing.

Sculpteo. (2017) The complete metal 3d printing guide.

Schuster, J. M. Schvezov, C. E and Rosenberger, M. R (2013) Analysis of the results of surface free energy measurement of Ti6Al4V by different methods. International Congress of Science and Technology of Metallurgy and Materials, SAM - CONAMET 2013. *Procedia Materials Science* **8**, pp. 732 – 741.

Shannahan, L. Barsoum, M.W and Lamberson, L (2017) Dynamic fracture behaviour of a MAX phase Ti3SiC2, *Engineering fracture mechanics* **169**, pp. 54 - 66.

Sharfrin, E.; Zisman, William A. (1960). Constitutive relations in the wetting of low energy surfaces and the theory of the retraction method of preparing monolayers. *The Journal of Physical Chemistry*, **64**(5), pp. 519 - 524.

Shen, H. Rometsch, P Wu, X and Huang, A, (2019) Influence of Gas Flow Speed on Laser Plume Attenuation and Powder Bed Particle Pickup in Laser Powder Bed Fusion. The 2nd asia-pacific international conference on additive manufacturing (apicam 2019), *JOM*, Vol. **72**, No. 3.

Shi, S.L. Pan, W. (2007) Toughening of Ti3SiC2 with 3Y-TZP addition by spark plasma sintering, *Materials science and engineering A* **447**, pp. 303 - 306.

Simchi, A. Petzoldt, F and Pohl, H. (2003) On the development of direct metal laser sintering of rapid tooling, *Journal of materials processing technology* **141**, pp. 319 - 328.

Simchi, A. (2006) Direct metal laser sintering of metal powders: mechanism, kinetics and microstructural features, *Materials science and engineering A* **428**, pp. 148 - 158.

Simonelli, M. Aboulkhair, N. T. Cohen, P. Murray, J. W. Clare, A.T. Tuck, C. Hague, R. J. M. (2018), A comparison of Ti-6Al-4V in-situ alloying in Selective Laser Melting using simply-mixed and satellited powder blend feedstocks, *Materials Characterization* **143**, pp. 118 - 126.

Singerman, S.A. Jackson, J.J. (1996) Titanium metal matrix composites for aerospace applications, The minerals, *metals and materials society*, pp. 579 - 586.

Singh, A. K. Soni, S and Rana, R. S (2020) A Critical Review on Synthesis of Aluminum Metallic Composites through Stir Casting: Challenges and Opportunities, *Advanced engineering journal*, **22**, pp. 1 - 29

Sivakumar, G. Ananthi, V and Ramanathan, S. (2016) Production and mechanical properties of nano SiC particle reinforced Ti-6Al-4V matrix composite, *Transactions of nonferrous metals society of china* **27**, pp. 82 - 90.

Slipenyuk, A. Kuprin, V. Milman, Y. Goncharuk, V. Eckert, J. (2006) Properties of P/M processed particle reinforced metal matrix composites specified by reinforcement concentration and matrix-to-reinforcement particle size ratio, *Acta Materialia* **54**, pp. 157 - 166

Sobczak, N. Singh, M and Asthana, R. (2005) High-temperature wettability measurements in metal/ceramic systems – some methodical issues, *Current opinion in solid state and materials Science* **9**, pp. 241 - 253.

Song, B. Dong, S. Zhang, B. Liao, H and Coddet, C (2012) Effects of processing parameters on microstructure and mechanical property of selective laser melted Ti6Al4V, *Materials and design* **35**, pp. 120 - 125.

Spierings, A B; Herres, N; Levy, G (2011). Influence of the particle size distribution on surface quality and mechanical properties in AM steel parts. *Rapid Prototyping Journal* Vol. 17 (3), pp. 195 - 202.

Srinivasa, C. K. Ramesh, C. S. Prabhakar, S. K. (2009) Blending of iron and silicon carbide powders for producing metal matrix composites by laser sintering process. Central manufacturing technology institute, Bangalore, India.

Sustarsic, B. Godec, M. Jenko, M. Drglin, T and Dolinsek, S. (2005) Bulk and surface characterisation of metal powders for direct laser sintering. *Vacuum* **80**, pp. 29 - 34.

Suarez, A. Tobar, M.J. Yanez, A. Perez, I. Sampedro, J. Amigo, V and Candel, J.J. (2011) Modeling of phase transformations in Ti6Al4V during laser metal deposition, *Physics procedia* **12**, pp. 666 - 673.

Sun, J and Gao, L. (2001) Dispersing SiC powder and improving its rheological behaviour, *Journal of the European ceramic society* **21**, pp. 2447 - 2451.

Sun, P. fang, Z. Z. zhang, Y and xia, Y (2017) Review of the Methods for Production of Spherical Ti and Ti Alloy Powder, The Minerals, *Metals & Materials Society*, JOM, Vol. 69, No. 10, pp. 1853 - 1860.

surfacemeasurementsystems.com

Suryanarayana, C. Chen, G.H. Froes, F.H. (1992) Scripta Metal Mater **26**: 1727 - 32.

Suryanarayana, C. (2001) Mechanical alloying and milling, *Process in materials Science* **46**, pp. 1 - 184.

Sustarsic, B. Godec, M. Jenko, M. Drglin, T and Dolinsek, S. (2005) Bulk and surface characterisation of metal powders for direct laser sintering, *Vacuum* **80**, pp. 29 - 34.

Sutton, A. T. Kriewell, C. S. Leu, M. C. and Newkirk, J. W. (2016), Powder characterisation techniques and effects of powder characteristics on part properties in powder-bed fusion processes. *Virtual and Physical Prototyping*, pp. 1745 - 2759

Tan, J. H. Leong, W. Wonga, E. Dalgarno, K. W. (2017), An overview of powder granulometry on feedstock and part performance in the selective laser melting process. *Additive Manufacturing*, **18**, pp. 228 - 255.

Tatarko, P. Chlup, Z. Mahajan, A. Casalegno, V. Saunders, T. G. Dlouhy, I. and Reece, M. J. (2017) High temperature properties of the monolithic CVD β-SiC materials joined with a pre-sintered MAX phase Ti3SiC2 interlayer via solid-state diffusion bonding, *Journal of the European ceramic society* **37**, pp. 1205 - 1216.

Taylor, C. M. Childs T.H.C. Hauser, C. (2002) Morphology of direct SLS-processed stainless steel layers. In: *Proc. Solid Freeform Fabrication Symposium*, pp. 530 - 537

Theodore, L. Kunz, R.G. (2005) Nanotechnology: Environmental implications and solutions, John Wiley & Sons.

Tjong, S. C. Mai, Y. (2008) Processing-Structure-property aspects of particulate and whisker-reinforced titanium matrix composites. *Composites Science and technology* **68**, pp. 583 - 601.

Tolochko, N. K. Mozzharov, S. E. Yadroitsev, I. A. Laoui, T. Froyen, L. Titou, V. I. and Ignatieu, M. B. (2004) Balling processes during selective laser treatment of powders, *Rapid prototype journal* **10**(2), pp. 78 - 87.

Vrancken, B. Thijs, L. Kruth, J.-P. and Van Humbeeck, J. (2014) Microstructure and mechanical properties of novel β titanium metallic composite by selective laser melting. *Acta Materialia* **68**, pp. 150 - 158.

Van Zyl, I. Yadroitsava, I. Yadroitsev, I. (2016). Residual stress in Ti6AL4V objects produced by direct metal laser sintering. *South African Journal of Industrial Engineering* Vol **27**(4), pp. 134 - 141.

Vluttert, N. (2016) The absorption of moisture by metal powder in a humid environment and the effects on its composition. University of Twente, Drienerlolaan 5, 7522 NB Enschede, The Netherlands.

Tucho, W. M. Lysne, V. H. Austbø, H. Sjolyst-Kverneland, A. Hansen, V. (2018) Investigation of effects of process parameters on microstructure and hardness of SLM manufactured SS316L, *Journal of Alloys and Compounds* **740**, pp. 910 - 925.

Wan, G.U. Yan-Chun, Z. (2006) Reactions between Ti and Ti_3SiC_2 in a temperature range of 1273-1573 K, Trans. Nonferrous Met. Soc. China 16, pp. 1281 - 1288.

Wang, Z. Song, M. Sun, C. He, Y. (2011) Effects of particle size and distribution on the mechanical properties of SiC reinforced Al–Cu alloy composites, *Materials Science and Engineering A* **528**, pp. 1131 - 1137

Wang, Z. Zhang, H. Liu, X. Jiang, Y. Gao, H and He, Y. (2018) Reactive synthesis of porous nanolaminates $Ti_3(Si, Al) C_2$ intermetallic compound, *Materials chemistry, and physics* **208**, pp. 85 - 90.

Ward, J. Middleburgh, S. Topping, M. Garner, A. Stewart, D. Barsoum, M. W. Preuss, M. and Frankel, P. (2018) Crystallographic evolution of MAX phase in proton irradiating environments, *Journal of nuclear materials* **502**, pp. 220 - 227.

Warwick machine tools Ltd, Unit 8 Runway Farm, Kenilworth, UK, CV8 1NQ. Tel: 01676 534534

Wdowik, U. D. Twardowska, A. and Medala-Wasik, M. (2015) Lattice dynamics of binary and ternary phases in Ti-Si-C system: A combined Raman spectroscopy and density functional theory study, *Materials chemistry and physics* **168**, pp. 58 - 65.

Wegner, A. Witt, G. (2012) Correlation of process parameters and part properties in laser sintering using response surface modelling. *Physics Procedia* **39**, pp. 480 - 490.

Watanabe, T. Shiroki, M. Yanagisawa, A. and Sasaki, T. (2010) Improvement of mechanical properties of ferritic stainless-steel weld metal by ultrasonic vibration, *Journal of materials processing technology* **210**, pp. 1646 - 1651.

Weilhammer, J. (2011), EOS International User Meeting (IUM), Bad Wörishofen, April 2011.

Whittaker, J. T. Hess, D. P. Cai, W and Crane, N (2015) Ductility and Use of Titanium Alloy and Stainless-Steel Aerospace Fasteners. *University of South Florida Scholar Commons.*

Wilkinson, S. Rolls-Royce (2009) Productionising powder manufacture in an aerospace environment.

Williams, J. Miller, D. Deckard, C. (1996) Selective laser sintering part strength as a function of Andrew number, scan rate and spot size. Clemson University, pp. 549 - 559.

Withers, P. J. Bennett, J. A. Kuroda, M. (2010) Interfacial shear strength behaviour of Ti/SiC metal matrix composites at room and elevated temperature, *Acta meterialia* **58**, pp. 6090 - 6103.

Wits, W. W. De Smit, M. Al-Hamdani, K and Clare A. T (2019) Laser powder bed fusion of a Magnesium-SiC metal matrix composite, *52nd CIRP Conference on Manufacturing Systems, Procedia CIRP* **81**, pp. 506 – 511.

Witsa, W.W. Bruinsb, R. Terpstraa, L. Hulsb, R.A. Geijselaers, H.J.M. (2016) Single scan vector prediction in selective laser melting, *Additive Manufacturing* **9**, pp. 1 - 6

Yadroitsev, I. Yadroitsava, I. Bertrand, P and Smurov, I. (2012) Factor analysis of selective laser melting process parameters and geometrical characteristics of synthesized single tracks, *Rapid Prototyping Journal* **18**(3), pp. 201 - 208

Yadroitsev, I. Gusarov, A. Yadroitsava, I. Smurov, I. (2010) Single track formation in selective laser melting of metal powders. *Journal of materials processing technology* **210**, pp. 1624 - 1631.

Yadroitsev, I. Krakhmalev, P. Yadroitsava, I. Johansson, S. Smurov, I. (2013) Energy input effect on morphology and microstructure of selective laser melting single track from metallic powder. *Journal of materials processing technology* **213**, pp. 606 - 613.

Yadroitsev, I. Krakhmalev, P. Yadroitsava, I. (2014) Selective laser melting of Ti6Al4V alloy for biomedical applications: temperature monitoring and microstructural evolution. *Journal of alloys and compounds* **583**, pp. 404 - 409.

Yadroitsev, I. Smurov, I. (2010) Selective laser melting technology: from single laser melted track stability to 3D parts of complex shape. *Physics Procedia* **5**, pp. 551 - 560.

Yadroitsev, I. Smurov, I. (2011) Surface morphology in selective laser melting of metal powders. *Physics Procedia* **12**, pp. 264 - 270.

Yadroitsev, I. Thivillon, L. Bertrand, P. H. Smurov, I. (2007) Strategy of manufacturing components with designed internal structure by selective laser melting of metal powders. *Applied surface science* **254**, pp. 980 - 983.

Yamada K., Mohri M. (1991) Properties and Applications of Silicon Carbide Ceramics. In: Sömiya S., Inomata Y. (eds) Silicon Carbide Ceramics -1, pp. 13-44 Springer, Dordrecht.

Yin, Y.F. Xu, W. Sun, Q.Y. Xiao, L and Sun, J. (2015) Deformation and fracture behaviour of commercially pure titanium with gradient nano-to-micro-grained surface layer, *Transactions of nonferrous metals society of china* **25**(3), pp. 738 - 747.

Yuan, P and Gu, D. (2015) Molten pool behaviour and its physical mechanism during selective laser melting of TiC/AlSi10Mg nanocomposites: simulation and experiments, *Journal of Physics D: Applied Physics* **48**, pp 1 – 16.

Zadra, M. Girardini, L. (2014) High Performance, Low cost Titanium metal matrix composites, *Materials Science and Engineering A*, **608**, pp. 155 - 163.

Zhang, B. n, Dembinski, L. Coddet, C. (2013) The study of the laser parameters and environment variables effect on mechanical properties of high compact parts elaborated by selective laser melting 316L powder, *Materials Science & Engineering A* **584**, pp. 21 - 31

Zhang, S. Li, J. Kou, H. Yang, J. Yang, G and Wang, J (2016) Effects of thermal history on the microstructure evolution ofTi-6Al-4V during solidification. *Journal of Materials Processing Technology* **227**, pp. 281 – 287.

Zhang. Z, Luo. Y, Xu. C. (2012) Phase and morphology evaluation of TiC in the Ti-Si-C System. International Journal of Refractory Metals and Hard Materials.

Zhao, X. Fan, Y. Wang, H. Liu, Y. (2015) Revealing the surface nano-enhancing mechanism of α-titanium alloy by microstructure evolution, *Materials Letters* **160** pp. 51 - 54

Zoz Group, Maltoz-Straße, D-57482 Wenden, GmbH. Tel: +49 (0) 2752 9756-0.

Zoz, H. (2008) Simoloyer ®: major characteristics and features. Zoz GmbH, Germany.

Zoz, H. Ernst, D. SLM, I. S. Kwon, W. H. (2008) Mechanical alloying of Ti-Ni based materials using the Simoloyer® Zoz GmbH, Germany.

Zoz, H. Ernst, Weiss, H. Magini, M. Powell, C. Suryanarayana, C. Froes, F. H. (2008) Mechanical alloying of Ti-24Al-11Nb (AT %) using the Simoloyer® Zoz GmbH, Germany.

Zoz, R.H. Kaupp, H. Naimi-Jamal, G. (2008) Environmentally protecting reactive milling. Zoz GmbH, Germany.

Zoz, H. Ren, H. (2008) Processing of ceramic powder using high energy milling. Zoz GmbH, Germany.

Zoz, H. Ren, H. Reichardr, R. Benz, H. U. (2012) High energy milling / mechanical alloying / reactive milling, Part 1. Zoz GmbH, Germany.

Appendices

Appendix 1, Zoz Maltoz 3.2.1 software configuration.

Appendix 2, Struers, Titanium Alloys (DiaPro, Application Notes)

Titanium Alloys (DiaPro, Application Note)

Select equipment disc size: 300 mm

Method details

Method number:	1417
Download documents:	Print method

These methods are meant as a guide

All methods are generic methods. This means that the methods have been developed according to the following standard: 6 specimens of 30 mm diameter clamped in a specimen holder of 160 mm diameter (MAXCY).

Grinding

Step	PG	FG
Surface	MD-Mezzo 220	MD-Largo
Abrasive Type		DiaPro Allegro/Largo 9 µm
Lubricant Type	Water	
Speed (rpm)	300	150
Force (N) / Specimen	40	30
Holder direction	>>	>>
Time (min)	01:00	04:00

Polishing

Step	OP
Surface	MD-Chem
Abrasive Type	OP-S, 0.04 µm
Lubricant Type	
Speed (rpm)	150
Force (N) / Specimen	30
Holder direction	><
Time (min)	05:00

Appendix 3, Phase 1b, Baseline Assessment Images of Ti6Al4V Single Beads Evaluated Against Energy Density At 150 W

Ti6Al4V Vertical (10 x magnification)	Ti6Al4V Transverse (20 x magnification)	Results
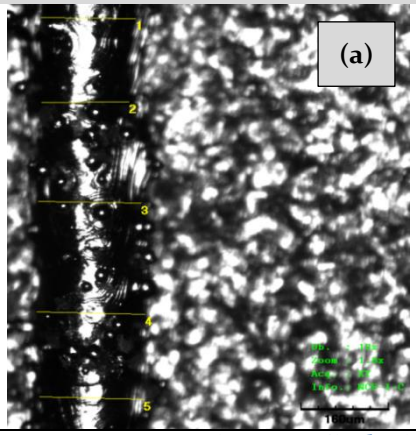	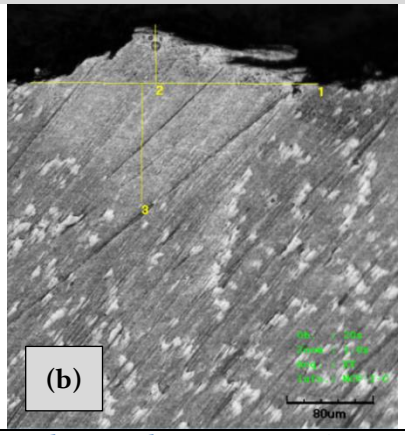	**Energy density** 250 J/mm³ **Scan speed** 200 mm/s **Mean bead width, vertical** 186.287 µm (σ 15.5 µm) **Bead continuity** continuous **Cracking and discoloration** No cracking or discoloration **h1 (Bead height)** 55.004 µm **h2 (Substrate penetration)** 112.502 µm **w1 (Bead width)** 273.128 µm **w2 (width of dilution area)** 273.128 µm

Figure 146 - Single Ti6Al4V Bead at 150 W laser power, 250 J/mm³ energy density

Ti6Al4V Vertical (10 x magnification)	Ti6Al4V Transverse (20 x magnification)	Results
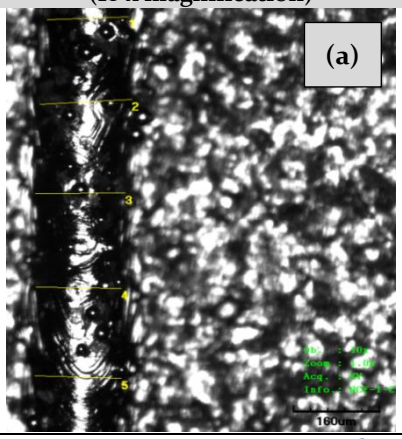	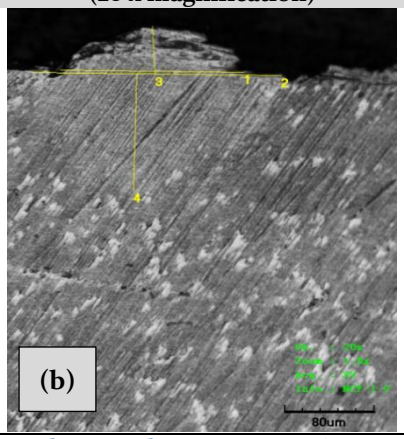	**Energy density** 225 J/mm³ **Scan speed** 222 mm/s **Mean bead width, vertical** 165.852 µm (σ 7.8 µm) **Bead continuity** continuous **Cracking and discoloration** No cracking or discoloration **h1 (Bead height)** 47.566 µm **h2 (Substrate penetration)** 115.042 µm **w1 (Bead width)** 168.144 µm **w2 (width of dilution area)** 228.771 µm

Figure 147 - Single Ti6Al4V Bead at 150 W laser power, 225 J/mm³ energy density

Ti6Al4V Vertical (10 x magnification)	Ti6Al4V Transverse (20 x magnification)	Results
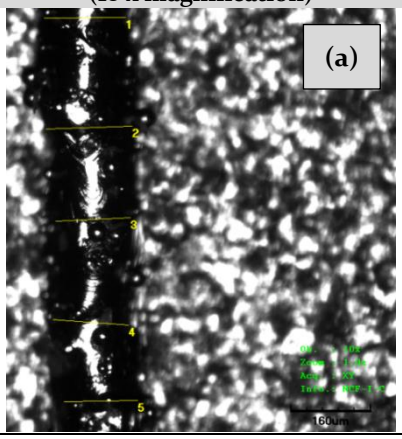	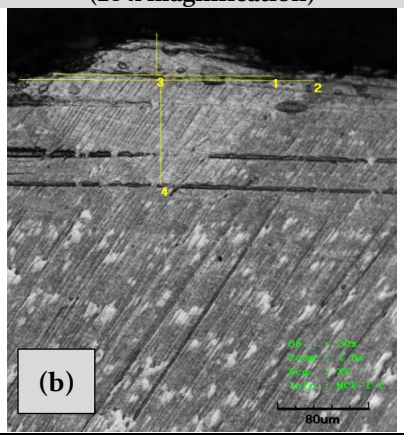	**Energy density** 200 J/mm³ **Scan speed** 250 mm/s **Mean bead width, vertical** 161.505 µm (σ 11.1 µm) **Bead continuity** continuous **Cracking and discoloration** No cracking or discoloration **h1 (Bead height)** 40.625 µm **h2 (Substrate penetration)** 101.875 µm **w1 (Bead width)** 196.884 µm **w2 (width of dilution area)** 265.628 µm

Figure 148 - Single Ti6Al4V Bead at 150 W laser power, 200 J/mm³ energy density

Ti6Al4V Vertical (10 x magnification)	Ti6Al4V Transverse (20 x magnification)	Results
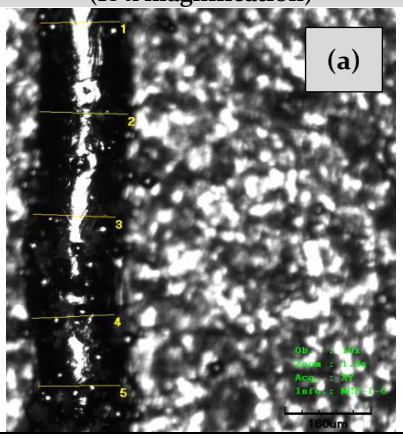	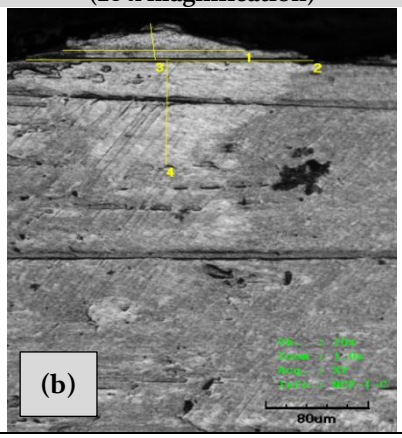	**Energy density** 175 J/mm³ **Scan speed** 286 mm/s **Mean bead width, vertical** 151.271 µm (σ 6.1 µm) **Bead continuity** continuous **Cracking and discoloration** No cracking or discoloration **h1 (Bead height)** 35.200 µm **h2 (Substrate penetration)** 100.627 µm **w1 (Bead width)** 145.000 µm **w2 (width of dilution area)** 229.376 µm

Figure 149 - Single Ti6Al4V Bead at 150 W laser power, 175 J/mm³ energy density

Ti6Al4V Vertical (10 x magnification)	Ti6Al4V Transverse (20 x magnification)	Results
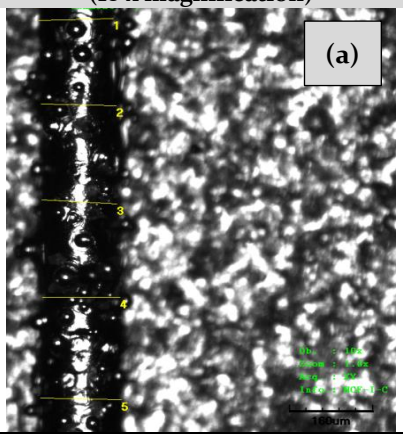	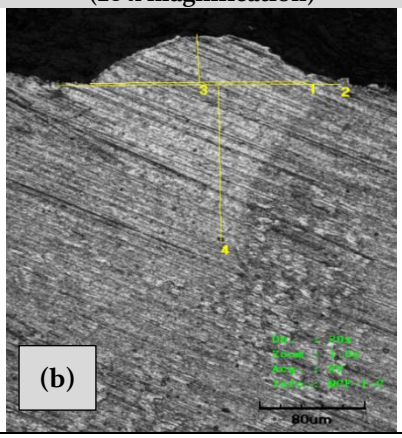	**Energy density** 150 J/mm³ **Scan speed** 333 mm/s **Mean bead width, vertical** 150.580 µm (σ 5.2 µm) **Bead continuity** continuous **Cracking and discoloration** No cracking or discoloration **h1 (Bead height)** 44.415 µm **h2 (Substrate penetration)** 145.012 µm **w1 (Bead width)** 170.010 µm **w2 (width of dilution area)** 221.879 µm

Figure 150 - Single Ti6Al4V Bead at 150 W laser power, 150 J/mm³ energy density

Ti6Al4V Vertical (10 x magnification)	Ti6Al4V Transverse (20 x magnification)	Results
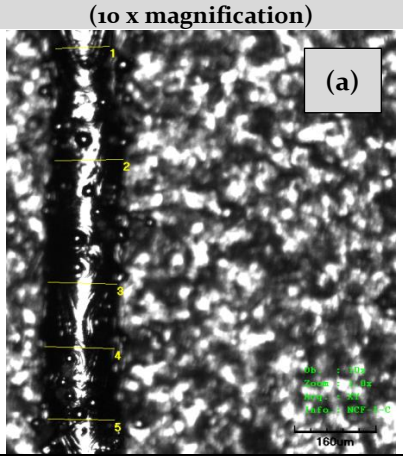	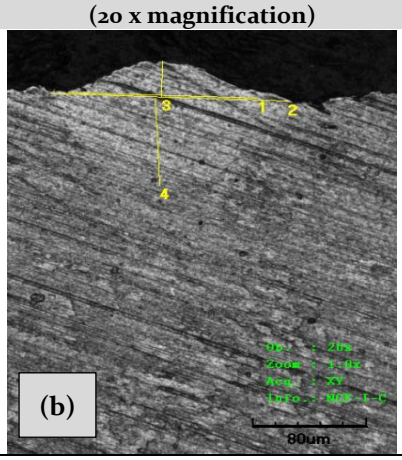	**Energy density** 125 J/mm³ **Scan speed** 400 mm/s **Mean bead width, vertical** 131.802 µm (σ 13.0 µm) **Bead continuity** continuous **Cracking and discoloration** No cracking or discoloration **h1 (Bead height)** 28.757 µm **h2 (Substrate penetration)** 70.694 µm **w1 (Bead width)** 136.945 µm **w2 (width of dilution area)** 171.364 µm

Figure 151 - Single Ti6Al4V Bead at 150 W laser power, 125 J/mm³ energy density

Ti6Al4V Vertical (10 x magnification)	Ti6Al4V Transverse (20 x magnification)	Results
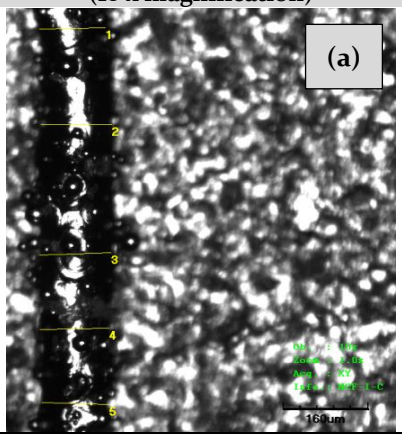	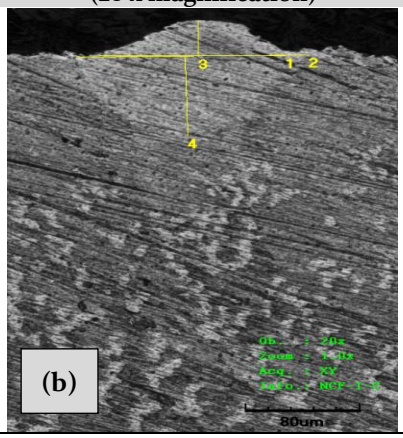	**Energy density** 100 J/mm³ **Scan speed** 500 mm/s **Mean bead width, vertical** 133.288 µm (σ 4.6 µm) **Bead continuity** continuous **Cracking and discoloration** No cracking or discoloration **h1 (Bead height)** 32.500 µm **h2 (Substrate penetration)** 71.899 µm **w1 (Bead width)** 133.750 µm **w2 (width of dilution area)** 166.261 µm

Figure 152 - Single Ti6Al4V Bead at 150 W laser power, 100 J/mm³ energy density

Ti6Al4V Vertical (10 x magnification)	Ti6Al4V Transverse (20 x magnification)	Results
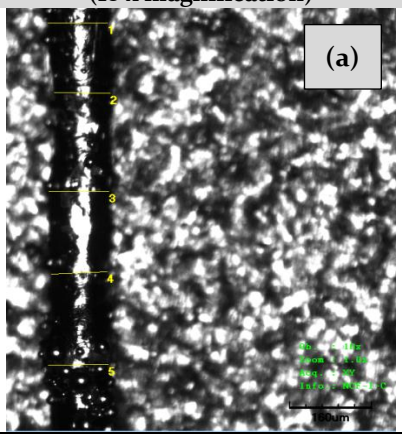	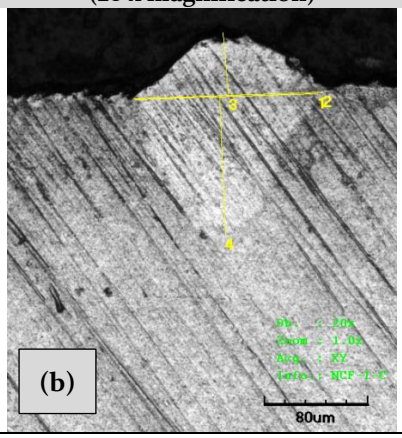	**Energy density** 75 J/mm³ **Scan speed** 667 mm/s **Mean bead width, vertical** 116.275 µm (σ 4.5 µm) **Bead continuity** continuous **Cracking and discoloration** No cracking or discoloration **h1 (Bead height)** 49.568 µm **h2 (Substrate penetration)** 108.838 µm **w1 (Bead width)** 145.066 µm **w2 (width of dilution area)** 150.085 µm

Figure 153 - Single Ti6Al4V Bead at 150 W laser power, 75 J/mm³ energy density

Ti6Al4V Vertical (10 x magnification)	Ti6Al4V Transverse (20 x magnification)	Results
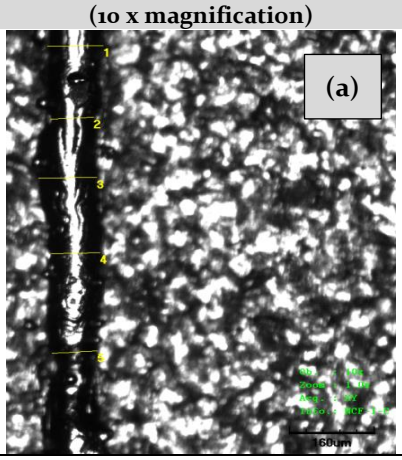	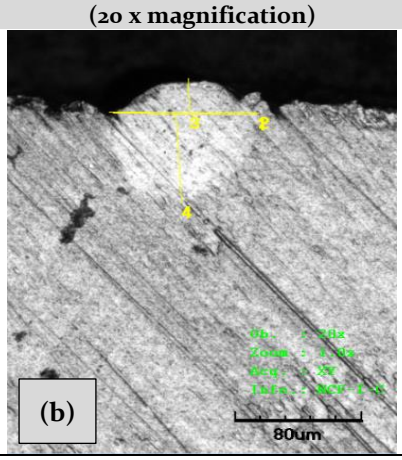	**Energy density** 50 J/mm³ **Scan speed** 1,000 mm/s **Mean bead width, vertical** 96.805 µm (σ 12.8 µm) **Bead continuity** continuous **Cracking and discoloration** No cracking or discoloration **h1 (Bead height)** 25.633 µm **h2 (Substrate penetration)** 65.108 µm **w1 (Bead width)** 93.133 µm **w2 (width of dilution area)** 96.877 µm

Figure 154 - Single Ti6Al4V Bead at 150 W laser power, 50 J/mm³ energy density

Ti6Al4V Vertical (10 x magnification)	Ti6Al4V Transverse (20 x magnification)	Results
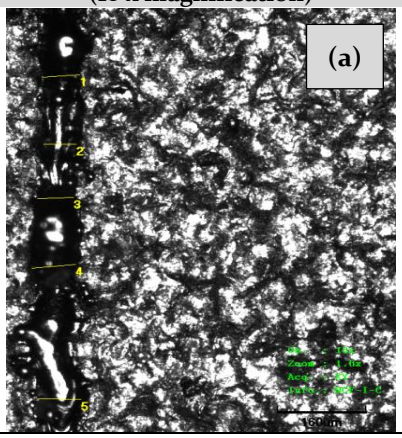	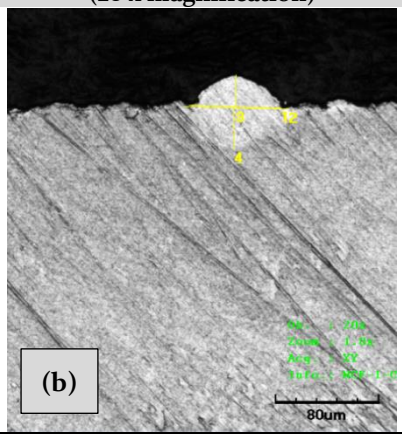	**Energy density** 25 J/mm³ **Scan speed** 2,000 mm/s **Mean bead width, vertical** 70.618 µm (σ 8.8 µm) **Bead continuity** Not continuous **Cracking and discoloration** No cracking or discoloration **h1 (Bead height)** 27.500 µm **h2 (Substrate penetration)** 33.756 µm **w1 (Bead width)** 72.543 µm **w2 (width of dilution area)** 82.521 µm

Figure 155 - Single Ti6Al4V Bead at 150 W laser power, 25 J/mm³ energy density

Appendix 4, Phase 1b, Baseline Assessment Images of Ti6Al4V Single Beads Evaluated Against Energy Density At 250 W

Ti6Al4V Vertical (10 x magnification)	Ti6Al4V Transverse (20 x magnification)	Results
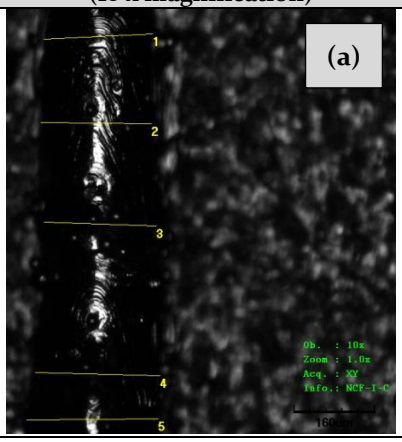		**Energy density** 417 J/mm³ **Scan speed** 200 mm/s **Mean bead width, vertical** 239.340 µm (σ 20.2 µm) **Bead continuity** continuous **Cracking and discoloration** No cracking or discoloration **h1 (Bead height)** 96.323 µm **h2 (Substrate penetration)** 79.375 µm **w1 (Bead width)** 312.576 µm **w2 (width of dilution area)** 315.675 µm

Figure 156 - Single Ti6Al4V Bead at 250 W laser power, 417 J/mm³ energy density

Ti6Al4V Vertical (10 x magnification)	Ti6Al4V Transverse (20 x magnification)	Results
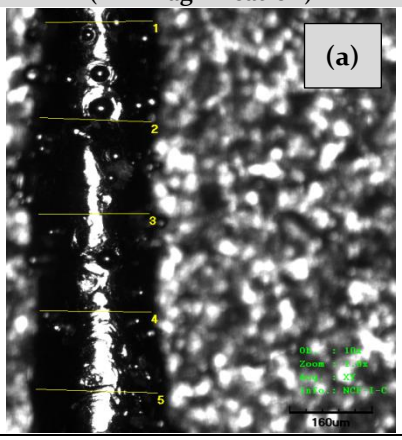		Energy density 375 J/mm³ Scan speed 222 mm/s Mean bead width, vertical 223.314 µm (σ 10.7 µm) Bead continuity continuous Cracking and discoloration No cracking or discoloration h1 (Bead height) 115.652 µm h2 (Substrate penetration) 90.020 µm w1 (Bead width) 240.742 µm w2 (width of dilution area) 243.847 µm

Figure 157 - Single Ti6Al4V Bead at 250 W laser power, 375 J/mm³ energy density

Ti6Al4V Vertical (10 x magnification)	Ti6Al4V Transverse (20 x magnification)	Results
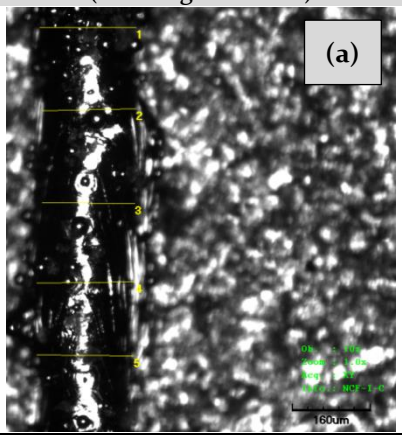		**Energy density** 333 J/mm³ **Scan speed** 250 mm/s **Mean bead width, vertical** 201.514 µm (σ 5.4 µm) **Bead continuity** continuous **Cracking and discoloration** No cracking or discoloration **h1 (Bead height)** 95.402 µm **h2 (Substrate penetration)** 74.441 µm **w1 (Bead width)** 249.488 µm **w2 (width of dilution area)** 246.251 µm

Figure 158 - Single Ti6Al4V Bead at 250 W laser power, 333 J/mm³ energy density

Ti6Al4V Vertical (10 x magnification)	Ti6Al4V Transverse (20 x magnification)	Results
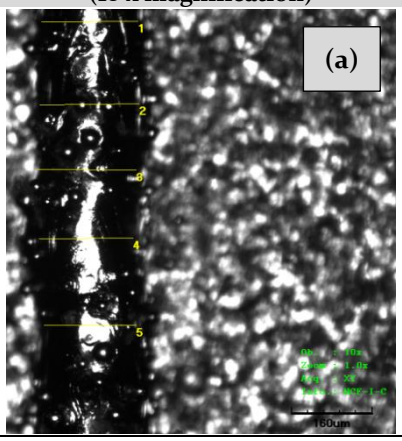	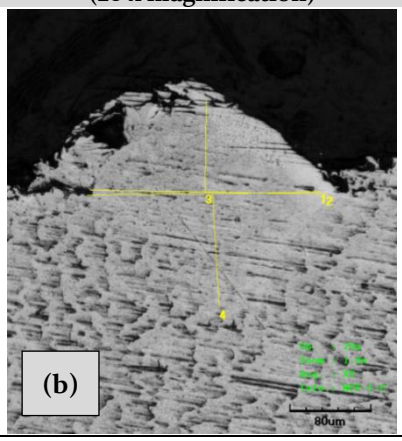	**Energy density** 291 J/mm³ **Scan speed** 286 mm/s **Mean bead width, vertical** 195.505 µm (σ 6.2 µm) **Bead continuity** continuous **Cracking and discoloration** No cracking or discoloration **h1 (Bead height)** 90.634 µm **h2 (Substrate penetration)** 113.334 µm **w1 (Bead width)** 235.646 µm **w2 (width of dilution area)** 238.779 µm

Figure 159 - Single Ti6Al4V Bead at 250 W laser power, 291 J/mm³ energy density

Ti6Al4V Vertical (10 x magnification)	Ti6Al4V Transverse (20 x magnification)	Results
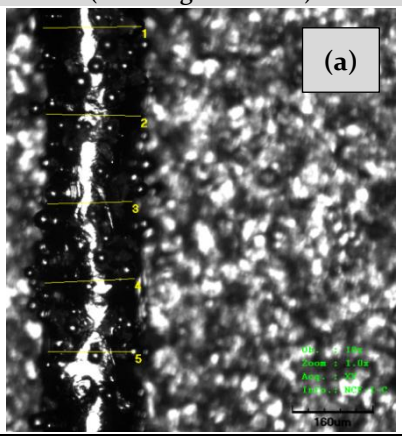	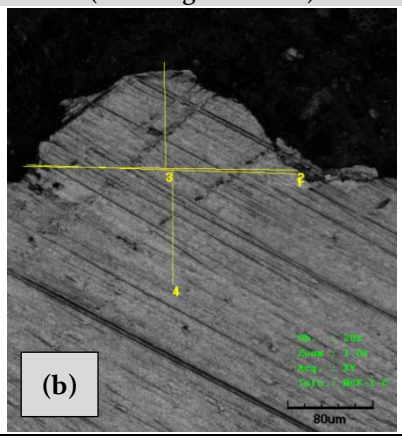	**Energy density** 250 J/mm³ **Scan speed** 333 mm/s **Mean bead width, vertical** 185.067 µm (σ 11.2 µm) **Bead continuity** continuous **Cracking and discoloration** No cracking or discoloration **h1 (Bead height)** 98.133 µm **h2 (Substrate penetration)** 105.000 µm **w1 (Bead width)** 259.502 µm **w2 (width of dilution area)** 263.769 µm

Figure 160 - Single Ti6Al4V Bead at 250 W laser power, 250 J/mm³ energy density

Ti6Al4V Vertical (10 x magnification)	Ti6Al4V Transverse (20 x magnification)	Results
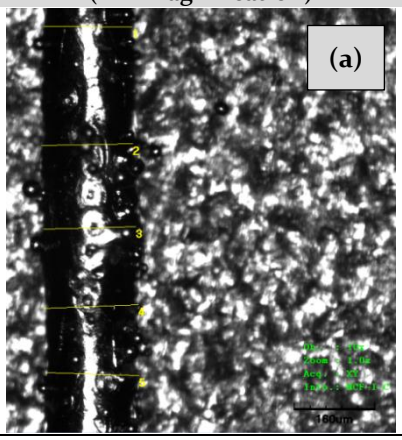	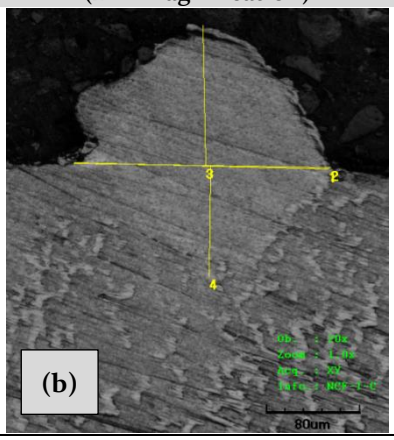	**Energy density** 208 J/mm³ **Scan speed** 400 mm/s **Mean bead width, vertical** 186.822 µm (σ 5.5 µm) **Bead continuity** continuous **Cracking and discoloration** No cracking or discoloration **h1 (Bead height)** 121.901 µm **h2 (Substrate penetration)** 95.633 µm **w1 (Bead width)** 223.821 µm **w2 (width of dilution area)** 226.281 µm

Figure 161 - Single Ti6Al4V Bead at 250 W laser power, 208 J/mm³ energy density

Ti6Al4V Vertical (10 x magnification)	Ti6Al4V Transverse (20 x magnification)	Results
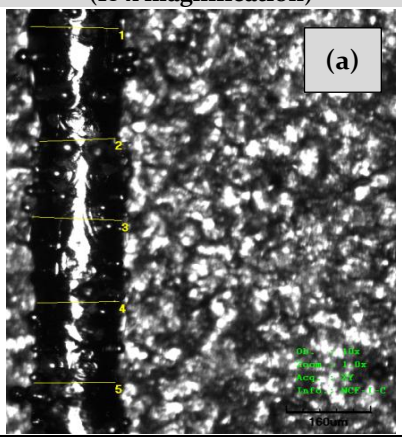	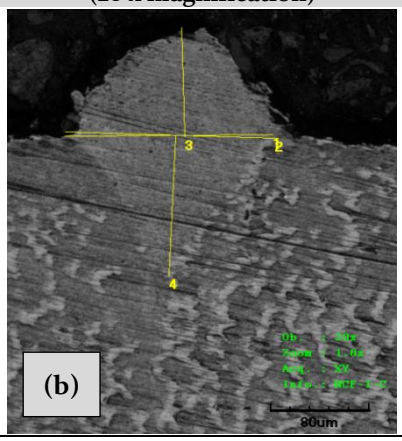	**Energy density** 167 J/mm³ **Scan speed** 500 mm/s **Mean bead width, vertical** 161.322 µm (σ 10.9 µm) **Bead continuity** continuous **Cracking and discoloration** No cracking or discoloration **h1 (Bead height)** 95.658 µm **h2 (Substrate penetration)** 122.005 µm **w1 (Bead width)** 173.130 µm **w2 (width of dilution area)** 174.466 µm

Figure 162 - Single Ti6Al4V Bead at 250 W laser power, 167 J/mm³ energy density

Ti6Al4V Vertical (10 x magnification)	Ti6Al4V Transverse (20 x magnification)	Results
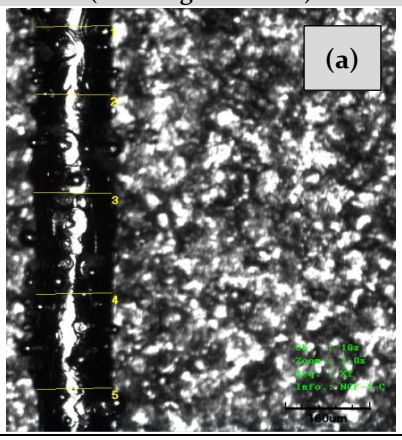	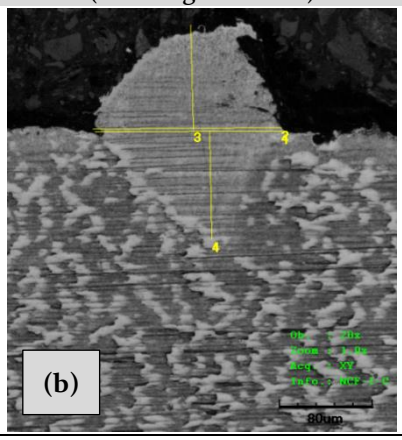	**Energy density** 125 J/mm³ **Scan speed** 667 mm/s **Mean bead width, vertical** 145.765 µm (σ 3.4 µm) **Bead continuity** continuous **Cracking and discoloration** No cracking or discoloration **h1 (Bead height)** 92.534 µm **h2 (Substrate penetration)** 95.643 µm **w1 (Bead width)** 165.001 µm **w2 (width of dilution area)** 166.255 µm

Figure 163 - Single Ti6Al4V Bead at 250 W laser power, 125 J/mm³ energy density

Ti6Al4V Vertical (10 x magnification)	Ti6Al4V Transverse (20 x magnification)	Results
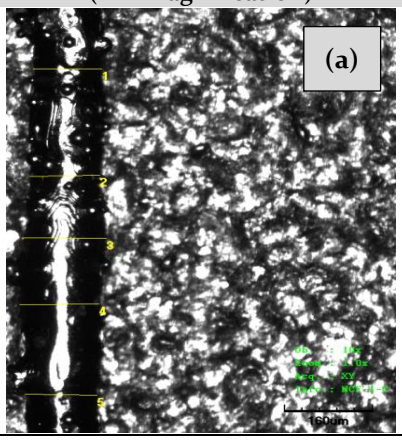	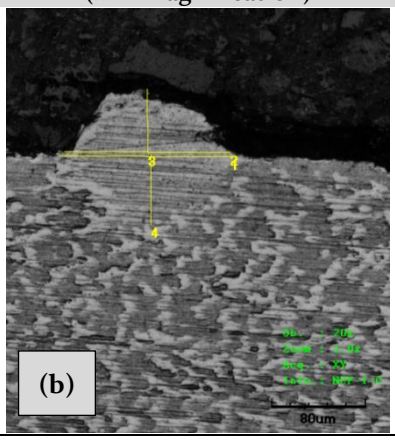	**Energy density** 83 J/mm³ **Scan speed** 1,000 mm/s **Mean bead width, vertical** 138.262 µm (σ 11.0 µm) **Bead continuity** continuous **Cracking and discoloration** No cracking or discoloration **h1 (Bead height)** 55.629 µm **h2 (Substrate penetration)** 60.625 µm **w1 (Bead width)** 150.001 µm **w2 (width of dilution area)** 145.001 µm

Figure 164 - Single Ti6Al4V Bead at 250 W laser power, 83 J/mm³ energy density

Ti6Al4V Vertical (10 x magnification)	Ti6Al4V Transverse (20 x magnification)	Results
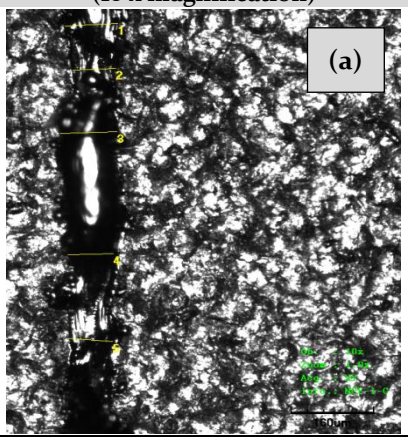	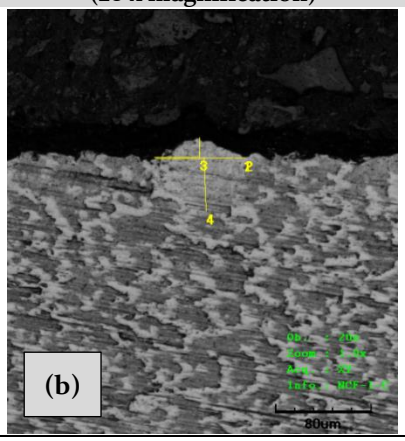	**Energy density** 42 J/mm³ **Scan speed** 2,000 mm/s **Mean bead width, vertical** 95.605 µm (σ 12.0 µm) **Bead continuity** Not continuous **Cracking and discoloration** No cracking or discoloration **h1 (Bead height)** 16.875 µm **h2 (Substrate penetration)** 45.039 µm **w1 (Bead width)** 75.003 µm **w2 (width of dilution area)** 77.503 µm

Figure 165 - Single Ti6Al4V Bead at 250 W laser power, 42 J/mm³ energy density

Appendix 5, Phase 1b, Baseline Assessment Images of Ti6Al4V Single Beads Evaluated Against Energy Density At 350 W

Ti6Al4V Vertical (10 x magnification)	Ti6Al4V Transverse (20 x magnification)	Results
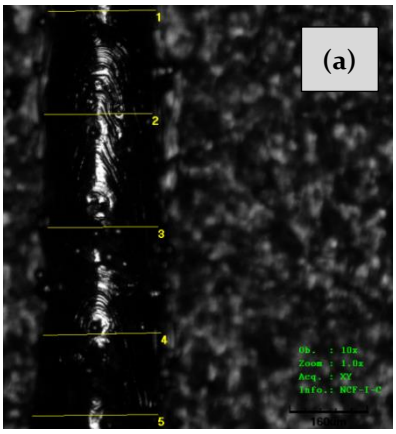	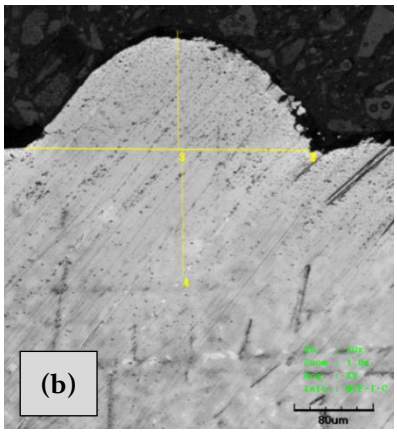	**Energy density** 583 J/mm³ **Scan speed** 200 mm/s **Mean bead width, vertical** 240.017 µm (σ 16.6 µm) **Bead continuity** continuous **Cracking and discoloration** No cracking or discoloration **h1 (Bead height)** 125.631 µm **h2 (Substrate penetration)** 133.126 µm **w1 (Bead width)** 296.886 µm **w2 (width of dilution area)** 293.756 µm

Figure 166 - Single Ti6Al4V Bead at 350 W laser power, 583 J/mm³ energy density

Ti6Al4V Vertical (10 x magnification)	Ti6Al4V Transverse (20 x magnification)	Results
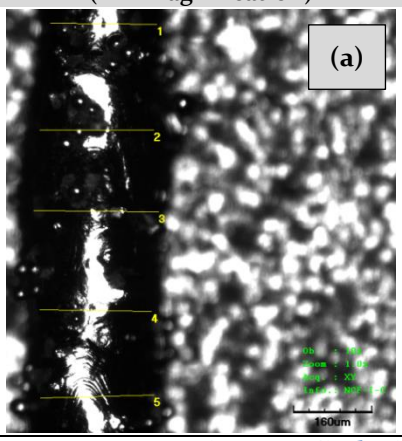	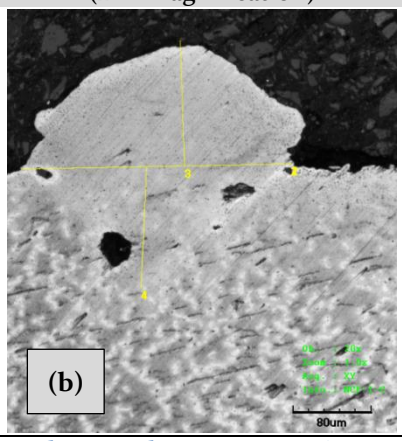	**Energy density** 526 J/mm³ **Scan speed** 222 mm/s **Mean bead width, vertical** 238.778 µm (σ 14.1 µm) **Bead continuity** continuous **Cracking and discoloration** No cracking or discoloration **h1 (Bead height)** 126.950 µm **h2 (Substrate penetration)** 122.005 µm **w1 (Bead width)** 281.919 µm **w2 (width of dilution area)** 282.544 µm

Figure 167 - Single Ti6Al4V Bead at 350 W laser power, 526 J/mm³ energy density

Ti6Al4V Vertical (10 x magnification)	Ti6Al4V Transverse (20 x magnification)	Results
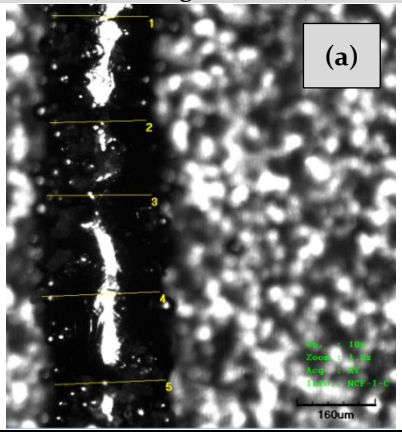	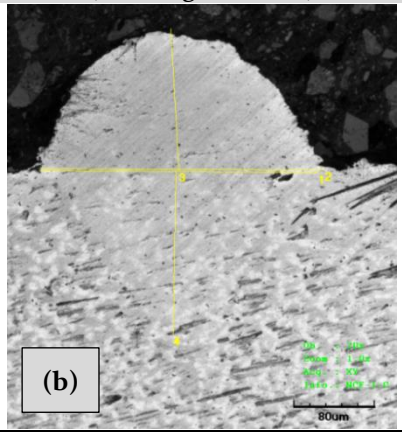	**Energy density** 467 J/mm³ **Scan speed** 250 mm/s **Mean bead width, vertical** 220.097 µm (σ 19.7 µm) **Bead continuity** continuous **Cracking and discoloration** No cracking or discoloration **h1 (Bead height)** 148.972 µm **h2 (Substrate penetration)** 171.893 µm **w1 (Bead width)** 283.761 µm **w2 (width of dilution area)** 290.003 µm

Figure 168 - Single Ti6Al4V Bead at 350 W laser power, 467 J/mm³ energy density

Ti6Al4V Vertical (10 x magnification)	Ti6Al4V Transverse (20 x magnification)	Results
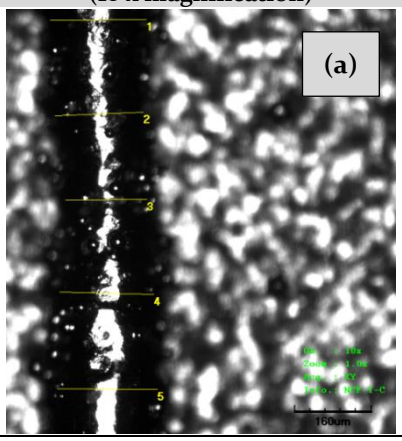	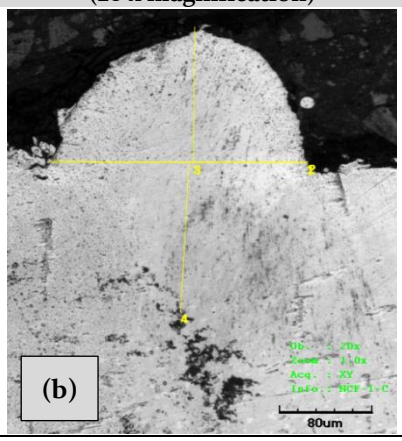	**Energy density** 408 J/mm³ **Scan speed** 286 mm/s **Mean bead width, vertical** 196.545 µm (σ 15.6 µm) **Bead continuity** continuous **Cracking and discoloration** No cracking or discoloration **h1 (Bead height)** 131.256 µm **h2 (Substrate penetration)** 142.697 µm **w1 (Bead width)** 228.758 µm **w2 (width of dilution area)** 228.126 µm

Figure 169 - Single Ti6Al4V Bead at 350 W laser power, 408 J/mm³ energy density

Ti6Al4V Vertical (10 x magnification)	Ti6Al4V Transverse (20 x magnification)	Results
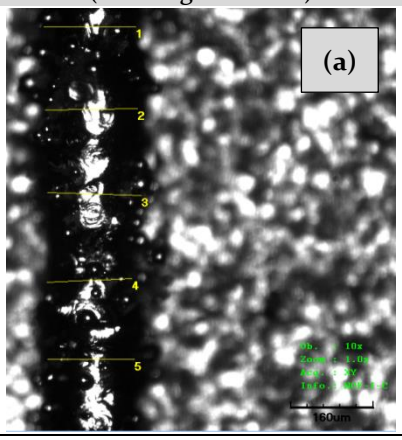	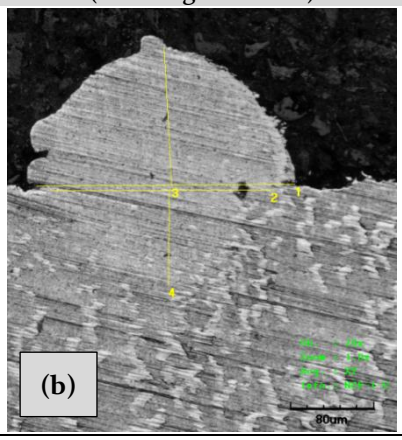	**Energy density** 350 J/mm³ **Scan speed** 333 mm/s **Mean bead width, vertical** 178.808 µm (σ 7.6 µm) **Bead continuity** continuous **Cracking and discoloration** No cracking or discoloration **h1 (Bead height)** 134.584 µm **h2 (Substrate penetration)** 91.252 µm **w1 (Bead width)** 253.757 µm **w2 (width of dilution area)** 215.626 µm

Figure 170 - Single Ti6Al4V Bead at 350 W laser power, 350 J/mm³ energy density

Ti6Al4V Vertical (10 x magnification)	Ti6Al4V Transverse (20 x magnification)	Results
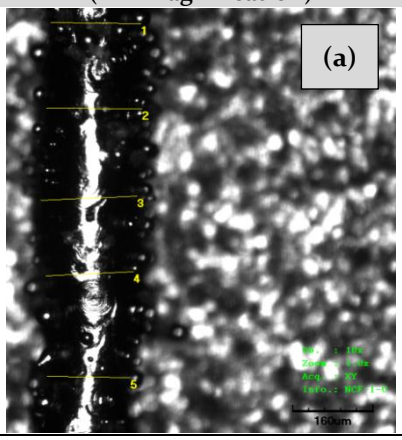	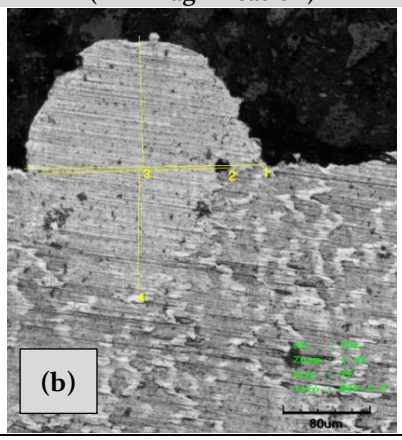	**Energy density** 292 J/mm³ **Scan speed** 400 mm/s **Mean bead width, vertical** 184.840 µm (σ 11.1 µm) **Bead continuity** continuous **Cracking and discoloration** No cracking or discoloration **h1 (Bead height)** 123.807 µm **h2 (Substrate penetration)** 113.757 µm **w1 (Bead width)** 177.570 µm **w2 (width of dilution area)** 224.406 µm

Figure 171 - Single Ti6Al4V Bead at 350 W laser power, 292 J/mm³ energy density

Ti6Al4V Vertical (10 x magnification)	Ti6Al4V Transverse (20 x magnification)	Results
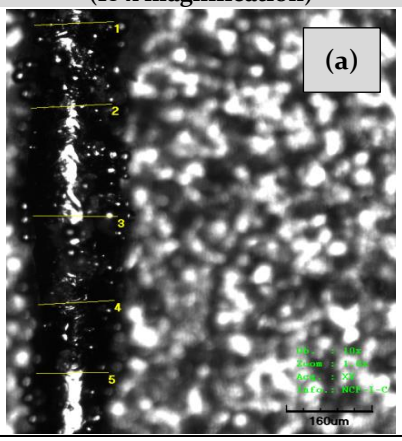	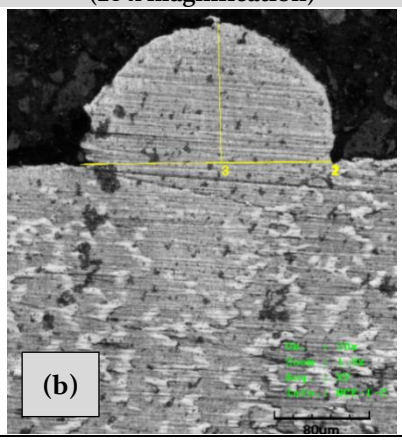	**Energy density** 233 J/mm³ **Scan speed** 500 mm/s **Mean bead width, vertical** 149.892 µm (σ 9.0 µm) **Bead continuity** continuous **Cracking and discoloration** No cracking or discoloration **h1 (Bead height)** 124.400 µm **h2 (Substrate penetration)** - µm **w1 (Bead width)** 216.273 µm **w2 (width of dilution area)** 213.129 µm

Figure 172 - Single Ti6Al4V Bead at 350 W laser power, 233 J/mm³ energy density

Ti6Al4V Vertical (10 x magnification)	Ti6Al4V Transverse (20 x magnification)	Results
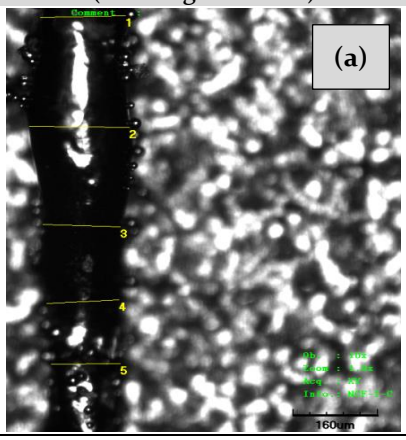	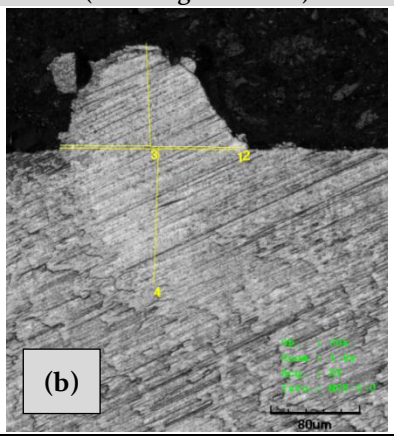	**Energy density** 175 J/mm³ **Scan speed** 667 mm/s **Mean bead width, vertical** 156.570 µm (σ 23.9 µm) **Bead continuity** continuous **Cracking and discoloration** No cracking or discoloration **h1 (Bead height)** 93.825 µm **h2 (Substrate penetration)** 123.827 µm **w1 (Bead width)** 162.505 µm **w2 (width of dilution area)** 168.135 µm

Figure 173 - Single Ti6Al4V Bead at 350 W laser power, 175 J/mm³ energy density

Ti6Al4V Vertical (10 x magnification)	Ti6Al4V Transverse (20 x magnification)	Results
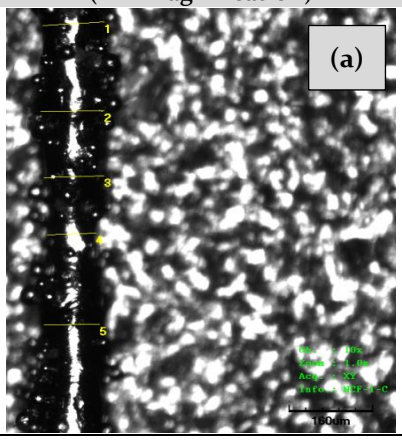	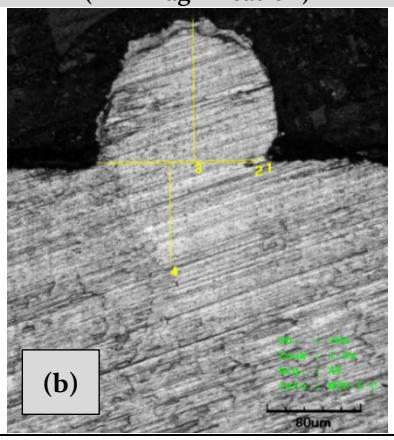	**Energy density** 117 J/mm³ **Scan speed** 1,000 mm/s **Mean bead width, vertical** 113.076 µm (σ 11.5 µm) **Bead continuity** continuous **Cracking and discoloration** No cracking or discoloration **h1 (Bead height)** 127.506 µm **h2 (Substrate penetration)** 90.627 µm **w1 (Bead width)** 148.146 µm **w2 (width of dilution area)** 128.756 µm

Figure 174 - Single Ti6Al4V Bead at 350 W laser power, 117 J/mm³ energy density

Ti6Al4V Vertical (10 x magnification)	Ti6Al4V Transverse (20 x magnification)	Results
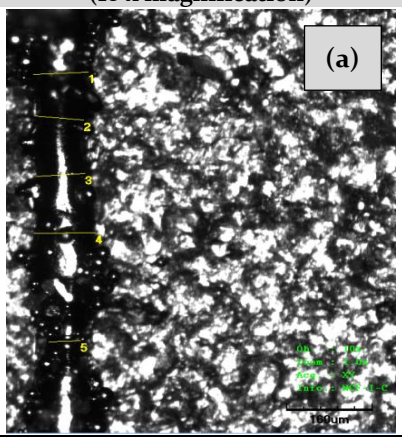	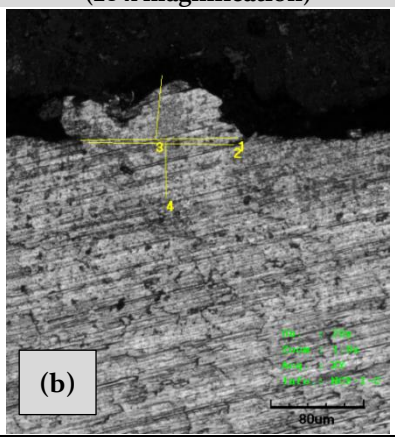	**Energy density** 58 J/mm³ **Scan speed** 2,000 mm/s **Mean bead width, vertical** 93.909 µm (σ 21.4 µm) **Bead continuity** Not continuous **Cracking and discoloration** No cracking or discoloration **h1 (Bead height)** 55.287 µm **h2 (Substrate penetration)** 48.754 µm **w1 (Bead width)** 138.763 µm **w2 (width of dilution area)** 128.139 µm

Figure 175 - Single Ti6Al4V Bead at 350 W laser power, 58 J/mm³ energy density

Appendix 6, Phase 3a; MMC Single Bead Evaluation Images Against Energy Density Compared to Baseline Results At 150 W

Ti6Al4V Vertical (10 x magnification)	Ti6Al4V Transverse section (20 x magnification)	MMC Vertical (10 x magnification)	MMC Transverse section (20 x magnification)
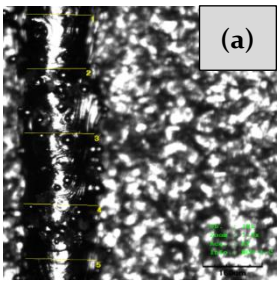	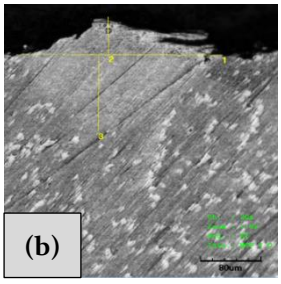	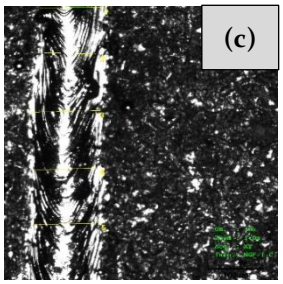	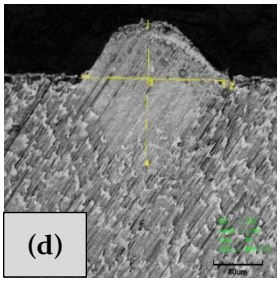
E = 250 J/mm³ **V** = 200 mm/s **Mean bead width, vertical** = 186.287 µm (σ 15.5 µm) **h1** = 55.004 µm **h2** = 112.502 µm **w1** = 273.128 µm **w2** = 273.128 µm		**E** = 250 J/mm³ **V** = 200 mm/s **Mean bead width, vertical** = 199.316 µm (σ 6.3 µm) **h1** = 85.021 µm **h2** = 117.581 µm **w1** = 232.568 µm **w2** = 251.288 µm	

Figure 176 - Single Ti6Al4V Bead at 150 W laser power, 250 J/mm³ energy density in comparison to MMC material

Ti6Al4V Vertical (10 x magnification)	Ti6Al4V Transverse section (20 x magnification)	MMC Vertical (10 x magnification)	MMC Transverse section (20 x magnification)
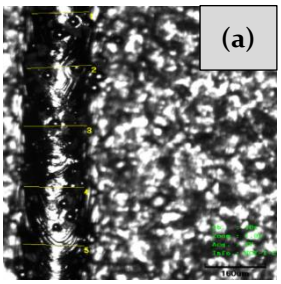	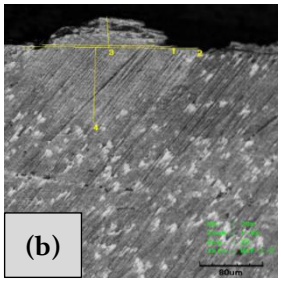	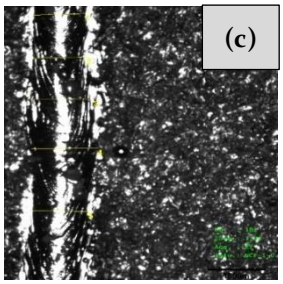	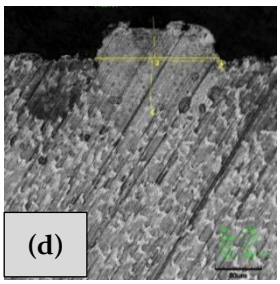
E = 225 J/mm³ **V** = 222 mm/s **Mean bead width, vertical** = 165.852 µm (σ 7.8 µm) **h1** = 47.566 µm **h2** = 115.042 µm **w1** = 168.144 µm **w2** = 228.771 µm		**E** = 225 J/mm³ **V** = 222 mm/s **Mean bead width, vertical** = 192.458 µm (σ 3.3 µm) **h1** = 68.197 µm **h2** = 78.187 µm **w1** = 221.875 µm **w2** = 222.514 µm	

Figure 177 - Single Ti6Al4V Bead at 150 W laser power, 225 J/mm³ energy density in comparison to MMC material

Ti6Al4V Vertical (10 x magnification)	Ti6Al4V Transverse section (20 x magnification)	MMC Vertical (10 x magnification)	MMC Transverse section (20 x magnification)
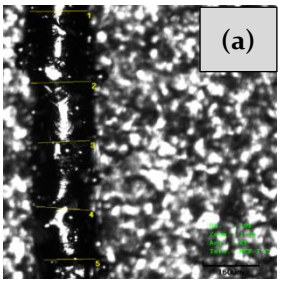	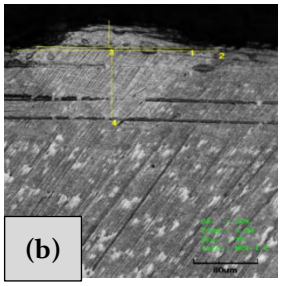	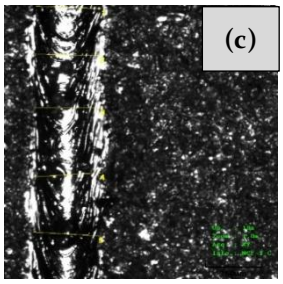	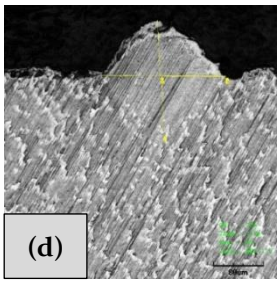
E = 200 J/mm³ **V** = 250 mm/s **Mean bead width, vertical** = 161.505 µm (σ 11.1 µm) **h1** = 40.625 µm **h2** = 101.875 µm **w1** = 196.884 µm **w2** = 265.628 µm		**E** = 200 J/mm³ **V** = 250 mm/s **Mean bead width, vertical** = 172.530 µm (σ 21.2 µm) **h1** = 86.985 µm **h2** = 91.259 µm **w1** = 198.759 µm **w2** = 200.004 µm	

Figure 178 - Single Ti6Al4V Bead at 150 W laser power, 200 J/mm³ energy density in comparison to MMC material

Ti6Al4V Vertical (10 x magnification)	Ti6Al4V Transverse section (20 x magnification)	MMC Vertical (10 x magnification)	MMC Transverse section (20 x magnification)
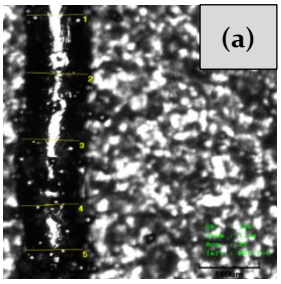	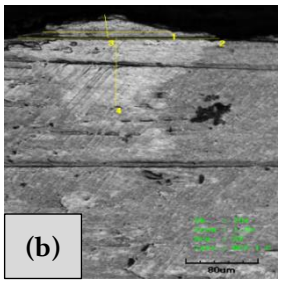	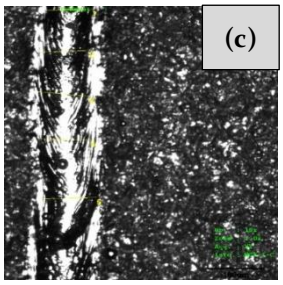	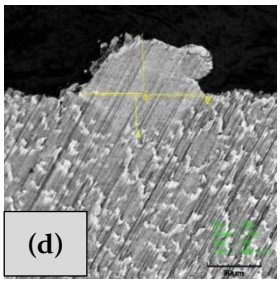
E = 175 J/mm³ **V** = 286 mm/s **Mean bead width, vertical** = 151.271 µm (σ 6.1 µm) **h1** = 35.200 µm **h2** = 100.627 µm **w1** = 145.000 µm **w2** = 229.376 µm		**E** = 175 J/mm³ **V** = 286 mm/s **Mean bead width, vertical** = 147.963 µm (σ 10.2 µm) **h1** = 91.909 µm **h2** = 53.125 µm **w1** = 191.259 µm **w2** = 193.775 µm	

Figure 179 - Single Ti6Al4V Bead at 150 W laser power, 175 J/mm³ energy density in comparison to MMC material

Ti6Al4V Vertical (10 x magnification)	Ti6Al4V Transverse section (20 x magnification)	MMC Vertical (10 x magnification)	MMC Transverse section (20 x magnification)
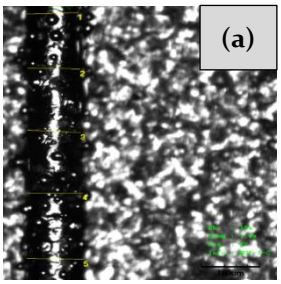	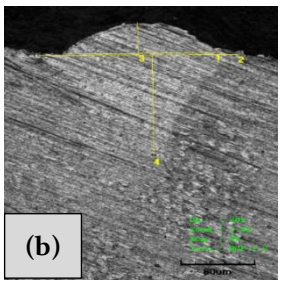	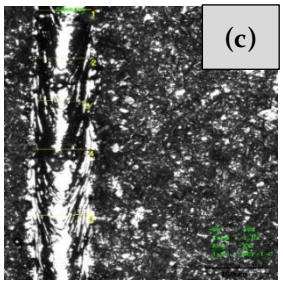	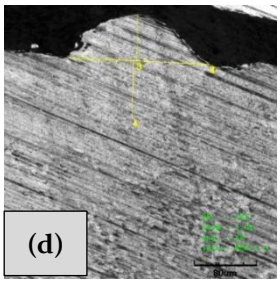
E = 150 J/mm³ **V** = 333 mm/s **Mean bead width, vertical** = 150.580 µm (σ 5.2 µm) **h1** = 44.415 µm **h2** = 145.012 µm **w1** = 170.010 µm **w2** = 221.879 µm		**E** = 150 J/mm³ **V** = 333 mm/s **Mean bead width, vertical** = 152.777 µm (σ 8.6 µm) **h1** = 62.512 µm **h2** = 74.378 µm **w1** = 186.553 µm **w2** = 190.772 µm	

Figure 180 - Single Ti6Al4V Bead at 150 W laser power, 150 J/mm³ energy density in comparison to MMC material

Ti6Al4V Vertical (10 x magnification)	Ti6Al4V Transverse section (20 x magnification)	MMC Vertical (10 x magnification)	MMC Transverse section (20 x magnification)
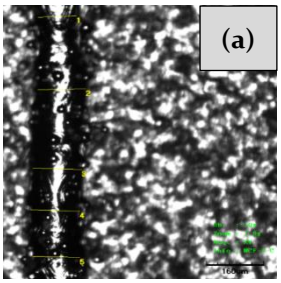	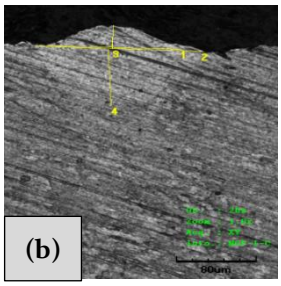	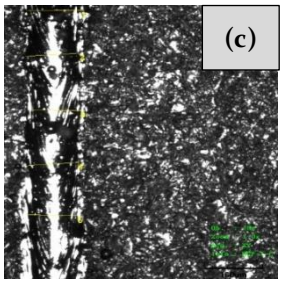	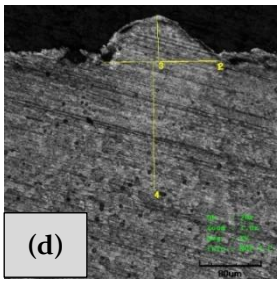
E = 125 J/mm³ **V** = 400 mm/s **Mean bead width, vertical** = 131.802 µm (σ 13.0 µm) **h1** = 28.757 µm **h2** = 70.694 µm **w1** = 136.945 µm **w2** = 171.364 µm		**E** = 125 J/mm³ **V** = 400 mm/s **Mean bead width, vertical** = 149.158 µm (σ 5.3 µm) **h1** = 60.654 µm **h2** = 169.380 µm **w1** = 150.005 µm **w2** = 155.011 µm	

Figure 181 - Single Ti6Al4V Bead at 150 W laser power, 125 J/mm³ energy density in comparison to MMC material

Ti6Al4V Vertical (10 x magnification)	Ti6Al4V Transverse section (20 x magnification)	MMC Vertical (10 x magnification)	MMC Transverse section (20 x magnification)

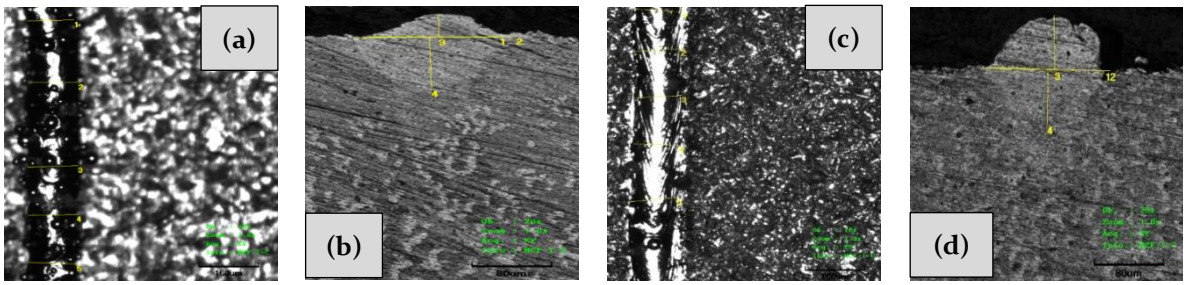

E = 100 J/mm³ **V** = 500 mm/s **Mean bead width, vertical** = 133.288 µm (σ 4.6 µm) **h1** = 32.500 µm **h2** = 71.899 µm **w1** = 133.750 µm **w2** = 166.261 µm	**E** = 100 J/mm³ **V** = 500 mm/s **Mean bead width, vertical** = 132.086 µm (σ 2.9 µm) **h1** = 65.003 µm **h2** = 63.128 µm **w1** = 133.803 µm **w2** = 152.532 µm

Figure 182 - Single Ti6Al4V Bead at 150 W laser power, 100 J/mm³ energy density in comparison to MMC material

Ti6Al4V Vertical (10 x magnification)	Ti6Al4V Transverse section (20 x magnification)	MMC Vertical (10 x magnification)	MMC Transverse section (20 x magnification)

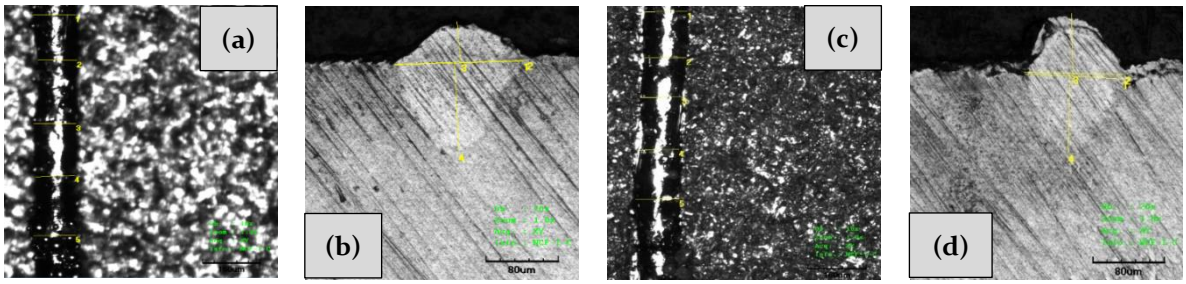

E = 75 J/mm³ **V** = 667 mm/s **Mean bead width, vertical** = 116.275 µm (σ 4.5 µm) **h1** = 49.568 µm **h2** = 108.838 µm **w1** = 145.066 µm **w2** = 150.085 µm	**E** = 75 J/mm³ **V** = 667 mm/s **Mean bead width, vertical** = 120.770 µm (σ 2.6 µm) **h1** = 69.386 µm **h2** = 89.395 µm **w1** = 112.016 µm **w2** = 115.652 µm

Figure 183 - Single Ti6Al4V Bead at 150 W laser power, 75 J/mm³ energy density in comparison to MMC material

Ti6Al4V Vertical (10 x magnification)	Ti6Al4V Transverse section (20 x magnification)	MMC Vertical (10 x magnification)	MMC Transverse section (20 x magnification)

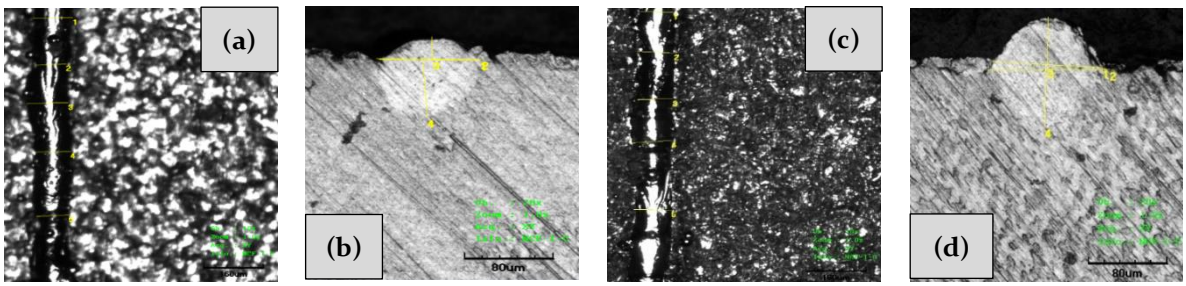

E = 50 J/mm³ **V** = 1,000 mm/s **Mean bead width, vertical** = 96.805 µm (σ 12.8 µm) **h1** = 25.633 µm **h2** = 65.108 µm **w1** = 93.133 µm **w2** = 96.877 µm	**E** = 50 J/mm³ **V** = 1,000 mm/s **Mean bead width, vertical** = 98.851 µm (σ 7.3 µm) **h1** = 51.879 µm **h2** = 61.878 µm **w1** = 115.170 µm **w2** = 126.877 µm

Figure 184 - Single Ti6Al4V Bead at 150 W laser power, 50 J/mm3 energy density in comparison to MMC material

Ti6Al4V Vertical (10 x magnification)	Ti6Al4V Transverse section (20 x magnification)	MMC Vertical (10 x magnification)	MMC Transverse section (20 x magnification)
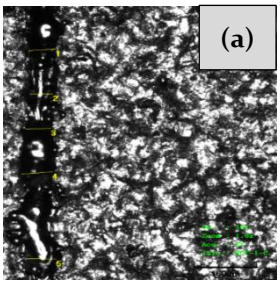	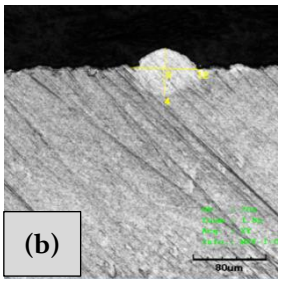	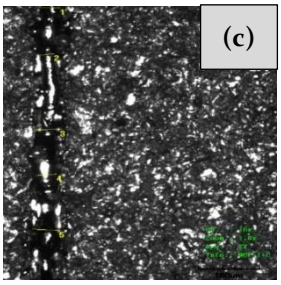	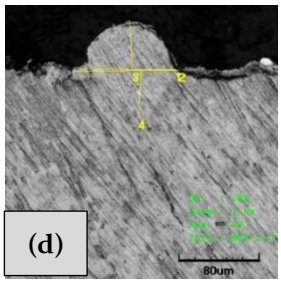
E = 25 J/mm³ **V** = 2,000 mm/s **Mean bead width, vertical** = 70.618 µm (σ 8.8 µm) **h1** = 27.500 µm **h2** = 33.756 µm **w1** = 72.543 µm **w2** = 82.521 µm		**E** = 25 J/mm³ **V** = 2,000 mm/s **Mean bead width, vertical** = 57.883 µm (σ 12.4 µm) **h1** = 50.687 µm **h2** = 48.226 µm **w1** = 96.877 µm **w2** = 108.127 µm	

Figure 185 - Single Ti6Al4V Bead at 150 W laser power, 25 J/mm³ energy density in comparison to MMC material

Appendix 7, Phase 3a; MMC Single Bead Evaluation Images Against Energy Density Compared to Baseline Results At 250 W

Ti6Al4V Vertical (10 x magnification)	Ti6Al4V Transverse section (20 x magnification)	MMC Vertical (10 x magnification)	MMC Transverse section (20 x magnification)
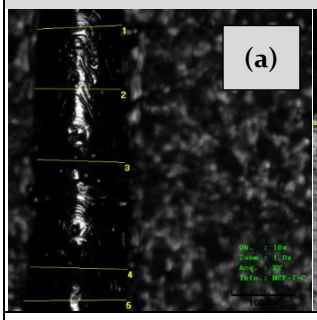	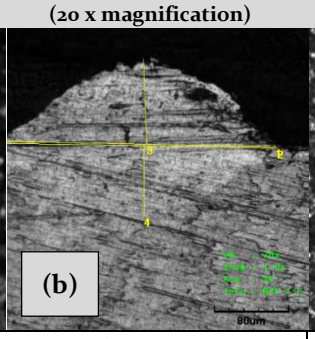	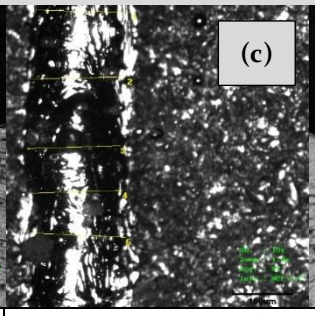	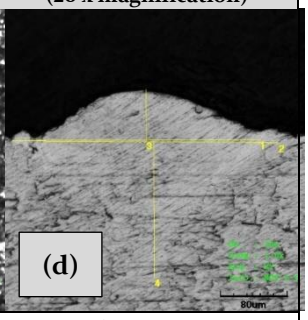
E = 417 J/mm³ **V** = 200 mm/s **Mean bead width, vertical** = 239.340 µm (σ 20.2 µm) **h1** = 96.323 µm **h2** = 79.375 µm **w1** = 312.576 µm **w2** = 315.675 µm		**E** = 417 J/mm³ **V** = 200 mm/s **Mean bead width, vertical** = 260.883 µm (σ 6.6 µm) **h1** = 62.503 µm **h2** = 168.126 µm **w1** = 273.751 µm **w2** = 326.885 µm	

Figure 186 - Single Ti6Al4V Bead at 250 W laser power, 417 J/mm³ energy density in comparison to MMC material

Ti6Al4V Vertical (10 x magnification)	Ti6Al4V Transverse section (20 x magnification)	MMC Vertical (10 x magnification)	MMC Transverse section (20 x magnification)
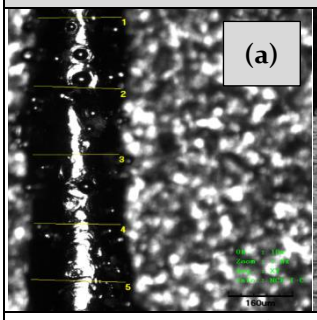	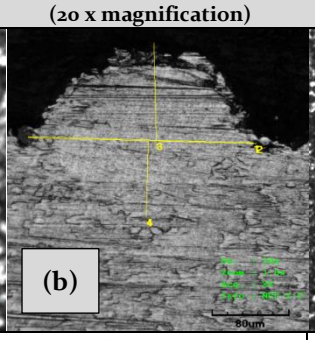	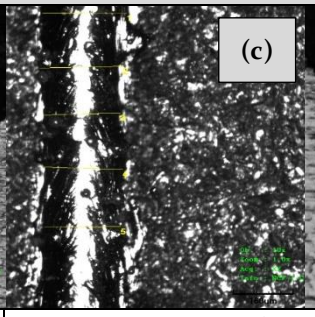	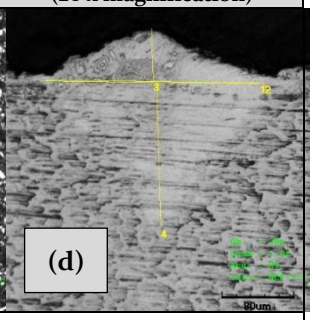
E = 375 J/mm³ **V** = 222 mm/s **Mean bead width, vertical** = 223.314 µm (σ 10.7 µm) **h1** = 115.652 µm **h2** = 90.020 µm **w1** = 240.742 µm **w2** = 243.847 µm		**E** = 375 J/mm³ **V** = 222 mm/s **Mean bead width, vertical** = 217.052 µm (σ 11.5 µm) **h1** = 60.029 µm **h2** = 166.325 µm **w1** = 243.779 µm **w2** = 255.019 µm	

Figure 187 - Single Ti6Al4V Bead at 250 W laser power, 375 J/mm³ energy density in comparison to MMC material

Ti6Al4V Vertical (10 x magnification)	Ti6Al4V Transverse section (20 x magnification)	MMC Vertical (10 x magnification)	MMC Transverse section (20 x magnification)
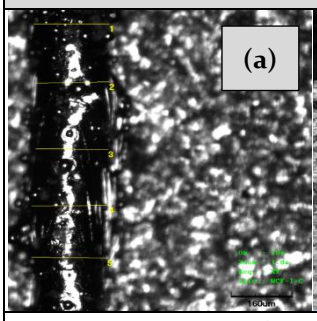	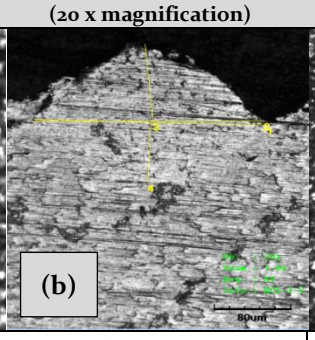	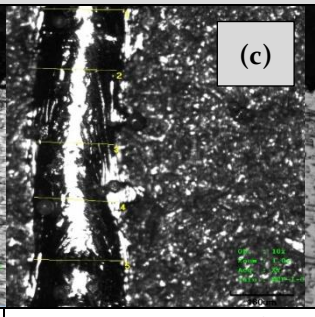	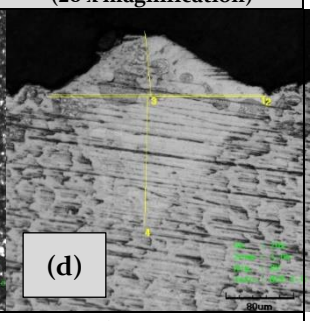
E = 333 J/mm³ **V** = 250 mm/s **Mean bead width, vertical** = 201.514 µm (σ 5.4 µm) **h1** = 95.402 µm **h2** = 74.441 µm **w1** = 249.488 µm **w2** = 246.251 µm		**E** = 333 J/mm³ **V** = 250 mm/s **Mean bead width, vertical** = 217.671 µm (σ 13.5 µm) **h1** = 78.484 µm **h2** = 158.156 µm **w1** = 253.125 µm **w2** = 264.376 µm	

Figure 188 - Single Ti6Al4V Bead at 250 W laser power, 333 J/mm³ energy density in comparison to MMC material

Ti6Al4V Vertical (10 x magnification)	Ti6Al4V Transverse section (20 x magnification)	MMC Vertical (10 x magnification)	MMC Transverse section (20 x magnification)

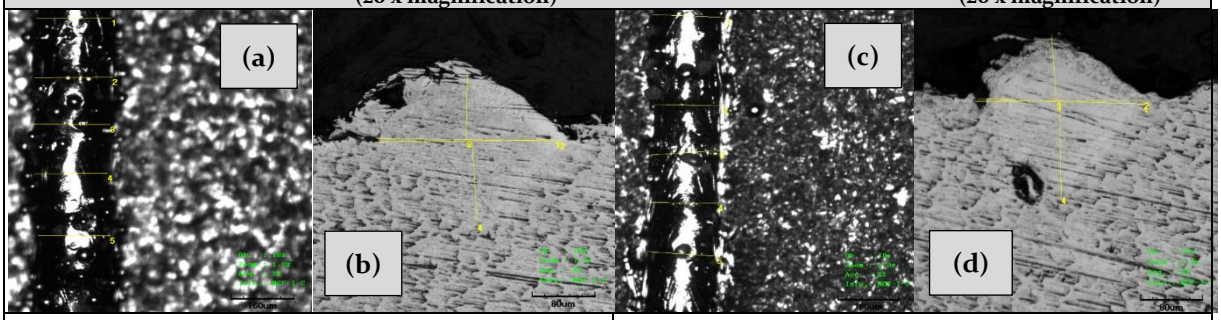

E = 291 J/mm³ **V** = 286 mm/s **Mean bead width, vertical** = 195.505 µm (σ 6.2 µm) **h1** = 90.634 µm **h2** = 113.334 µm **w1** = 235.646 µm **w2** = 238.779 µm	**E** = 291 J/mm³ **V** = 286 mm/s **Mean bead width, vertical** = 187.973 µm (σ 6.3 µm) **h1** = 87.723 µm **h2** = 123.764 µm **w1** = 219.483 µm **w2** = 223.753 µm

Figure 189 - Single Ti6Al4V Bead at 250 W laser power, 291 J/mm³ energy density in comparison to MMC material

Ti6Al4V Vertical (10 x magnification)	Ti6Al4V Transverse section (20 x magnification)	MMC Vertical (10 x magnification)	MMC Transverse section (20 x magnification)

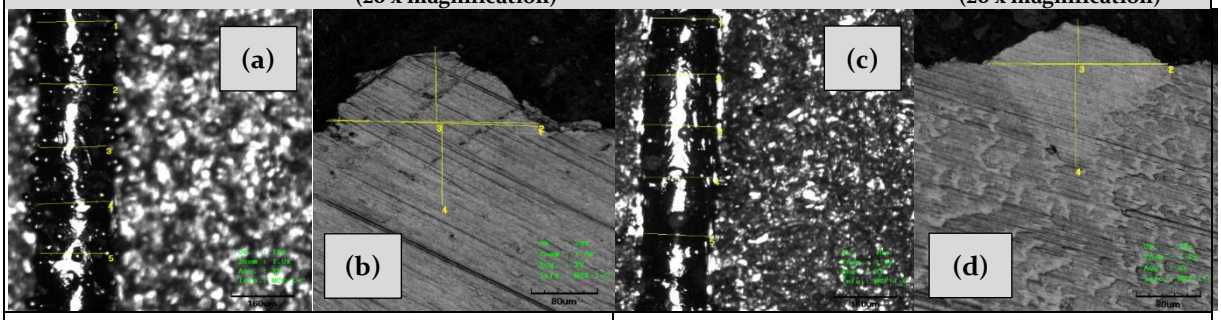

E = 250 J/mm³ **V** = 333 mm/s **Mean bead width, vertical** = 185.067 µm (σ 11.2 µm) **h1** = 98.133 µm **h2** = 105.000 µm **w1** = 259.502 µm **w2** = 263.769 µm	**E** = 250 J/mm³ **V** = 333 mm/s **Mean bead width, vertical** = 182.331 µm (σ 9.5 µm) **h1** = 56.606 µm **h2** = 131.251 µm **w1** = 231.253 µm **w2** = 232.503 µm

Figure 190 - Single Ti6Al4V Bead at 250 W laser power, 250 J/mm³ energy density in comparison to MMC material

Ti6Al4V Vertical (10 x magnification)	Ti6Al4V Transverse section (20 x magnification)	MMC Vertical (10 x magnification)	MMC Transverse section (20 x magnification)

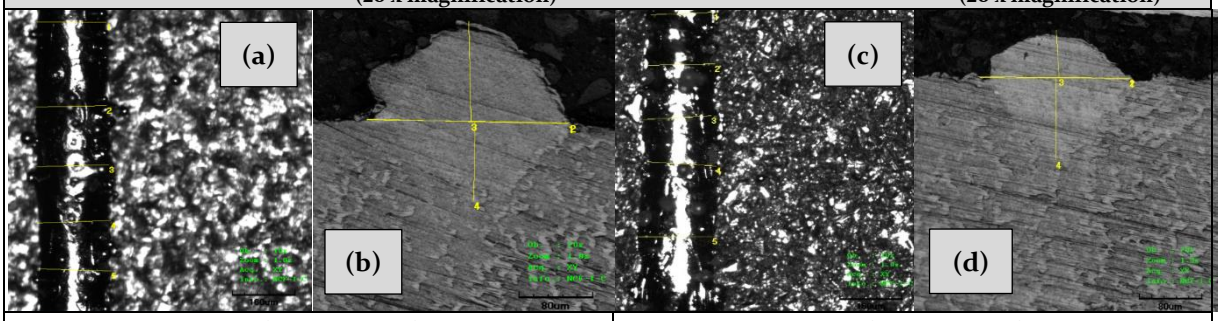

E = 208 J/mm³ **V** = 400 mm/s **Mean bead width, vertical** = 186.822 µm (σ 5.5 µm) **h1** = 121.901 µm **h2** = 95.633 µm **w1** = 223.821 µm **w2** = 226.281 µm	**E** = 208 J/mm³ **V** = 400 mm/s **Mean bead width, vertical** = 179.433 µm (σ 10.0 µm) **h1** = 61.330 µm **h2** = 106.875 µm **w1** = 196.259 µm **w2** = 198.129 µm

Figure 191 - Single Ti6Al4V Bead at 250 W laser power, 208 J/mm³ energy density in comparison to MMC material

Ti6Al4V Vertical (10 x magnification)	Ti6Al4V Transverse section (20 x magnification)	MMC Vertical (10 x magnification)	MMC Transverse section (20 x magnification)

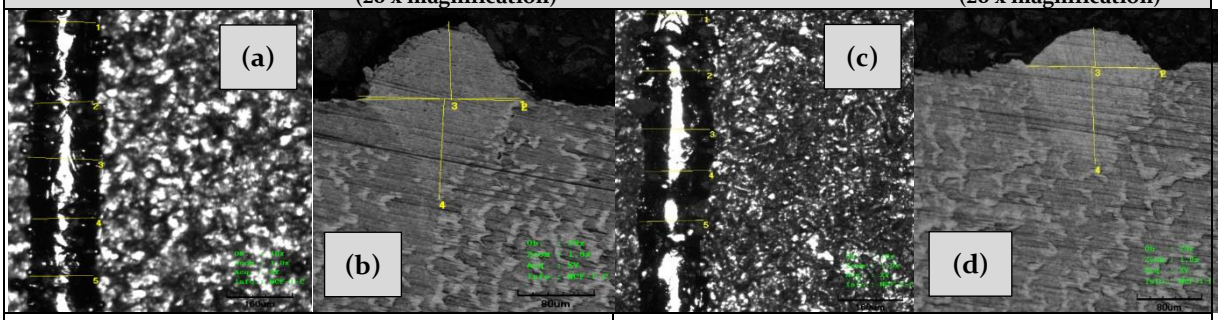

E = 167 J/mm³ **V** = 500 mm/s **Mean bead width, vertical** = 161.322 µm (σ 10.9 µm) **h1** = 95.658 µm **h2** = 122.005 µm **w1** = 173.130 µm **w2** = 174.466 µm	**E** = 167 J/mm³ **V** = 500 mm/s **Mean bead width, vertical** = 161.322 µm (σ 9.0 µm) **h1** = 50.035 µm **h2** = 122.578 µm **w1** = 168.779 µm **w2** = 169.385 µm

Figure 192 - Single Ti6Al4V Bead at 250 W laser power, 167 J/mm³ energy density in comparison to MMC material

Ti6Al4V Vertical (10 x magnification)	Ti6Al4V Transverse section (20 x magnification)	MMC Vertical (10 x magnification)	MMC Transverse section (20 x magnification)

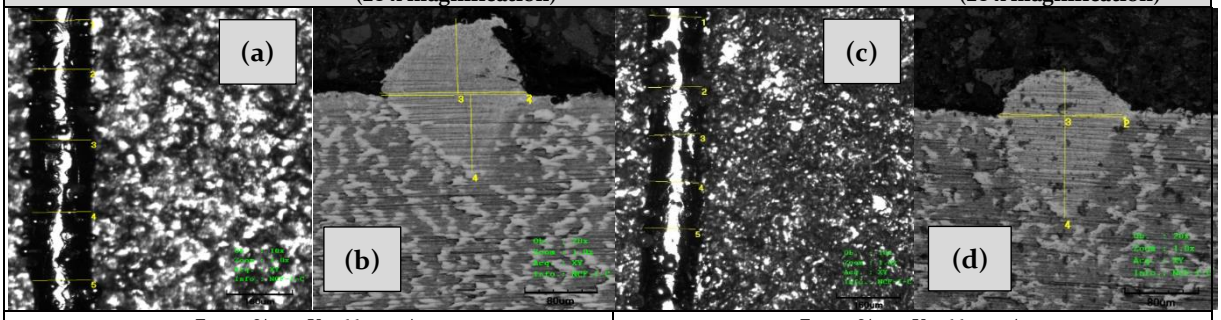

E = 125 J/mm³ **V** = 667 mm/s **Mean bead width, vertical** = 145.765 µm (σ 3.4 µm) **h1** = 92.534 µm **h2** = 95.643 µm **w1** = 165.001 µm **w2** = 166.255 µm	**E** = 125 J/mm³ **V** = 667 mm/s **Mean bead width, vertical** = 131.603 µm (σ 4.0 µm) **h1** = 52.504 µm **h2** = 115.002 µm **w1** = 137.523 µm **w2** = 137.551 µm

Figure 193 - Single Ti6Al4V Bead at 250 W laser power, 125 J/mm³ energy density in comparison to MMC material

Ti6Al4V Vertical (10 x magnification)	Ti6Al4V Transverse section (20 x magnification)	MMC Vertical (10 x magnification)	MMC Transverse section (20 x magnification)

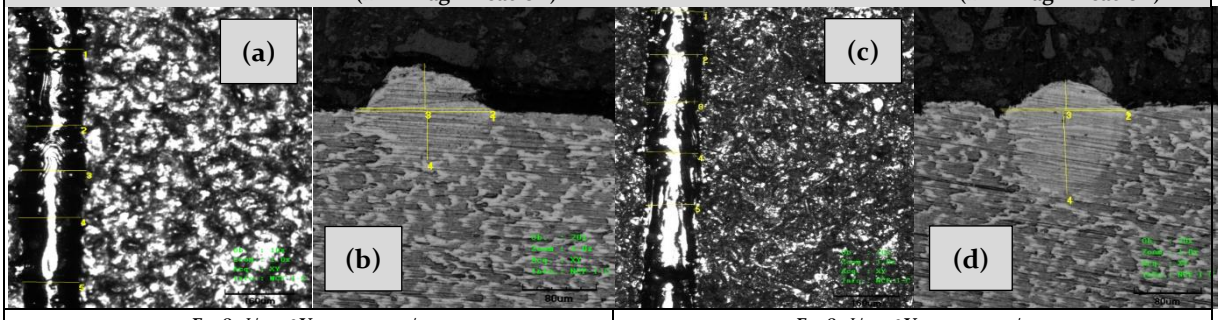

E = 83 J/mm³ **V** = 1,000 mm/s **Mean bead width, vertical** = 138.262 µm (σ 11.0 µm) **h1** = 55.629 µm **h2** = 60.625 µm **w1** = 150.001 µm **w2** = 145.001 µm	**E** = 83 J/mm³ **V** = 1,000 mm/s **Mean bead width, vertical** = 129.547 µm (σ 3.4 µm) **h1** = 35.630 µm **h2** = 102.593 µm **w1** = 151.251 µm **w2** = 151.251 µm

Figure 194 - Single Ti6Al4V Bead at 250 W laser power, 83 J/mm³ energy density in comparison to MMC material

Ti6Al4V Vertical (10 x magnification)	Ti6Al4V Transverse section (20 x magnification)	MMC Vertical (10 x magnification)	MMC Transverse section (20 x magnification)
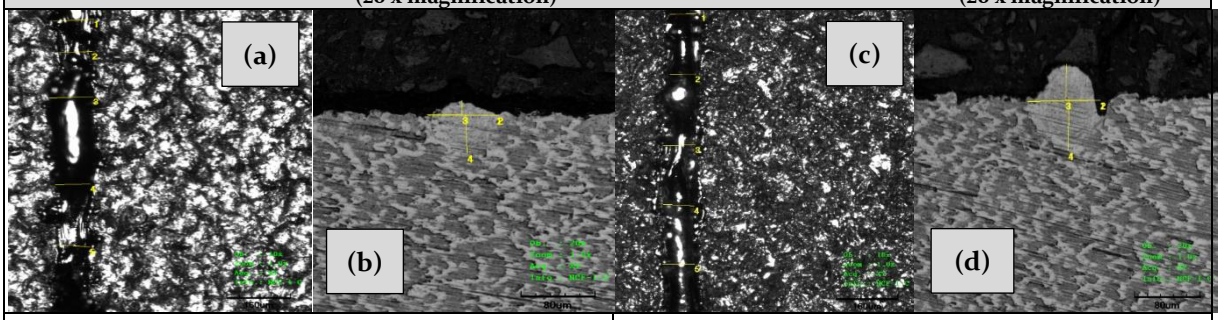			
E = 42 J/mm³ **V** = 2,000 mm/s **Mean bead width, vertical** = 95.605 µm (σ 12.0 µm) **h1** = 16.875 µm **h2** = 45.039 µm **w1** = 75.003 µm **w2** = 77.503 µm		**E** = 42 J/mm³ **V** = 2,000 mm/s **Mean bead width, vertical** = 82.548 µm (σ 10.1 µm) **h1** = 45.017 µm **h2** = 62.503 µm **w1** = 87.502 µm **w2** = 90.644 µm	

Figure 195 - Single Ti6Al4V Bead at 250 W laser power, 42 J/mm³ energy density in comparison to MMC material

Appendix 8, Phase 3a; MMC Single Bead Evaluation Images Against Energy Density Compared to Baseline Results At 350 W

Ti6Al4V Vertical (10 x magnification)	Ti6Al4V Transverse section (20 x magnification)	MMC Vertical (10 x magnification)	MMC Transverse section (20 x magnification)
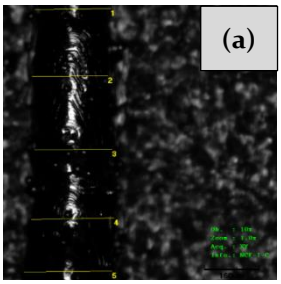	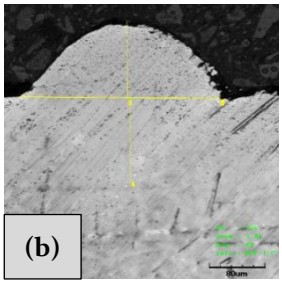	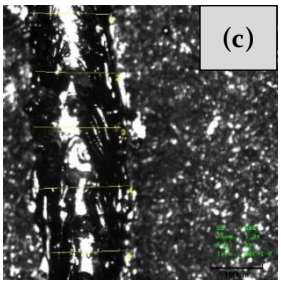	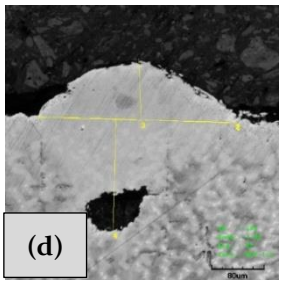
E = 583 J/mm3 V = 200 mm/s **Mean bead width, vertical** = 240.017 µm (σ 16.6 µm) h1 = 125.631 µm h2 = 133.126 µm w1 = 296.886 µm w2 = 293.756 µm		E = 583 J/mm3 V = 200 mm/s **Mean bead width, vertical** = 265.808 µm (σ 16.2 µm) h1 = 96.925 µm h2 = 175.005 µm w1 = 310.807 µm w2 = 309.466 µm	

Figure 196 - Single Ti6Al4V Bead at 350 W laser power, 583 J/mm³ energy density in comparison to MMC material

Ti6Al4V Vertical (10 x magnification)	Ti6Al4V Transverse section (20 x magnification)	MMC Vertical (10 x magnification)	MMC Transverse section (20 x magnification)
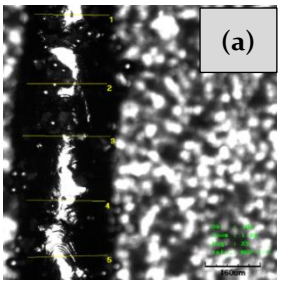	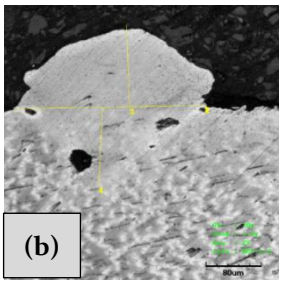	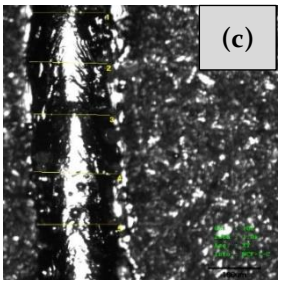	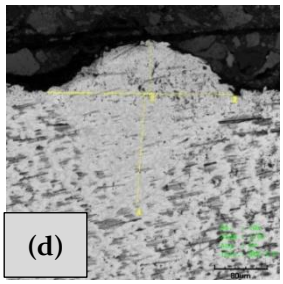
E = 526 J/mm3 V = 222 mm/s **Mean bead width, vertical** = 238.778 µm (σ 14.1 µm) h1 = 126.950 µm h2 = 122.005 µm w1 = 281.919 µm w2 = 282.544 µm		E = 526 J/mm3 V = 222 mm/s **Mean bead width, vertical** = 244.538 µm (σ 12.1 µm) h1 = 84.375 µm h2 = 176.069 µm w1 = 290.649 µm w2 = 286.267 µm	

Figure 197 - Single Ti6Al4V Bead at 350 W laser power, 526 J/mm³ energy density in comparison to MMC material

Ti6Al4V Vertical (10 x magnification)	Ti6Al4V Transverse section (20 x magnification)	MMC Vertical (10 x magnification)	MMC Transverse section (20 x magnification)
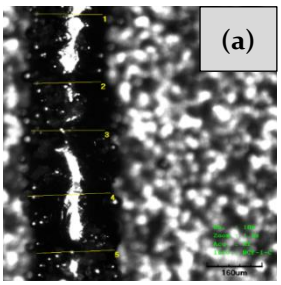	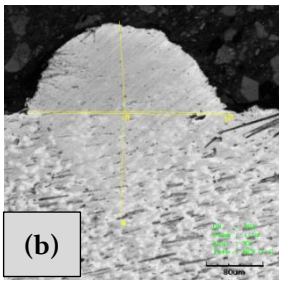	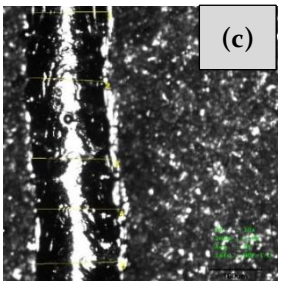	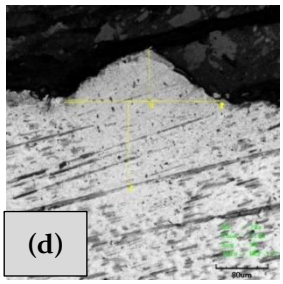
E = 467 J/mm3 V = 250 mm/s **Mean bead width, vertical** = 220.097 µm (σ 19.7 µm) h1 = 148.972 µm h2 = 171.893 µm w1 = 283.761 µm w2 = 290.003 µm		E = 467 J/mm3 V = 250 mm/s **Mean bead width, vertical** = 246.832 µm (σ 14.1 µm) h1 = 82.509 µm h2 = 126.877 µm w1 = 241.257 µm w2 = 242.513 µm	

Figure 198 - Single Ti6Al4V Bead at 350 W laser power, 467 J/mm³ energy density in comparison to MMC material

Ti6Al4V Vertical (10 x magnification)	Ti6Al4V Transverse section (20 x magnification)	MMC Vertical (10 x magnification)	MMC Transverse section (20 x magnification)
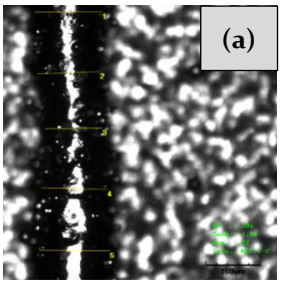	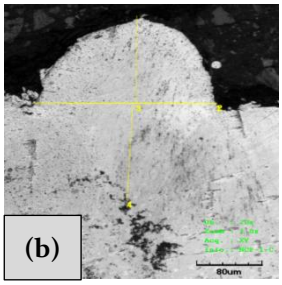	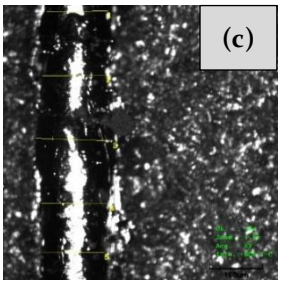	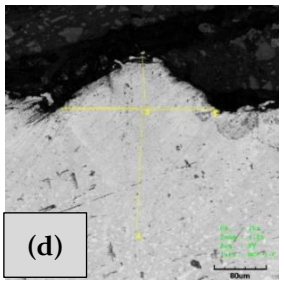
E = 408 J/mm3 V = 286 mm/s **Mean bead width, vertical** = 196.545 µm (σ 15.6 µm) h1 = 131.256 µm h2 = 142.697 µm w1 = 228.758 µm w2 = 228.126 µm		E = 408 J/mm3 V = 286 mm/s **Mean bead width, vertical** = 206.038 µm (σ 20.2 µm) h1 = 85.147 µm h2 = 191.480 µm w1 = 240.000 µm w2 = 240.001 µm	

Figure 199 - Single Ti6Al4V Bead at 350 W laser power, 408 J/mm³ energy density in comparison to MMC material

Ti6Al4V Vertical (10 x magnification)	Ti6Al4V Transverse section (20 x magnification)	MMC Vertical (10 x magnification)	MMC Transverse section (20 x magnification)
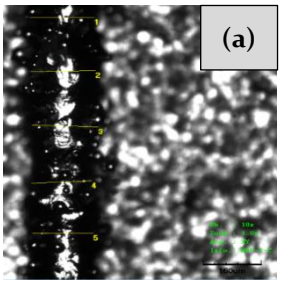	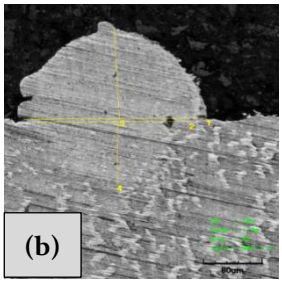	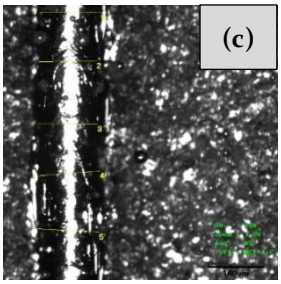	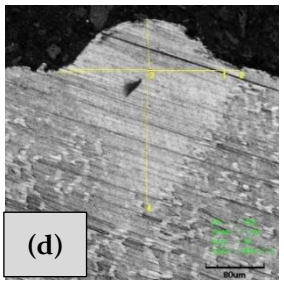
E = 350 J/mm3 V = 333 mm/s **Mean bead width, vertical** = 178.808 µm (σ 7.6 µm) h1 = 134.584 µm h2 = 91.252 µm w1 = 253.757 µm w2 = 215.626 µm		E = 350 J/mm3 V = 333 mm/s **Mean bead width, vertical** = 181.692 µm (σ 11.4 µm) h1 = 74.469 µm h2 = 183.751 µm w1 = 213.126 µm w2 = 256.257 µm	

Figure 200 - Single Ti6Al4V Bead at 350 W laser power, 350 J/mm³ energy density in comparison to MMC material

Ti6Al4V Vertical (10 x magnification)	Ti6Al4V Transverse section (20 x magnification)	MMC Vertical (10 x magnification)	MMC Transverse section (20 x magnification)
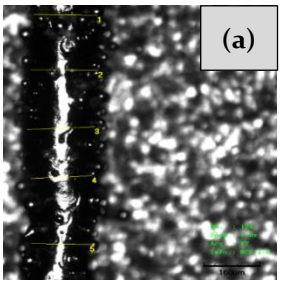	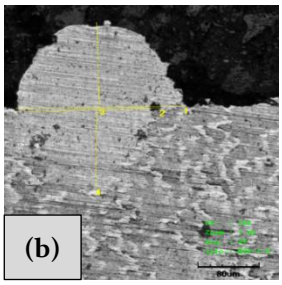	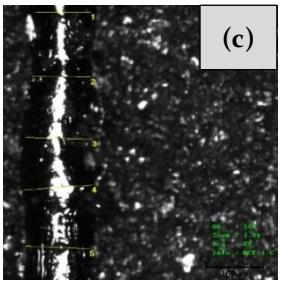	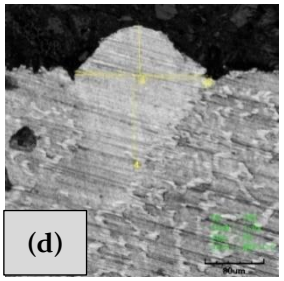
E = 292 J/mm3 V = 400 mm/s **Mean bead width, vertical** = 184.840 µm (σ 11.1 µm) h1 = 123.807 µm h2 = 113.757 µm w1 = 177.570 µm w2 = 224.406 µm		E = 292 J/mm3 V = 400 mm/s **Mean bead width, vertical** = 177.424 µm (σ 16.3 µm) h1 = 70.636 µm h2 = 116.875 µm w1 = 179.768 µm w2 = 185.010 µm	

Figure 201 - Single Ti6Al4V Bead at 350 W laser power, 292 J/mm³ energy density in comparison to MMC material

Ti6Al4V Vertical (10 x magnification)	Ti6Al4V Transverse section (20 x magnification)	MMC Vertical (10 x magnification)	MMC Transverse section (20 x magnification)
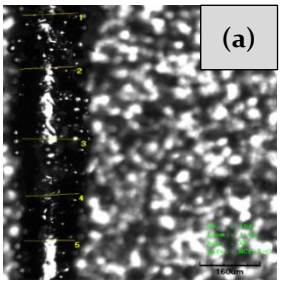	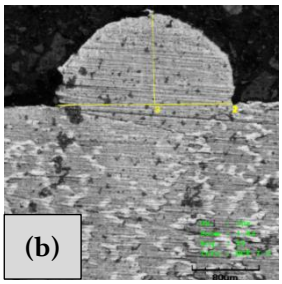	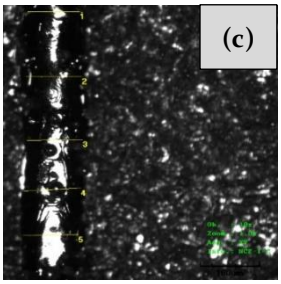	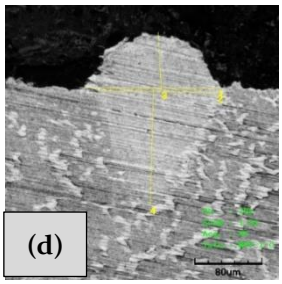
E = 233 J/mm3 V = 500 mm/s **Mean bead width, vertical** = 149.892 µm (σ 9.0 µm) h1 = 124.400 µm h2 = - µm w1 = 216.273 µm w2 = 213.129 µm		E = 233 J/mm3 V = 500 mm/s **Mean bead width, vertical** = 152.307 µm (σ 5.8 µm) h1 = 70.137 µm h2 = 138.801 µm w1 = 161.876 µm w2 = 146.271 µm	

Figure 202 - Single Ti6Al4V Bead at 350 W laser power, 233 J/mm³ energy density in comparison to MMC material

Ti6Al4V Vertical (10 x magnification)	Ti6Al4V Transverse section (20 x magnification)	MMC Vertical (10 x magnification)	MMC Transverse section (20 x magnification)
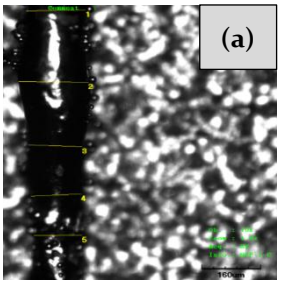	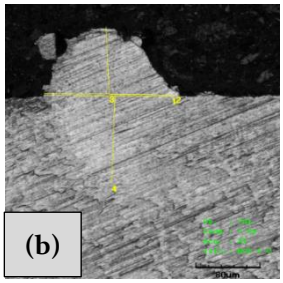	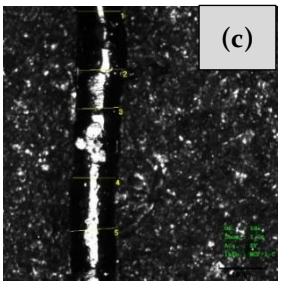	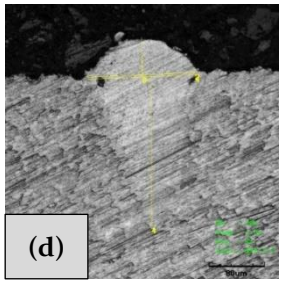
E = 175 J/mm3 V = 667 mm/s **Mean bead width, vertical** = 156.570 µm (σ 23.9 µm) h1 = 93.825 µm h2 = 123.827 µm w1 = 162.505 µm w2 = 168.135 µm		E = 175 J/mm3 V = 667 mm/s **Mean bead width, vertical** = 148.590 µm (σ 3.3 µm) h1 = 56.253 µm h2 = 221.876 µm w1 = 159.523 µm w2 = 159.551 µm	

Figure 203 - Single Ti6Al4V Bead at 350 W laser power, 175 J/mm³ energy density in comparison to MMC material

Ti6Al4V Vertical (10 x magnification)	Ti6Al4V Transverse section (20 x magnification)	MMC Vertical (10 x magnification)	MMC Transverse section (20 x magnification)
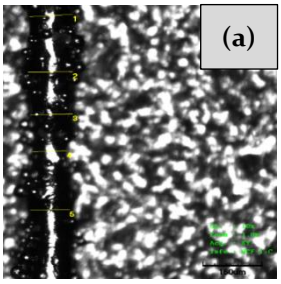	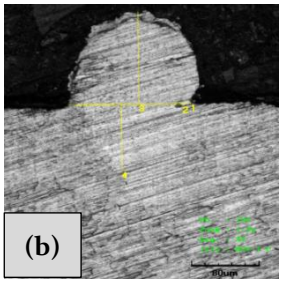	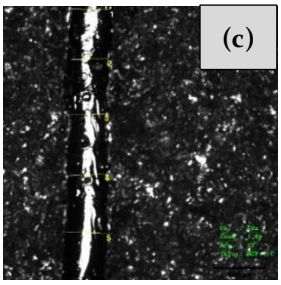	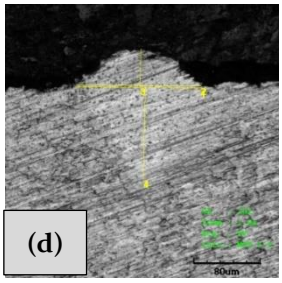
E = 117 J/mm3 V = 1,000 mm/s **Mean bead width, vertical** = 113.076 µm (σ 11.5 µm) h1 = 127.506 µm h2 = 90.627 µm w1 = 148.146 µm w2 = 128.756 µm		E = 117 J/mm3 V = 1,000 mm/s **Mean bead width, vertical** = 118.803 µm (σ 6.9 µm) h1 = 45.642 µm h2 = 113.141 µm w1 = 153.755 µm w2 = 152.501 µm	

Figure 204 - Single Ti6Al4V Bead at 350 W laser power, 117 J/mm³ energy density in comparison to MMC material

Ti6Al4V Vertical (10 x magnification)	Ti6Al4V Transverse section (20 x magnification)	MMC Vertical (10 x magnification)	MMC Transverse section (20 x magnification)
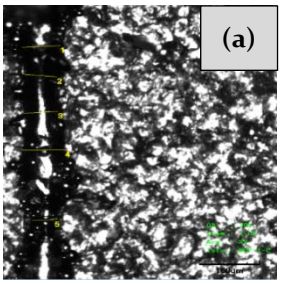	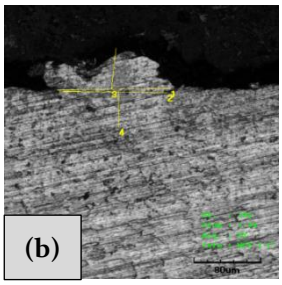	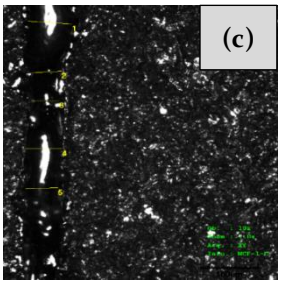	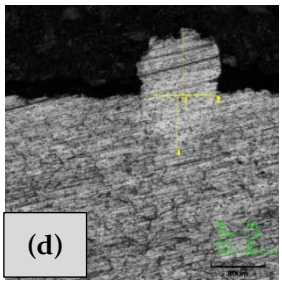
E = 58 J/mm3 V = 2,000 mm/s **Mean bead width, vertical** = 93.909 µm (σ 21.4 µm) h1 = 55.287 µm h2 = 48.754 µm w1 = 138.763 µm w2 = 128.139 µm		E = 58 J/mm3 V = 2,000 mm/s **Mean bead width, vertical** = 96.847 µm (σ 20.1 µm) h1 = 102.502 µm h2 = 77.540 µm w1 = 114.377 µm w2 = 113.765 µm	

Figure 205 - Single Ti6Al4V Bead at 350 W laser power, 58 J/mm³ energy density in comparison to MMC material

Appendix 9 Hatch spacing Results

40 % ($w1$)	60 % ($w1$)	80 % ($w1$)
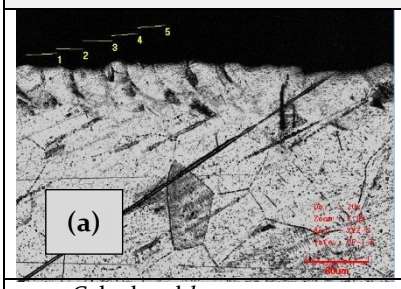	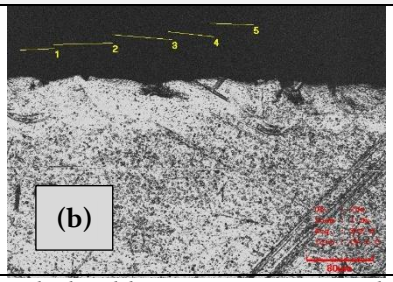	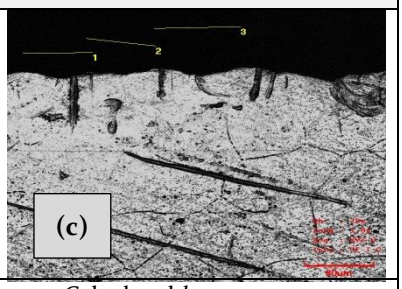
Calculated h = 0.040 mm, Measured h = 0.037 mm σ = 2.8 µm	Calculated h = 0.059 mm, Measured h = 0.060 mm σ = 13.3 µm	Calculated h = 0.079 mm, Measured h = 0.088 mm σ = 11.5 µm
100 % ($w1$)	120 % ($w1$)	140 % ($w1$)
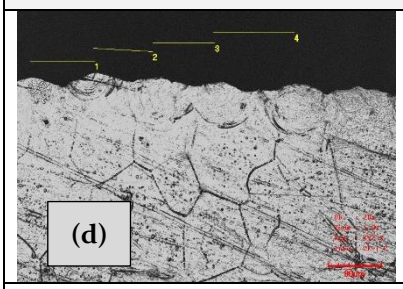	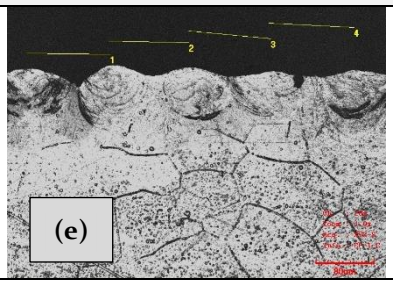	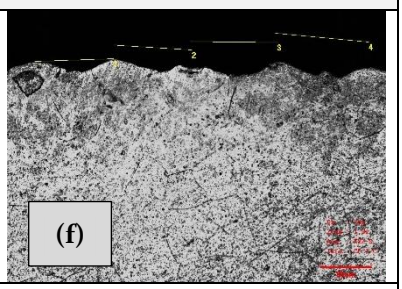
Calculated h = 0.099 mm, Measured h = 0.101 mm σ = 14.9 µm	Calculated h = 0.119 mm, Measured h = 0.116 mm σ = 3.2 µm	Calculated h = 0.139 mm, Measured h = 0.137 mm σ = 11.6 µm

Figure 206 - Transverse sectional Views of Hatch Spacing, 150 (W), 1,000 mm/s (v) 0.030 mm (t).

40 % ($w1$)	60 % ($w1$)	80 % ($w1$)
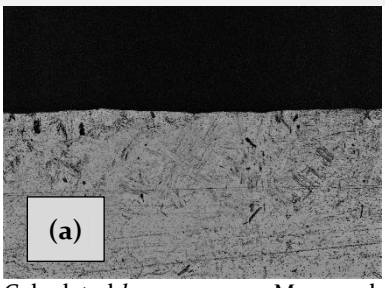	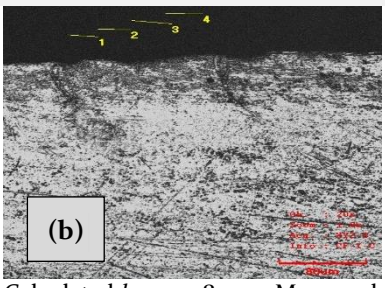	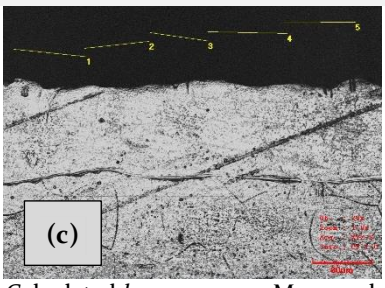
Calculated h = 0.052 mm, Measured h = - σ = -	Calculated h = 0.078 mm, Measured h = 0.033 mm σ = 3.8 µm	Calculated h = 0.104 mm, Measured h = 0.096 mm σ =11.0 µm
100 % ($w1$)	120 % ($w1$)	140 % ($w1$)
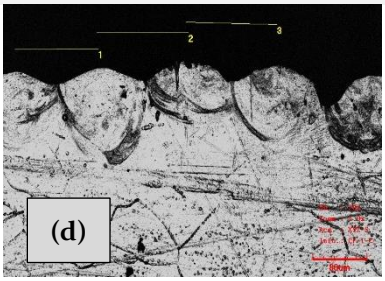	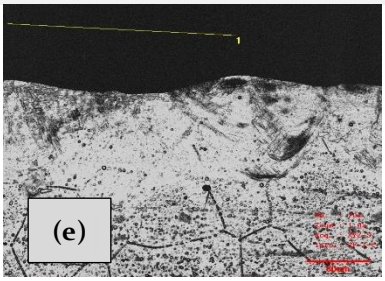	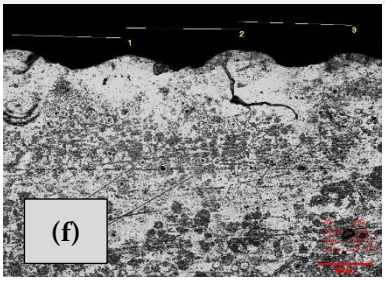
Calculated h = 0.130 mm, Measured h = 0.134 mm σ = 6.9 µm	Calculated h = 0.156 mm, Measured h = 0.303 mm σ = 0.0 µm	Calculated h = 0.182 mm, Measured h = 0.174 mm σ = 2.6 µm

Figure 207 - Transverse sectional Views of Hatch Spacing, 250 (W), 1,000 mm/s (v) 0.030 mm (t).

40 % ($w1$) | 60 % ($w1$) | 80 % ($w1$)

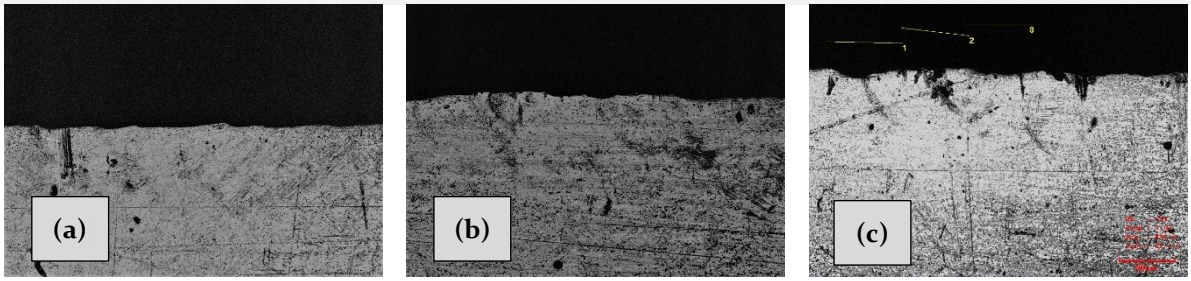

Calculated h = 0.053 mm, Measured h = - σ = -

Calculated h = 0.079 mm, Measured h = - σ = -

Calculated h = 0.106 mm, Measured h = 0.102 mm σ = 9.6 µm

100 % ($w1$) | 120 % ($w1$) | 140 % ($w1$)

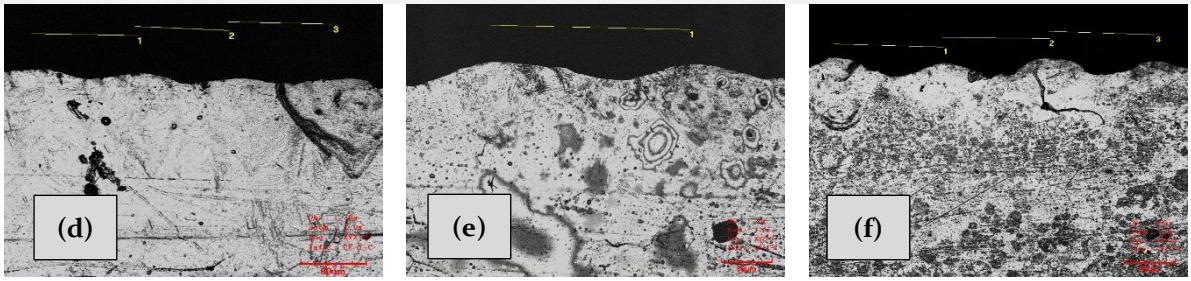

Calculated h = 0.132 mm, Measured h = 0.128 mm σ = 8.1 µm

Calculated h = 0.158 mm, Measured h = 0.319 mm σ = 0.0 µm

Calculated h = 0.185 mm, Measured h = 0.174 mm σ = 2.6 µm

Figure 208 - Transverse sectional Views of Hatch Spacing, 250 (W), 667 mm/s (v) 0.030 mm (t).

40 % ($w1$) | 60 % ($w1$) | 80 % ($w1$)

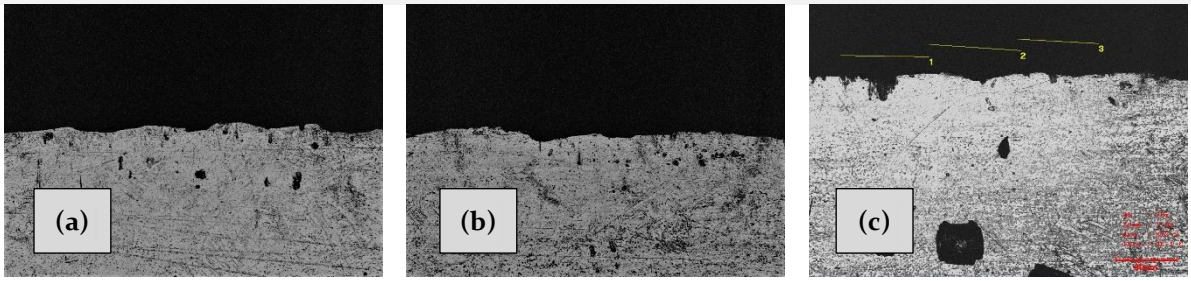

Calculated h = 0.065 mm, Measured h = - σ = -

Calculated h = 0.097 mm, Measured h = - σ = -

Calculated h = 0.130 mm, Measured h = 0.116 mm σ = 7.0 µm

100 % ($w1$) | 120 % ($w1$) | 140 % ($w1$)

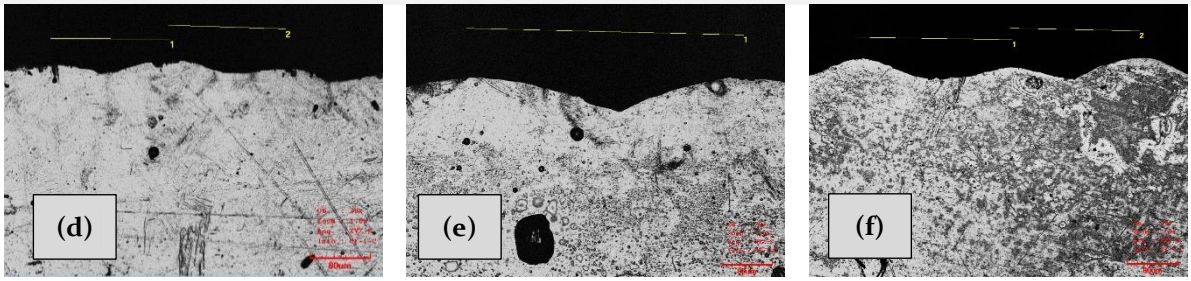

Calculated h = 0.162 mm, Measured h = 0.162 mm σ = 1.8 µm

Calculated h = 0.194 mm, Measured h = 0.452 mm σ = 0.0 µm

Calculated h = 0.227 mm, Measured h = 0.229 mm σ = 29.6 µm

Figure 209 - Transverse sectional Views of Hatch Spacing, 250 (W), 500 mm/s (v) 0.030 mm (t).

40 % (*w*1) | 60 % (*w*1) | 80 % (*w*1)

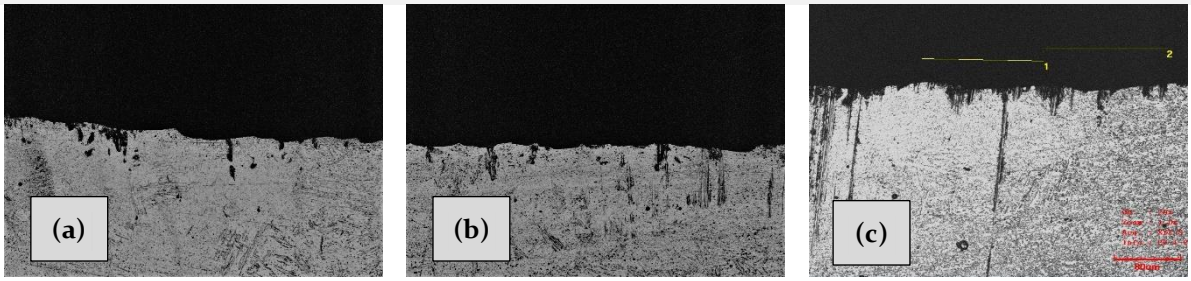

Calculated *h* = 0.073 mm, Measured *h* = - σ = -

Calculated *h* = 0.109 mm, Measured *h* = - σ = -

Calculated *h* = 0.146 mm, Measured *h* = 0.150 mm σ = 1.3 µm

100 % (*w*1) | 120 % (*w*1) | 140 % (*w*1)

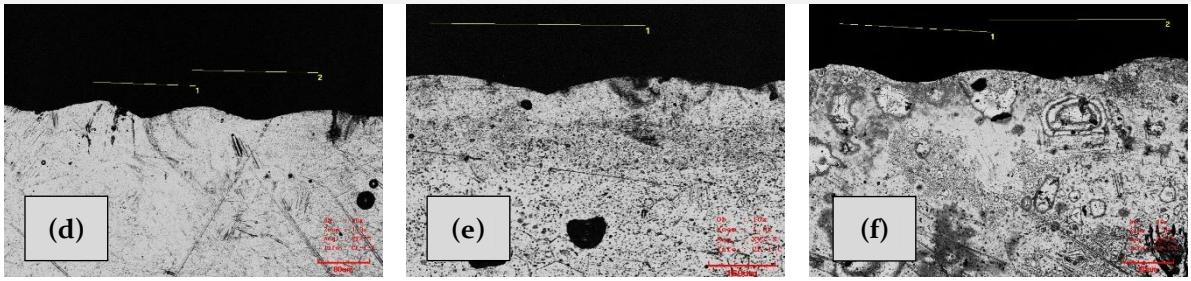

Calculated *h* = 0.182 mm, Measured *h* = 0.180 mm σ = 26.0 µm

Calculated *h* = 0.218 mm, Measured *h* = 0.530 mm σ = 0.0 µm

Calculated *h* = 0.255 mm, Measured *h* = 0.270 mm σ = 29.2 µm

Figure 210 - Transverse sectional Views of Hatch Spacing, 250 (W), 333 mm/s (v) 0.030 mm (t).

40 % (*w*1) | 60 % (*w*1) | 80 % (*w*1)

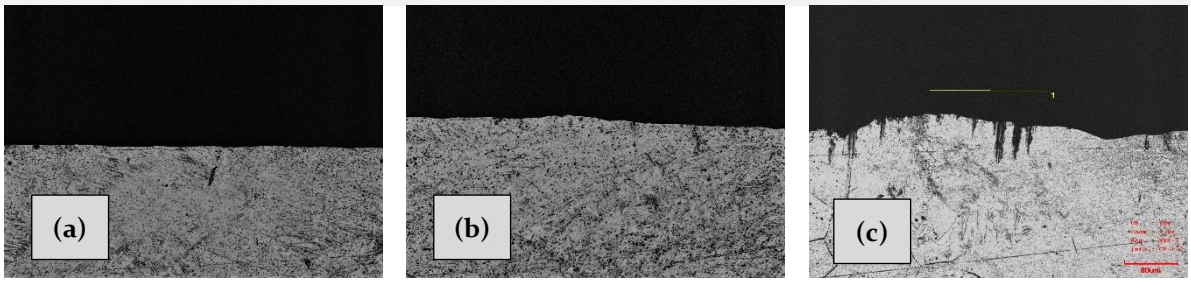

Calculated *h* = 0.048 mm, Measured *h* = - σ = -

Calculated *h* = 0.071 mm, Measured *h* = - σ = -

Calculated *h* = 0.095 mm, Measured *h* = 0.188 mm σ = 0.0 µm

100 % (*w*1) | 120 % (*w*1) | 140 % (*w*1)

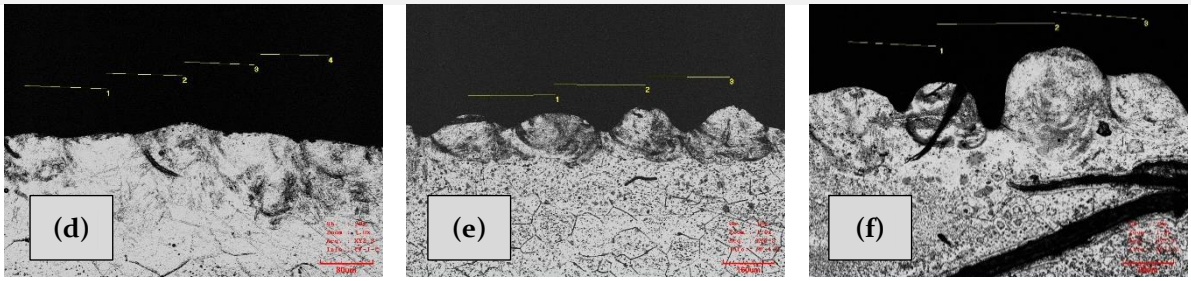

Calculated *h* = 0.119 mm, Measured *h* = 0.118 mm σ = 7.8 µm

Calculated *h* = 0.143 mm, Measured *h* = 0.285 mm σ = 9.9 µm

Calculated *h* = 0.167 mm, Measured *h* = 0.163 mm σ = 25.4 µm

Figure 211 - Transverse sectional Views of Hatch Spacing, 350 (W), 1,000 mm/s (v) 0.030 mm (t).

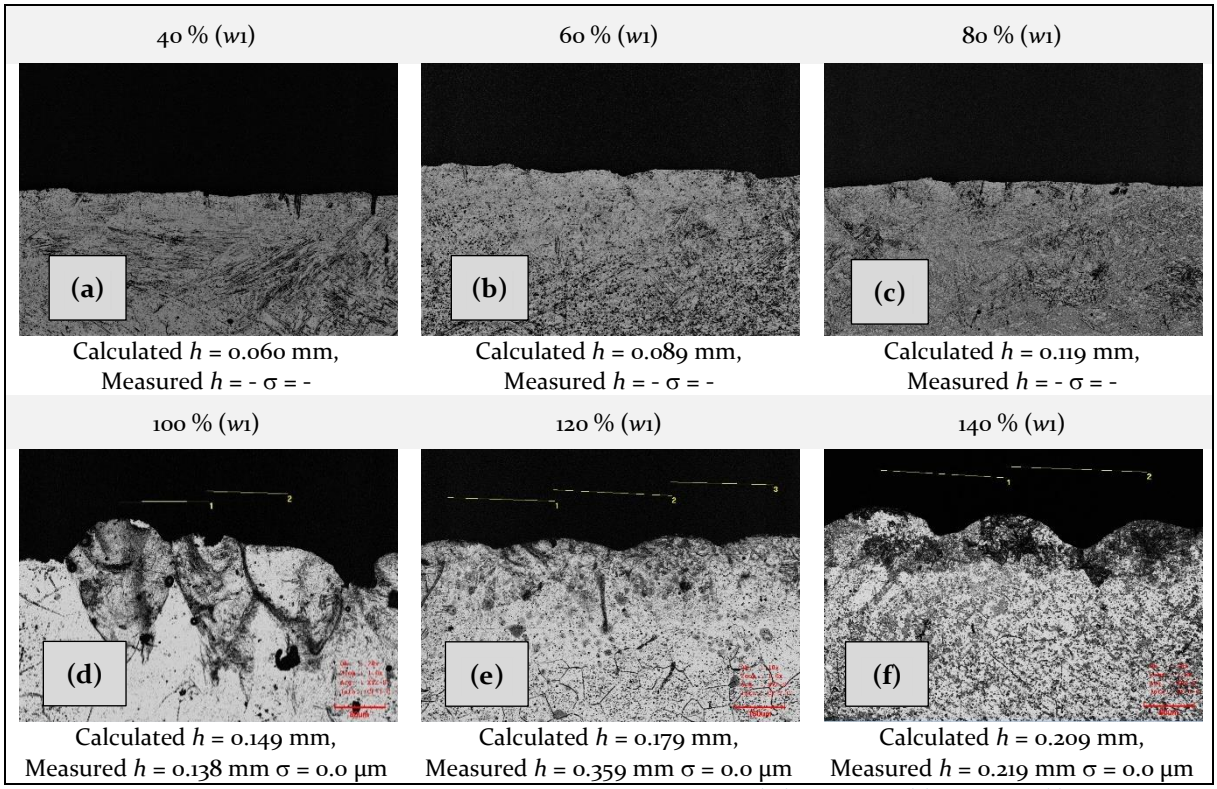

Figure 212 - Transverse sectional Views of Hatch Spacing, 350 (W), 667 mm/s (v) 0.030 mm (t).

Appendix 10, XRD Analysis Results

Anchor Scan Parameters

Dataset Name: TiSiC

File name: C:\XRD Data\TiSiC_TiSiC.xrdml

Sample Identification: TiSiC

Comment: Configuration=Reflaction-transmission spinner, Owner=User-1, Creation date=6/28/2012 10:39:29 AM

Goniometer=Theta/Theta; Minimum step size 2Theta:0.0001; Minimum step size Omega:0.0001

Sample stage=Reflection-transmission spinner; Minimum step size Phi:0.1

Diffractometer system=EMPYREAN

Measurement program=C:\PANalytical\Data Collector\Programs\powder 15mm PDS.xrdmp, Identifier={69CD223E-1BDD-4632-83DC-936429B8747A}

Batch program=C:\PANalytical\Data Collector\Programs\Changer 1 sample.xrdmp, Identifier={80E5EB34-F8D8-417D-BE8A-B1D9D16B193E}

Measurement Date / Time: 1/29/2020 2:43:27 PM

Operator: Univ Wolverhampton

Raw Data Origin: XRD measurement (*.XRDML)

Scan Axis: Gonio

Start Position [°2Th.]: 5.0064

End Position [°2Th.]: 79.9904

Step Size [°2Th.]: 0.0130

Scan Step Time [s]: 8.6700

Scan Type: Continuous

PSD Mode: Scanning

PSD Length [°2Th.]: 3.35

Offset [°2Th.]: 0.0000

Divergence Slit Type: Automatic

Irradiated Length [mm]: 15.00

Specimen Length [mm]: 10.00

Measurement Temperature [°C]: 25.00

Anode Material: Cu

K-Alpha1 [Å]: 1.54060

K-Alpha2 [Å]:1.54443

K-Beta [Å]: 1.39225

K-A2 / K-A1 Ratio: 0.50000

Generator Settings: 40 mA, 40 kV

Diffractometer Type: 00000000001126545

Diffractometer Number: 0

Goniometer Radius [mm]: 240.00

Dist. Focus-Diverg. Slit [mm]: 100.00

Incident Beam Monochromator: No

Spinning: Yes

Graphics

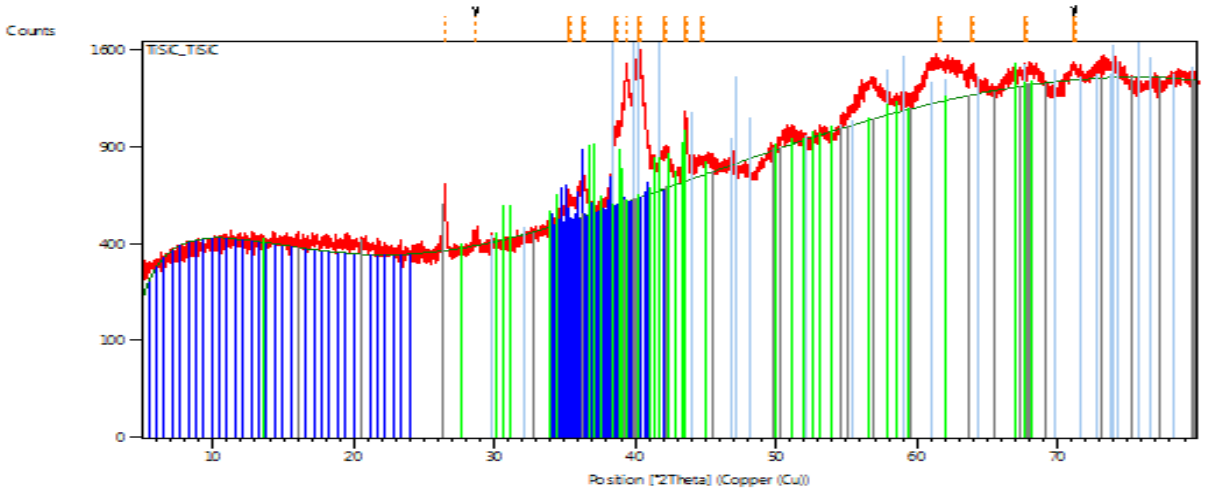

Pattern List

Visible	Ref.Code	Score	Compound Name	Displ.[°2Th]	Scale Fac.	Chem. Formula
*	98-002-8341	45	Silicon Carbide	0.447	0.222	C1 Si1
*	00-023-1079	32	Titanium Silicide	-0.313	0.234	Ti5 Si4
*	98-003-9830	37	Silicon Oxide - Al..	-0.283	0.127	O2 Si1

Graphics

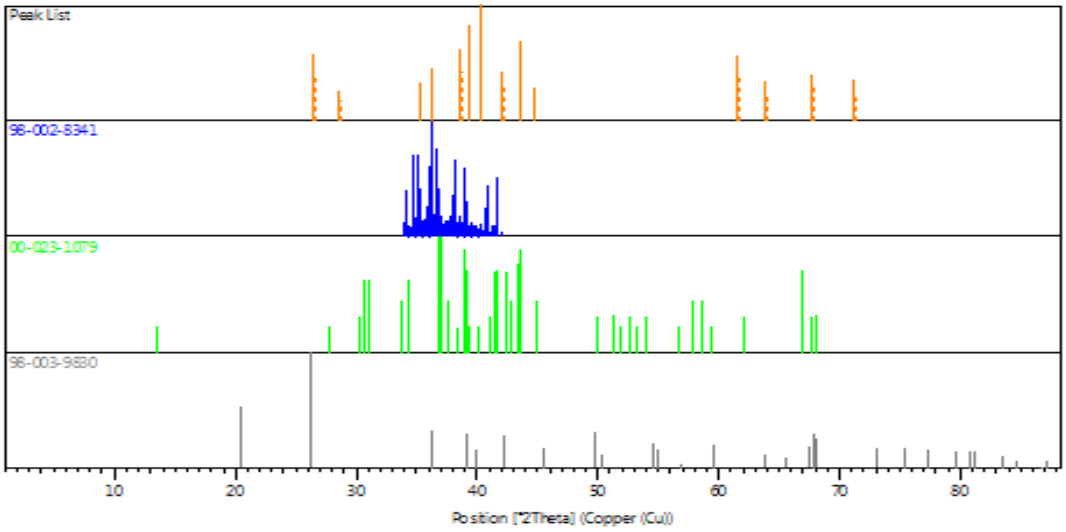

Name and formula

Reference code: 98-002-8341

Compound name: Silicon Carbide

Common name: Silicon Carbide

Chemical formula: C_1Si_1

Crystallographic parameters

Crystal system: Hexagonal

Space group: R 3 m

Space group number: 160

a (Å): 3.0790

b (Å): 3.0790

c (Å): 475.9780

Alpha (°): 90.0000

Beta (°): 90.0000

Gamma (°): 120.0000

Calculated density (g/cm^3): 3.22

Volume of cell (10^6 pm^3): 3907.84

Z: 189.00

RIR: 0.54

Subfiles and quality

Subfiles: User Inorganic

Quality: User from Structure (=)

Comments

Creation Date: 1/1/1980

Modification Date: 7/15/2000

Original ICSD space group: R3MH

Zhdanov-symbol: ((34)8 43)3. At least one temperature factor missing in the paper. No R value given in the paper. Standard deviation missing in cell constants. Polytype structure 189R

Recording date: 1/1/1980

Modification date: 7/15/2000

ANX formula: NO

Z: 189

Calculated density: 3.22

Pearson code: hR126

Wyckoff code: a126

Structure TIDY: TRANS -x,-y,-z origin 0 0 .47752

Publication title: A new polytype of silicon carbide, 189R

ICSD collection code: 28341

Chemical Name: Silicon Carbide

Second Chemical Formula: Si C

Stick Pattern

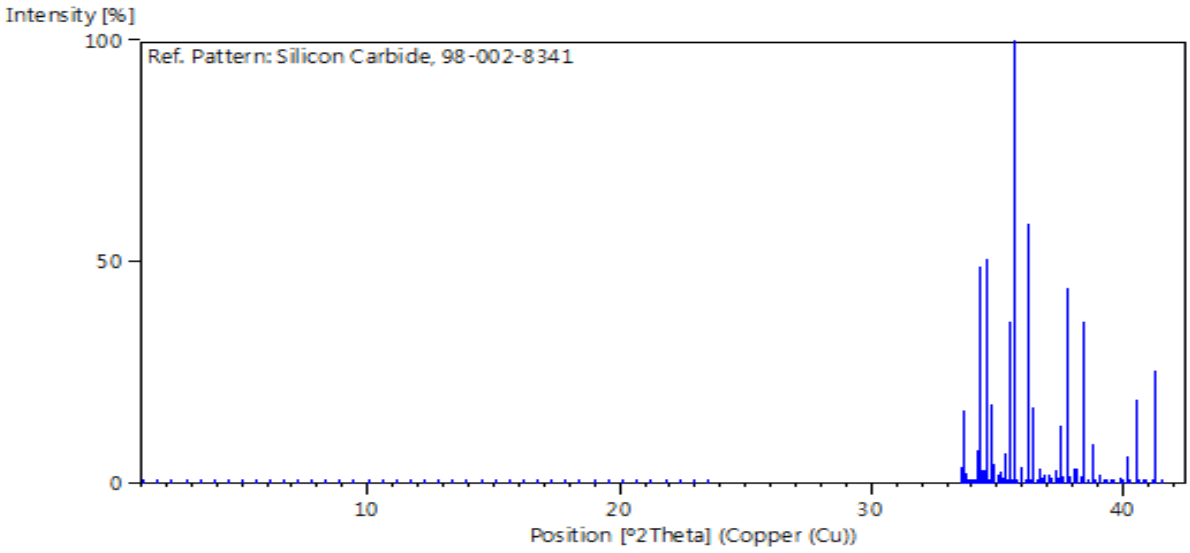

Name and formula

Reference code: 00-023-1079

Compound name: Titanium Silicide

PDF index name: Titanium Silicide

Empirical formula: Si_4Ti_5

Chemical formula: Ti_5Si_4

Crystallographic parameters

Crystal system: Orthorhombic

Space group: Pbnm

Space group number: 62

a (Å): 6.6450

b (Å): 6.5060

c (Å): 12.6900

Alpha (°): 90.0000

Beta (°): 90.0000

Gamma (°): 90.0000

Volume of cell (10^6 pm^3): 548.62

Z: 4.00

RIR: -

Subfiles and quality

Subfiles: Alloy, metal or intermetallic Inorganic

Quality: Indexed (I)

Comments

Creation Date: 1/1/1970

Modification Date: 1/1/1970

Comment: High temperature modification of Ti_5Si_4.

Stick Pattern

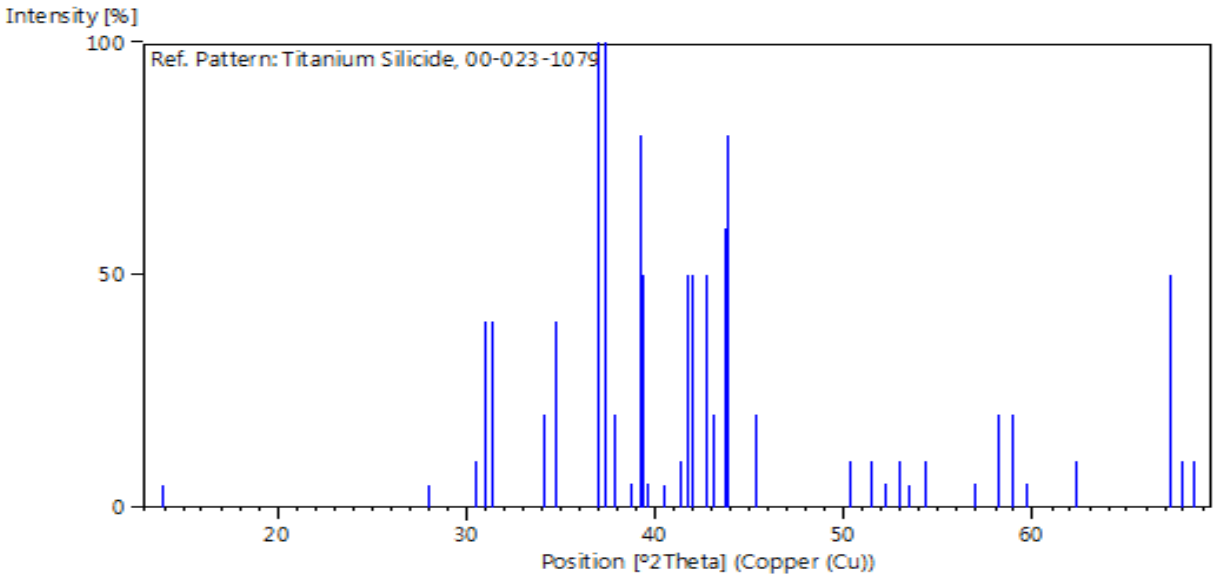

Name and formula

Reference code: 98-003-9830

Compound name: Silicon Oxide - Alpha

Common name: Silicon Oxide - Alpha

Chemical formula: O_2Si_1

Crystallographic parameters

Crystal system: Anorthic

Space group: P 1

Space group number: 1

a (Å): 4.9160

b (Å): 4.9165

c (Å): 5.4070

Alpha (°): 90.0000

Beta (°): 90.0000

Gamma (°): 119.9900

Calculated density (g/cm^3): 2.64

Volume of cell (10^6 pm^3): 113.19

Z: 3.00

RIR: 1.06

Subfiles and quality

Subfiles: User Inorganic

Quality: User from Structure (=)

Comments

Creation Date: 10/17/1995

Modification Date: 2/1/2012

Original ICSD space group: P1

AE: Si1-3: O4; O1-6: Si2; mean T-O: 1.61; mean Si-O-Si: 143,5 degree. At least one temperature factor is implausible or meaningless but agrees with the value given in the paper. No R value given in the paper. X-ray diffraction from single crystal. Structure type: SiO2(aP9). Temperature factors available. Structure type prototype: SiO2(aP9). The structure has been assigned a PDF number (experimental powder diffraction data): 77-1060.

Structure type: SiO2(aP9).

Recording date: 10/17/1995.

Modification date: 2/1/2012.

ANX formula: AX2. Z: 3.

Calculated density: 2.64.

R value: 0.046.

Pearson code: aP9.

Wyckoff code: a9.

PDF code: 01-077-1060

Structure TIDY: TRANS -a,a+b,-c -x,-y,-z origin .41510 .26740 .45320

Publication title: On the structure of alpha-Si O2 crystals doped with Fe3+

ICSD collection code: 39830

Structure: SiO2(aP9)

Chemical Name: Silicon Oxide - Alpha

Second Chemical Formula: Si O2

Stick Pattern

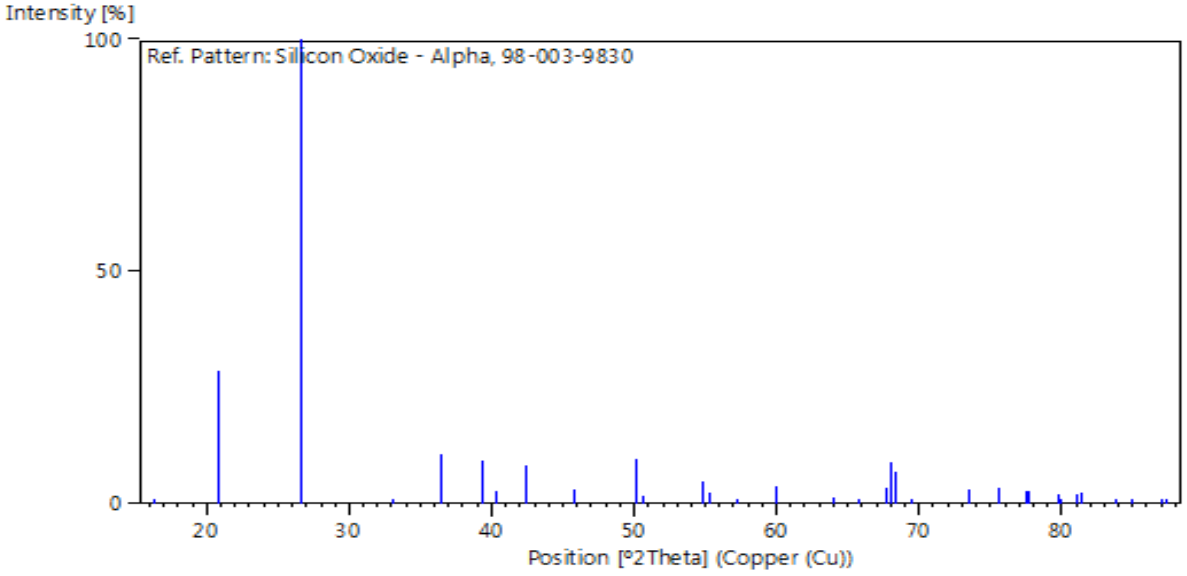
Intensity [%]
100
50
0
Ref. Pattern: Silicon Oxide - Alpha, 98-003-9830
20
30
40
50
60
70
80
Position [°2Theta] (Copper (Cu))